Normandie Université

THÈSE

Pour obtenir le diplôme de doctorat

Spécialité PHYSIQUE

Préparée au sein de l'Université de Caen Normandie

Etude de l'interaction faible dans la décroissance de l'32 AR

Présentée et soutenue par
FEDERICA CRESTO

Thèse soutenue le 19/01/2023
devant le jury composé de

M. DAVID LUNNEY	Directeur de recherche au CNRS, UNIVERSITE PARIS 11 PARIS-SUD	Rapporteur du jury
M. KARSTEN RIISAGER	Professeur, Université d'Aarhus - Danemark	Rapporteur du jury
M. GILLES BAN	Professeur des universités, ENSICAEN	Membre du jury
M. JEAN-CHARLES THOMAS	Chargé de recherche au CNRS, 14 GANIL de CAEN	Membre du jury
M. XAVIER FLECHARD	Directeur de recherche, Université de Caen Normandie	Directeur de thèse
M. BERTRAM BLANK	Directeur de recherche au CNRS, UNIVERSITE BORDEAUX 1 SCIENCES ET TECHNOLOGIE	Co-directeur de thèse

Thèse dirigée par XAVIER FLECHARD (Laboratoire de physique corpusculaire (Caen)) et BERTRAM BLANK (UNIVERSITE DE BORDEAUX)

Abstract

Over the past decades, the nuclear β-decay has steadily demonstrated as a reliable instrument to improve our understanding of the weak interaction, extensively permitting to precisely search for the possible existence of physics not originally predicted within the Standard Model (SM) of particle physics. Radioactive nuclei offer indeed unique opportunities to study the structure and the symmetries of the weak interaction, as well as to be competitive with high-energy experiments in the investigation for the possible presence of exotic scalar and tensor interactions not included within the SM firmly established vector – axial-vector (V-A) description of the weak interaction. In this framework, the experimental determination of the $\tilde{a}_{\beta\nu}$ coefficient - function of both the beta-neutrino angular correlation coefficient ($a_{\beta\nu}$) and the correlated Fierz term (b_F) - for pure both Fermi and Gamow-Teller transitions directly allows to set new limits on the existence of scalar and tensor currents, respectively.

A fundamental contribution to improve the present constraints on the scalar and tensor interactions is currently coming from the measurements performed on the kinematic energy shift of the β-delayed protons emitted by ^{32}Ar studied at the WISArD (Weak Interaction Studies with ^{32}Ar Decay) experiment, permanently installed at ISOLDE/CERN. After a successful proof-of-principle experiment and a complete estimation of the associated systematic uncertainties, an upgrade of the existing experimental set-up has been realized through the past two years, potentially permitting to reach the aimed precision of the permil level on the determination of the $\tilde{a}_{\beta\nu}$ coefficient. In this manuscript, the new experimental campaign conduced at ISOLDE in October 2021 will be presented and the related data analysis, numerical simulations and preliminary results will be discussed.

Keywords: Standard Model - V-A Theory - β-delayed proton decay - Proton-rich nuclei - ^{32}Ar - CERN - ISOLDE - WISArD experiment - Kinematic energy shift - Exotic currents - Scalar current

Resumé

La désintégration nucléaire bêta a représenté pendant plus d'un demi-siècle un terrain d'expérimentation florissant pour le Modèle Standard (MS), contribuant notamment au développement de la théorie de l'interaction électrofaible. En fait, la grande variété d'états nucléaires et de transitions bêta fournit un outil très remarquable et compétitif avec les expériences de physique des hautes énergies dans la recherche de la présence éventuelle de contributions non-MS à la description fermement établie vecteur - vecteur axial (V-A) de l'interaction faible. En particulier, la détermination expérimentale conjointe ($\tilde{a}_{\beta\nu}$) du coefficient de corrélation angulaire bêta-neutrino ($a_{\beta\nu}$) et du terme de Fierz ainsi corrélé (b_F) pour des transitions pures de Fermi et de Gamow-Teller permet directement de fixer des nouvelles limites sur l'existence de courants scalaires et tenseurs, respectivement.

La façon la plus directe d'accéder à $a_{\beta\nu}$ serait donc de mesurer la corrélation entre les leptons émis lors de la désintégration bêta; comme une mesure directe du neutrino est presque impossible, le coefficient mixte $\tilde{a}_{\beta\nu}$ peut être déterminé à partir du recul du noyau fils, qui peut être mesuré soit directement au moyen de mesures de pièges, soit indirectement, en exploitant le décalage cinématique qu'il induit sur la distribution d'énergie des particules β-retardées émises en cas de noyaux fils instables, comme envisagé par l'expérience WISArD au CERN.

L'expérience WISArD (Weak Interaction Studies with ^{32}Ar Decay) vise à une mesure précise du coefficient $\tilde{a}_{\beta\nu}$ (dépendent à la fois de a$_{\beta\nu}$ et b_F) pour des transitions Fermi et Gamow-Teller en utilisant le déplacement d'énergie cinématique des protons β-retardés émis dans la même direction ou dans la direction opposée au positron emis lors de la décroissance bêta de l'^{32}Ar. Une expérience de preuve de principe, bien que limitée en statistique et réalisée via une configuration expérimentale encore rudimentaire, a été réalisée avec succès à ISOLDE/CERN en novembre 2018, conduisant déjà à la troisième meilleure mesure de $\tilde{a}_{\beta\nu}$ pour les transitions de Fermi. Après avoir déterminé et estimé les erreurs systématiques, une mise à niveau du dispositif expérimental a été commisionée et réalisée au cours des deux dernières années, permettant potentiellement d'atteindre dans une nouvelle campagne expérimentale la précision visée du niveau du pour mille sur la détermination de $\tilde{a}_{\beta\nu}$. Dans cet objectif, une nouvelle campagne expérimentale a été conduite à ISOLDE en octobre 2021.

Dans la suite, tout d'abord une introduction générale au modèle standard de la physique des particules et à la description solidement établie vecteur – vecteur axial (V-A) de l'interaction faible sera donnée. De plus, les differentes possibilités offertes par la désintégration bêta nucléaire pour rechercher de l'éventuelle physique exotique, non prévue à l'origine dans le modèle standard, seront illustrées. Le principe de la mesure du décalage cinématique sera précisé, avec la description du dispositif experimental utilisé pour la campagne experimentale en octobre 2021. Le pre-traitement des données et la relative analyse, ainsi que les simulations Geant4 du dispositif experimental et une comparaison entre résultats experimentaux et simulés seront discutés.

Mots clés: Modèle Standard - Théorie V-A - Décroissance β-proton - Noyaux riches en protons - ^{32}Ar - CERN - ISOLDE - Expérience WISArD - Déplacement d'énergie cinématique - Courants exotiques - Courant scalaire

Contents

General introduction

The Standard Model (SM) of particle physics has represented for more than half a century a noticeably successful theory in describing elementary particles and their interactions. Over the decades, its internal consistency has been repeatedly proved either by the use of TeV-scale particle collisions at colliders or via complementary experiments at a much lower energy scale involving nuclear β-decays, which in recent years have progressively shown up as an invaluable tool to precisely test discrete symmetries and search for the existence of exotic interactions not originally included within the SM firmly established vector – axial-vector (V-A) description of the weak interaction. In this framework, the experimental determination of the $\tilde{a}_{\beta\nu}$ coefficient - function of both the beta-neutrino angular correlation coefficient ($a_{\beta\nu}$) and the correlated Fierz term (b_F) - for pure both Fermi and Gamow-Teller transitions directly permits to set new limits on the existence of scalar and tensor currents, respectively.

The most intuitive way to retrieve directly the value of the $a_{\beta\nu}$ coefficient would be to measure the correlation between the leptons emitted in the β-decay. However, as a direct measurement of the neutrino is almost impossible, the $\tilde{a}_{\beta\nu}$ mixed coefficient can be rather determined from the recoil of the daughter nucleus, which can be measured either directly by means of trap measurements or via the kinematic shift it induces on the energy distribution of the β-delayed particles emitted in case of unstable daughter nuclei. The latter approach is currently being studied at the WISArD experiment at CERN.

The WISArD (Weak Interaction Studies with ^{32}Ar Decay) experiment aims at a precise measurement of the $\tilde{a}_{\beta\nu}$ coefficient for both Fermi and Gamow-Teller transitions by using the kinematic energy shift of the β-delayed protons emitted in the same or the opposite direction to the β-particle from ^{32}Ar. A proof-of-principle experiment, though limited in statistics and performed via a still rudimental experimental set-up, has been successfully accomplished at ISOLDE in November 2018, already leading to the third best measurement of $\tilde{a}_{\beta\nu}$ for Fermi transitions. After determining and estimating the systematic errors, an upgrade of the experimental set-up has been realized through the past two years, potentially permitting to reach the aimed precision of the permil level on the determination of the $\tilde{a}_{\beta\nu}$ coefficient.

In this manuscript, the new experimental campaign with ^{32}Ar conduced at the WISArD experiment at the low-energy ion beam facility ISOLDE at CERN in October 2021 will be presented, along with the related comparison between the results from the data analysis and the associated numerical simulations. The contents presented hereinafter are organized in the following way:

- in Chapter 1, a general introduction to the Standard Model of particle physics and to the firmly established vector – axial-vector (V-A) description of the weak interaction will be given. In addition, the various possibilities offered by nuclear β-decay to search for eventual exotic physics, not originally predicted within the Standard Model, will be illustrated;
- in Chapter 2, the principle of the kinematic shift measurement will be clarified. The experimental set-up employed during the experimental campaign with ^{32}Ar at the WISArD experiment at ISOLDE in 2021 will be described, along with the differences with respect to the one used in the proof-of-principle experiment in 2018;
- in Chapter 3, the data analysis related to the single proton and the β-coincident events of the most intense pure Fermi transition of ^{32}Ar recorded during the experimental campaign in 2021 will be presented;

- in Chapter 4, the Geant4 simulations reproducing both the experimental conditions and the detection set-up will be illustrated;
- in Chapter 5, a discussion on the comparison between the experimental and the simulated data will be given. The comparison between the experimental and the simulated β-spectra will be shown, along with the comparison between the experimental and the simulated proton energy shifts. The final extraction of the $\tilde{a}_{\beta\nu}$ coefficient for pure Fermi transitions will be discussed and the preliminary studies on the associated systematic uncertainties will be presented;
- in Chapter 6, the conclusions on the work carried out and described in the previous chapters will be summarized.

In addition, the manuscript includes different appendices, comprehending additional information on the work performed and described in the previous chapters. The appendices are organized in the following way:

- in Appendix A, further complements to the theory of the electroweak interaction will be reported;
- in Appendix B, a complete description of the WISArD beamline and of the superconducting magnet section in which the detection set-up is located will be given;
- in Appendix C, additional details on data analysis and simulations will be illustrated. In particular, the computation of the statistics error on the proton energy shifts will be explained and the description of the differences between the various Geant4 *PhysicsList* packages will be detailed;
- in Appendix D, specific measurements on β-particle backscattering and further tests with radioactive calibration sources performed by means of dedicated set-ups at LP2I Bordeaux and with the WISArD proof-of-principle detection set-up in 2019 will be described. The related data analysis, Geant4 simulations and comparison between the experimental and the simulated data will be presented, together with the conclusions on the numerical constraints which have been considered for the realization of the Geant4 simulations for the 2021 experiment.

Chapter 1

The Standard Model and beyond

Ever since its formulation, the Standard Model of particle physics has represented for more than half a century a noticeably successful theory in describing elementary particles and their interactions. Having withstood more than twenty years of precision tests at high-energy particle accelerators, its internal consistency has been firmly proved, making it considerable far and away as the most complete theoretical model to describe the properties and the interactions of all the known fundamental particles up to the Planck scale, at about 10^{19} GeV. However, in spite of its incredible precision and accuracy in its predictions, the Standard Model does still leave unanswered several crucial questions, such as the origin of gravity and dark matter, whether quarks and leptons are really the most fundamental particles and why they are organised into three families, the matter-antimatter asymmetry and a physical explanation for the several parameters the model itself is based on, which have to be determined from experiments but whose theoretical origins are still unknown. In order to straighten out these and other queries, different experimental approaches have been adopted, either by exploiting astrophysical and cosmological observations, or by the use of hardly reachable TeV-scale particle collisions at colliders or, even, via more feasible experiments at a much lower energy scale, including nuclear β-decay.

In the following, the main aspects of the Standard Model relevant to β-decay will be discussed and the theoretical framework of the β-decay interaction will be presented, as well as the possibility given by β-decays to probe possible physics beyond the Standard Model.

1.1 Introduction

It was year 1898 when Ernest Rutherford dived into the study of the phenomenon recently discovered by Becquerel and which Marie Curie called radioactivity, and 1911 when he broke the mould proposing the theory of the atom [1]. Only a few decades later, the steady technological progress and the enthusiastic interest for the newly-born cosmic ray and particle accelerator physics led rapidly to the discovery of the neutron [2], the positron [3], the muon [4] and the π meson predicted by Yukawa [5]; right after, the first strange particles and resonances were observed [6]. In parallel, the rapid development of quantum mechanics and group theory fired for the first time an intense debate amidst the theoretician community on the possibility to describe all the laws of nature as a combination of different *gauge* quantum field theories, each of them reflecting the different behaviours that the fundamental interactions were reported to have with respect to different symmetry principles, in particular regarding the newly discovered isospin and strangeness conservation, as well as the sacred space-time symmetry and the recently theorized discrete symmetries of parity and charge conjugation.

Yet, following the discovery of dozens of new particles at colliders, the amount of particle species that had seemed so tiny at the end of the 1930's had rapidly multiplied into an untamed zoo by the beginning of the 1960's, and the need for a clear and solid theoretical framework that would account for the existence of such a large number of different particles and group them according to their different properties became then soon a requirement of primary exigence. Actually, the major aspiration among the international community at that time was to arrive at the elaboration of a renormalizable unique theoretical model, capable of solely describing all particles and fundamental interactions in nature as coming from a common physical origin and as related one to each other by mathematical symmetries. A first great breakthrough in this sense was made right in the mid-60s, when Glashow, Weinberg and Salam contributed independently to the formulation of the theory of the electroweak interaction [7–9], a self-consistent *gauge* theory capable of bringing together the quantum electrodynamics (QED) - the successful modern theory of the electromagnetic force - and Fermi's theory developed in the 1940's to describe for the first time via a unique formalism both the electromagnetic and the weak interaction. Concurrently, a second brilliant headway came by Gell-Mann who, similarly to what Mendeleev did with the periodic table of the elements, through the introduction of the *Eightfold Way* [10] finally succeeded to put order in the particle zoo and chart down all the known particles according to their properties of charge and strangeness, as well as to predict several still unobserved particles where gaps in his table were left; later on, together with his PhD student Zweig, he pushed even further, expounding that all the particles he had so diligently arranged in his precise classification scheme were in fact all made of few fundamental massive building blocks, called quarks. Straight after, the rapid discovery at colliders of the particles predicted by Gell-Mann (*i.e.* the η meson, the first observation of Ξ baryons and the Ω^- baryon [11]), together with the postulation of the color charge and the concept of asymptotic freedom provided the basis for the birth of the quantum chromodynamics (QCD), the mathematical description of the strong interaction.

At the beginning of the 1970's, all the joint efforts of both theoretical and experimental physicists led finally to the formulation of the Standard Model of particle physics, a single theoretical formalism regrouping both the theory of the electroweak interaction and the QCD. Henceforth, the *November revolution* triggered by the discovery of the *charm* (1974) and the *bottom* (1977) quarks from the dileptonic decay of the J/ψ [12, 13] and of the Υ mesons [14], the sensational discovery of the $W^{\pm}$ and Z boson at CERN SPS in 1983, the precision physics program conducted at LEP in the 1990's, the discovery of the *top* quark at Fermilab in 1994 [15] and the Higgs boson at the LHC in 2012 [16] represented just the icing on the cake that confirmed even more its exquisite mathematical rigour and predictive power.
After the formulation of the Standard Model, one may arguably say that the world of Particle Physics had officially entered the dawn of a new, flourishing era. However, despite its remarkable agreement with experiments, the Standard Model permits to explain only a minor fraction of our Universe, not taking into account gravity and concurrently leaving many other observations unexplained. Thus, it inherently suggests that it cannot realistically represent the ultimate theory, strongly highlighting the need for more tests of its theoretical predictions and search for evidence of new physics that may appear beyond its own frontiers.

1.2 The Standard Model of particle physics

The Standard Model (SM) is a renormalizable *gauge* theory that describes three of the four fundamental interactions acting among elementary particles (*i.e.* electromagnetic, weak and strong interaction) by employing a unique mathematical formalism, relying on the principle of local *gauge* invariance and based on the Higgs mechanism for the particle mass generation. From a theoretical point of view, the Standard Model proceeds on the assumption that all interactions in nature are manifestation of specific symmetry properties and that they can be described in terms of irreducible representations of symmetry groups. A lot of efforts have been historically spent to identify the correct group of transformations, finally resulting in the unitary product group:

$$SU(3)_C \otimes SU(2)_L \otimes U(1)_Y \tag{1.1}$$

where $SU(3)_C$ describes so the strong sector and $SU(2)_L \otimes U(1)_Y$ is related to the electroweak sector. In particular, $SU(3)_C$ is the symmetry group of the quantum chromodynamics (QCD), $SU(2)_L$ is the weak isotopic spin group acting on left-handed doublets of fermions in the weak interaction and $U(1)_Y$ represents the hypercharge symmetry group of the right-handed fermion singlets in the framework of the quantum electrodynamics (QED).

1.2.1 Elementary particles and fundamental interactions

In the Standard Model, the fundamental building blocks of matter are represented by semi-integer spin particles, the *fermions*, which interact electromagnetically, weakly and strongly through the exchange of spin-integer particles, the *bosons*.

In particular, according to specific theoretical considerations[1], the fermions are classified into three generations of quarks (u,d), (c,s), (t,b) and three generations of leptons (e,ν_e), (μ,ν_μ), (τ,ν_τ), each of them along with their corresponding antiparticles. Specifically, quarks are characterized by a fractional electrical charge and do not exist freely but bound together through the strong interaction to make hadrons; still, leptons, differently from quarks, are defined by an integer electrical charge, can exist on their own and do interact only via the electromagnetic and the weak force. Yet, the *gauge* bosons are the mediators of the fundamental forces and each of them is associated to a specific interaction: the electromagnetic force, acting within both electric and magnetic fields, is carried by the photon (γ), whereas the weak force, responsible for nuclear decays and reactions, is carried by the electrically charged $W^{\pm}$ and the neutral Z bosons and the strong force, which binds together the atomic nuclei to make them stable, is carried by the gluons (g). In particular, photons and gluons are massless and mediate respectively a long-term ($r \longrightarrow \infty$) and a short-term interaction ($r \sim 10^{-15}$ m), while the $W^{\pm}$ and Z bosons, due to the spontaneous symmetry breaking introduced by the Higgs mechanism [18–20], are indeed characterized by a large mass - more than eighty times the proton mass - and result the only responsible for the very short-term weak interaction mediation ($r \sim 10^{-18}$ m). Fermion and *gauge* boson fundamental properties are schematically resumed in Table 1.1 and 1.2, respectively.

Quarks (spin = 1/2)				**Leptons (spin = 1/2)**		
		Q	m [GeV/c^2]	flavour	Q	m [GeV/c^2]
1^{st}	u up	2/3	0.0022	e electron	-1	0.000511
	d down	-1/3	0.0047	ν_e electron neutrino	0	$< 1 \times 10^{-8}$
2^{nd}	c charm	2/3	1.27	μ muon	-1	0.106
	s strange	-1/3	0.0934	ν_μ muon neutrino	0	< 0.0002
3^{rd}	t top	2/3	172.69	τ tau	-1	1.7771
	b bottom	-1/3	4.18	ν_τ tau neutrino	0	< 0.02

Table 1.1: The three generations of fermions, *i.e* the fundamental constituents of matter.

---

[1] In the Lagrangian of $SU(2)_L \otimes \mathrm{U}(1)_Y$, the neutral-current part remains unchanged if expressed in terms of the mass eigenstates, generating in the model a natural suppression for the flavour-changing neutral currents (GIM mechanism) [17], later on confirmed by experiments. Moreover, three generations are also needed to cancel triangular anomalies and to obtain a renormalizable theory. Nowadays there are no evidences of further generations.

Unified Electroweak (spin = 1)			**Strong (color) (spin = 1)**		
Name	Q	m [GeV/c^2]	Name	Q	m [GeV/c^2]
γ photon	0	0	g gluon	0	0
W^-	-1	80.433			
W^+	+1	80.433			
Z^0	0	91.188			

Table 1.2: The *gauge* bosons, *i.e.* the force carriers.

1.2.2 Gauge invariance and symmetry properties

The Standard Model is inherently a relativistic Quantum Field Theory (QFT), in which the concept of *gauge* invariance plays a role of key importance for the description of all the fundamental interactions in nature. Basically, in QFT a physical system is described by the Euler-Lagrange field equation, in which the presence of internal symmetry properties of the Lagrangian with respect to the action of *gauge* groups permits to deduce particular conservation laws (global invariance) or to describe interactions (local invariance).

More specifically, all the elementary particles and the fundamental interactions between them can be described in theory as quanta of fields, physical systems with infinite degrees of freedom which can be fermionics, if they represent fields of matter, or bosonics, if they are mediators of forces. The dynamics of these fields is described through appropriate Lagrangians and the Principle of Minimum Action is exploited to derive the particle equations of motion. Yet, whenever the equations of motion result invariant in form under certain transformations of the dynamic variables, it becomes straightforwardly possible to identify the symmetries of a system, which can be either global or local, continuous or discrete.

Peculiarly, in the case of a continuous global symmetry, the Noether's Theorem [21] guarantees the existence of conserved physical quantities, expressed through conservation laws. In the SM, important results of global invariance are given by the conservation of the electric charge and of the total number of quarks and leptons. Additionally, as a consequence of the covariant characteristics of the physics laws themselves, the classic space-time symmetries imply the conservation of even more physical quantities, notably the energy, the momentum and the angular momentum associated to a particle as a consequence of the invariance under a translation in time, a translation in space or rotation in space respectively.

On the other hand, in case of presence of a local invariance, the *gauge* field theory permits to derive automatically the interactions between the fermionic matter fields and the *gauge* fields, whose quanta are interpreted as the bosons mediator of the fundamental interactions. In particular, the number of bosonic fields needed to be introduced to describe an interaction is equal to the number of generators of the same *gauge* group generating the local symmetry.

The very heart of the Standard Model is then composed of three local symmetry groups ($U(1)_Y$, $SU(3)_C$, $SU(2)_L$) capable of describing the three fundamental interactions (*i.e.* electromagnetic, strong and weak) and whose mathematical derivations and consequences are illustrated within the corresponding quantum theories, QED, QCD and electroweak theory respectively. On top of these continuous symmetries, there are three more discrete symmetries, all associated to fundamental properties of a physical system: the first one is related about what happens if replacing every particle, interaction, and decay with its mirror-image counterpart (*parity*), the next one refers to what happens in case of replacing every particle by its anti-particle and vice versa (*charge*) and the last one states that the laws of physics affecting the interactions of particles behave exactly the same way for time flowing forwards or backwards ($time - reversal$). In the following, the main features of the three *gauge* theories composing the SM will be briefly illustrated and an overview on the discrete CPT symmetries, particularly important for the description of the weak interaction, will be given.

1.2.2.1 Quantum electrodynamics (QED)

A first and brilliant simple example of the importance played by the Lagrangian density symmetries in the mathematical derivation of the fundamental interactions is given by quantum electrodynamics. Quantum electrodynamics (QED) is the abelian *gauge* theory of electrodynamics, which mathematically describes all phenomena involving electrically charged particles interacting by means of exchange of photons.

In principle, assuming natural units ($c = \hbar = 1$), the Lagrangian for Dirac fermions with mass m and associated quantum field ψ is given by:

$$\mathcal{L}_D = i\overline{\psi}\gamma^{\mu}\partial_{\mu}\psi - m\psi\overline{\psi} \tag{1.2}$$

The Dirac Lagrangian is inherently invariant under a global *gauge* phase space transformation:

$$\psi(x) \to \psi^{'}(x) = e^{i\alpha}\psi(x) \qquad\qquad \overline{\psi}(x) \to \overline{\psi}^{'}(x) = e^{-i\alpha}\overline{\psi}(x) \tag{1.3}$$

where the phase $i\alpha$ is in principle independent of the space-time coordinates. However, in nature the phase of wavelengths associated to particles is generally not constant and assumes a different value at each space-time point. Consequently, the phase can be simply rewritten as $i\alpha(x)$, *i.e.* as an arbitrary function of the space-time coordinates with the only requirement of dying off suitably quickly for spatial $x \to \infty$. The principle of invariance under phase transformation, this time applied locally with respect to a particular space-time coordinate x, requires the newly transformed wavefunctions to be equal to, respectively:

$$\psi(x) \to \psi^{'}(x) = e^{i\alpha(x)}\psi(x) \qquad \overline{\psi}(x) \to \overline{\psi}^{'}(x) = e^{-i\alpha(x)}\overline{\psi}(x) \tag{1.4}$$

One now finds that local *gauge* invariance is not respected, since:

$$\begin{aligned} i\overline{\psi}(x)\gamma^{\mu}\partial_{\mu}\psi(x) &\to i\overline{\psi}(x)e^{-i\alpha(x)}\gamma^{\mu}\partial_{\mu}[e^{i\alpha(x)}\psi(x)] \\ &= i\overline{\psi}(x)\gamma^{\mu}\partial_{\mu}\psi(x) - \overline{\psi}(x)\gamma^{\mu}\psi(x)[\partial_{\mu}\alpha(x)] \end{aligned} \tag{1.5}$$

The $\partial_{\mu}\alpha(x)$ term does violate the local *gauge* invariance. The resolution is that one needs to replace the ordinary derivative ∂_{μ} by the covariant derivative D_{μ} which, by definition of covariance, is constructed in such a way that the application of the *gauge* transformation will transform $D_{\mu}\psi(x)$ exactly the same way as $\psi(x)$ itself. This means that:

$$D_{\mu}\psi(x) \to D_{\mu}^{\prime}\psi^{\prime}(x) = e^{i\alpha(x)}(D_{\mu}\psi(x)) \tag{1.6}$$

and by requiring this condition, the covariant derivative is consequently defined as:

$$D_{\mu} \equiv \partial_{\mu} + ieA_{\mu} \tag{1.7}$$

where the newly introduced vector field A_{μ} which couples to the Dirac particle has transformation properties such that the unwanted term in Eq. 1.5 is canceled. In particular, under a local *gauge* transformation the vector field A_{μ} transforms as:

$$A_{\mu} \to A_{\mu}^{'} = A_{\mu} - \frac{1}{e}\partial_{\mu}\alpha(x) \tag{1.8}$$

which represents exactly the form of the electromagnetic *gauge* field.

Finally, by adding the Lagrangian a term corresponding to its kinetic energy, the full Lagrangian for charged Dirac fermions with mass m and associated field ψ interacting with the electromagnetic field becomes then:

$$\mathcal{L}_{\mathcal{QED}} = \mathcal{L}_{em} + \mathcal{L}_{D} = -\frac{1}{4}F_{\mu\nu}F^{\mu\nu} + i\overline{\psi}\gamma^{\mu}(\partial_{\mu} + ieA_{\mu})\psi - m\psi\overline{\psi} \tag{1.9}$$

where $F^{\mu\nu} = \partial^{\mu}A^{\nu} - \partial^{\nu}A^{\mu}$ is the electromagnetic field strength tensor and A_{μ} is the electromagnetic four-potential. By internal construction $F^{\mu\nu}$, and so $\mathcal{L}_{em}$, is invariant under transformation $A^{\mu} \to A^{'\mu} = A^{\mu} - \partial^{\mu}\alpha(x)$.

The full Lagrangian is then invariant both globally and locally with respect to the phase space transformation, described theoretically by the abelian *gauge* group $U(1)$. Concretely, this means that the Noether's current $J^{\mu} = \overline{\psi}\gamma^{\mu}\psi$ is conserved and so the electric charge[2]. As

---

[2] The electric charge is defined as Q = $\int d^3xJ^0$, so $\partial_{\mu}j^{\mu} = 0$ shows that it is conserved.

well, it can be noted that an addition of a mass term $\frac{1}{2}m^2 A_\mu A^\mu$ in Eq. 1.9, is prohibited, as it would break the *gauge* invariance; therefore, the corresponding *gauge* particle (photon) is massless and, consequently, the corresponding electromagnetic field has an infinite range. Moreover, the coupling constant between the fermion and photon fields is equal to e, the electric charge of the electron, which indeed gives the magnitude of the electromagnetic interaction term in Eq. 1.9. It is often expressed in terms of the *fine-structure constant*, a dimensionless quantity defined as $\alpha = \frac{e^2}{4\pi\varepsilon_0\hbar c} \approx \frac{1}{137}$.
Precision measures, such as the one of the anomalous magnetic moment of the electron [22] and the Lamb shift of hydrogen energy levels [23], have shown an impressive agreement between QED predictions and experimental data.

1.2.2.2 Quantum chromodynamics (QCD)

Quantum Chromodynamics (QCD) is the *gauge* field theory which mathematically describes the strong interaction occurring between quarks and gluons, which is characterized by six different colors (red, green, blue and the corresponding anticolors).
Its Lagrangian, symmetric under transformation of the $SU(3)_C$ group, can be written as:

$$\mathcal{L}_{QCD} \;=\; -\frac{1}{4}\, G_a^{\mu\nu}\, G^a_{\mu\nu} \;+\; \sum_f \overline{q_f}\,(i\,\gamma_\mu\, D_\mu \;-\; m_f)\, q_f \tag{1.10}$$

where $G_a^{\mu\nu}$ is the gluon field tensor, q_f represents the quark field, γ_μ the Dirac matrices and m_f the quark mass, while a and f are the gluon color and the flavour indexes. Similarly to QED, the invariance under local *gauge* transformations is required introducing the covariant derivative $D_\mu \equiv \delta^\mu + i g_s \frac{\lambda^a}{2} G_a^\mu$, which explicitly contains λ^a, which correspond to the eight generators of the fundamental representation of $SU(3)$ represented by the Gell-Mann matrices. The gluon tensor can be decomposed as:

$$G_a^{\mu\nu} \;=\; \partial^\mu\, G_a^\nu \;-\; \partial_\nu\, G_a^\mu \;-\; g_s \sum_{b,c=1}^{8} f_{abc}\, G^{\mu b}\, G^{\nu c} \tag{1.11}$$

where G_a^ν is the gluon field and f_{abc} the structure constants of $SU(3)$.
So far, the precedent relations fully describe the characteristics of the strong interaction. In particular, this formalism clearly states that all interactions between quarks and gluons are given in terms of g_s, the strong coupling constant standardly rewritten as $\alpha_s = g_s^2/4\pi$. Moreover, the first term in Eq. 1.10 defines the *gluon self-interaction*, a property deriving directly from the non-abelian character of the color group and which gives rise to the main features that differentiate QCD from QED. Practically, this is responsible for the main concepts of QCD, *i.e. asymptotic freedom* and *color confinement*. In fact, in QED the

electromagnetic field intensity progressively decreases with the distance from the source, which means theoretically that the associated coupling constant decreases at large distances, an effect that can be intuitively explained considering the charge screening generated by a virtual fermion pair. Differently, in QCD this self-interaction causes the potential between quarks to increase with distance, so more and more energy is required to pull them apart. In other words, gluons, differently from photons, do have an additional property of color charge and this property indeed determines an increase of the strong field at large distances, also called *anti-screening*. In particular, the dependence of the strong coupling constant on the momentum transferred in the interaction can be written as:

$$\alpha_s(Q^2) = \frac{\alpha_0}{1 + \alpha_0 \frac{33-2n_f}{12+\pi} \ln \frac{Q^2}{\mu^2}} \tag{1.12}$$

where α_0 is the coupling constant for a given momentum transferred Q and n_f is the number of quark flavours. From this expression it can straightforwardly be observed that the strength of the strong coupling constant decreases for short distances ($Q \to \infty$), allowing quarks to behave as quasi-free particles. This particular property is called *asymptotic freedom* and it allows to treat QCD as a perturbative theory when $\alpha_s \to 0$. On the contrary, for large distances ($Q \to 0$), the coupling constant becomes large and color charges appeared to be bound within hadrons, in the so called *confinement regime*.

1.2.2.3 Electroweak theory

The electroweak theory aims at unifying the theory of weak and electromagnetic interactions. It is entirely based on the concept of chirality, a fundamental property of particles which refers to the way the particle wave function behaves under particle rotation, *i.e.* after a change in the complex phase of the wave function itself. The particle chirality determines in a sense which way around the complex plane this phase travels to reach -1, either in a left-handed way from 1 to -1 or in a right-handed way from 1 to -1.

Practically, the effect of chirality can be seen in the different way the weak interaction treats particles and antiparticles. In particular, fermions are grouped according to the their chirality eigenstate, *i.e.* in left–handed and right–handed fields $\psi_{L,R}$, where:

$$\psi_L = P_L \psi = \frac{1}{2}(1-\gamma^5)\psi \qquad\qquad \psi_R = P_R \psi = \frac{1}{2}(1+\gamma^5)\psi \tag{1.13}$$

and $P_{L,R}$ is the left(right)-handed projection operator expressed as a function of the γ-matrices. However, after the evidence of the parity violation from the Madame Wu's experiment [24] and the determination of the helicity of the neutrino by Goldhaber [25], it was concluded that the weak current mediated by what nowadays is called the W boson acts only on left-chiral fermions (and right anti-fermions). On the other hand, from a theoretical point of view, only elements regrouped in $SU(2)_L$ doublets interact with the W boson. Consequently, the joint conclusion is that the weak interaction can act uniquely on left-handed particles (and right-handed antiparticles) described as $SU(2)_L$ doublets, while right-handed fermions (and left-handed antifermions) should be described as $SU(2)_L$ singlets in order to avoid their interaction with the W boson.

Hence, there are three families of quarks:

$$\begin{pmatrix} \mathrm{u} \\ \mathrm{d} \end{pmatrix}_L, \begin{pmatrix} \mathrm{c} \\ \mathrm{s} \end{pmatrix}_L, \begin{pmatrix} \mathrm{t} \\ \mathrm{b} \end{pmatrix}_L, \qquad (\mathrm{u})_R, (\mathrm{d})_R, (\mathrm{c})_R, (\mathrm{s})_R, (\mathrm{t})_R, (\mathrm{b})_R \tag{1.14}$$

and, analogously, three families of leptons:

$$\begin{pmatrix} \nu_e \\ \mathrm{e} \end{pmatrix}_L, \begin{pmatrix} \nu_\mu \\ \mu \end{pmatrix}_L, \begin{pmatrix} \nu_\tau \\ \tau \end{pmatrix}_L, \qquad (\mathrm{e})_R, (\mu)_R, (\tau)_R \tag{1.15}$$

The electroweak theory is invariant under transformation of the group $SU(2)_L \otimes \mathrm{U}(1)_Y$. In particular, weak hypercharge and electric charge are linked to the weak isospin by the relation:

$$Q = I_3 + \frac{Y}{2} \tag{1.16}$$

where Q is the electric charge (in elementary charge units) of the particle and I_3 is the third component of its weak isospin. Hypercharge symmetry involves both chiralities, *i.e.* the Lagrangian density is invariant under the transformations of the $U(1)_Y$ *gauge* group:

$$\psi_{L,R} \quad \rightarrow \quad \psi_{L,R} \; e^{i\alpha(x)\frac{Y}{2}\psi_{L,R}} \tag{1.17}$$

while weak isospin symmetry involves only left–handed doublets, with invariance under transformations of $SU(2)$:

$$\psi_{L,R} \quad \rightarrow \quad \psi_{L,R} \; e^{i\beta_\alpha(x)\frac{\tau^a}{2}\psi_L} \tag{1.18}$$

where $\tau^a/2$ are the Pauli matrices, corresponding to the generators of $SU(2)$ itself. Similarly to the process shown for the electromagnetic interaction in Sec. 1.2.2.1, it is possible to derive the Lagrangian density for the electroweak interaction and subsequently study its symmetry properties. In particular, in total analogy with QED, four new *gauge* fields, mediated by a triplet of vector boson W_i^μ (i = 1,2,3) for $SU(2)$ and by a singlet B^μ for $U(1)_Y$, need to be introduced. Specifically, while the W_i^μ fields couple only to left–handed fermion fields, B^μ couples to fermions of both chirality. Physical fields, corresponding to the four observed bosons – two neutral, the photon and the Z boson, and two charged, the W^+ and W^- bosons –

can be then obtained with the linear combinations:

$$\begin{aligned} A^{\mu} &= \sin\theta_W \, W_3^{\mu} \; + \; \cos\theta_W \, B^{\mu} \\ Z^{\mu} &= \cos\theta_W \, W_3^{\mu} \; - \; \sin\theta_W \, B^{\mu} \\ W_{\pm}^{\mu} &= \frac{W_1^{\mu} \mp iW_2^{\mu}}{\sqrt{2}} \end{aligned} \tag{1.19}$$

where θ_W is the weak mixing angle. From the expression of the covariant derivative in the electroweak Lagrangian, one can express g and g', the coupling constants of $SU(2)$ and $U(1)$, as a function of the unique parameter θ_W via the following relations:

$$\sin\theta_W \; = \; \frac{g'}{\sqrt{g^2+g'^2}} \qquad\qquad \cos\theta_W \; = \; \frac{g}{\sqrt{g^2+g'^2}} \tag{1.20}$$

Moreover, the electric charge e can be rewritten as $e = g\sin\theta_W = g'\cos\theta_W$.

1.2.2.4 CKM matrix

For completeness, the electroweak Lagrangian density can be rewritten as the sum of two terms, one including the interactions between the Neutral Current and the A_μ and Z_μ field bosons (NC) and another describing the interaction of the $W_\mu^{\pm}$ with the Charged Current (CC):

$$\mathcal{L}_{\mathcal{EW}} \; = \; \mathcal{L}_{\mathcal{NC}} \; + \; \mathcal{L}_{\mathcal{CC}} \tag{1.21}$$

with:

$$\begin{cases} \mathcal{L}_{\mathcal{NC}} \; = \; -\,e\,J_{\mu}^{em}\,A^{\mu} \; + \; \frac{g}{2\,\cos\theta_W}\; J_{\mu}^{0}\; Z^{\mu} \\ \mathcal{L}_{\mathcal{CC}} \; = \; \frac{g}{2\,\sqrt{2}}\; (J_{\mu}^{+}\,W_{\mu}^{+} \; + \; J_{\mu}^{-}\,W_{\mu}^{-}) \end{cases} \tag{1.22}$$

where the charged weak currents of quarks can be rewritten as:

$$J^{\mu} \; = \; (\overline{\psi_u}\;\bar{c}\;\bar{t})\;\; \frac{\gamma_\mu\;(1\;-\;\gamma^5)}{2}\; V_{CKM}\; \begin{pmatrix} d \\ s \\ b \end{pmatrix} \tag{1.23}$$

In particular, weak charged currents are the only tree-level interaction in the SM that may induce a change of flavour. This means that the emission of a W boson transforms an up-type quark into a down-type quark, or equivalently a ν_ℓ neutrino into a ℓ^- charged lepton. Concretely, if considering as an example a u quark, which represents intrinsically a mass eigenstate, the emission of a W turns it into its weak isospin partner, the down-type quark state d', which in general does not coincide with its original mass eigenstate due to the symmetry-breaking mechanism that gives the quarks their different masses. In other words, the weak interaction does rotate the quark states and the mixing between their generations is theoretically described by the unitary matrix derived by Cabibbo, Kobayashi and Maskawa (CKM):

$$V_{CKM} = \begin{pmatrix} V_{ud} & V_{us} & V_{ub} \\ V_{cd} & V_{cs} & V_{cb} \\ V_{td} & V_{ts} & V_{tb} \end{pmatrix} \tag{1.24}$$

All the properties of the weak quark interaction are codified inside the CKM matrix. Indeed, the CKM matrix is, by construction, unitary and consequently its nine elements can be standardly parametrized as a function of only four independent parameters, *i.e.* three Euler rotating angles (θ_{12}, θ_{13}, θ_{23}) and a complex phase term (δ_{13}), whose imaginary part does represent the source of the CP-violating phenomena mediated by the weak interaction. Furthermore, its structure incorporates the GIM mechanism, which explains from a theoretical point of view the suppression of the flavour-changing neutral-currents observed in experiments. Moreover, the unitarity of V_{CKM} ($V^{\dagger}\text{V} = VV^{\dagger} = 1$) implies three relations of universality of the weak interaction that only involve the moduli of the matrix elements:

$$\sum\nolimits_{i\,=\,d,s,b} |V_{ai}^2| = 1, \qquad a = u,\, c,\, t \tag{1.25}$$

and three further triangular relations that also depend on their phases:

$$\sum\nolimits_{i\,=\,d,s,b} V_{ai}^2\;(V_{bi}^*) = 0, \qquad a \neq b = u,\, c,\, t \tag{1.26}$$

The values of the CKM matrix, related through the precedent relations, are not fixed by theory and must be evaluated on the basis of the available experimental information. Yet, the only thing known from theory is that, by rewriting V_{CKM} as a function of the four Wolfenstein parameters A, λ, $\overline{\rho}$ and $\overline{\eta}$, the three diagonal terms describing the transitions between quarks of the same generation are $\mathcal{O}(1)$, while the off-diagonal elements related to transitions between different generations get progressively smaller for higher mass states[3]. This highly predictive framework motivated many experiments to try to measure all the parameters of the CKM matrix by studying specific classes of processes and by exploiting the relations between the experimental determinations of decay rates or branching ratios and the relevant matrix elements. Specifically, concerning the first row, V_{ud} is determined by *superallowed*

---

[3] Transitions between families $1 \rightarrow 2$, $2 \rightarrow 3$ and $1 \rightarrow 3$ are suppressed by a factor λ, λ^2 and λ^3, respectively.

transitions, neutron and pion decay, V_{us} from kaon and hyperon semileptonic decays and V_{ub} from leptonic and semileptonic B decays. In the second row, V_{cd} has been historically inferred from neutrino-antineutrino interactions on valence d quarks inside a proton and subsequently from semileptonic charmed meson decays, V_{cs} and V_{cb} from semileptonic decays of D and B mesons, respectively. In the third row, V_{tb} can be derived from single top quark production cross sections at hadron colliders, while limits on $|V_{td}/V_{ts}|$ can be obtained from $B-\overline{B}$ oscillations.

Up to now, the most stringent limits on the magnitude of the elements of V_{CKM} are[4] [11]:

$$V_{CKM} = \begin{pmatrix} 0.97435 \pm 0.00016 & 0.22500 \pm 0.00067 & 0.00369 \pm 0.00011 \\ 0.22486 \pm 0.00067 & 0.97349 \pm 0.00016 & 0.04182^{+0.00085}_{-0.00074} \\ 0.00857^{+0.00020}_{-0.00018} & 0.04110^{+0.00083}_{-0.00072} & 0.999118^{+0.000031}_{-0.000036} \end{pmatrix} \quad (1.27)$$

The most striking feature is that the diagonal elements are clearly dominant, meaning that the weak transitions between different quark generation are indeed strongly suppressed.

As will be discussed in Sec. 1.4, tests of unitarity of the CKM matrix represent a fundamental tool in the search for physics beyond the Standard Model.

1.2.2.5 CPT symmetry

For a long time now physicists have done their utmost to find out the intimate connection between geometric symmetries and the dynamic behaviour of material bodies. In particular, beside the *gauge* symmetry properties exquisitely derived from quantum field theory summarized in Sec. 1.2.2, two further concepts which indeed reflect the fundamental symmetries of nature have been introduced to explain all the known physics phenomena: Lorentz-invariance and CPT symmetry. Yet, Lorentz-invariance is the basic continuous symmetry of space-time, stating that all physics laws are invariant under space-time translations and spatial rotation, with the consequent conservation of particle momentum, total energy and angular momentum respectively. Conversely, the CPT symmetry involves the discrete charge conjugation (C), space (P) and time (T) inversion operators and it is inherently linked to the homonymous theorem, which imposes the invariance of a physical system under the operations of spatial inversion, time inversion and charge conjugation.

Theoretically constructed on the principle of Lorentz-invariance, the CPT theorem has been mathematically proved for the first time by Lüders and Pauli [26, 27] via the Hamiltonian formulation of quantum field theory, based on the principle of locality of the interaction. Subsequently, a more general demonstration, based on the principle of weak local commutativity,

---

[4] The value of V_{ud} and its associated uncertainty depend on theoretical corrections still under investigation. The ongoing work, especially on these corrections, will likely lead to different values of V_{ud}.

was made by Jost [28] in the framework of the axiomatic formulation of quantum field theory, thus eliminating any reference to any specific form of interaction. Basically, it says that any physical system made of particles that moves forwards in time will obey the same laws as the identical physical system made of antiparticles, reflected in terms of spacial coordinates, that moves backwards in time. Fundamentally, one can consider the following discrete operator:

$$\Phi = CPT \tag{1.28}$$

which is given by the composition of the charge, parity and time-reversal operators, respectively. By applying it to any particle described by a square-summable wave function[5] ψ, one obtains its CPT-conjugate state:

$$|\Phi\,\psi\rangle = \Phi\,|\psi\rangle \equiv |\overline{\psi}\rangle \tag{1.29}$$

The primary physical consequence is that the particles and the corresponding antiparticles, obtained one from each other via the application of the charge-conjugation operator, must have opposite electrical charge and exactly the same mass, lifetimes and gyromagnetic ratios; over the decades, this assumption has been univocally demonstrated to be correct [11]. A second fundamental implication is that, consequently to any violation of one of the fundamental symmetries (or a pair of them), there must be a concomitant compensating violation of the other two (or the other one) in order to ensure the overall exact symmetry under CPT transformation.

In particular, the electromagnetic and the strong interaction conserve the three discrete symmetries, while the weak interaction violates singularly both parity and charge conjugation, and in addition also the combined CP-symmetry. Effectively in the 1940's, at the early heyday of nuclear physics, two new particles having the same mass and lifetime but decaying in different modes were surprisingly discovered: θ^+, decaying into two pions, and τ^+, decaying into three charged pions. As parity is a multiplicative quantity, the conclusion was that either the two mesons were indeed different particles or parity was not conserved. The groundbreaking solution for the $\tau - \theta$ puzzle was initially suggested by Lee and Yang [29], who controversially proposed that the problem could be solved by accepting parity violation; later on, this scenario was dramatically confirmed by the Wu's experiment on ^{60}Co parity violation [24], definitely decreeing that the two particles were in fact one and the same particle, later know as the K^+ meson. Thus, the weak interaction does violate P, whereas it generally preserves invariance under CP transformation, with the only exceptions found

---

[5] Formally, ψ belongs to the unitary complex L^2 Hilbert space, whose main characteristics are the presence of a positive-defined inner product operation, fundamental to guarantee the probabilistic interpretation of the wave functions in quantum mechanics, and the completeness of the metric space, assured by the Riesz-Fisher theorem and necessary to rewrite the particle state as an infinite sum of definite momentum or energy states.

in the neutral K^0 and B^0 systems. In particular, in the first case the evidence for a slight CP violation comes from the fact that the short-living symmetric linear combination of the K^0 and $\overline{K^0}$ states, invariant under charge-parity conjugation, has always been observed to decay into two pions as expected, while the long-living antisymmetric linear combination, not invariant under CP transformation and thus predicted to decay into three pions, has been observed to decay into a couple $\pi^+\pi^-$ at the level of $\sim 2 \times 10^{-3}$ in experiments E731 [30] and E832 [31] at Fermilab and at NA31 [32], NA48 [33] and CPLEAR [34, 35] at CERN. Evidence for CP violation has been found also from differences in the decay rates of some final states of B^0-$\overline{B^0}$ couples, produced in the strong decay of $\Upsilon(4S)$ created by means of high-energy electron-positron collisions at the B-factories, *i.e.* BaBar at SLAC [36], Belle II at KEK [37] and LHCb at CERN [38, 39].

Experimentally, although the individual symmetries, or a combination of them, have been observed to be violated in the weak interaction, no evidence for violation has ever been observed for their combined product, CPT, which remarkably remains an exact symmetry.

1.3 Nuclear β-decay and the $V-A$ theory

Nuclear β-decay has represented for more than four decades a blooming testing ground for the Standard Model, becoming definitely the most fully investigated manifestation of the weak force and contributing particularly to the development of the theory of the electroweak interaction. Consisting in a rapid charge-changing process mediated by the highly massive $W^{\pm}$ and Z bosons, as all weak processes occurring at energy scales characteristic of nuclear reactions it has been primarily rather well described by Fermi as an effective point-like interaction and subsequently, a few decades later and at a higher level of precision, via the actually firmly established vector–axial-vector (V-A) theory.

In the following, the main characteristics of nuclear β-decay will be presented and the progress towards the formalism of the V-A theory will be discussed.

1.3.1 Nuclear β-decay

The phenomenon of creation and expulsion by the nucleus of high energy electrons in the course of a radioactive change had already been observed by Rutherford in 1899, and the related process of positron emission in a radioactive decay was discovered by the Joliot-Curies way after, in 1934. Both decays, together with the electron capture theorized in the same year and discovered a few years later, were straightforwardly grouped under the common name of nuclear β-decay.

Nuclear β-decay is a nuclear process characterized by the decay of a neutron into a proton (or vice versa) accompanied to the emission of two leptons, an electron (positron) and an antineutrino (neutrino), thus ensuring the conservation of the lepton number and total angular momentum and determining in both cases the change of the charge of the parent nucleus by one unit. Specifically, three types of such nuclear weak processes do exist:

- β^--decay: $n \longrightarrow p + e^- + \overline{\nu_e}$ $(A,Z) \longrightarrow (A,Z+1) + e^- + \overline{\nu_e}$
- β^+-decay: $p \longrightarrow n + e^+ + \nu_e$ $(A,Z) \longrightarrow (A,Z-1) + e^+ + \nu_e$
- electron capture: $p + e^- \longrightarrow n + \nu_e$ $(A,Z) + e^- \longrightarrow (A,Z-1) + \nu_e$

In particular, all the leptons present in the final states are created directly during the interaction. Moreover, the process of electron capture, occurring when the parent nucleus captures one of its shell electrons, generally competes with the β^+-decay in proton-rich nuclei when the available decay energy (Q-value) is above the threshold of 1022 keV.
As first suggested by Pauli and later on confirmed by Fermi, in nuclear β-decay the energy of the system in the final channel is divided among the daughter nucleus and the charged (e^-/e^+) and neutral ($\nu_e/\overline{\nu_e}$) leptons, so that the resulting lepton energy (or momentum) spectra are given by a continuous distribution, varying individually from zero up to the *endpoint* value, equal to the energy difference between the initial and the final states. In particular, energy and momentum spectra of a given nucleus coming from β^+-decay result in values higher than that corresponding to a β^- decay of the same nucleus, due to Coulomb repulsion between the positron and the positively charged daughter nucleus.
According to the Fermi's theory of beta decay, originally formulated in 1934 [40], the decay rate per time interval can be obtained through Fermi's golden rule as:

$$d\omega = \frac{g^2}{2\,\pi^3\,\hbar^7\,c^3}\,|M_{if}|^2\,F(Z_D,E_e)\,(E_f - E_e)\,\sqrt{(E_f - E_e)^2 - m_\nu^2\,c^4}\,p_e^2\,dp_e \qquad (1.30)$$

where g is the Fermi coupling constant that characterizes the strength of the interaction, E_f is the energy available in the final state, E_e and p_e are the β-particle energy and momentum and $F(Z,E_e)$ represents the Fermi function, which describes the deformation of the β-spectrum due to the electromagnetic interaction of the β-particle with the Coulomb field of the daughter nucleus. Furthermore, M_{if} is the nuclear-dependent transition matrix, whose square norm expresses the probability for the interaction to occur and which can be rewritten as:

$$M_{if} = g\,\langle \psi_f \,|\, \sum_i \mathcal{O}_i \,|\, \psi_i \rangle \qquad (1.31)$$

where the sum $\sum_i$ is over all the nucleons of the decaying nucleus, ψ_i (ψ_f) represents the total wave function of the parent (daughter) nucleus and $\mathcal{O}_i$ indicates the operators describing the transitions in the spin and the isospin space. In particular, M_{if} is strictly intertwined to a main observable of β-decay, the ft-value, which can be interpreted as the nucleus mean lifetime corrected by nuclear effects (Z_D, charge of the daughter nucleus) and the available β-decay energy (η_0). The mutual relation can be expressed as:

$$ft - value \;=\; f(Z_D, \eta_0)\, t_{1/2} \;=\; \frac{2\,\pi^3 \hbar\,(\hbar c)^6}{(m_e\,c^2)^5}\,\frac{1}{g^2\,|M_{if}|^2} \;=\; \frac{const.}{g^2\,|M_{if}|^2} \tag{1.32}$$

The value of ft varies from a minimum of 10^3 for the most probable to a maximum of 10^{22} for the rarest β-decays. Specifically, the most probable decays, so-called *allowed*, correspond to no change in parity and to a net orbital angular momentum $\ell = 0$, while the rarest processes, also called *forbidden*, occur when $\ell > 0$ (for details see Appendix A). Moreover, beyond this distinction, nuclear β-decays can also be classified into three other types: pure Fermi, where the emitted leptons are in a singlet state due to their anti-parallel spin vectors, pure Gamow-Teller, in which the leptons appear in a triplet state due to their parallel spin vectors, and mixed Fermi–Gamow-Teller, satisfying both Fermi and Gamow-Teller selection rules and typically occurring between mirror nuclei and in odd-A proton-rich nuclei. In particular, for a pure allowed Fermi transition, also referred to as *superallowed*, the coupling constant g in Eq. 1.32 identifies the weak coupling constant (also named g_V), and the transition operator, *e.g.* in β^--decay, is $\mathcal{O} \equiv \tau^+$, with τ^+ the isospin raising operator which increases the isospin of the system by one unit, thus accounting for the transition of a neutron into a proton[6]; instead, in the case of a pure allowed Gamow-Teller transition, this operator can be expressed as $\mathcal{O} \equiv \sigma\tau^+$, where $\sigma \equiv (\sigma_1, \sigma_2, \sigma_3)$ represents the vector of Pauli spin matrices and the constant g identifies the axial-vector coupling constant (g_A) associated to the weak processes.

1.3.2 Fermi's four-point interaction

The seventh Solvay Conference, held in Brussels in 1933, had represented a milestone of invaluable importance in the history of nuclear physics. Drawing the most brilliant luminaries of two generations of physicists, such as Marie Curie, Bohr, Lise Meitner, Heisenberg, Chadwick, Pauli, Fermi and a George Gamow just escaped from the Soviet Union, it gave rise to an intense debate on the critical points of the atomic physics of the period, including the discovery of the neutron, the nature of the positron and the neutrino hypothesis [41]. In this context, Enrico Fermi had the opportunity to know the state of art of nuclear physics which, a few months later, allowed him to complete the major theoretical work of his life, the formulation of the first β-decay theory.

---

[6] The isospin associated to neutrons is $-\frac{1}{2}$ and that for protons is $+\frac{1}{2}$. Conversely, for a β^+-decay, $\mathcal{O} \equiv \tau^-$.

In total analogy to the electromagnetic interaction, consisting at a quantum level by the emission of a photon by the electron, Fermi described the weak interaction responsible for nuclear β-decay as a point interaction of four participating fermions, specifically consisting in the emission of an electron-neutrino pair by the neutron, which conversely converts itself into a proton, in the case of a β^--decay, and vice versa in case of a β^+-decay. In particular, according to QED, the electromagnetic interaction is explained in terms of an interplay between the electromagnetic vector current J_E associated to the charged particle and the electromagnetic vector potential A, which is the quantum version of the vector potential in classical electrodynamics from which the electric and magnetic field can be properly derived and which represents the field operator for the photon:

$$\mathcal{L}_{int}^{\mathcal{QED}} = e\, J_E^{\mu}\, A_{\mu} \tag{1.33}$$

where e represents the numerical value of the electrical charge of the electron and characterizes the strength of the electromagnetic interaction[7]. Analogously, Fermi described the weak interaction as a point interaction of four fermions structured into two charged four-currents (the nucleon and the lepton one), presenting again vector transformation properties. Specifically, the interaction term in the Hamiltonian of a β^--decay is hence given by [40]:

$$\begin{aligned}\mathcal{H}_{int}^{\beta^-} &= -\frac{G_F}{\sqrt{2}}\,[\,\overline{\psi_p}(x)\,\gamma_\mu\,\psi_n(x)\,]\,[\,\overline{\psi_e}(x)\,\gamma^\mu\,\psi_\nu(x)\,] + h.c.\\ &= -\frac{G_F}{\sqrt{2}}\,[J_l^\dagger(x) + J_h^\dagger(x)\,]\,[J_l(x) + J_h(x)] + h.c.\\ &= -\frac{G_F}{\sqrt{2}}\,J_l^\mu(x)\,J_\mu^h(x) + h.c.\end{aligned} \tag{1.34}$$

where J_l and J_h are the four-vectors representing the leptonic and hadronic currents respectively. Moreover, Fermi's Hamiltonian predicts in fact the universality of the weak interaction, as it depends only on the Fermi coupling constant G_F, which actually characterizes the strength of the weak interaction and has been experimentally determined to be $G_F/(\hbar c)^3 = 1.16639(1) \times 10^{-5}\ GeV^{-2}$ [42]. Effectively, similarly to the QED Lagrangian, expressed in the form $\mathcal{L}_{QED}^{int} \propto J^\mu A_\mu$, the weak Lagrangian is characterized by the fermion charged current $J^\mu = \overline{\psi}\gamma^\mu\psi$ and is intrinsically given by the product of four fermion fields $\overline{\psi_p}\psi_n\overline{\psi_e}\psi_\nu$, which represent indeed in modern QFT the particle and antiparticle creation and annihilation operators responsible for the increasing (decreasing) of the electrical charge by one unity in nuclear $\beta^\pm$-decay.

---

[7] Eq. 1.33 represents the interaction term of the QED Lagrangian (see Eq. 1.9), denoting the corresponding electron-photon vertex function. J_E is the sum of all the charged particle-antiparticle field operator products ($e.g.$ $\psi_p\overline{\psi_p}$, $\psi_e\overline{\psi_e}$).

Finally, in order to make this four-term product a Lorentz invariant, a current-current product $J^{\mu} J_{\mu}$ has been introduced.

1.3.3 The $V-A$ theory

Despite being derived almost exclusively on an intuitive basis, Fermi's theory of the weak interaction stood the test of time for more than two decades, until the discovery of parity violation made it necessary to incorporate attendant amendments to the original mathematical description. Indeed, as the nuclear β-decay was then associated to the maximal expression of parity symmetry violation, the corresponding Hamiltonian was subsequently described independently by Sudarshan and Marshak, Gell-Mann, Feynman and Sakurai in 1957 as an equal mixture of both the original vector (V) and the newly introduced axial-vector (A) currents. Effectively, while vector components remain the same under parity transformation, the axial-vector ones behave differently, changing sign by moving from a left to the corresponding right-handed coordinate system.

However, more generally, the only theoretical constraint for the construction of the Hamiltonian associated to nuclear β-decay consists in the requirement of its Lorentz-invariance. According to QFT, there are five different ways to rewrite a physical law such that it is Lorentz covariant. In particular, the β-decay Hamiltonian can be rewritten as the sum of five different Dirac bilinear covariant fields expressed via the Dirac γ-matrices:

$$\mathcal{H}_{\beta} = \sum_{i} g_i \left(\overline{\psi_p}\, \mathcal{O}_i\, \psi_n\right) \left(\overline{\psi_e}\, \mathcal{O}_i\, \psi_\nu\right) + h.c. \qquad i = S, V, T, A, P \tag{1.35}$$

where $g_i = g_F\, C_i$, with g_i the overall coupling constant measuring the strength of the weak interaction and C_i the coupling constants expressing the relative strength of the five different interaction types. As well, $\mathcal{O}_i$ are the Dirac bilinear forms, which owe their names and differ one from the other on their properties under Lorentz transformation:

$$\begin{aligned}
\mathcal{O}_S &= 1 && Scalar\ (S)\\
\mathcal{O}_V &= \gamma_\mu && Vector\ (V)\\
\mathcal{O}_T &= \sigma_{\mu\nu} \equiv \frac{i}{2}\left(\gamma_\mu\, \gamma_\nu - \gamma_\nu\, \gamma_\mu\right) && Tensor\ (T)\\
\mathcal{O}_A &= \gamma_5\, \gamma_\mu && Axial-Vector\ (A)\\
\mathcal{O}_P &= \gamma_5 && Pseudoscalar\ (P)
\end{aligned} \tag{1.36}$$

Furthermore, even more generally speaking, the requirement of a Lorentz-invariant Hamiltonian taking properly into account parity violation does result in the demand for an Hamiltonian given by the superposition of both a scalar ($\mathcal{H}_{even}$) and a pseudoscalar ($\mathcal{H}_{odd}$) component, which respectively persist unmodified and change sign under parity transformation. Definitely, the most generalized form of the Hamiltonian can be written as:

$$\begin{aligned} \mathcal{H}_\beta &= \mathcal{H}_{even} + \mathcal{H}_{odd} \\ &= g_F \sum_i (\overline{\psi_p}\, \mathcal{O}_i\, \psi_n)\, (\overline{\psi_e}\, \mathcal{O}_i\, (C_i + C_i^{'}\, \gamma_5)\, \psi_\nu) + h.c. \end{aligned} \tag{1.37}$$

which extensively becomes:

$$\begin{aligned} \mathcal{H}_\beta &= \frac{G_F}{\sqrt{2}} V_{ud} 2pt[(\overline{\psi_p}\, \psi_n)\, (\overline{\psi_e}\, (C_S + C_S^{\prime}\, \gamma_5)\, \psi_\nu) \\ &\quad + (\overline{\psi_p}\, \gamma_\mu\, \psi_n)\, (\overline{\psi_e}\, \gamma^\mu\, (C_V + C_V^{\prime}\, \gamma_5)\, \psi_\nu) \\ &\quad + \frac{1}{2}\, (\overline{\psi_p}\, \sigma_{\lambda\mu}\, \psi_n)\, (\overline{\psi_e}\, \sigma^{\lambda\mu}\, (C_T + C_T^{\prime}\, \gamma_5)\, \psi_\nu) \\ &\quad - (\overline{\psi_p}\, \gamma_\mu\, \gamma_5\, \psi_n)\, (\overline{\psi_e}\, \gamma^\mu\, \gamma_5\, (C_A + C_A^{\prime}\, \gamma_5)\, \psi_\nu) \\ &\quad + (\overline{\psi_p}\, \gamma_5\, \psi_n)\, (\overline{\psi_e}\, \gamma_5\, (C_P + C_P^{\prime}\, \gamma_5)\, \psi_\nu) \\ &\quad + h.c. \end{aligned} \tag{1.38}$$

with C_i the coupling constants associated to the scalar (even) Hamiltonian and $C_i^{'}$ the corresponding ones related to the pseudoscalar (odd) Hamiltonian. In particular, considering the non-relativistic limit, the vector and the scalar coupling constants are associated to Fermi transitions, while the axial-vector and tensor ones lead to Gamow-Teller decays. As well, the pseudoscalar component has been commonly neglected at low-energies, peculiar to the nuclear β-decay.

In principle, there are no theoretical restrictions to be applied on C_i and $C_i^{'}$, which should then be all complex quantities. However, the time-reversal invariance requires them to be real up to a common phase [43] and the maximal parity violation imposes that specular currents need to have the same magnitude but opposite sign, *i.e.* $|C_i| = |C_i^{'}|$. Furthermore, the electroweak theory implemented within the Standard Model involves only V and A interactions, while all the other coupling constants are zero; consequently, SM predicts that $C_V = C_V^{'}$ and $C_A = C_A^{'}$, while $C_S = C_S^{'} = C_T = C_T^{'} = C_P = C_P^{'} = 0$.

Additionally, according to the Conserved Vector Current (CVC) hypothesis [44], experimentally proved at the level of 1.2×10^{-4} [45], the two charge-changing vector currents of the weak interaction[8], together with the pure vector electromagnetic current, can be interpreted as the three conserved components of a vector in the isospin space; indeed, in total analogy with the conservation of the electric charge even within the nuclear medium, weak vector currents are then supposed also to be conserved, thus determining the vector coupling

---

[8] Vector currents can be classified as charge-raising or charge-lowering for β^- and β^+-decay, respectively

constants not to be re-normalized in the nuclear medium and consequently independent of the nuclear transition. Consequently, $C_V = C_V^{'} = 1$. On the other hand, as stated by the Partially Conserved Axial-Vector Current (PCAC) hypothesis [46], the continuous process of virtual pion exchange in nucleons results in a reinforcement of the strength of the Gamow-Teller transitions with respect to the Fermi ones, thus demanding the axial-vector coupling constant to be re-normalized in the nuclear medium, estimated to be $C_A = C_A^{'} \simeq 1.27$.

1.3.4 Angular correlations in nuclear β-decay

The different coupling constants introduced in Eq. 1.38 strongly influence the angular correlation of the leptons emitted in the β-decay. Effectively, the expression of the β-decay rate, describing both the electron-neutrino angular, energy and electron polarization direction $\overrightarrow{\sigma}$ distribution from a β-decay of a polarized parent nucleus, is generally given by [47]:

$$\begin{aligned}
&\omega\left(\langle\overrightarrow{I}\rangle, \overrightarrow{\sigma}|E_e,\Omega_e,\Omega_\nu\right)dE_e d\Omega_e d\Omega_\nu \propto \\
&\qquad F\left(\pm Z,E_e\right)p_e\left(E_0-E_e\right)^2 dE_e d\Omega_e d\Omega_\nu \times \\
&\qquad \xi\Bigg\{1+\frac{\overrightarrow{p_e}\cdot\overrightarrow{p_\nu}}{E_eE_\nu}a_{\beta\nu}+\frac{m_e}{E_e}b+ \\
&\qquad \frac{\overrightarrow{I}}{I}\cdot\left[\frac{\overrightarrow{p_e}}{E_e}A+\frac{\overrightarrow{p_\nu}}{E_\nu}B+\frac{\overrightarrow{p_e}\times\overrightarrow{p_\nu}}{E_eE_\nu}D\right]+ \\
&\qquad \overrightarrow{\sigma}\cdot\left[\frac{\overrightarrow{p_e}}{E_e}G+\frac{\langle\overrightarrow{I}\rangle}{I}N+\frac{\overrightarrow{p_e}}{E_e+m_e}\left(\frac{\langle\overrightarrow{I}\rangle}{I}\cdot\frac{\overrightarrow{p_e}}{E_e}\right)Q+\frac{\langle\overrightarrow{I}\rangle}{I}\times\frac{\overrightarrow{p_e}}{E_e}R\right]
\end{aligned} \tag{1.39}$$

where $\langle\overrightarrow{I}\rangle$ is the initial polarization vector of the decaying system, $E_{e,\nu}$, $p_{e,\nu}$ and $\Omega_{e,\nu}$ refer to the lepton total energies, momenta and angular coordinates, $F(\pm Z,E_e)$ is the Fermi function accounting for the electromagnetic interaction between the emitted β-particle and the parent nucleus and E_0 represents the endpoint of the β-energy spectrum. Furthermore, ξ is a parameter depending both on the nuclear matrix elements and on the weak coupling constants:

$$\begin{aligned}
\xi &= |\mathcal{M}_F|^2\ \left(|C_S|^2 + |C_V|^2 + |C_S^{'}|^2 + |C_V^{'}|^2\right) \\
&+ |\mathcal{M}_{GT}|^2\left(|C_T|^2 + |C_A|^2 + |C_T^{'}|^2 + |C_A^{'}|^2\right)
\end{aligned} \tag{1.40}$$

whereas the correlation parameters $a_{\beta\nu}$, b, A, B, D, G and R are all expressed as a function of the C_i and $C_i^{'}$ coupling constants and denote, respectively, the β-ν angular correlation coefficient, the Fierz interference term, the β-asymmetry parameter, the neutrino asymmetry parameter, the D-triple correlation, the longitudinal β-polarization and the R-triple correlation coefficients. The numerical values of all these correlation parameters cannot be estimated directly from theory, but rather inferred from experimental measurements. In particular, the experimental determination of each correlation coefficient constitutes a suitable testing ground for the predictions contained in the Standard Model, concomitantly contributing to the search for the possible existence of non-zero exotic scalar and tensor contributions to the theory of the weak interaction (mainly via $a_{\beta\nu}$ and b); in parallel, it helps to shed more light on the possible existence of non-symmetric left-right extensions of the SM (typically via A, B, G) and to test the time-reversal invariance (D,R).

Specifically, the complete expression of the β-ν angular correlation coefficient is given by:

$$\begin{aligned} a_{\beta\nu}\xi \; &= \; |\mathcal{M}_F|^2 \left[-|C_S|^2 + |C_V|^2 - |C_S^{'}|^2 + |C_V^{'}|^2 \mp 2\,\frac{\alpha Z m}{p_e}\, Im\left(C_S\, C_V^{*} + C_S^{'}\, C_V^{'*} \right) \right] \\ &+ \frac{|\mathcal{M}_{GT}|^2}{3} \left[|C_T|^2 - |C_A|^2 + |C_T^{'}|^2 - |C_A^{'}|^2 \pm 2\,\frac{\alpha Z m}{p_e}\, Im\left(C_T\, C_A^{*} + C_T^{'}\, C_A^{'*} \right) \right] \end{aligned} \tag{1.41}$$

whereas the Fierz interference term can be rewritten as:

$$b\xi \; = \; \pm 2\Gamma Re \left[|\mathcal{M}_F|^2 \left(C_S\, C_V^{*} + C_S^{'}\, C_V^{'*} \right) + |\mathcal{M}_{GT}|^2 \left(C_T\, C_A^{*} + C_T^{'} C_A^{'*} \right) \right] \tag{1.42}$$

The maximal sensitivity to the possible existence of exotic scalar and tensor weak currents occurs in case of pure Fermi and pure Gamow-Teller transitions, respectively[9]. Indeed, in these cases, as a consequence of the imposition of time-reversal invariance the αZ-order Coulomb correction is canceled out and the expressions for $a_{\beta\nu}$ and b coefficients reduce respectively, at a level of precision of few permil [48], to:

$$\begin{aligned} a_{\beta\nu}^{F} \; &\simeq \; 1 - \frac{|C_S|^2 + |C_S^{'}|^2}{C_V^2} & a_{\beta\nu}^{GT} \; &\simeq \; -\frac{1}{3}\left[1 - \frac{|C_T|^2 + |C_T^{'}|^2}{C_A^2} \right] \\ b_F^{'} \; &\simeq \; \pm \frac{\Gamma m_e}{E_e} Re \left(\frac{C_S + C_S^{'}}{C_V} \right) & b_{GT}^{'} \; &\simeq \; \pm \frac{\Gamma m_e}{E_e} Re \left(\frac{C_T + C_T^{'}}{C_A} \right) \end{aligned} \tag{1.43}$$

where $b^{'} \equiv b\frac{m_e}{E_e}$. In the SM, the predicted values for the β-ν angular correlation coefficient are then, respectively, $a_{\beta\nu}^{F}$ = 1 and $a_{\beta\nu}^{GT}$ = -1/3, while the Fierz interference term, depending only on the scalar and the tensor coupling constants, is always predicted to be zero. In particular, the linear dependence of the Fierz term with respect to the exotic coupling constants, in contrast to the quadratic one shown by the β-ν correlation coefficient, straightforwardly

---

[9] In case of mirror transitions, which satisfy both Fermi and Gamow-Teller selection rules, the $a_{\beta\nu}$ coefficient depends also on the mixing parameter $\rho = \frac{C_A M_{GT}}{C_V M_F}$, which expresses the relative amplitude strengths of F and GT decays and which has to be determined from experiments again, thus introducing a major relative uncertainty on the experimental value of $a_{\beta\nu}$. For further details see Appendix A.

indicates the b coefficient to be the most suitable correlation parameter to be determined experimentally as precisely as possible in order to set the most stringent limits on the exotic scalar and tensor coupling constants.

Furthermore, the Fierz term, as it depends only on the total energy of the emitted β-particle without any other dependence neither on the spin nor on the particle momentum direction, represents indeed an integral part of all measurements related to any theoretical correlation coefficient $\mathcal{X}$, which is then retrieved experimentally in the following approximation[10]:

$$\widetilde{\mathcal{X}} \sim \frac{\mathcal{X}}{1 + \langle b' \rangle} \tag{1.44}$$

where $\mathcal{X} = a_{\beta\nu}, A, B, D, G, R$ and $\langle b^{'} \rangle$ represents the weighted average of $b^{'} \equiv b\frac{m_e}{E_e}$ on the observed β-energy spectrum.

Therefore, in order to test in the most accurate way possible the predictions of the SM related to the theory of the weak interaction and so, concomitantly, remaining competitive with high-energy experiments in the assessment of newly stringent limits on the values of the exotic coupling constants, the correlation coefficients should be determined with a precision of at least several permil. However, in this case, theoretical higher-order effects need to be taken into account and modeled as well, the major of which consisting in radiative corrections [50, 51], electromagnetic corrections [52, 53] and the recoil terms due to the interaction between the quark decaying in the β-decay with the surrounding nuclear medium.

1.4 Probe physics beyond the SM in the electroweak sector

Precision measurements related to nuclear β-decay have always played a role of primary importance in particle physics research. Effectively, the broad variety of nuclear states and β-transitions constitute a highly remarkable tool to be competitive with high-energy physics experiments in testing SM predictions and searching for physics beyond its frontiers.

In the following, the main opportunities offered by *superallowed* pure Fermi and mirror transitions to extract the V_{ud} element and test the unitarity of the CKM matrix, the possibility to determine the β-ν angular correlation coefficient and the Fierz interference term as well as tests of time-reversal symmetry violation aiming to shed more light on the possible existence of new non-SM hypothetical vector bosons that may alter the rate distribution and angular correlations of β-decays will be introduced, with particular care to the complementarity between nuclear β-decay and high-energy experiments at colliders in search for exotic scalar and tensor interactions.

---

[10] It has been demonstrated that this is an approximation and that the exact relation between $\widetilde{\mathcal{X}}$, $\mathcal{X}$ and b depends on the experimental technique and should be rather determined via numerical simulations [49].

1.4.1 $\mathcal{F}t$-values, V_{ud} and CKM unitarity

Nuclear *superallowed* pure Fermi and mirror transitions represent both a tool of invaluable importance, as they concurrently permit to experimentally extract numerical values of some free parameters of the SM and to provide new stringent limits on the existence of new particles not originally included within the SM itself, whose mass limits are easily located beyond the energy TeV-scale frontier actually reachable at particle colliders.
Indeed, as presented in Sec. 1.2.2.4, nuclear $\beta^{\pm}$-decay consists in an interaction between light quark and lepton currents mediated by the exchange of a $W^{\pm}$ boson, where the strength of the interaction is theoretically expressed by the V_{ud} element of the CKM mixing matrix. In particular, the experimental measurements of the $\mathcal{F}t$-value in both *superallowed* Fermi and mirror β-decays primarily contribute to the most precise determination of the V_{ud} element of the CKM matrix, concurring in tests of the SM in its prediction of the unitarity of the CKM matrix itself; in parallel, they also permit to set limits *a posteriori* on the value of the Fierz interference term, related, as expressed in Eq. A.9, to the existence of exotic interactions in the framework of physics beyond the Standard Model.
More specifically, the expression for the corrected $\mathcal{F}t$-value for a given i nuclear β-decay is given by [54]:

$$\mathcal{F}t_i \;\equiv\; ft_i\,(1 + \delta'_{R,i})\,(1 + \delta_{NS,i} - \delta_C) \;=\; \frac{K}{G_F^2\,V_{ud}^2\,(1 + \Delta_R^V)\,\left[1 + (f_{A,i}/f_{V,i})\,\rho_i^2\right]} \tag{1.45}$$

where $f_{A,i}$ and $f_{V,i}$ are the statistical rate functions for the A and V part respectively, t the partial half-life of the transition, $\delta'_{R,i}$ the radiative corrections depending only on Z of the mother nucleus and on E_0 of the emitted β-particle, $\delta_{NS,i}$ is the transition-dependent nuclear structure corrections and δ_C the isospin symmetry-breaking correction. Moreover, G_F is the universal Fermi coupling constant, $\frac{K}{(\hbar c)^6} = \frac{2\pi^3\hbar\ln 2}{(m_e c^2)^5} = 8120.2776(9) \times 10^{-10}\ \mathrm{GeV}^{-4}\ \mathrm{s}$ [11] and $\Delta_R^V = (2.361 \pm 0.038)\%$ [55] is the nucleus-independent radiative correction. Additionally, $\rho_i = \frac{C_A M_{GT}}{C_V M_F}\frac{(1+\delta_{NS}^A-\delta_C^A)^{1/2}}{(1+\delta_{NS}^V-\delta_C^V)^{1/2}}$ is the corrected Fermi–Gamow-Teller mixing ratio, where $\frac{C_A M_{GT}}{C_V M_F}$ is the pure Fermi–Gamow-Teller ratio in the isospin limit and $\delta_{NS,i}^A$ and δ_C^A are the axial-vector equivalents of $\delta_{NS,i}^V$ and δ_C^V, respectively.
In particular, according to the CVC hypothesis, all the $0^+ \longrightarrow 0^+$ *superallowed* Fermi transitions, identified by a pure vector character and so for which $\rho = 0$, should have the same decay strength. Currently, the most precise estimate of the average $\mathcal{F}t$-value from the fifteen best known pure Fermi transitions is $\langle\overline{\mathcal{F}t}\rangle = (3071.81 \pm 0.83)$ s [45], thus permitting to extract the element $V_{ud} = 0.97425(22)$ and testing the unitarity of the CKM matrix at the 6×10^{-4} level, with an error mainly dominated by the nucleus-independent Δ_R^V parameter. On the other hand, experimental measurements related to the ^{19}Ne, ^{21}Na, ^{29}P, ^{35}Ar and ^{37}K

mirror transitions have allowed an estimate for $\langle\overline{\mathcal{F}t'}\rangle$ = (6173 ± 22) s, thus permitting to independently test the CKM unitarity at the 4×10^{-3} level and to extract the element V_{ud} = 0.9719(17) [56]. Further results have been obtained from measurements on the free neutron decay [11], leading to V_{ud} = 0.9741(20), and from pion β-decay ($\pi^+ \longrightarrow \pi^0 e^+ \nu_e$), a pure $0^- \longrightarrow 0^-$ transition having the advantage of not depending on the nuclear structure but yet characterized by a very low branching ratio of the order of 10^{-8}, which consequently causes relevant experimental difficulties and a loss of precision in the extraction of V_{ud}, yielding V_{ud} = 0.9728(30) in its best estimate [57]. A more recent theoretical estimate has been performed as an extraction from the Wilson coefficients and lead to a V_{ud} = 0.97370(25) [58].
Beside the possibility to test the CKM unitarity prediction of the SM, both Fermi and Gamow-Teller transitions allow also in principle to set new limits on the possible existence of exotic interactions and, therefore, to shed light on the eventual existence of new particles, such as the theorized leptoquarks or W^0 bosons, responsible for the mediation of these eventual new types of interaction not originally implemented within the SM. Effectively, the $\mathcal{F}t$-value is related to physics beyond the SM in the framework of the weak interaction via the Fierz term, as follows [58]:

$$\mathcal{F}t_i \equiv \frac{f_{V,i}\,(1 + \delta_i)\ln 2}{\Gamma_i} = \frac{4\,\pi^3 \ln 2}{M_F^2\, m_e^5}\left[\hat{\xi}_i + \gamma_i\,\hat{\xi}_i\,\langle b_i^{'}\rangle\right]^{-1} \tag{1.46}$$

where $1+\delta_i = (1+\delta_{R,i}^{'})(1+\delta_{NS,i}-\delta_C)$, $b_i^{'} = b_i\langle\frac{m_e}{E_e}\rangle_i$ and $\hat{\xi}_i$ is derived from Eq. A.8[11] (for details see Appendix A). In particular, for *superallowed* transitions $M_F = \sqrt{2}$ and $\rho_i = 0$, while for mirror decays $M_F = 1$ and, in this case, the expression for $\mathcal{F}t_i$, comparing to the Eq. 1.45, consequently results dependent on the transition-dependent mixing ratio ρ_i via the Fierz coefficient b_i. Hence, according to the CVC hypothesis and considering that b_i is always predicted to be zero, all the $\mathcal{F}t$-values associated to *superallowed* transitions should have the same values in the pure SM scenario; however, in case of measurements of a non-zero Fierz term, the CVC hypothesis would trickle away as the $\mathcal{F}t$-values would depend on the particular transition via the Fierz factor $b_i^{'}$.
Therefore, the steady progress in the development of advanced accurate Penning traps and even more precisely calibrated detectors precisely has progressively permitted more precise measurements of half-lives, the total transition energy Q_{EC} and branching ratios related to both *superallowed* and mirror transitions (see *e.g.* [59, 60, 45]), thus ensuring the measurement of $\mathcal{F}t$-values and the extrapolation of the Fierz interference at the level of precision of 10^{-3} needed to both test the CKM unitarity in the SM and search for new physics beyond it.

---

[11] The mathematical relation is given by $\hat{\xi}_i = \frac{2}{M_F^2}\,\xi_i$.

1.4.2 Search for exotic interactions

As presented in Sec. 1.3.4, the possible existence of exotic interactions would be theoretically reflected in terms of non-zero scalar and tensor coupling constants directly affecting the description of the experimentally observed β-decay spectrum. In particular, the correlation term $\frac{\vec{p_e}\cdot\vec{p_\nu}}{E_e E_\nu}$ between the momenta and the energies of the leptons emitted in the β-decay results directly proportional to the $a_{\beta\nu}$ angular correlation coefficient, quadratically dependent on the exotic coupling constants themselves.

The most forthcoming way to retrieve the $a_{\beta\nu}$ coefficient for both Fermi and Gamow-Teller transitions would be to measure the correlation between the leptons emitted in the decay. Yet, as a direct measurement of the neutrino is almost impossible, $\tilde{a}_{\beta\nu}$ can be determined from the recoil of the daughter nucleus, which can be measured either directly by means of trap measurements or indirectly via the kinematic shift it induces on the energy distribution of the β-delayed particles emitted in case of unstable daughter nuclei. In this regard, over the past two decades several precise measurements have been performed for pure Fermi transitions, concerning the measure of the Doppler shift induced on the γ-rays emitted following the β-decay of ^{18}Ne in 1997 [61] and of ^{14}O in 2003 [62], leading to measurements of $\tilde{a}^F_{\beta\nu}$ equal to 1.06(19) and to 1.00(3), respectively. Further measurements of the kinematic shift induced on protons by the recoiling daughter ions in the β-p decay of ^{32}Ar have been performed by Adelberger *et al.* at ISOLDE/CERN in 1999 [63], leading to $0.9989(52)_{stat}(39)_{syst}$. Complementary, measurements in coincidence between the emitted β-particle and the recoiling ion have also been performed on ^{38}K^m radioactive ions confined in a magneto-optical trap at TRIUMF [64], providing a relative precision of 0.46%; by using a similar technique, $\tilde{a}^F_{\beta\nu}$ has also been measured in the mixed β-decay of ^{21}Na at Berkeley [65], obtaining a relative precision at the level of 1%. Concerning the pure Gamow-Teller transitions, measurements have been historically accomplished on ^{23}Ne [66–68] and on ^{6}He [68–71], with the estimates of $\tilde{a}^{GT}_{\beta\nu}$ performed on ^{6}He made by Johnson *et al.* [68] in 1961 and by Fléchard *et al.* at LPCTrap in 2011 [71], providing a relative uncertainty of the percent order. Additional studies have also been recently carried out at Argonne on the β-decay of ^{8}Li, by measuring the energy distribution of the α-particles coming from the following breakup of ^{8}Be [72], with uncertainty at the percent [73] and the subpercent [74] level. Further studies have also been carried out with ^{6}He at MOT in Seattle [75] and via the WITCH experiment at the ISOLDE facility [76–78], which has made use of a double Penning ion trap and a retardation spectrometer to measure the energy spectrum of the recoiling ions after the β-decay of ^{35}Ar. Further measurements aiming to extract $\tilde{a}^{F,GT}_{\beta\nu}$ from the β-p decay of ^{32}Ar are currently planned at the WISArD experiment at CERN [79] and at TAMUTRAP at Texas A&M University [80]. Up to date, the most precise estimates for the angular correlation coming from nuclear β-decay provide $\tilde{a}^{F}_{\beta\nu}$ = 0.9989(52)$_{stat}$(39)$_{syst}$ [63] and $\tilde{a}^{GT}_{\beta\nu}$ = -0.3325(13)$_{stat}$(19)$_{syst}$ [74].

In parallel, further information on the possible existence of exotic interactions can be derived from the determination of the Fierz interference term. The b term is indeed, as illustrated in Sec. 1.3.4, integrally present in all measurements of any other correlation coefficient, but it can also be directly inferred from precise measurements of the β-spectrum shape [81], as performed for the pure GT decay of ^{114}In at the WISArD experiment [82]. Yet, the most precise limits for Fermi transitions have been determined by Hardy and Towner from a global fit to multiple *superallowed* $\mathcal{F}$t-values, resulting in $b_F = 0.0022 \pm 0.0026$ (or, equivalently, $|b_F| < 0.0043$ at 90% C.L.) [45]. Further experiments have as well allowed the extrapolation of b_{GT} from the β-asymmetry in the β-decay of ^{60}Co [83], ^{107}In [84], ^{114}In [85] and ^{19}Ne [86, 87], with a recent evaluation from the neutron decay furnishing $b_{GT} = 0.017 \pm 0.021$ (68.7% C.L.) [88]. Additional experimental campaigns, aiming to measure the Fierz term ideally with an uncertainty at the level of 10^{-3}, are planned with ^{6}He at the ^{6}He-CRES experiment at Washington [89] and at the b-STILED experiment at GANIL [49].

Globally, a combined analysis of relevant experimental data related to correlation coefficients extracted from both neutron and nuclear β-decay has permitted to set limits for the scalar and tensor coupling constants in a scenario admitting both left-handed and right-handed neutrinos, respectively equal to $|C_S/C_V| < 0.07$ and $|C_T/C_A| < 0.08$ (95.5% C.L) [90], thus stating limits on non-negligible contributions of the exotic currents to the weak interaction. More recent results in this sense have been derived by Falkowski et al. [58], who also underlined the importance of precise measurements in nuclear β-decay in the low-energy scenario and in particle collisions at the high-energy scale as complementary tools to search for new physics. Indeed, as in QFT each current is considered to be responsible for a specific interaction and so mediated by the presence of a particular *gauge* boson, the possible existence of new scalar and tensor currents not originally predicted in the SM would consequently point out the existence of new mediating vector bosons not formerly theorized neither discovered, characterized by masses fairly beyond the energy frontier actually accessible at high-energy particle colliders. Effectively, the search for physics BSM has been traditionally pursued on two parallel sectors, historically first via low-energy precision experiments, seeking for tiny deviations in low-energy observables attributable to exotic interactions not predicted by the SM, and then secondly by means of high-energy experiments, traditionally aiming to directly search for new particles by exploiting the relativistic transparency regime created by the punctual high-energy transfer in particle collisions. The theoretical bridgehead between the two worlds is offered by the Effective Field Theory (EFT), which can be applied to both domains by requiring no other light degrees of freedom except for those of the SM[12] and, eventually, the right-handed neutrino ν_e, thus allowing for a re-parametrization of the measured observables in neutron, nuclear and pion β-decay at high-transverse mass and so permitting the extraction of limits on the exotic currents on a similar level of precision for both low- and high-energy physics. Specifically, the nucleon-level Lagrangian associated to the Hamiltonian reported in Eq. 1.38 can be expressed in EFT as the quark-level Lagrangian [58]:

$$\begin{aligned}
&\mathcal{L}_{quark-level} \supset \\
&-\frac{V_{ud}}{v^2}\big[(1+\varepsilon_L)\overline{\psi_e}\gamma_\mu\,\psi_{\nu,L}\cdot\overline{\psi_u}\gamma^\mu(1-\gamma_5)\,\psi_d+\tilde{\varepsilon}_L\overline{\psi_e}\gamma_\mu\,\psi_{\nu,R}\cdot\overline{\psi_u}\gamma^\mu(1-\gamma_5)\psi_d \\
&+\varepsilon_R\overline{\psi_e}\gamma_\mu\,\psi_{\nu,L}\cdot\overline{\psi_u}\gamma^\mu(1+\gamma_5)\,\psi_d+\tilde{\varepsilon}_R\overline{\psi_e}\gamma_\mu\,\psi_{\nu,R}\cdot\overline{\psi_u}\gamma^\mu(1+\gamma_5)\,\psi_d \\
&+\frac{1}{4}\varepsilon_T\,\overline{\psi_e}\sigma_{\mu\nu}\,\psi_{\nu,L}\cdot\overline{\psi_u}\sigma^{\mu\nu}(1-\gamma_5)\,\psi_d+\frac{1}{4}\tilde{\varepsilon}_T\,\overline{\psi_e}\sigma_{\mu\nu}\,\psi_{\nu,R}\cdot\overline{\psi_u}\sigma^{\mu\nu}(1+\gamma_5)\,\psi_d \\
&+\varepsilon_S\overline{\psi_e}\,\psi_{\nu,L}\cdot\overline{\psi_u}\,\psi_d+\tilde{\varepsilon}_S\overline{\psi_e}\,\psi_{\nu,R}\cdot\overline{\psi_u}\,\psi_d-\varepsilon_P\overline{\psi_e}\,\psi_{\nu,L}\cdot\overline{\psi_u}\gamma_5\,\psi_d-\tilde{\varepsilon}_P\overline{\psi_e}\,\psi_{\nu,R}\cdot\overline{\psi_u}\gamma_5\,\psi_d\big] \\
&+h.c.
\end{aligned} \tag{1.47}$$

where ψ_e, ψ_u and ψ_d are the wavefunctions associated to the electron, up and down quark respectively, $\psi_{\nu,L,R} \equiv \frac{1\pm\gamma_5\psi_\nu}{2}$ are the wavefunctions related to left-handed and right-handed electron neutrinos and $v = \sqrt{\frac{1}{\sqrt{2}G_F}} \sim 246.22$ GeV. Moreover, the Wilson coefficients $\varepsilon_{\mathcal{X}}$ and $\tilde{\varepsilon}_{\mathcal{X}}$ ($\mathcal{X}$ = L, R, T, S, P), all null within the SM-scenario, theoretically reflect the effects of possible BSM particles on the weak interaction Lagrangian. For completeness, the relations between the C_i and $C_i^{'}$ coupling constants reported in Eq. 1.38 and the Wilson coefficients are shown in Appendix A.

In particular, results indicating non-null Wilson coefficients directly permit to set mass limits on the new hypothetical *gauge* bosons mediating the non-SM exotic interactions, specifically identified either in leptoquarks, hybrid colour-triplet particles interacting with both quarks and leptons theorized in the Pati-Salam model, or in $W^{'}$ bosons, depicted in the left-right symmetric extensions of the Standard Model. However, whereas the construction of a phenomenological model centered on leptoquarks based on the results obtained in *pp* collisions for the Drell-Yan process at the LHC [92] is progressively resulting a rather challenging objective to be achieved, the introduction of a new boson W_R coupling only to

---

[12] Effectively, for neutrinos interacting with matter, the cosmological constraints [91] show that $\sum_i m_{\nu,i} < 0.12$ eV (i = e, μ, τ), which makes them negligible in mass terms at the β-decay energy scale.

right-handed particles and acquiring by spontaneous symmetry breaking a mass (m_2) fairly larger than the corresponding W_L (m_1) boson coupling only to left-handed particles seems way more feasible for constructing a theoretical BSM-scenario that would also try to explain the observed maximal parity violation in the weak interaction. Effectively, the weak interaction eigenstates $W_{L,R}$ can be written in this case as:

$$W_L = \cos\zeta W_1 + \sin\zeta W_2 \qquad\qquad W_R = -\sin\zeta W_1 + \cos\zeta W_2 \tag{1.48}$$

where ζ represents the mixing angle and $\delta \equiv \left(\frac{m_1}{m_2}\right)^2$ is the model scale. In minimal left-right symmetric extensions of the SM, ζ and δ are the only parameters that permit to distinguish between the left- and right-handed descriptions, while in generic extensions all the other parameters (*e.g.* coupling constant g_R, CKM element $V_{ud,R}$) also differ one from each other. In particular, according to Eq. 1.47, in case of uniquely left-handed particles, as the present limits on C_S and C_T are $\mathscr{O}_{1/v^2}(10^{-3})$, the experimental observables should become sensitive on the new physics at an energy scale between ~ 10 and ~ 100 TeV, in case of partial or maximal strong coupling to the SM respectively. Otherwise, in presence of right-handed neutrinos, the expressions of the observable correlation coefficients become affected also from the quadratic contribution coming from the non-null right-handed parameters, affected by an uncertainty of $\mathscr{O}_{1/v^2}(10^{-1})$; therefore, the mass limits would be in this case reduced by two orders of magnitude, resulting in overall constraints set between 100 GeV and 1 TeV. Further constraints on right-handed currents from low-energy physics come from longitudinal positron polarization experiments [93–96], neutron decay [97, 98], longitudinal polarization of positrons emitted by polarized nuclei [99–101] and the $\mathcal{F}t$-values of the *superallowed* $0^+ \longrightarrow 0^+$ transitions [45]. In particular, the latter approach has permitted to set the currently strongest limits on the mixing angle, which appears limited in the milliradian region $-0.0011 \leq \zeta \leq 0.0013$ (90% C.L.).

1.4.3 Test of T-reversal invariance and other correlation measurements

Tests of time-reversal invariance allow for a complementary search in physics beyond the SM, particularly concerning the search for new sources of CP-violation with the final aim to shed more light on the possible origin of the matter-antimatter asymmetry. In the low-energy sector, searches for T-violation have been traditionally centered on measurements of the D triple correlation coefficient, which is T-odd and P-even, and on the R coefficient, which is instead both T-odd and P-odd.

The D triple correlation coefficient, driving the term $\frac{\vec{I}}{I} \cdot \frac{\vec{p_e}\times\vec{p_\nu}}{E_e E_\nu}$ in Eq. 1.39, has to be estimated by definition (details in Appendix A) via mixed transitions and is inferred from measurements of the momenta of the β-particle and of the neutrino (via the recoil of the daughter nucleus) emitted in mutually perpendicular directions in a plane perpendicular to the nuclear spin axis. Following first measurements on neutron decay [102, 103], further efforts have been put on the extraction of the D coefficient by employing a cold polarized neutron beam at the emiT experiment at NIST and at the Trine experiment at ILL, leading respectively to D_n = [-0.6 $\pm$ 1.2 (stat.) $\pm$ 0.5 (syst.)] $\times 10^{-3}$ [104] and D_n = [-2.8 $\pm$ 6.4 (stat.) $\pm$ 3.0 (syst.)] $\times 10^{-4}$ [105]. However, the most precise measurements comes from the combined result from the nuclear β-decay of the mirror nucleus ^{19}Ne, D = 0.0001(6) [106], which currently represents the most stringent limit on a T-violating angular correlation in a weak decay process. These measurements were also the first in their kind to test time-reversal invariance in any weak process at a level below the limit coming from the CP violation in the kaon sector, equal to 2.3 $\times$ 10^{-3} [107]. So far, no evidence for any T-reversal violation has been highlighted. Presently, further studies on the D coefficient are foreseen within the MORA project on the ^{23}Mg^{+} ion decay at JYFL and later on at GANIL [108].

The R coefficient, driving the term $\vec{\sigma} \cdot \left[\frac{\langle \vec{I} \rangle}{I} \times \frac{\vec{p_e}}{E_e}\right]$ in Eq. 1.39, can be experimentally inferred via the transverse polarization of the β-particle obtained via Mott scattering. Experiments have been performed by exploiting again the β-decay of ^{19}Ne, leading to R = 0.079(53) [109], and via the Gamow-Teller decay of ^{8}Li, produced by means of a vector-polarized deuteron beam on an enriched ^{7}Li target cooled to few K to achieve a polarization relaxation time way longer than the mean lifetime, thus leading to R = 0.0009 (22) $\times 10^{-3}$ [110], which has sensibly improved by around an order of magnitude the limits for T-violating tensor couplings, providing -0.008 < $\frac{Im(C_T+C_T^{'})}{C_A}$ < 0.014 (90% C.L.).

1.5 WISArD goals

Currently, the most precise limits on the exotic scalar coupling constant, derived from the most precise measurements of the $\tilde{a}_{\beta\nu}$ and the b coefficients for pure Fermi transitions, are summarized in the exclusion plot in Fig. 1.1. The current most precise constraints on the $\tilde{a}^{F}_{\beta\nu}$ coefficient at low-energy have been obtained by measurements performed by Adelberger in 1999 with ^{32}Ar [63], by Gorelov with an experimental campaign on ^{38}K^{m} by means of the magneto-optical trap at TRIUMF in 2009 [64] and by the WISArD proof-of-principle experiment with ^{32}Ar in 2018 [111]. The most precise limits have been though achieved at high-energy in the analysis of the Missing Transverse Energy (MET) in pp collisions at $\sqrt{s_{NN}}$ = 8 TeV [112] and at $\sqrt{s_{NN}}$ = 13 TeV [113] at the CMS experiment, at the Large Hadron Collider (LHC) at CERN. Further constraints coming from the measurements of the b_F term have been obtained from the $0^{+} \longrightarrow 0^{+}$ *superallowed* Fermi transitions [114].

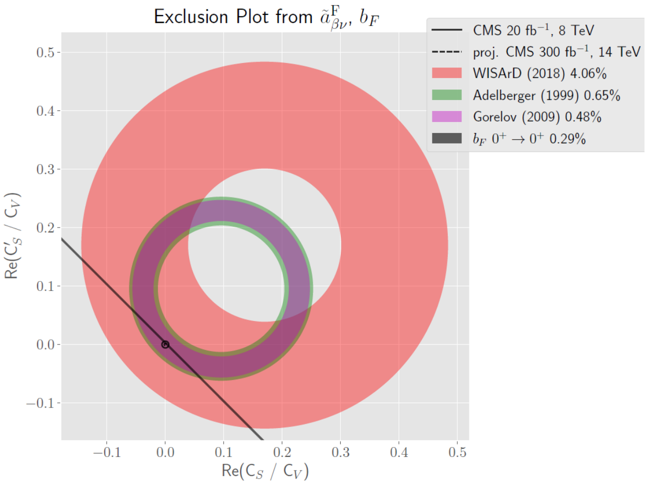

Figure 1.1: Current limits for the exotic scalar contribution, obtained from precise measurements on the $\tilde{a}_{\beta\nu}$ coefficient performed by Adelberger with ^{32}Ar [63] (green circle), Gorelov with ^{38}K^m[64] (pink circle) and the WISArD proof-of-principle experiment [111] (red circle). Further limits have been obtained from the CMS experiment at the LHC [112, 113] (black dot). The black line represents the limits on the b_F term from the $0^+ \longrightarrow 0^+$ *superallowed* Fermi transitions [114]. All limits are calculated at 90% C.L. Adapted from [115].

The aimed goals for the WISArD experiment performed in 2021, after a full upgrade of the detection set-up and a better understanding and reduction of the systematic uncertainties, are shown in Fig. 1.2. A 0.1-0.2% precision level on the final determination of $\tilde{a}_{\beta\nu}$ is attended; if reached, it would constitute the most precise measurement of the β-ν angular correlation coefficient at the low-energy scale up to now.

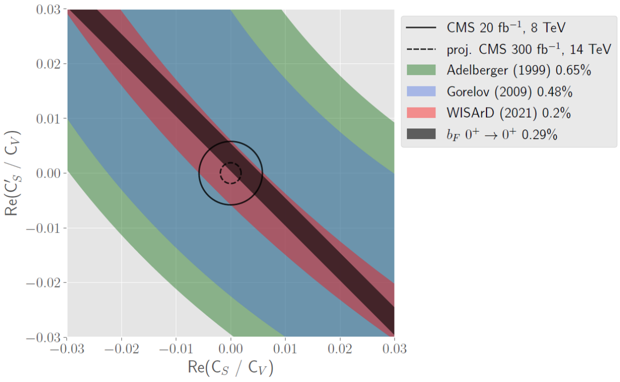

Figure 1.2: Expected constraints for the scalar contribution related to the WISArD experiment performed in 2021, after a full upgrade of the detection set-up and a better understanding and reduction of the systematic uncertainties. The expected projections for proton-proton collisions ($pp \longrightarrow e + MET + X$) at $\sqrt{s_{NN}}$ = 14 TeV at Run 3 (2022-2024) at the LHC are also shown. All exclusion contours are given for one standard deviation [111].

Chapter 2

The WISArD experiment

The WISArD (Weak Interaction Studies with ^{32}Ar Decay) experiment [79] aims at a precise determination of the $\tilde{a}_{\beta\nu}$ coefficient for both Fermi and Gamow-Teller transitions by using the kinematic mean energy shift of the β-delayed protons emitted in the same or the opposite direction to the β-particles in the decay of ^{32}Ar. A proof-of-principle experiment, though limited in statistics and performed via a still rudimental experimental set-up, has been successfully accomplished at ISOLDE/CERN in November 2018, already leading to the third best measurement of $\tilde{a}_{\beta\nu}$ for Fermi transitions [111]. After determining and estimating the systematic errors, a consistent upgrade of the experimental set-up has been commissioned and realized through the past two years, potentially permitting to reach the aimed precision of the permil level on the determination of $\tilde{a}_{\beta\nu}$.
In this chapter, the upgraded experimental set-up employed in the WISArD experiment will be reviewed and the new experimental campaign conduced in October 2021 will be presented.

2.1 The kinematic shift measurement

A first effort in this sense has already been made in 1993 by Schardt and Riisager [116], who observed a significant broadening of the β-delayed IAS proton line in the ^{32}Ar spectrum. The broadening effect is due to the fact that the ^{32}Ar nuclei undergo first a β-decay and immediately after the daughter nuclei decay by proton emission while in flight; consequently, the emitted β-delayed protons will be characterized by a kinematic shift depending on the direction of emission with respect to the recoiling emitting nucleus. Particularly, as the recoil is isotropic, the net result is then a visible broadening in the energy distribution of the collected proton spectrum. Despite the low statistics collected, due to the particle detection limited to a small solid angle, this work permitted to obtain one of the most precise estimations of $\tilde{a}_{\beta\nu}$ for Fermi transitions, mainly thanks to the excellent proton detector energy resolution.

The value measured by Schardt and Riisager for pure Fermi transitions was equal to 1.00(8). A few years later, in 1999, a further study on ^{32}Ar has been performed by Adelberger et al. [63]. Basically, the idea of measuring the broadening of the proton lines was replicated, this time by employing cooled PIN-diode proton detectors. However, in that case, the experimental set-up was placed inside a superconducting magnet operating at B = 3.5 T, in order to directly separate β-particles and protons (bending radius of $\approx$ 0.55 cm and $\approx$ 7.14 cm, respectively); consequently, by eliminating the addition of a β-background in the proton energy spectra, possible distortions in the shape of the broadened proton peaks were directly avoided. Once again, the most challenging task in the proton broadening measurement was to characterize the detector response function with sufficient accuracy; in this sense, by making use of cooled detectors and a temperature-controlled electronics, an improved proton energy resolution of $\approx$ 4.5 keV ($\approx$ 3 keV of electronic noise) was obtained. Results from fitting the shape of the IAS proton line and comparing to theoretical expectations yielded $\tilde{a}_F = 0.9989 \pm 0.0052$ (stat.) $\pm$ 0.0039 (syst.), thus improving the limits on the existence of a possible scalar current contribution. The associated systematic error was mainly due to the uncertainty on the mass of ^{32}Ar, obtained at that time from a fit to the Isobaric Multiplet Mass Equation [117]. In the meantime, a direct measurement on the mass of ^{32}Ar has been performed at the ISOLTRAP set-up at ISOLDE [118].

In this framework, the WISArD experiment aims at a possible most precise measurement of $\tilde{a}_{\beta\nu}$ for both Fermi and Gamow-Teller transitions by measuring, differently from the previous works, not the broadening of the proton peak lines but rather the kinematic mean energy shifts characterizing the β-delayed protons emitted in the decay of ^{32}Ar.
The detection apparatus, located again inside a superconducting magnet at B = 4 T, is conceived as composed by two types of detectors: first, a unique plastic scintillator coupled to a SiPM, for the detection of the β-particles emitted in the upper hemisphere; secondly, an array of eight silicon detectors disposed symmetrically with respect to the beam implantation point, four in the upper and four in the lower hemisphere, respectively. In this way, it is possible to record β-proton coincident events in the two cases of emission of protons, either in the same (up-up) or in the opposite (up-down) direction with respect to the detected β-particle. Consequently, it is possible to measure the associated mean upper and lower proton energy shifts, which appear directed, respectively, towards lower energies in case of protons emitted in the same direction as the β-particle and instead transferred towards higher energies in case of protons emitted in opposite direction with respect to the β-particle. Particularly, the kinematic shift becomes apparent if comparing the proton spectra acquired by the same detectors with and without imposing the condition on having a β-coincident event. Moreover, the measurement of the kinematic energy shift is in principle easier and

more feasible than a broadening one, as it does not require an absolutely perfect knowledge of both the proton detector response function and the proton line fitting function, which should include varied effects not straightforwardly quantifiable, spanning from the pulser resolution to the Fano factor, the electronic and nuclear straggling in the catcher foil and the proton detector dead layer, the escape of silicon x-rays and the energy loss in form of phonon excitations in the detector. Finally, the mean energy shift depends linearly on the $\tilde{a}_{\beta\nu}$ coefficient[1]. Consequently, a linear interpolation of the shifts of the centroids of the experimental proton energy distributions compared to their respective simulated ones can allow to determinate in an easier and in principle more precise way the values of $\tilde{a}_{\beta\nu}$ for both Fermi and Gamow-Teller transitions.

In particular, the ^{32}Ar isotope appears to be a powerful candidate for the measurement of the angular correlation coefficient for both Fermi and Gamow-Teller transitions, permitting to set new limits on the possible existence of new types of interactions, scalar and tensor ones respectively. A simplified decay scheme of ^{32}Ar is reported in Fig. 2.1.

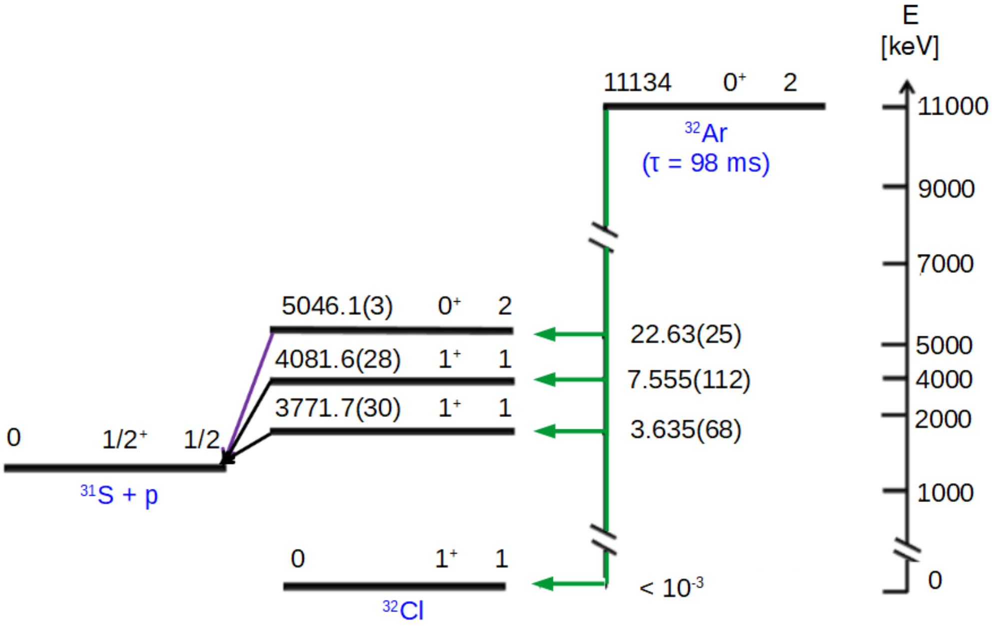

Figure 2.1: Simplified decay scheme of ^{32}Ar, showing the main β (green) and proton (IAS in purple, others in black) lines. Above each state, from left to right, the excitation energy (in keV), the spin (with parity) and the isospin values are reported. On the left with respect to the vertical green line, the branching ratios (%) of the β-transitions [119].

---

[1] After integrating its theoretical expression on all β-energies and solid angles.

Fairly well produced via the ISOL technique at ISOLDE, the ^{32}Ar ($T_{1/2}$ = 98 ms, Q_{EC} = 11134(19) keV) offers indeed primarily the possibility to precisely study the proton emission following the superallowed $0^+ \rightarrow 0^+$ Fermi transition to the T = 2 state of ^{32}Cl (E^* = 5046.1(3) keV), characterized by a branching ratio of 22.63(25)%. Additionally, further proton lines allow to perform similar studies on proton emission after Gamow-Teller transitions; specifically, the ones capable of providing sufficient statistics to possibly improve the current limits on the tensor interactions follow the pure $1^+ \rightarrow 0^+$ Gamow-Teller transitions on the T = 1 states of ^{32}Cl (E^* = 4081.6(28) and 3771.7(30) keV), with branching ratio of 7.555(112) % and 3.635(68)% respectively. A complete study on the ^{32}Ar decay scheme is reported in [119].

2.2 ISOLDE and the ^{32}Ar production at CERN

From the early days of nuclear physics, the first pioneering attempts to artificially produce radioactive isotopes had already led to the identification of new species, *e.g* ^{13}N and ^{30}P by Joliot and Curie in 1934 [120], as well as to the production of many neutron-rich radioactive isotopes in the 1940s thanks to the development of the first controlled fission reactor [121]. However, the advent of new powerful accelerators in the following decades finally played a key role for the progress in the exploration of the nuclear chart.
In particular, starting from the 1950s, two complementary methods of producing nuclei far from stability have been rapidly developed: the Isotope Separation OnLine (ISOL) and the so called In-Flight separation techniques. In the ISOL technique [122], the primary beam is composed of light particles impinging on a thick target, which gives rise to a huge amount of reaction products created mainly via spallation and fission; subsequently, the reaction products are thermalized, ionized and then post-accelerated, resulting in beams of excellent quality in terms of emittance, energy resolution and time structure, but as well very poorly produced if considering short-lived nuclei or isotopes coming from refractory elements.
In contrast, in the In-Flight method [123] the heavy and highly energetic primary particles impinge on a thin target, in order to have the reaction products, produced by fragmentation of the projectile, directly recoiling out of the target in the forward direction; in this case, in spite of the larger emittance of production and the need for slowing down the secondary beam, the primary advantages are the quick separation, that makes this technique applicable also to very short-lived nuclei ($\tau \sim \mu$s), and the possibility to produce radioactive ions regardless of their atomic and chemical properties.

The ISOL technique is used to produce radioactive nuclei near stability at the low-energy beam facility Isotope Separation OnLine Device (ISOLDE) at CERN. Notably, a proton beam produced in Linac4 [124] and accelerated by the Proton Synchrotron Booster (PSB), with an energy of 1.4 GeV and an intensity up to 2 μA, bombards a thick target (up to a few 100 g/cm^2) material, which has been specifically composed of nano-structured CaO powder for both the WISArD proof-of-principle experiment in 2018 and the experimental campaign in 2021. Consequently, a wide variety of nuclides is produced inside the target by spallation reactions; however, by progressively interacting with the surrounding target material, the reaction products are neutralized and thermalized in the target volume. Subsequently, due to the heating of the target at high temperature (typically between 1000 and 2000 K), the newly created radioactive isotopes are evaporated and effuse via a transfer line to the plasma region where they are ionized and then post accelerated, with energies usually between 30 and 60 keV [125].

A schematic representation of the ISOLDE experimental hall, with a focus on the experimental platform around which the WISArD experiment is installed, is shown in Fig. 2.2.

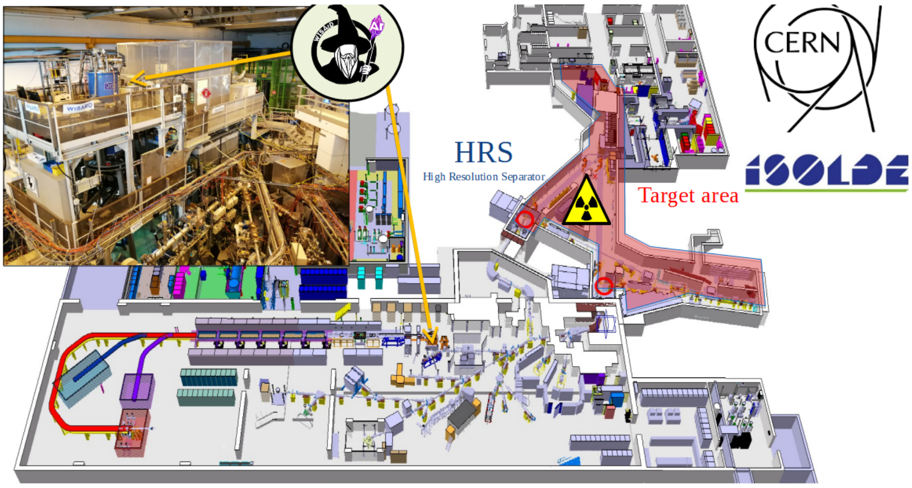

Figure 2.2: A schematic representation of the ISOLDE experimental hall. The proton beam from the PSB, coming at an energy of 1.4 GeV, bombards a thick target (up to a few 100 g/cm^2), from which the reaction products are extracted, ionised and post-accelerated at 30 keV. In case of the WISArD experiment, after the mass separation operated by the General Purpose Separator (GPS), the singly-ionized ^{32}Ar beam is transferred to the detection set-up located inside the WISArD superconducting magnet, high-lightened in the left picture.

Particularly, in case of the WISArD experimental campaign, the ^{32}Ar$^+$ singly-charged ions were extracted, post-accelerated at 30 keV and transported through one of the two available electromagnetic separators, either the General Purpose Separator (GPS) or the High-Resolution Separator (HRS), having mass resolving power up to $m/\Delta m$ = 1000 and 7000, respectively [126, 127]. After the mass selection operated by the GPS, the 30 keV ^{32}Ar$^+$

beam was sent into the REX-ISOLDE set-up [128], operating in continuous transmission mode, and finally delivered to the WISArD beamline and focused all the way up to the catcher foil which constitutes the implantation point, located inside the Oxford Instruments WISArD superconducting magnet.

Overall, in the 2021 campaign the average $^{32}\mathrm{Ar}^{+}$ production yield was estimated to be $\simeq 1500$ pps, more than a factor two below the ISOLDE standard capability [129]; the percentages of beam transmission through the REX-ISOLDE set-up and the WISArD beamline were estimated to be both around 50%, resulting in a total implantation rate of roughly 360 pps. Further details concerning the WISArD beamline are given in Appendix B.

2.3 The experimental set-up

A successful proof-of-principle experiment has been performed at ISOLDE in November 2018, permitting to demonstrate the applicability of the approach and to investigate the statistical and systematic effects influencing the level of precision on the final measurements. Despite the employment of a rather rudimental detection set-up and a limitation in terms of the statistics acquired, the experimental campaign already led to the third best measurement of $\tilde{a}_{\beta\nu}$ for Fermi transitions [111]. After investigating and estimating the systematic errors, a consistent upgrade of the experimental set-up has been commissioned and realized in the past two years, in order to potentially achieve the aimed precision of the permil level on the determination of $\tilde{a}_{\beta\nu}$. A new experimental campaign has been conduced in October 2021.

2.3.1 Principle of the experimental set-up

In both 2018 and 2021 campaigns, the detection apparatus, schematically sketched in Fig. 2.3, has been located at the centre of the superconducting solenoid magnet of the former WITCH experiment [6], capable of generating a uniform magnetic field along the z-axis with an intensity in the range [0, 9] T.

In both cases, the experimental set-up is comprehensive of eight silicon detectors for proton detection and a plastic scintillator coupled to a silicon photomultiplier for β-particle detection. The incoming $^{32}\mathrm{Ar}^{+}$ nuclei, with an energy of 30 keV, are implanted within the first (47 ± 14) nm of the catcher (longitudinal straggling, according to SRIM [130]), composed of a 6 μm Mylar foil, having a diameter of 20 mm, in which the decay takes place. Specifically, the positrons produced in the β-decay can be emitted either in the lower or in the upper hemisphere, being in both cases tightly confined by the vertical 4 T magnetic field and then, respectively, lost in the beam pipe or guided towards the plastic scintillator with an efficiency of 100%. On the contrary, the protons emitted right after, only slightly affected by the magnetic field due to their higher mass, spiral with a larger radius along the magnetic field lines and can be detected either by the four upper silicon detectors (commonly labeled Si1U to Si4U) or by the four lower silicon detectors (labeled Si1D to Si4D), disposed in a mirrored geometrical configuration with respect to the position of the catcher foil.

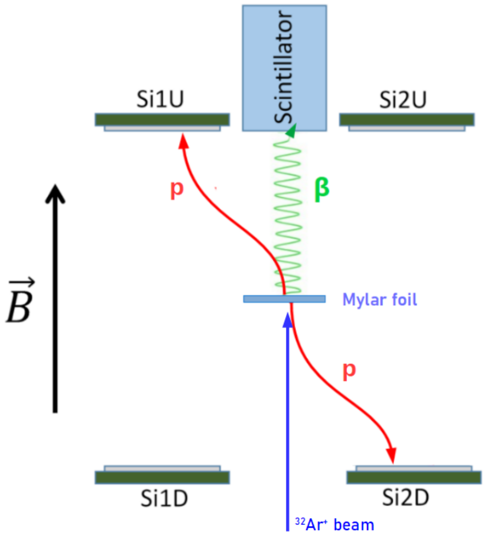

Figure 2.3: Schematic sectional view of the 2018 detection set-up with four silicon detectors visible. The incoming beam is implanted and then decays in the Mylar foil. The protons (red) emitted in the radioactive decays of ^{32}Ar are slightly bent by the magnetic field to the upper or lower silicon detectors, while the positrons (green) are either guided towards the plastic scintillator or lost in the lower beam pipe.

The detection set-up also includes two rotatory rods, which can be controlled from outside the magnet. On the first rod, a two-position arm permits to rotate and place right in the centre with respect to the direction of the incoming beam either the catcher foil or a 4-α radioactive source (^{148}Gd, ^{239}Pu, ^{241}Am, ^{244}Cu), used for beam implantation and calibration purposes respectively. In particular, the alpha source, as shown in Fig. 2.6, is always held between two aluminum plates if not in use.

2.3.2 Detection set-up in the 2018 proof-of-principle experiment

More specifically, the detection set-up employed in the proof-of-principle experiment performed in November 2018 was comprehensive of eight silicon detectors (300 μm thick, ϕ = 30 *mm* effective diameter) disposed in two parallel planes located at 65.5 *mm* from the catcher, each of them connected to a taylor-made preamplifier manufactured at LP2i-Bordeaux, employed for β-delayed proton detection. Furthermore, a EJ200-type (polystirene) plastic scintillator (ϕ = 20 *mm*, L = 50 *mm*), optically coupled to a silicon photomultiplier (Hamamatsu S13360-6050PE) and placed parallel to the z-axis at again 65.5 *mm* from the catcher, was used for the detection of scintillation photons created by the energy deposit of the β-particles.

2.3.3 Detection set-up in the 2021 experiment

Significant improvements have been carried out in the realization of taylor-made silicon detectors and SiPMs for the experiment in 2021. A schematic representation of the different experimental set-ups employed in the proof-of-principle experiment and in the 2021 campaign is shown in Fig. 2.4.

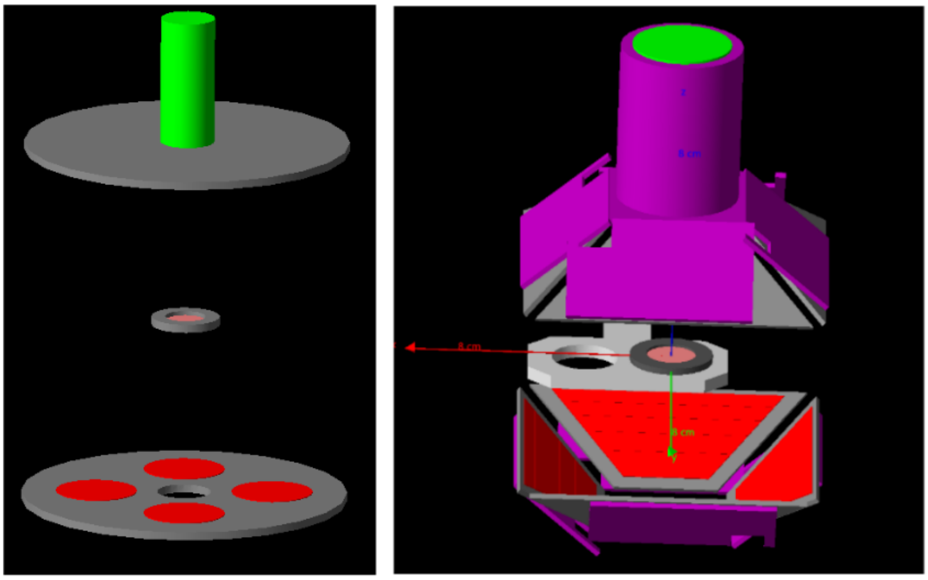

Figure 2.4: A schematic representation of the WISArD experimental set-ups used in the proof-of-principle experiment (left) and in the 2021 campaign (right). The Mylar foil is depicted in both cases in pink, the silicon detectors for the proton detection in red and the plastic scintillator in green. Further supporting mechanical structures are represented in grey and magenta. The Cartesian coordinate system is also represented.

2.3.3.1 Proton detection set-up

Yet, in order to enhance at the same time the solid angle coverage and the detector energy resolution with respect to the proof-of-principle experiment, for the 2021 experimental campaign new taylor-made silicon detectors were designed specifically for WISArD and subsequently manufactured by Micron [131]. In particular, each new detector, differently from the unique silicon blocks used previously, has been fabricated as a 300 μm-thick single-sided strip silicon detector, characterized by a new trapezoidal shape and divided into five strips, having each the same geometrical area. Once mounted on their mechanical support, the eight silicon detectors appear now spatially disposed onto two truncated pyramid-like structures disposed symmetrically with respect to the catcher foil, as shown in Fig. 2.5 and in Fig. 2.6.

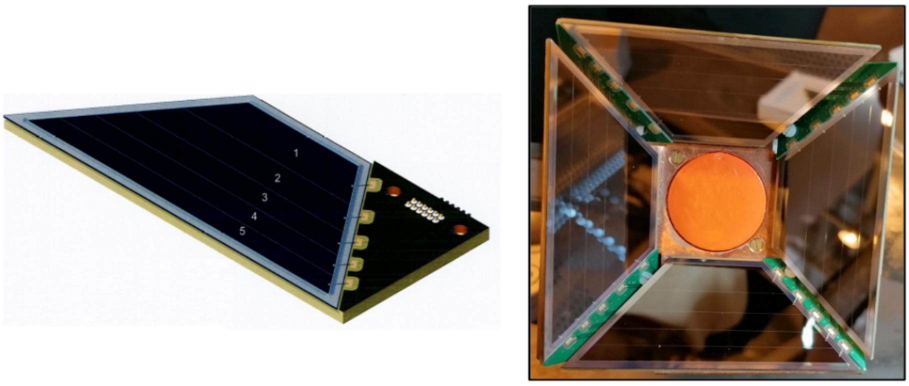

Figure 2.5: Right: CAD drawing of one single-sided strip silicon detector, with numeric labels on its five strips. Left: picture of one of the two truncated pyramid-like structures, on which four silicon detectors have been mounted.

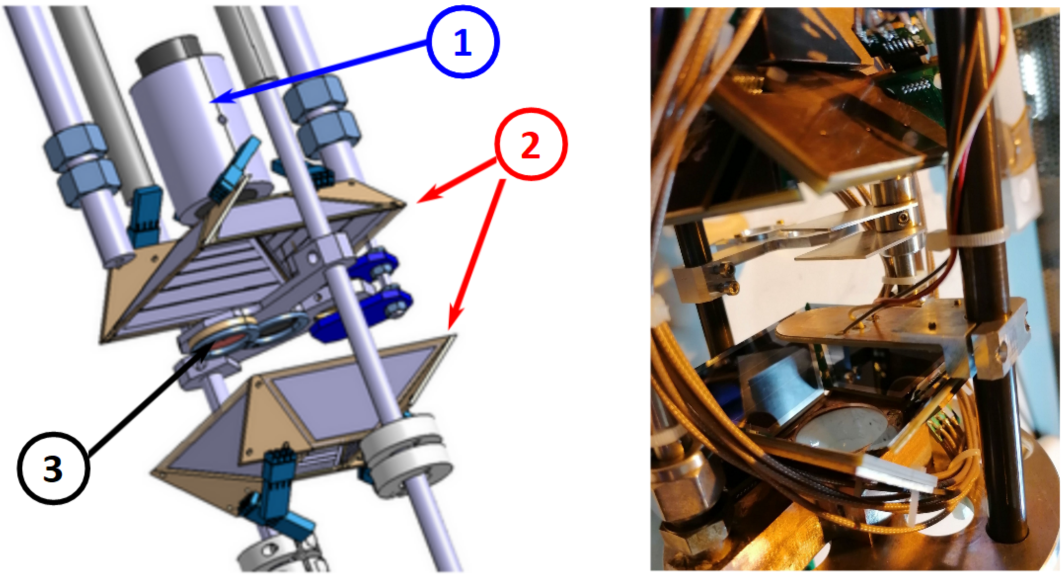

Figure 2.6: On the left, CAD drawing of the detection set-up, with the arrows pointing on the β-detection assembly (1), the two pyramids holding the stripped silicon detectors (2) and the mechanical support holding the catcher foil (3). On the right, a picture of the corresponding final assembling.

Such a structure permits to have a good solid angle coverage while keeping incident angles for the protons close to 90°, resulting in a higher detection efficiency with respect to the proof-of-principle experiment (enhanced from $\sim$ 8 % in 2018 to a maximum of 57% in 2021). Moreover, custom made low-noise preamplifier cards based on the CAEN preamplifiers A1422H [132] were also designed to accompany the detectors. Particularly, as the strip layout is designed to keep a constant capacitance of approximately 100 pF per strip, a very similar preamplifier response is achieved for each strip of the silicon detectors, thus reducing eventual systematic differences in the response function of multiple strips in the same detector. In particular, the electronic noise obtained for all preamplifiers with a charge of 100 pF is below 4 keV, thus reaching the cutting edge for silicon detectors.

According to the specification data provided by Micron, the detectors are expected to have a dead layer thickness not superior to 100 nm. Yet, as the dead layer thickness affects the energy calibration of the proton spectra recorded by the detectors, further studies aimed at the experimental determination of its value have been made at LP2i-Bordeaux. The tests have been performed by means of a 700 keV alpha beam produced at the AIFIRA accelerator [133] by placing the detectors at 90° and 45° with respect to the direction of the incoming beam. On average, the detector resolution has been estimated to be (7 ± 3) keV (FWHM) for all five strips and the extrapolated dead layer thickness has been evaluated to (100.0 ± 30.2) nm (around three times lower with respect to the estimated value for the detectors used in the proof-of-principle experiment [111]), thus determining an energy loss inside it of the order of 1 keV for IAS protons of energy around 3.3 MeV.

2.3.3.2 β-detection set-up

A second significant improvement in the WISArD detection set-up concerns the β-detector. The detection principle remains unchanged, being based on a plastic scintillator optically coupled to silicon photomultipliers (SiPMs), nevertheless a certain amount of modifications were made to lower the detection threshold as much as possible. Effectively, as reported in the error budget of the proof-of-principle experiment [111], one of the main contributions to the systematic uncertainty on the determination of the $\tilde{a}_{\beta\nu}$ parameter is given by the backscattering of the positrons inside the catcher foil and on the plastic scintillator, which both lead to a non-detection of a fraction of the positrons originally emitted in the upward direction. In this sense, the detection threshold needs to be lowered to the minimum value achievable, in order to reduce the dependence on Geant4 simulation models for the determination of the missing events not recorded by the SiPMs as coming below the detection threshold. In the 2021 campaign, a plastic scintillator (ϕ = 30 mm, L = 50 mm) from ELJEN [134] has been used, coupled with an array of 3×3 MicroFJ-60035-TSV-TR1, J-Series type 6×6 mm^2 SiPM sensors provided by Onsemi [135], in order to enhance the geometrical ratio between the area of the SiPMs array and of the scintillator base, thus permitting to finally collect as much scintillation light as possible.

Each sensor is then connected to a preamplifier, provided by the IFIN-HH in Bucharest [136]. Furthermore, each preamplifier is capable of providing a dual-range output, resulting either in a low-gain or in a high-gain signal. Specifically, while the low-gain outputs permit to measure the full β-spectrum up to the endpoint, the corresponding high-gain ones, amplified by a factor of ten in terms of signal amplitude with respect to the associated low-gain ones, allow to precisely characterize the low-energy part of the spectrum, concerned by the effect of the β-detection threshold.

Pictures of the β-detection set-up employed for the experimental campaign in 2021 are shown in Fig. 2.7.

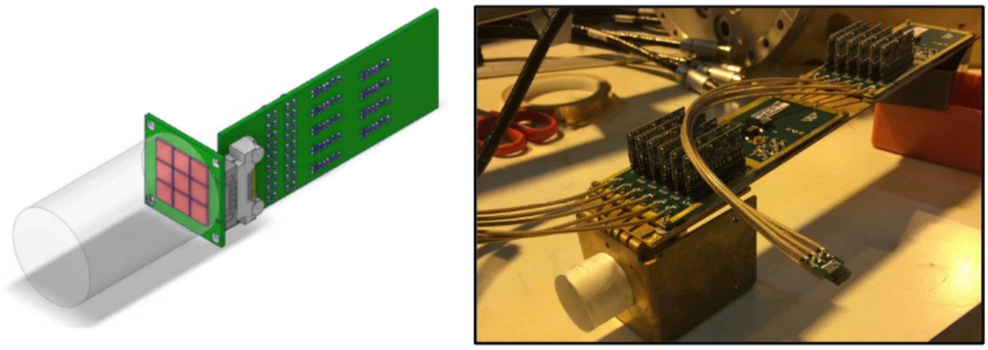

Figure 2.7: Left: CAD drawing relative to the 3×3 SiPMs array (red) coupled to the plastic scintillator (in transparency); the front-end electronics related to the low and high gain outputs (green) is also visible. Right: picture of the β-detection assembly; the plastic scintillator coupled to the SiPMs array is mounted on its cubic copper support.

2.3.3.3 Further details on the detection set-up

During the 2021 campaign, two different catcher foils have been employed, mounted on their aluminum mechanical support. The first one, a 6 μm thick Mylar foil, was identical in terms of material and thickness to the one employed in the proof-of-principle experiment and will permit to directly compare the data acquired in the two experimental campaigns. The second one, a 0.8 μm aluminized Mylar catcher, has been used in the second part of the data taking in order to study the systematic effects on the proton energy calibration and the β-particle backscattering due to the employment of different implantation foils.

The second rod hosts a four-segmented Faraday cup, also visible in Fig. 2.6, which can be rotated and placed perpendicularly to the incoming beam direction and used to monitor the beam intensity.

Finally, differently from the proof-of-principle experiment, even if the experimental set-up is located inside the cold bore of the superconducting magnet, an additional active glycol-based cooling system has been implemented. Its purpose is to speed up the thermalization process and keep the temperature of both the β-particle and the proton detectors stable, in order to avoid as much as possible fluctuations in temperature that would reflect in fluctuations in the response function of the detectors themselves within the data taking. The proton detectors, once cooled down, were showing a temperature of about -5° C (read by thermocouples placed on their mechanical supports) and a reverse current of 3 nA.

The experimental set-up fully assembled is shown in Fig. 2.6. Further details on it and on the upgrade of the WISArD beamline since the proof-of-principle experiment are more extensively reported in Appendix B.

2.3.3.4 FASTER acquisition system

The signals coming from the strips of the silicon detectors and from both the low-gain and high-channels composing the SiPMs array were read out by the FASTER data acquisition system, developed and provided by LPC CAEN [137]. FASTER is a high-performance, modular digital acquisition system based on a synchronized tree model. In particular, forty-eight ADC channels (MOSAHR) were employed to digitize the proton signals from the silicon detectors and eighteen QDC channels (CARAS) were used to process the β-particle signals sent by both the high gain and low gain SiPMs cells.

For ADC channels, the data sent to the PC comprises the timestamp of the first triggering cell, as well as the maximum height of the signal (in mV) after proper filtering by a CRRC4 filter, a time reference for this maximum (relative to the trigger), a pile-up flag indicating a possible pile-up event and a saturation flag saying if the signal height was higher than the maximum voltage range. In case of QDC channels, the charge of the digitized signals can be integrated over up to four different time windows. The data sent to the PC comprises the time stamp of the trigger, the integrated charges and a saturation flag.

The DAQ was configured in lossless mode, so that all data were recorded. A "trigger-merger" was also configured to group the data in case of at least three HG SiPM cells triggered within a 200 ns time window. In that case, any other data from signals occurring less than 1 μs before the trigger and less than 2 μs after the trigger was grouped with the others, which allowed to observe online the β-proton coincidences.

The recorded data were then split into different run files, characterized by a different acquisition time, radioactive beam implantation and calibration or background measurements.

Chapter 3

Data analysis

In this chapter, the analysis of the data collected during the experimental campaign on ^{32}Ar conducted at the WISArD experiment in October 2021 will be presented.

In the following, the data taking conditions will be described, the algorithm developed to presort the data will be introduced and the procedure adopted for the energy calibration of both the SiPMs array and the silicon detectors will be detailed. Afterwards, the experimental energy shifts related to the most intense ^{32}Ar proton peaks recorded in coincidence with β-particles will be computed and the related values, to be later on compared to the specular ones obtained via Geant4 simulations, will be reported.

3.1 Data sample and event selection

The WISArD experiment aims at a simultaneous measurements of the β-ν angular correlation coefficient ($a_{\beta\nu}$) and the Fierz interference term (b) for pure Fermi and pure Gamow-Teller transitions from β-proton decay by exploiting the kinematic shift technique, as described in Sec. 2.1.

After a successful proof-of-principle experiment performed in 2018 [111], permitting to demonstrate the applicability of the approach and to investigate the statistical and systematic effects influencing the level of precision on the final measurements, a new experimental campaign has been conduced on the β-delayed proton decay of ^{32}Ar in October 2021.

Specifically, the 2021 run, subdivided into a total of ten shifts, concomitantly allowed to test the newly designed mechanical set-up, the new SiPMs array and the custom-made silicon detectors, illustrated in more detail in Sec. 2.3 and in Appendix B. Furthermore, new data useful for reaching a final higher precision on the determination of $\tilde{a}_{\beta\nu}$ for both Fermi and Gamow-Teller transitions were acquired.

3.1.1 Data sample and experimental conditions

During the 10 shifts ($\sim$ 80 h of data taking), a total of 36 runs ($\sim$ 43 h) were acquired with ^{32}Ar beam and 8 runs ($\sim$ 7 h) were dedicated to the collection of spectra from the decay of the more intensely produced ^{33}Ar, later on used for calibration purpose. At the beginning and at mid-data taking, two technical problems appeared related to the ^{32}Ar beam extraction from the target and transmission through the WISArD beamline, respectively.
Effectively, the initial average ^{32}Ar$^+$ production yield[1] was estimated to be $\simeq$ 500 pps, more than a factor five below the ISOLDE standard capability [129], thus determining a loss in statistics in the first runs acquired. However, after retuning the beam through the REX set-up and performing a joint proton scan and target heating (target current was increased from 245 to 252 A), a factor three in terms of beam production was immediately gained, thus leading to an estimated ^{32}Ar$^+$ production yield of roughly 1500 pps, right after the first few hours of data taking. The percentages of beam transmission through the REX-ISOLDE set-up and the WISArD beamline were estimated to be both around 50%, resulting in a total implantation rate of roughly 360 pps.
Secondly, at around mid-beamtime the power supply of a drift electrode of the WISArD vertical beamline, employed for beam optimization (VBDRIF01, for further details see Sec. B.1.2 in Appendix B) and originally set at 1000 V, was tripped due to excessive current and, after being restarted, it was not able to operate with voltages greater than 900 V. Suddenly, its trip provoked an electrical discharge which resulted in an immediate strong degradation in the energy resolution of all the four upper silicon detectors. In order to investigate this issue, the control system normally maintaining a secondary vacuum (p $\sim 10^{-7}$ mbar) inside the magnet bore was turned off and the tower on which the detection set-up is mounted was taken out of the magnet. After disconnecting and recabling the upper silicon detectors to their respective preamplifiers, the tower was placed back in the bore and the vacuum control system was restarted. Right after, the silicon detectors were reported to work normally again, with an energy resolution estimated to be indeed between 7 and 15 keV. However, since then the silicon detector spectra presented a clear four-peak contamination coming from the α-particles emitted from the multiple-α radioactive source (^{148}Gd, ^{239}Pu, ^{241}Am, ^{244}Cu) mounted adjacently to the catcher foil on the same two-position aluminum arm. This contamination, absent in the previous runs and present in all silicon detector spectra, is very likely due to an accidental movement of the upper aluminum plate, normally covering the source if not in use, occurred while taking the tower out of the magnet bore for investigation on the detectors.

---

[1] For further details on the estimation of the ion beam production yields and implantation rates during the experiment see Appendix C.

It is also worth mentioning that, during all data taking, a SiPM HG channel (HG4) was not operative and a SiPM LG channel (LG9) was not connected due to a lack of connector spots available on the top flange of the tower. So, the β-particle signals were acquired with a total of eight cells out of the nine cells originally available for both HG and LG channels.

3.1.2 Proton single and β-coincident event selection

As explained in Sec. 2.3.3.4, the signals from the silicon detectors and from the SiPM cells were digitized by the respective MOSAHR and CARAS channels of the FASTER acquisition system. During data taking, the DAQ was configured in lossless mode, so that all data were recorded. Complementarily, an additional "trigger-merger" option was set in order to group the data in case of at least three HG SiPM cells firing within a 200 ns time interval; in that case, any other silicon or SiPM data occurring within a time window of [-1, 2] μs after the trigger was grouped with the others. In particular, the joint choice of setting the trigger multiplicity to at least three cells firing together and the time condition imposed for treating the signals as a part of common data groups has been taken in order to observe online the β-proton coincident spectra in the cleanest way possible, *i.e.* affected as little as possible by the contribution of eventual fake coincidences. In this way, the contribution to β-spectra not due to the energy released inside the scintillator by the incoming β-particles, but rather related to dark events typically triggering one cell only or, but very less likely, even a couple of cells at once was strongly limited.

Subsequently, further more stringent conditions were then imposed offline for the reconstruction of the single and β-coincident events. In particular, by observing the location of the peaks in the time difference distributions between the SiPMs trigger and the silicon signals, an additional time event selection was introduced, so that data were offline reconstructed into groups only in case of at least three SiPM cells firing almost at the same time with respect to the first one triggered (Δt_{LG} = [-20; 100] ns and Δt_{HG} = [-100; 150] ns with respect to the first triggering cell) and, concomitantly, the silicon signal coming within a very limited time interval (Δt_{Si} = [-200; 150] ns) with respect to the first triggering cell. In this way, signals due to fake coincidences were almost surely discarded. Examples of the typical time difference distributions for both the SiPM cells (Δt_{LG}) and the silicon detectors (Δt_{Si}) are reported in Fig. 3.1 and 3.2, respectively.

However, the effective correctness of the condition imposed online on the minimum SiPM trigger multiplicity, and an eventual decision of changing its value for the further analysis, will be systematically studied afterwards. Effectively, considering as a starting point the list of all the single data acquired in lossless mode, regardless of their belonging to a specific data group and chronologically ordered by acquisition time, it was later on possible to develop an offline sorting algorithm aiming to reconstruct the data groups in all conditions of LG and HG β-triggering, varying, respectively, from a minimum of one to a maximum of eight SiPM cells triggering at the same time.

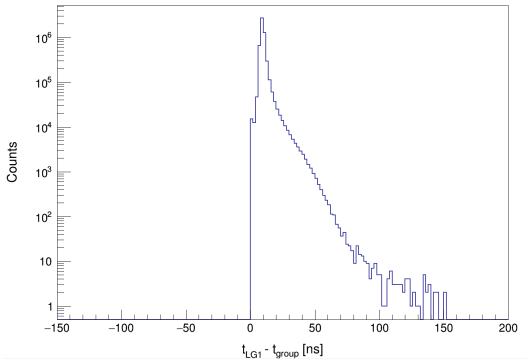

Figure 3.1: Time difference distribution between the signals registered by the LG1 SiPM cell and the corresponding signals registered by the LG3 SiPM cell firing almost at the same time with respect to the first one triggered (Δt_{LG} = [-20; 100] ns). Similar spectra can be obtained for the other LG and HG SiPM signals.

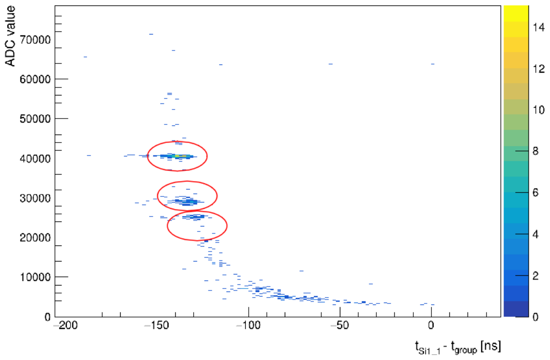

Figure 3.2: Bi-dimensional distribution showing the β-coincident proton signals registered by SiDet1 (strip 1) as a function of the time difference between the signals registered by the SiDet1 (strip 1) and the corresponding signals registered by the LG3 SiPM cell firing almost at the same time with respect to the first one triggered (Δt_{LG} = [-20; 100] ns). The shift in time as a function of the proton energy is due to the time walk induced by the simple threshold triggering effect on the signal registered by the silicon detectors, which causes a dependence of the trigger time on the peak height of the signal. The red circles refer to the proton peaks related to the transition from the IAS and following the first and the second most intense Gamow-Teller decays, respectively. Similar spectra can be obtained for the other silicon detectors.

3.2 Data analysis

In the following, the analysis of the experimental data related to the β-proton coincidence to the isobaric analogue state of ^{32}Ar (IAS, $0^+ \rightarrow 0^+$), which represents yet its most intense transition, will be presented. The silicon detector and the SiPMs array energy calibration will be illustrated. Furthermore, the offline algorithm developed to reconstruct the β-proton coincident spectra as a function of the β-trigger multiplicity will be described and the associated results will be presented. Subsequently, the effects on the β-spectra due to further cuts performed on the silicon detector signals will be shown. Finally, the experimental energy shifts associated to the IAS protons will be computed for each silicon detector.

3.2.1 Silicon detector energy calibration

All the eight silicon detectors, each of them providing signals from the five front strips and from the corresponding back-side, have been independently energy calibrated.
Specifically, the exploitable runs acquired with the ^{32}Ar beam were first summed together to make two unique cumulative runs, each of them referring to a different data taking condition relatively to the catcher foil employed (6 μm Mylar and 0.8 μm aluminized Mylar foil). Subsequently, the two collective runs were employed for determining all the forty-eight energy calibration linear fitting curves, by correlating the ADC channel positions related to the two most intense proton peak lines to their corresponding energies, at 2121.7(31) and 3356.0(7) keV respectively [119]. In particular, different experimental corrections to these two theoretical proton peak energies have been applied for each strip located on both the upper and the lower silicon detectors, in order to take into account the total energy partially lost by the protons before impacting on the detectors, firstly within the catcher foil and afterwards in the silicon detectors dead layer. Moreover, different corrections have been applied for each of the two cumulative runs, in order to correct independently the proton energies used for calibration with respect to the different thickness and material composing the catcher foil. Yet, it should be remembered that the post-accelerated ^{32}Ar$^+$ beam is always implanted at the very bottom of the catcher foil, roughly at (47 $\pm$ 14) nm in case of the Mylar foil and at (21 $\pm$ 8) nm in case of the aluminized Mylar foil according to SRIM [130]; this implicates that, as the implantation point is not consequently located symmetrically at the centre of the catcher foil, corrections to the energy calibration need indeed to be considered separately for the strips located on the upper and on the lower silicon detectors, *i.e.* accounting for the energy lost respectively both in the majority of thickness of the catcher foil and in the silicon detector dead layer (for the upper detectors) and within a very limited thickness of the catcher foil (corresponding to the implantation depth estimated via SRIM) and the silicon detector

dead layer again (for the lower detectors).

The references in terms of energy corresponding to the two most intense peaks on the raw spectra have then be computed in the following way:

$$\begin{cases} E^{i,j}_{cal,up}\,(s_c, s_{dL}) & = E_{th} - \Delta E_{catcher}(s^{i,j}_{c,up}) - \Delta E_{deadLayer}(s^{i,j}_{dL,up}) \\ E^{i,j}_{cal,down}\,(s_c, s_{dL}) & = E_{th} - \Delta E_{catcher}(s^{i,j}_{c,down}) - \Delta E_{deadLayer}(s^{i,j}_{dL,down}) \end{cases} \tag{3.1}$$

where E$_{cal}$ is the final proton peak energy employed for determining the calibration curve of the i-th strip (i in $\{1, 2, 3, 4, 5\}$) located either on an upper ($E_{cal,up}$) or on a lower ($E_{cal,down}$) silicon detector, in case of employment of a specific j-th catcher foil (either Mylar or aluminized Mylar). $\Delta E_{catcher}$ is the energy lost within the catcher foil (depending on the $s_c^{i,j}$, the real catcher thickness traversed by the protons inside the catcher foil and detected by the i-th strip of either an upper or a lower detector) and $\Delta E_{deadLayer}$ is the energy lost inside the silicon detector dead layer (depending on the $s^{i,j}_{dL}$, the real dead layer thickness traversed by the protons inside the silicon detector before being detected by the i-th strip of either an upper or a lower silicon detector).

As explained in Sec. 2.3.3.1, the spacial disposition of the silicon detectors is fixed and arranged in such a way that each of the five strips on all silicon detectors results symmetrically disposed around the catcher foil, but at a different relative angle with respect to the vertical z-axis; effectively, referring to Fig. 2.5, strip 1 in both the upper and lower silicon detectors is nearer to the z-axis, then strip 2, 3 and 4 are progressively further away, and strip 5 results placed at the highest angle with respect to the z-axis. This particular spacial configuration of the proton detection set-up directly implies that the protons, in case they are emitted within the same energy line and then detected by different strips in the same hemisphere, had been originally emitted during the decay with different angles with respect to the z-axis itself and, consequently, they had traversed a slightly different thickness within the catcher foil ($s_c^{i,j}$) and so deposited a slightly different amount of energy inside it ($\Delta E_{catcher}$ ($s_c^{i,j}$)) before being detected. In a similar way, these protons emitted at these different angles, transported subsequently within the magnetic field, will impinge on different strips with a different incident angle, thus traversing a slightly different thickness within the silicon detectors dead layer ($s^{i,j}_{dL}$) and resulting in a different value of energy lost inside it ($\Delta E_{deadLayer}$ ($s^{i,j}_{dL}$)). Hence, a very refined energy calibration needs to take into account precisely and independently the energy lost by each proton line (2121.7(31) and 3156.0(7) keV) within both the catcher foil and the silicon detector dead layer for each strip located either in the upper or in the lower hemisphere.

Practically, the angles of emission of the protons right after their creation, referred conventionally to the z-axis from now on, cannot be retrieved from experimental measurements.

Even more, corrections to the trajectory due to the curvature generated by the magnetic field result rather difficult to be estimated manually with an excellent precision. Yet, it still remains possible to evaluate precisely the mean energy lost both inside the catcher foil and within the detector dead layer by exploiting numerical simulations including an accurate replica of the WISArD detection set-up and of the data taking conditions.[2]. In this way, by simulating protons at energies equal to the two most intense peaks of ^{32}Ar, respectively at 2121.7(31) and 3356.0(7) keV [119] emitted in the decay from implantation points inside the catcher foil located at respectively (47 ± 14) nm and at (21 ± 8) nm, it is possible to estimate directly the energy lost by the protons both inside the catcher and in the dead layer, thus including automatically corrections for the bending radius inside the materials and also corrections for the incident angle on the different strips and the incident energy at the entrance of the active volume of the silicon detectors, reduced by the amount of energy previously lost within the catcher foil and the dead layer itself. Results related to the corrections to the energy calibration of the two most intense peaks of ^{32}Ar are reported in Table 3.2 and in Table 3.1, related to the aluminized Mylar and the Mylar catcher foil respectively.

	^{32}Ar corrected proton energy [keV] vs strip n° (AlMylar)				
Information	**1**	**2**	**3**	**4**	**5**
E_{th} [keV]	2121.7(31)	2121.7(31)	2121.7(31)	2121.7(31)	2121.7(31)
$\Delta E_{catcher}$ ($s_{c,up}$) [keV]	41.8(2)	45.5(2)	51.0(2)	57.3(2)	64.3(2)
$\Delta E_{deadLayer}$ ($s_{dL,up}$) [keV]	2.68(2)	2.66(2)	2.70(2)	2.78(2)	2.92(2)
$E_{cal,up}$ ($s_{c,up}$, $s_{dL,up}$) [keV]	2077.22(332)	2073.54(332)	2068.00(332)	2061.62(332)	2054.48(332)
E_{th} [keV]	2121.7(31)	2121.7(31)	2121.7(31)	2121.7(31)	2121.7(31)
$\Delta E_{catcher}$ ($s_{c,down}$) [keV]	1.12(1)	1.22(1)	1.35(1)	1.51(1)	1.63(1)
$\Delta E_{deadLayer}$ ($s_{dL,down}$) [keV]	2.69(2)	2.64(2)	2.65(2)	2.79(2)	2.79(2)
$E_{cal,down}$ ($s_{c,down}$, $s_{dL,down}$) [keV]	2117.89(31)	2117.84(31)	2117.70(31)	2117.40(31)	2117.28(31)
E_{th} [keV]	3356.0(7)	3356.0(7)	3356.0(7)	3356.0(7)	3356.0(7)
$\Delta E_{catcher}$ ($s_{c,up}$) [keV]	29.0(2)	32.0(2)	35.2(2)	39.4(2)	44.4(2)
$\Delta E_{deadLayer}$ ($s_{dL,up}$) [keV]	1.88(2)	1.88(2)	1.89(2)	1.93(2)	1.93(2)
$E_{cal,up}$ ($s_{c,up}$, $s_{dL,up}$) [keV]	3325.12(92)	3322.12(92)	3318.9(92)	3314.67(92)	3309.67(92)
E_{th} [keV]	3356.0(7)	3356.0(7)	3356.0(7)	3356.0(7)	3356.0(7)
$\Delta E_{catcher}$ ($s_{c,down}$) [keV]	0.81(1)	0.88(1)	0.96(1)	1.08(1)	1.18(1)
$\Delta E_{deadLayer}$ ($s_{dL,down}$) [keV]	1.86(2)	1.88(2)	1.90(2)	1.94(2)	1.99(2)
$E_{cal,down}$ ($s_{c,down}$, $s_{dL,down}$) [keV]	3353.33(73)	3353.24(73)	3353.14(73)	3352.98(73)	3352.83(73)

Table 3.1: Summary of the corrections to the energy calibration relatively to the two most intense proton energy peak lines of ^{32}Ar, at 2121.7(31) and 3356.0(7) keV respectively [119], along with their statistical uncertainties. Corrections for the energy lost inside the catcher foil and in the silicon detector dead layer have been retrieved via Geant4 simulations of the WISArD detection set-up, by generating mono-energetic protons at 2121.7 and 3356.0 keV implanted, concerning the x and y coordinates, at the centre of a 0.8 μm aluminized Mylar foil and, regarding the z coordinate, at 20.6 nm with respect to the bottom part of the catcher. Simulations have been performed assuming an initial proton Gaussian distribution around the implantation point (r = 2 mm, σ = 300 μm).

---

[2] Further details on the structure and processing of the WISArD Geant4 simulations will be given in Chapter 4.

	^{32}Ar corrected proton energy [keV] vs strip n° (Mylar)				
Information	**1**	**2**	**3**	**4**	**5**
E_{th} [keV]	2121.7(31)	2121.7(31)	2121.7(31)	2121.7(31)	2121.7(31)
$\Delta E_{catcher}$ ($s_{c,up}$) [keV]	141.8(2)	159.4(2)	178.4(2)	200.8(2)	227.4(2)
$\Delta E_{deadLayer}$ ($s_{dL,up}$) [keV]	2.82(2)	2.95(2)	2.97(2)	3.02(2)	3.10(2)
$E_{cal,up}$ ($s_{c,up}$, $s_{dL,up}$) [keV]	1977.08(332)	1959.35(332)	1940.33(332)	1917.88(332)	1891.20(332)
E_{th} [keV]	2121.7(31)	2121.7(31)	2121.7(31)	2121.7(31)	2121.7(31)
$\Delta E_{catcher}$ ($s_{c,down}$) [keV]	1.08(1)	1.22(1)	1.36(1)	1.53(1)	1.60(1)
$\Delta E_{deadLayer}$ ($s_{dL,down}$) [keV]	2.69(2)	2.63(2)	2.69(2)	2.73(2)	2.74(2)
$E_{cal,down}$ ($s_{c,down}$, $s_{dL,down}$) [keV]	2117.93(313)	2117.85(313)	2117.65(313)	2117.44(313)	2117.36(313)
E_{th} [keV]	3356.0(7)	3356.0(7)	3356.0(7)	3356.0(7)	3356.0(7)
$\Delta E_{catcher}$ ($s_{c,up}$) [keV]	98.2(2)	109.7(2)	122.4(2)	137.3(2)	154.7(2)
$\Delta E_{deadLayer}$ ($s_{dL,up}$) [keV]	1.94(2)	1.90(2)	1.91(2)	1.95(2)	2.01(2)
$E_{cal,up}$ ($s_{c,up}$, $s_{dL,up}$) [keV]	3255.86(92)	3244.4(92)	3231.69(92)	3216.75(92)	3199.29(92)
E_{th} [keV]	3356.0(7)	3356.0(7)	3356.0(7)	3356.0(7)	3356.0(7)
$\Delta E_{catcher}$ ($s_{c,down}$) [keV]	0.76(1)	0.85(1)	0.98(1)	1.09(1)	1.14(1)
$\Delta E_{deadLayer}$ ($s_{dL,down}$) [keV]	1.91(2)	1.85(2)	1.88(2)	1.92(2)	2.08(2)
$E_{cal,down}$ ($s_{c,down}$, $s_{dL,down}$) [keV]	3353.33(73)	3353.30(73)	3353.14(73)	3352.99(73)	3352.78(73)

Table 3.2: Summary of the corrections to the energy calibration relatively to the two most intense proton energy peak lines of ^{32}Ar, at 2121.7(31) and 3356.0(7) keV respectively [119], along with their statistical uncertainties. Corrections for the energy lost inside the catcher foil and in the silicon detector dead layer have been retrieved via Geant4 simulations of the WISArD detection set-up, by generating mono-energetic protons at 2121.7 and 3356.0 keV implanted, concerning the x and y coordinates, at the centre of a 6 μm Mylar foil and, regarding the z coordinate, at 47 nm with respect to the bottom part of the catcher. Simulations have been performed assuming an initial proton Gaussian distribution around the implantation point (r = 2 mm, σ = 300 μm).

As shown in Table 3.2 and in Table 3.1, the corrections to the proton energy detected by the five strips mounted on detectors in the upper and lower hemisphere are indeed different one from each other, taking into account at once the location of the real ^{32}Ar^{+} implantation point, the effects on the proton trajectory induced by the magnetic field, the real thickness and the nature of the composing material traversed by the protons inside both the catcher foil and the dead layer. As expected, the corrections to the energy lost are slightly more significant for protons at lower energy (2121.7 keV) with respect to the ones at higher energy (3356.0 keV); furthermore, at any given energy, corrections assume higher values for strips physically located further away from the z-axis, *i.e.* they become progressively more noteworthy from strip 1 to strip 5.

By comparing corrections to the energy peak for different target material, it can be noted that, at a given proton line, the energy lost inside the aluminized catcher foil is generally about four times smaller than the corresponding one lost within the Mylar catcher. In particular, this effect is due to a combination of causes: on one hand, knowing that at first-order the energy lost by a charged particle inside a material is linearly dependent to the thickness traversed, it can be remarked that there is an immediate reduction in the energy lost passing from the Mylar to the aluminized foil as a consequence of the different thickness of the catchers themselves

(6 μm and 0.8 μm respectively); however, the reduction is not directly equal to the ratio of the thicknesses, because at the level of chemical composition, Mylar results composed by a combination of hydrogen, carbon and oxygen (Poly(ethyl benzene-1,4-dicarboxylate))[3], which is overall fairly lighter with respect to the aluminum forming the chemical structure of the aluminized foil[4]. A visual representation of the correct energies, corresponding to the two most intense peaks of ^{32}Ar and employed to calibrate the strips located both on the upper and on the lower silicon detectors, is shown in Fig. 3.3 and in Fig. 3.4, respectively.

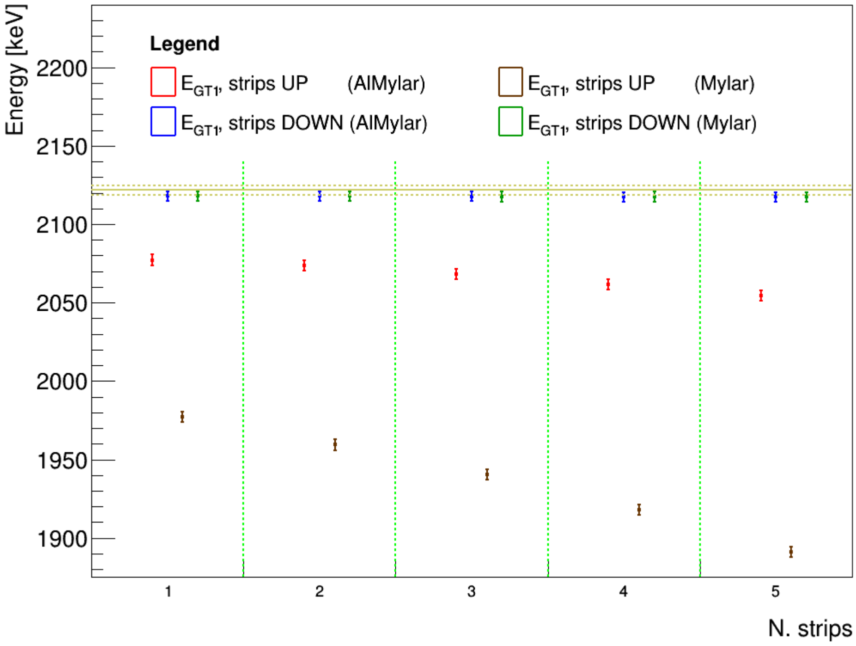

Figure 3.3: Energy values corresponding to the second most intense proton peak (GT) of ^{32}Ar employed for the energy calibration of the silicon detectors, estimated from precise Geant4 simulations of the WISArD detection set-up and automatically including corrections for the energy lost within the catcher foil and the silicon detector dead layer. The values, slightly spatially separated for graphics purpose, are reported for each of the five strips located both in the upper and in the lower hemisphere, in case of employment of the 6 μm Mylar (brown and green) and of the 0.8 μm aluminized Mylar (red and blue) foil. The horizontal olive lines show the value of the theoretical energy peak (continous) and the associated error (dashed), at 2121.7(31) keV [119]. The vertical error bars correspond to the statistical uncertainties. The vertical dashed green lines are for visual purpose.

---

[3] IUPAC nomenclature.

[4] The densities of Mylar and aluminum are equal to 1.38 and 2.70 $\frac{g}{cm^3}$, respectively.

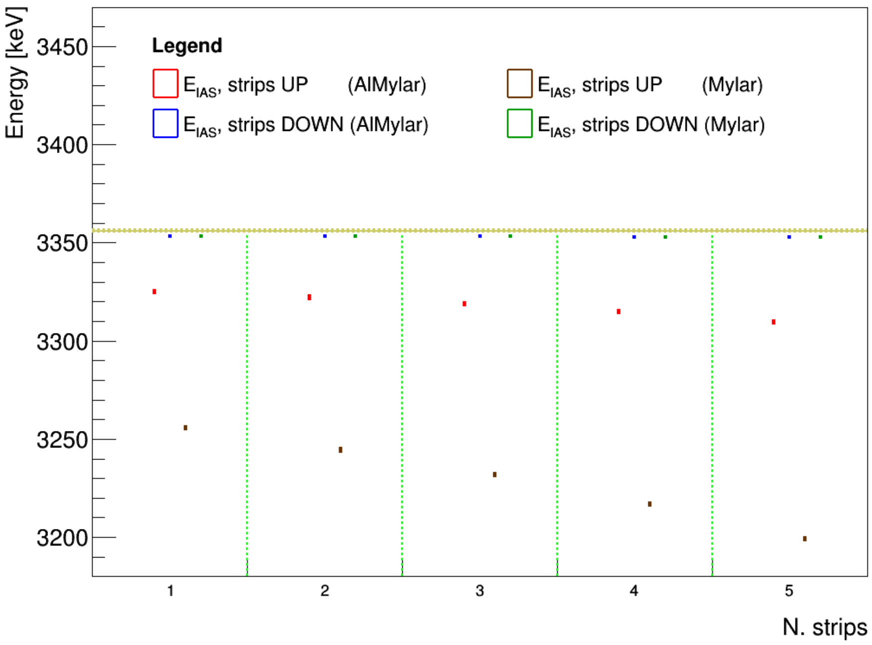

Figure 3.4: Energy values corresponding to the IAS proton peak of ^{32}Ar employed for the energy calibration of the silicon detectors, estimated from precise Geant4 simulations of the WISArD detection set-up and automatically including corrections for the energy lost within the catcher foil and the silicon detector dead layer. The values, slightly spatially separated for graphics purpose, are reported for each of the five strips located both in the upper and in the lower hemisphere, in case of employment of the 6 μm Mylar (brown and green) and of the 0.8 μm aluminized Mylar (red and blue) foil. The horizontal olive lines show the value of the theoretical energy peak (solid) and the associated error (dashed), at 3356.0(7) keV [119]. The vertical error bars correspond to the statistical uncertainties. The vertical dashed green lines are for visual purpose.

The different ^{32}Ar experimental spectra related to the signals acquired by each of the five strips both in the upper and lower hemisphere were then independently calibrated. In particular, different linear fitting curves have been retrieved by correlating the theoretical energy values of the first two most intense peaks of ^{32}Ar to the associated two ADC values, each of them corresponding to the average ADC value of the proton distribution in an energy window centered around the most intense Gamow-Teller and the IAS peak, respectively. Different fitting curves have been recovered for the different catcher foils employed. In Fig. 3.5, the superposition of the single and β-coincident ^{32}Ar energy-calibrated proton spectrum acquired by one silicon detector (all five strips, all runs summed) is shown. A contamination from the 4-α source is apparent in the proton single spectrum, but evidently not present in the corresponding β-proton coincident one. This contamination will not induce particular effects on the following analysis of the proton energy shifts, as the energy peaks due to the 4-α source are in general very well separated from the ^{32}Ar proton lines and, furthermore, located in energy regions far away from the energy peak considered in the further analysis. Nevertheless, in case of the data taken with the Mylar foil, a total of few strips on the upper detectors present a complete overlap between the peaks coming from the ^{148}Gd of the α-source and the IAS peak from ^{32}Ar, so that, as it would not be possible to separate completely the two contributions from each other, few strips will be excluded from the analysis. Further details about this aspect will be given in Sec. 3.2.5.

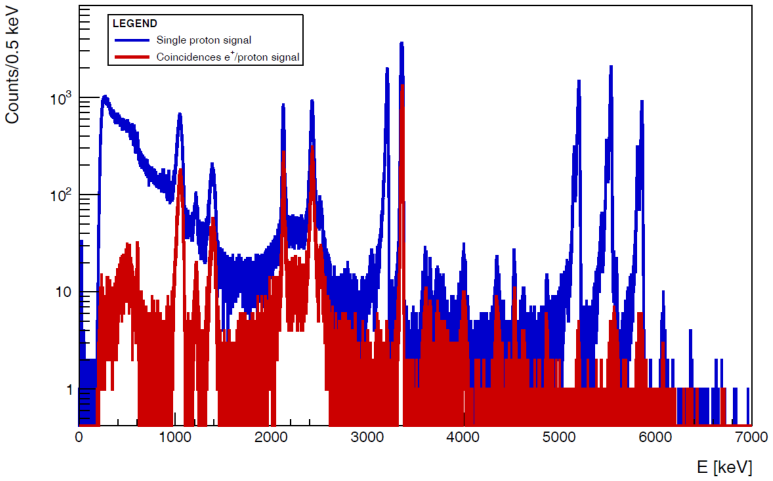

Figure 3.5: ^{32}Ar decay single (blue) and β-coincident (red) proton spectrum, acquired during the 2021 experimental campaign from one silicon detector (Si1D, all five strips and all runs summed). The contamination from the 4-α source (^{148}Gd, ^{239}Pu, ^{241}Am, ^{244}Cu) is clearly evident in the energy peaks at around 3271, 5156, 5486 and 5805 keV, which are present in the single proton spectrum but absent in the corresponding β-coincident one. The overall energy resolution obtained was 19 keV (FWHM).

3.2.2 SiPMs array energy calibration

The eight LG and HG active channels composing the SiPMs array were independently energy-calibrated at the first order by exploiting offline calibration runs acquired with a ^{90}Sr ($t_{1/2}$ = 28.9 years) radioactive source. In particular, the four runs recorded, each of them containing the spectra acquired at the same time by all the HG and LG SiPM channels, have been summed together into a cumulative one. A different energy calibration procedure has been followed relatively to the LG signals, which allow to measure the full β-spectrum up to the endpoint, and for the corresponding HG outputs, which are amplified by a factor of around ten times in terms of signal amplitude and, so, permit to precisely characterize the low-energy part of the spectrum, affected by the effect of the β-detection threshold. The calibration will be refined by comparison with the corresponding Geant4 simulations on ^{32}Ar.

3.2.2.1 Energy calibration of the SiPM low-gain channels

Concerning the energy calibration of the LG channels, a first subtraction of a linear background has been performed independently for each SiPM channel, by estimating its contribution via a linear fit to the region of the spectrum located at higher values with respect to the endpoint of the ^{90}Sr spectrum. After the background subtraction, a first-order approximated calibration curve has been extracted as a linear fit between the channel values corresponding to the endpoint of ^{90}Sr (Q = 546 keV) and the endpoint of its immediately β-decaying daughter, ^{90}Y ($t_{1/2}$ = 64.60 h, Q = 2279.4 keV). Specifically, the position corresponding to the endpoint of ^{90}Sr has been estimated as the second derivative in a limited region right before and after the change of slope clearly visible in the first half of the experimental spectrum; yet, the channel corresponding to the endpoint of ^{90}Y has been extracted as the intercept point between the horizontal line corresponding to the remaining background and a rectified Gaussian distribution, used to fit the high-energy part of the spectrum. An example of fit on the experimental spectrum of a LG channel is shown in Fig. 3.6.

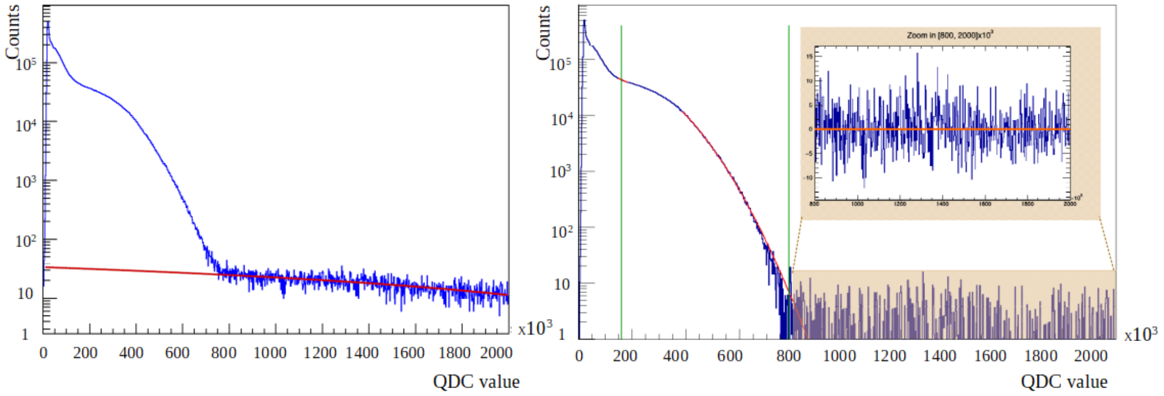

Figure 3.6: Left: ^{90}Sr cumulative decay spectrum registered by the SiPM LG3 channel (blue) and the linear fit to its background (red line). Right: ^{90}Sr spectrum after the background subtraction, with zoom in the high-energy part of the spectrum ([800000, 2000000] QDC value). The red curves indicate the region in which the second derivative relative to the endpoint of ^{90}Sr (546 keV) has been computed and the rectified Gaussian fit to the endpoint of ^{90}Y (2279.4 keV), respectively. The intersections between the vertical green lines and the red curves show the estimated positions of the two endpoints.

3.2.2.2 Energy calibration of the SiPM high-gain channels

The energy calibration relatively to each HG output has been performed on the base of the newly determined linear calibration fitting functions for the LG channels, by verifying that the output signals related to each HG channel were effectively corresponding to a factor of around ten in terms of amplification of the corresponding LG ones.

In this sense, the two-dimensional scatter plots showing the correspondence between the output signals registered by the specular HG and LG channels were first reconstructed. Subsequently, the respective profile histograms were derived from the scatter plots, each of them displaying the mean value of the scatter plot on the y-axis (HG QDC value) and its error (RMS) as a function of the channel bins represented on the x-axis (LG QDC value). For all the SiPM channels active during data taking, the corresponding profile spectrum appears to be divided into three different parts: first, a non-linear region at the very beginning ($0 \leq \mathrm{x} \lesssim 30000$ LG QDC channel), directly related to output signal distortions occurring at very low energy; secondly, an extended linear amplification regime ($30000 \leq \mathrm{x} \lesssim 300000$ LG QDC channel); finally, a new non-linear regime leading to a knee point and to the following saturation curve ($\mathrm{x} \gtrsim 300000$ LG QDC channel). In particular, a linear fitting function has been applied in the linear region for all the SiPM channels in order to quantify the linearity of the HG response as a function of the corresponding LG output.

In Fig. 3.7, an example of a two-dimensional scatter plot showing the correlation between HG and LG outputs for the same channel is reported, as well as the linear fitting function performed on the corresponding profile histogram.

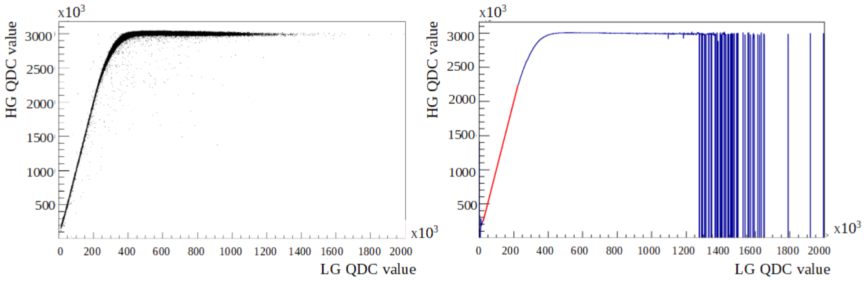

Figure 3.7: Left: two-dimensional scatter plot showing the correlation between HG and LG outputs for the same channel (SiPM HG3 and LG3, respectively). Right: profile histogram (blue) obtained from the scatter plot shown on the left, displaying the mean value of its y-axis (HG QDC value) and its error (RMS) for each bin on the x-axis (LG QDC value). The red line indicates the linear fitting function extrapolated in a region surely linear in terms of HG amplification of the output coming from the LG channel; effectively, the non-linear amplification regime at very low energy and the saturation region after the knee point have been excluded from the fitting and will not be taken into account in the construction of the energy-calibrated HG spectra.

The angular coefficients extrapolated from the linear fitting functions, directly indicating the amplification factor of the HG outputs with respect to the corresponding LG ones, are reported in Table 3.3. The intercept coefficients are in all cases compatible with zero within their respected error bars, as expected from the setting of the baseline restoration in the FASTER acquisition system at the beginning of the experimental campaign. The values have been computed for seven corresponding HG and LG channels only since, as mentioned in Sec. 3.1.1, SiPM HG4 was not operative and LG9 was not connected during data taking.
As displayed in Table 3.3, the HG amplification factor is in all cases around a factor of ten with respect to the corresponding LG output. Consequently, it is therefore possible to calibrate in energy also the SiPM HG spectra for the low energy part, corresponding to a linear response regime. Effectively, the HG channel energy calibration functions correspond to the respective LG ones, each of them multiplied by the correlated amplification factor.

SiPM channels	a_{coeff} **linear fitting function [a.u.]**
HG1 vs LG1	9.926 ± 0.001
HG2 vs LG2	9.966 ± 0.001
HG3 vs LG3	9.896 ± 0.001
HG4 vs LG4	-
HG5 vs LG5	9.989 ± 0.001
HG6 vs LG6	10.295 ± 0.001
HG7 vs LG7	10.042 ± 0.001
HG8 vs LG8	10.052 ± 0.001
HG9 vs LG9	-

Table 3.3: Summary of the correspondence between the SiPM HG and LG channels and the associated angular coefficients extrapolated from the linear fitting functions to the two-dimensional scatter plots showing the HG outputs as a function of the corresponding LG one. The angular coefficient values indicate directly the amplification factor of the HG response with respect to the corresponding LG output. No information is provided for channel 4 and 9, as SiPM HG4 was not operative and LG9 was not connected during data taking.

The calibrated LG and HG spectra, collected in coincidence with the ^{32}Ar IAS protons, are shown in Fig. 3.8. Both spectra will be later on compared to the corresponding ones obtained via Geant4 simulations. In particular, the LG spectrum will allow to adjust and evaluate the numerical reproduction of the overall experimental spectrum up to the endpoint ($Q_{\beta-IAS}$ = 5046.1(3) keV [119]), while the HG one, characterized by a finer zoom in the low-energy region, will be employed to figure out the value of the β-detection threshold, which represents one of the main systematic contributions to the final uncertainty on the measurement.

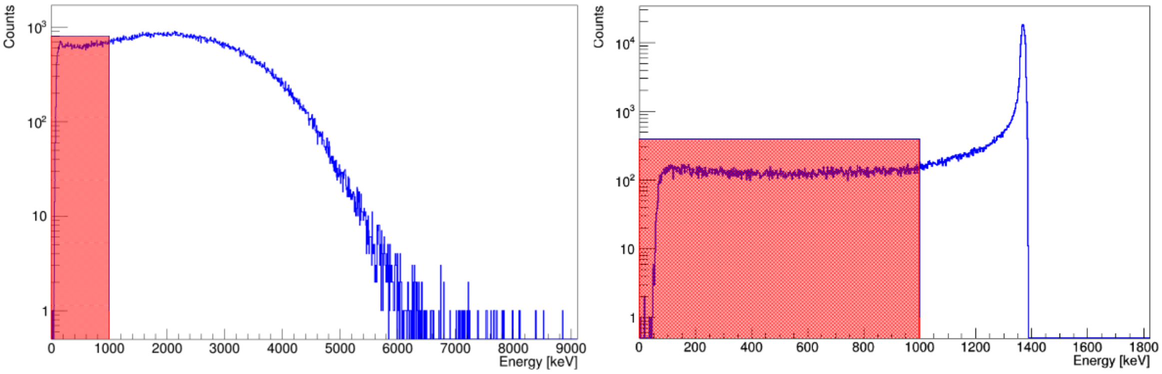

Figure 3.8: ^{32}Ar LG (left) and HG (right) energy-calibrated β-spectrum acquired by LG3 in coincidence with IAS protons, with the online condition of trigger set at a multiplicity of at least three LG and HG cells fired at the same time, respectively. The red box, extending from 0 to 1000 keV, indicates in both cases the low-energy region to which the HG spectrum is particularly sensitive; in the HG spectrum, this region corresponds to a perfectly linear amplification of the LG channel outputs and it will be later on compared to simulations in order to figure out the value of the β-detection threshold.

3.2.3 Systematic study of the β-proton spectra as a function of the SiPMs trigger multiplicity

As mentioned in Sec. 3.1.2, both single β and β-proton coincident data acquired by the SiPMs array have been independently recorded. In particular, in both cases the online trigger condition set to register the incoming signals as common data groups was set to a minimum of three SiPM cells out of nine potentially firing at the same time. The decision of acquiring data in groups in case of multiplicity at least three was taken in order to reduce as much as possible the contribution to β-spectra coming not from the energy released inside the scintillator by the incoming β-particles, but rather due to the dark events typically triggering one cell or very less likely a couple of cells at once. However, this means that eventually some physics data indeed related to a low energy deposit from a β-particle inside the detector, but triggering only one or two SiPM cells, could have been also indirectly considered as a contribution from the noise and consequently lost in the online reconstruction of both the β-single and the β-proton coincident spectra. Moreover, the percentage of physics events lost in such a way would be rather hard to estimate theoretically and would contribute at an unknown level to a final trigger-related systematic uncertainty.

3.2.3.1 Offline sorting algorithm on different SiPMs trigger multiplicity

In order to fix such an issue, an offline sorting algorithm aiming to reconstruct both the single and the β-proton coincident spectra for both LG and HG channels as a function of all the possible SiPM trigger multiplicities has been developed.

Effectively, all the data related to each HG and LG SiPM cell and to all the silicon detector strips and backs providing an output signal over the threshold, previously set in the FASTER DAQ, were also concomitantly saved in lossless mode, regardless of their belonging to a specific data group. In this way, the pure list of each data recorded either by a SiPM cell or by a silicon detector strip or back-side, chronologically ordered by acquisition time, has been considered as a starting point. Specifically, each line in the raw data list was composed by three elements: detector numerical label (LG channels from 1 to 9, HG ones from 10 to 18 and silicon detector outputs from 19 to 66), the associated QDC channel linearly proportional to the energy deposit registered by the detector and the timestamp related to the particle arrival time on the detector (in *ns*). For completeness, all timestamps have been recorded for all runs progressively in chronological order with respect to a common time reference, corresponding to the initial reset and initialization of the FASTER module parameters. Moreover, each event detected by the FASTER-QDC-TDC modules associated to the CARAS boards, employed for SiPMs signal processing, is timestamped with a 2 ns accuracy; on the contrary, each event registered by the FASTER-ADC modules associated to the MOSAHR boards, used for proton signal treatment, are timestamped with a 8 ns precision[5].

Though, considering the complete data list for all runs, data groups were reformed by requiring all the possible SiPM LG and HG cumulative multiplicity conditions, *i.e.* all the possible minimum values of LG and HG cells fired within the same very restricted time window. In particular, a certain number of data lines were considered as forming a common LG-triggering data group in case other LG SiPM cells triggering had timestamps coming in a delay of [0, 150] ns with respect to the timestamp of the first LG SiPM cell chronologically triggering in the group. Eventual proton signals coming in coincidence with the SiPM outputs, typically quicker to be processed due to the faster response time of the silicon detectors, were considered as a part of the group when registered in a window of [-200, 150] ns with respect to the first triggering cell. So, for each group the associated LG multiplicity corresponds to the amount of LG SiPM cells (labeled from 1 to 9) triggering within the group time interval. A specular analysis has been performed in case of the HG channels.

---

[5] The QDC-TDC Measurement-numerical-Modules (MnMs) are signal processing modules planned to receive data at a frequency of 500 MHz, while the digitizing algorithm treats them under a 125 MHz clock; the employment of an additional module containing a SerDes circuit before MnM allows then to treat a four data sample group every 8 ns, so a single data sample every 2 ns. The ADC MnMs, used for silicon signal processing, due to their fourth-order CR-RC filter, convert each single data every 8 ns [137].

Finally, for both LG and HG data groups, the histograms related to a β-proton coincident event have been filled only if the proton signal was registered by both a strip and the back-side of the silicon detector and, concomitantly, in case the absolute difference between the energy-calibrated strip and back-side signals was lower than three times the root sum square of their resolution ($|E_{strip} - E_{back}| < 3 * \sqrt{\sigma^2_{strip} + \sigma^2_{back}}$). Basically, the cases of a single strip or a single back-side signal, as well as multiple strip signals (with or without the corresponding back-side output) possibly corresponding to noise or to a proton signal shared between adjacent strips were not considered in the reconstruction of single and coincident events.

By exploiting this custom-made offline sorting algorithm, the eight LG and HG β-spectra, each of them characterized by a different trigger multiplicity, have therefore been reconstructed. Subsequently, the corresponding spectra related to the data acquired with all the possible minimum multiplicities of cells triggered have been created, by making a progressive cumulative sum on the previously created β-spectra (*e.g.* the spectrum corresponding to at least four cells triggered was reconstructed by summing the spectra acquired with multiplicity exactly equal to four, five, six, seven and eight cells). In this way, spectra similar for construction to the ones registered online by imposing the condition of at least three cells firing at the same time were obtained. Furthermore, it has been crosschecked that the newly created offline cumulative spectrum corresponding to a minimum trigger multiplicity of three cells was exactly overlapping with the one acquired online during data taking.

3.2.3.2 Systematic study of the β-spectra as a function of the SiPMs trigger multiplicity

The cumulative β-spectra reconstructed by means of the offline algorithm previously described have been calibrated in energy via the linear calibration functions obtained from the analysis of the ^{90}Sr spectra, as explained in Sec. 3.2.2. In Fig. 3.9, the superposition of the LG and HG β-spectra acquired in coincidence with the IAS protons as a function of the SiPM trigger multiplicity is shown for qualitative comparison.

Each LG and HG cumulative spectrum presented, corresponding to a minimum trigger multiplicity M_x, is then composed by all the signals acquired with at least x either LG or HG cells firing at the same time, and so reconstructed as a part of a same data group by the offline sorting algorithm. Consequently, the spectra reconstructed at M_3 are identical to the ones acquired by imposing the online trigger condition of at least three cells firing at the same time. In particular, as visible in the zoomed regions in Fig. 3.9, the main differences between the reconstructed histograms are located, as expected, in the low-energy part of the β-spectra.

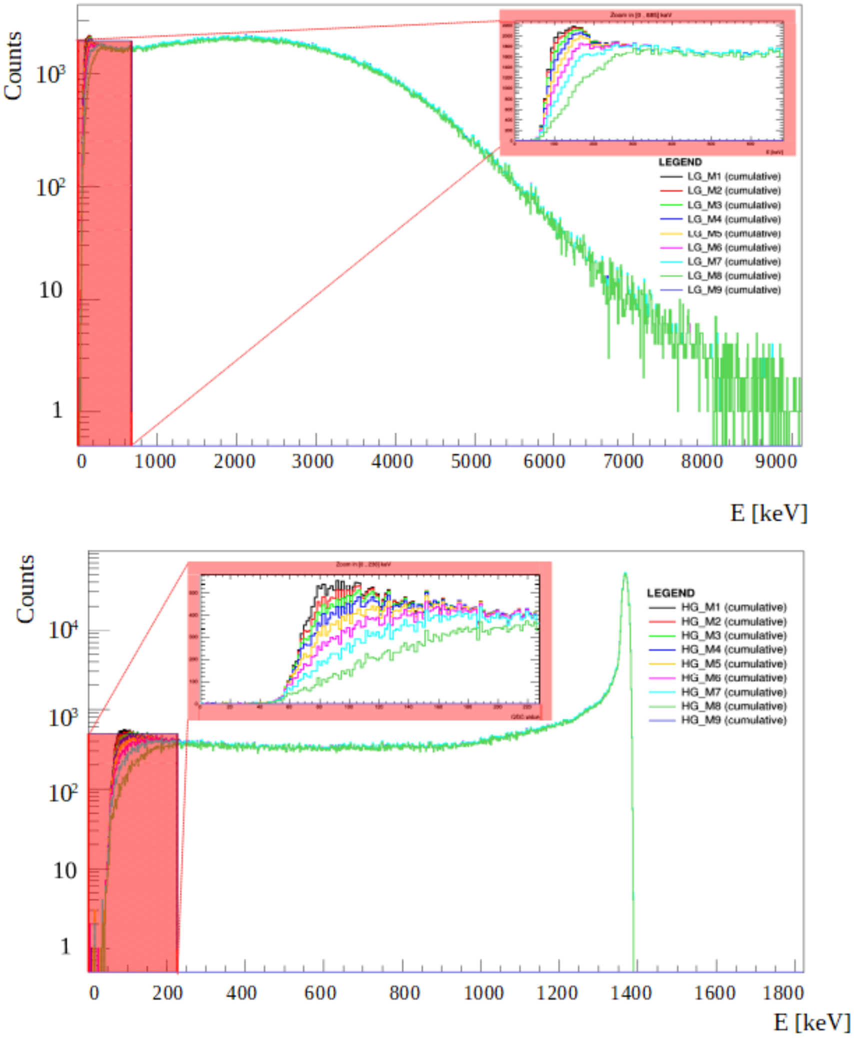

Figure 3.9: Superposition of all the ^{32}Ar cumulative β-spectra (coincident with IAS protons) registered by one SiPM cell reconstructed as a function of all the possible SiPM LG and HG minimum trigger multiplicities. Each spectrum, corresponding to a given LG or HG minimum trigger multiplicity M_x, is built as the cumulative sum of the LG or HG signals registered for trigger multiplicities varying from exactly M_x up to exactly M_9, so it is composed by the signals acquired with at least M_x. On top right, a zoom in the low-energy region ([0, 685] keV for LG and [0,230] keV for HG), in which the differences between the spectra are evident. No signals have been acquired with M_9 multiplicity, as channel HG4 was not operative and LG9 was disconnected during data taking.

As attended, an augmentation in the minimum trigger multiplicity changes the shape of the low-part of the β-spectrum, thus affecting the determination of the β-energy threshold and, consequently, leading to a non-detection of a certain fraction of events.

Therefore, by subtracting one by one the adjacent spectra, it is now possible to quantitatively evaluate the individual contributions coming from the data acquired at exactly x cell firing with respect to the M3 cumulative spectrum originally considered for the further analysis. Subsequently, the amount of data due to signals associated to exactly one or two cells firing at the same time, originally cut by definition in the M3 spectra, can now be evaluated. In Table 3.4, the individual and the total percentages relatively to the amount of data acquired with exactly x cells firing at the same time with respective to the cumulative M3 LG and HG spectra are resumed. Data are related to SiPM signals recorded in coincidence with protons located in the IAS region ([3250, 3450] keV).

LG trigger									
Percentage	**M1**	**M2**	**M3**	**M4**	**M5**	**M6**	**M7**	**M8**	**M9**
Individual [%]	-0.74	-0.61	0.53	0.76	0.67	0.66	4.73	92.65	0.00
Total [%]	-1.35	-0.61	0.53	1.29	1.96	2.62	7.35	100.00	100.00

HG trigger									
Percentage	**M1**	**M2**	**M3**	**M4**	**M5**	**M6**	**M7**	**M8**	**M9**
Individual [%]	-1.14	-0.59	0.50	0.94	0.45	0.83	4.98	92.31	0.00
Total [%]	-1.73	-0.59	0.50	1.44	1.89	2.72	7.69	100.00	100.00

Table 3.4: Summary of the LG and HG percentage contributions to the respective cumulative M3 spectrum (spectrum acquired with at least three cells firing at the same time) by the spectra acquired with exactly M$_x$ multiplicity (x in [1, 9]), in coincidence with a IAS proton. The first row indicates the percentage of data not considered in the cumulative M3 spectrum due to exactly one or two triggering cells (negative values) and the single percentage contribution to the M3 cumulative spectrum due to exactly x cells firing at the same time (positive values). The second row indicates, before the bold vertical line, the sum of the percentages of data not considered by the cumulative M3 spectrum (higher if lowering the trigger multiplicity) and, after the bold line, the sum of the percentages of data composing the cumulative M3 spectrum itself.

The percentage of data acquired with exactly one or two cells firing at the same, and so not originally considered by definition in the cumulative M3 spectrum, is equal to -1.35% and -1.73% for LG and HG trigger, respectively.

For completeness, similar percentages can be computed also for the single β-spectrum, acquired without imposing any condition on coincident signals from the silicon detectors. In this case, the contributions to the spectra related to noise can be more evidently represented. The amount of the data collected in single mode as a function of all the possible cumulative trigger multiplicities is reported in Fig. 3.10.

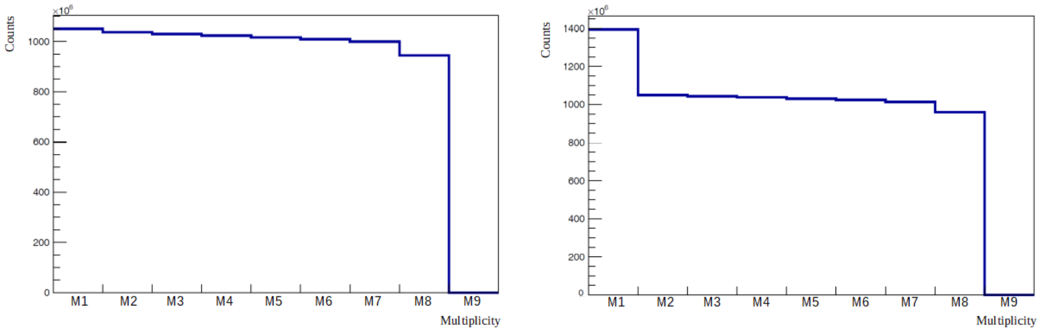

Figure 3.10: Amount of the data collected in single mode as a function of all the possible LG (left) and HG (right) cumulative trigger multiplicities.

Effectively, it can be seen that the amount of data acquired in case of LG trigger reduces always almost constantly while increasing the minimum cumulative trigger multiplicity. However, in case of the HG channels, the passage from a trigger multiplicity equal to a minimum of one to a minimum of two cells, leads to a net reduction in the number of β-signals acquired, whereas the following progressive reduction in trigger multiplicity is associated again to a steady reduction of data recorded. Thus, in the following analysis on the proton energy shifts, the experimental data acquired with at least two cells firing at the same time will be exploited. The percentages related to the contribution of exactly all M$_x$ multiplicities, calculated with respect to the M3 cumulative spectrum, are resumed in Table 3.5.

LG trigger									
Percentage	**M1**	**M2**	**M3**	**M4**	**M5**	**M6**	**M7**	**M8**	**M9**
Individual [%]	-1.34	-0.66	0.62	0.72	0.71	0.91	5.30	91.74	0.00
Total [%]	-2.00	-0.66	0.62	1.34	2.05	2.96	8.26	100.00	100.00

HG trigger									
Percentage	**M1**	**M2**	**M3**	**M4**	**M5**	**M6**	**M7**	**M8**	**M9**
Individual [%]	-33.07	-0.62	0.54	0.70	0.62	0.96	5.18	92.00	0.00
Total [%]	-33.69	-0.62	0.54	1.24	1.86	2.82	8.00	100.00	100.00

Table 3.5: Summary of the LG and HG percentage contributions to the respective cumulative global M3 spectrum (spectrum acquired with at least three cells firing at the same time) by the spectra acquired with exactly M$_x$ multiplicity (x in [1, 9]). The first row indicates the percentage of data not considered in the cumulative M3 spectrum due to exactly one or two triggering cells (negative values) and the single percentage contribution to the M3 cumulative spectrum due to exactly x cells firing at the same time (positive values). The second row indicates, before the bold vertical line, the sum of the percentages of data not considered by the cumulative M3 spectrum (higher if lowering the trigger multiplicity) and, after the bold line, the sum of the percentages of data composing the cumulative M3 spectrum itself.

As shown in Fig. 3.10 and quantified in Table 3.5, the overall contribution due to data recorded with one only SiPM cells is more than 30% higher with respect to the amount of data composing the M3 cumulative spectrum, whereas the contribution due to two cells triggering at the same to the full spectrum reduces drastically by two order of magnitudes, playing a part on the permil level only. It is also evident the majority of data have been collected with multiplicity equal to eight cells.

Finally, by comparing also with the values obtained in Table 3.4, it can be concluded that the data acquired for both β-proton coincident and β-single events were almost always recorded with the totality of the active LG and HG SiPM cells firing at the same time. Moreover, the trigger multiplicity condition imposed online to reconstruct the β-coincident events can be offline lowered to two cells firing within the same 200 ns window; effectively, in this case the huge amount of signals recorded with multiplicity one and primarily due to noise are still discarded, but, at the same time, a little amount of exploitable data can be gained back and additionally considered for the following analysis.

A further study, comprehensive of the comparison between all the spectra reconstructed as a function of the different trigger multiplicities and the simulated β-spectrum acquired by the plastic scintillator, will be given in Chapter 5.

3.2.4 Further cuts on silicon detector signals

As explained in the previous section, β-proton coincident events have been considered only in case of SiPM signals coming in coincidence with energy compatible signals from a single strip and the back-side output of the same silicon detector within the same data group. Basically, cases with a single strip or a single back-side signal, as well as multiple strip signals (with or without their back-side output) were directly excluded, as they cannot be associated with certainty to a signal from a single proton impinging and releasing energy inside one strip, and consequently in the back-side, only.

In particular, the signals coming from only one silicon strip or from only its back-side can be related either to noise in their electrical component or to a non functioning of the corresponding either back-side or strips during data taking, respectively. On the other hand, the signals coming from multiple strips hit at the same time (with or without the corresponding back-side output) correspond either to an effective proton signal shared between adjacent strips or to a coincident collection of a proton from one strip and signal due to noise in the adjacent one.

In order to quantitatively evaluate the different nature of the collected data, the origin of each silicon detector output in a data group has been studied as a function of different energy thresholds applied on the silicon calibrated signal (0, 500, 650 and 800 keV). The results, presented in forms of multiple histograms, are shown in Fig. 3.11.

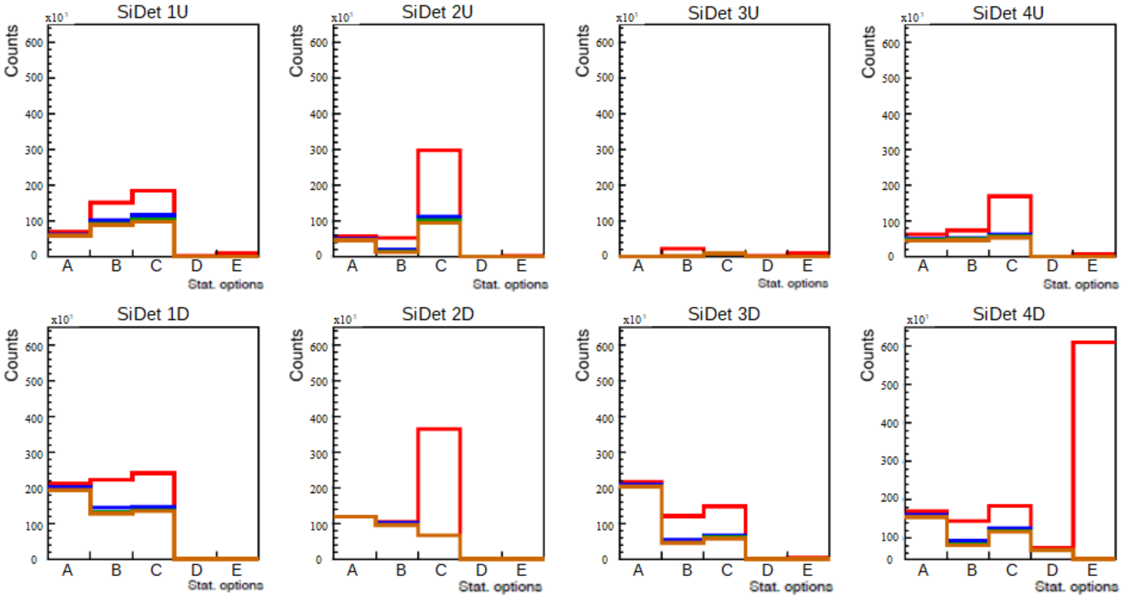

Figure 3.11: Histograms related to the origin of the signals acquired by the four upper (first row) and four lower (second row) silicon detectors. In all cases, the amount of data recorded are presented as a function of five different categories, alphabetically labeled on the x-axis: signals within a data group coming from only one strip and the back-side (A), from only one strip (B), from only the back-side (C), from multiple strips and the associated back-side output (D) and from multiple strips without the related back-side output (E). Results are presented as a function of different silicon energy cut thresholds (0 keV in red, 500 keV in blue, 650 keV in green and 800 keV in orange). For all detectors, only the signals registered by only one strip and its associated back-side and higher than a threshold finally set at 500 keV in order to cut on signals due to detector noise (option 'A', blue curve) will be considered for the construction of the associated β-proton coincident spectra and exploited in the following analysis.

As shown in Fig. 3.11, most of the signals composing the data groups have been acquired in case of only one strip or only the back-side of the silicon detectors hit and, in case of a single detector (SiDet 4D), in case of multiple strips not associated to the corresponding back-side output. However, as it can be seen from the different colored histograms, the majority of these cases are strongly reduced if imposing the condition of even the lowest energy threshold on the silicon signals (equal to 500 keV), which is fairly below the first low-energy proton peak lines of ^{32}Ar [119]; consequently, it is reasonable to conclude that these data are most likely due to noise triggering either one strip or the back-side only and, also, to the fact that few strips or back-sides were not working during data takin. Yet, it can be also seen that the amount of data that will be exploited in the following analysis, corresponding to the data registered by both a single strip and the rear-side of a silicon detector (option ’A’ in the figure), corresponds to the only category which does not sensibly reduce as a function of the thresholds applied. It can be though concluded that the associated signals truly correspond to energy deposits coming from a real proton inside the silicon detectors and can be therefore considered for the further analysis on the computation of the kinematic energy shifts.

Furthermore, the effect on the full ^{32}Ar β-spectrum recorded by the SiPMs array in case of β-proton coincident events has also been studied as a function of the energy threshold cuts applied on the signals registered within the same time window by a single strip and the back-side of the eight silicon detectors. The superposition of the LG and HG β-spectra reconstructed for a minimum trigger multiplicity of three cells (M3) as a function of the different silicon signal thresholds, set at 0, 500, 650 and 800 keV, is shown in Figs. 3.12 and 3.13 respectively.

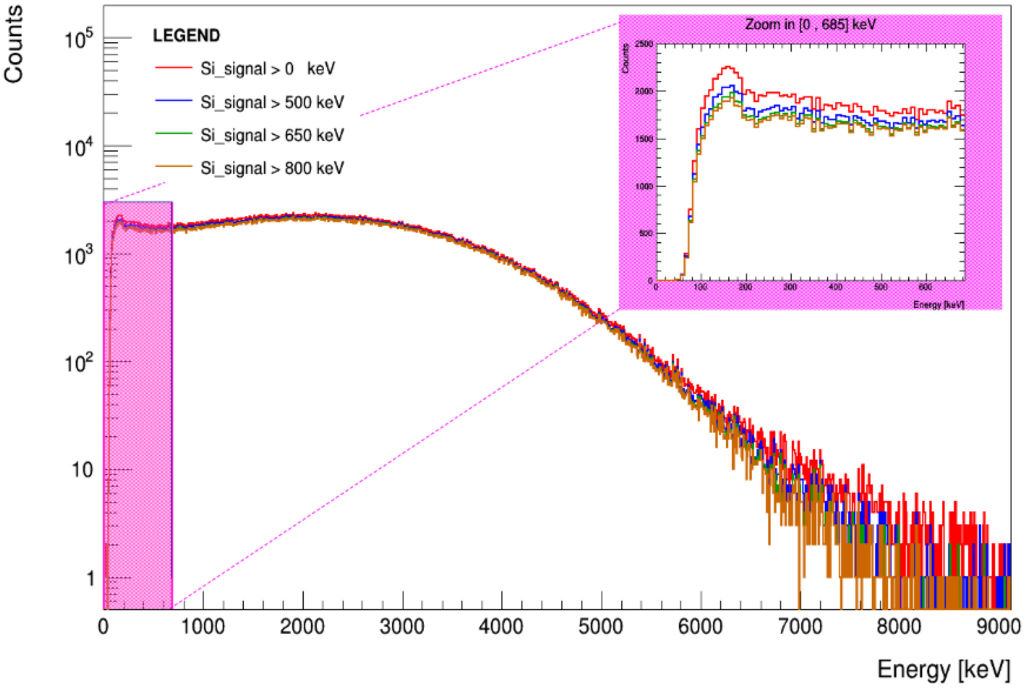

Figure 3.12: Superposition of the ^{32}Ar LG β-spectra reconstructed for β-proton coincident events for a minimum trigger multiplicity of three cells (M3) as a function of the different energy cuts applied on the associated signals registered by the silicon detectors (0 keV in red, 500 keV in blue, 650 keV in green and 800 keV in orange). On top right, a linear zoom in the low-energy region ([0, 685 keV]), in which the differences between the spectra are more evident.

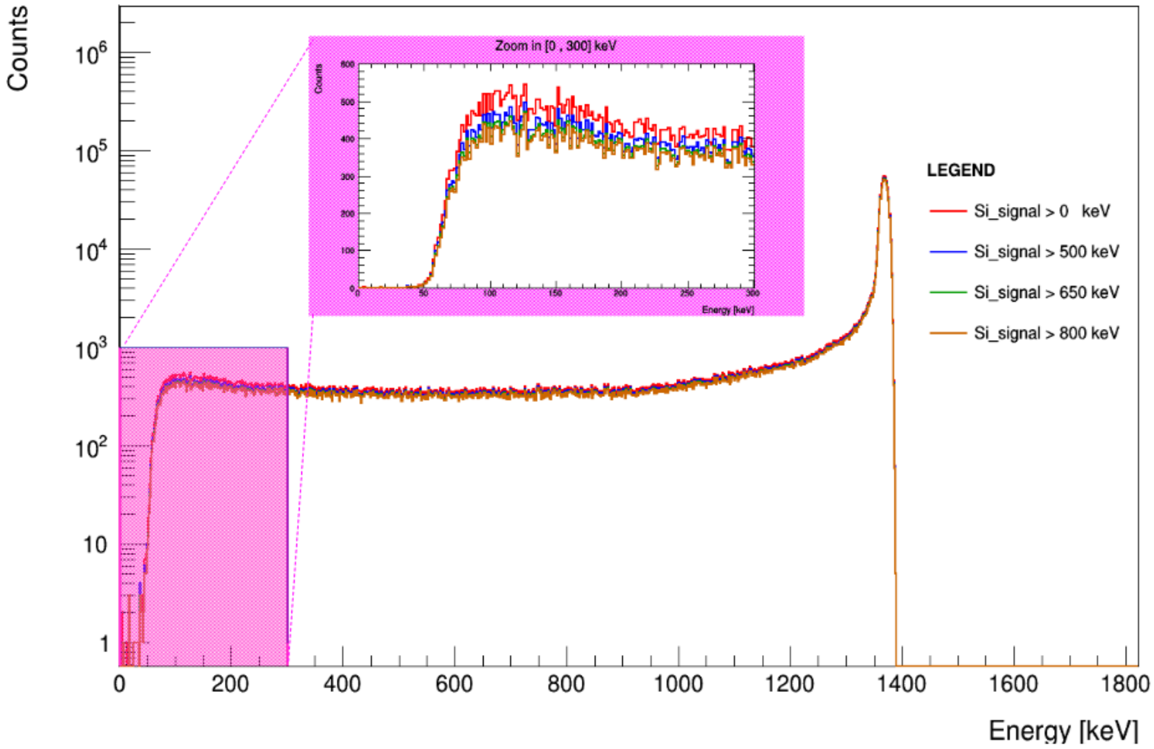

Figure 3.13: Superposition of the ^{32}Ar HG β-spectra reconstructed for β-proton coincident events for a minimum trigger multiplicity of three cells (M3) as a function of the different energy cuts applied on the associated signals registered by the silicon detectors (0 keV in red, 500 keV in blue, 650 keV in green and 800 keV in orange). On top right, a linear zoom in the low-energy region ([0, 300 keV]), in which the differences between the spectra are more evident.

In both cases, the major differences between the spectra appear in the low-energy region. In particular, in Fig. 3.12, a further difference is visible in the high-energy part of the spectra; effectively, the lower the energy thresholds applied on the silicon detector signals, the higher is the endpoint of the ^{32}Ar β-spectrum. This is particularly visible if comparing the β-spectrum acquired in coincidence with a silicon signal at thresholds equal to 0 and 500 keV, respectively. This observation, not intrinsically beneficial for the further analysis, may eventually suggest the existence of ^{32}Ar proton peak lines at an energy lower than the lowest one already observed (E = 627.3(1) keV [119]) not measured in previous experiments due to the background contribution dominating the low-energy part of the collected spectra.

3.2.5 Experimental energy shifts

Both the single and the β-coincident proton spectra have been then calibrated in energy and the related data were selected accordingly to the selections applied on the signals recorded by the silicon detector, as described in Secs. 3.2.1 and 3.2.4. The spectra collected in each run, with a SiPMs trigger condition set at least two cells firing at the same time and with no further offline threshold applied, were them summed up into a cumulative file.

The experimental energy shifts of the IAS peaks, related to the single and the β-coincident proton spectra in the final cumulative run, have then been calculated for each of the five strips composing the silicon detectors, differently for the strips located in the upper and in the lower hemisphere. In particular, the kinematic shifts have been computed for each strip as the absolute difference between the statistic means of the single and the β-coincident proton distribution in the energy region containing the IAS peak, in case of associated signal coming from the β-detector higher than the β-detection threshold (at 100 keV, for further detail see Sec. 5.1). An illustrative example of the IAS energy distributions obtained for the five strips located on an upper silicon detector (SiDet3) and on a lower silicon detector (SiDet7) is shown in Fig. 3.14.

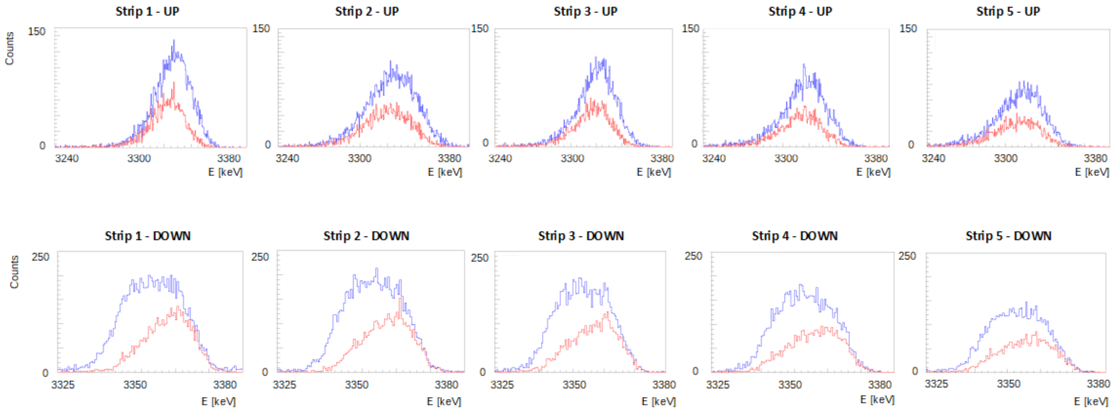

Figure 3.14: Illustrative example showing the superposition of the IAS proton single (blue) and the corresponding β-coincident (red) energy distributions for each of the five strips located on an upper (SiDet3) or lower (SiDet7) silicon detector (aluminized Mylar foil). The associated proton energy shifts are calculated as the absolute difference between the means of the proton energy distributions in the range [3240, 3380] and [3325, 3380] keV, for the upper and the lower detectors respectively. As expected by kinematics, the shifts are directed towards lower energies for the upper detectors and towards higher energies for the lower ones. The statistics in the lower detectors is higher, due to issues occurred to the upper detectors during data taking (for further details see Sec. 3.1.1).

By comparing the single (blue) and β-coincident (red) IAS proton distributions, it is apparent that, as expected, the mean upper energy shifts, corresponding to protons emitted in the same direction of the β-particles, are directed towards lower energies, whereas the mean lower energy shifts, associated to protons emitted in the opposite directions with respect to the positrons, are directed towards higher energies. The amount of data collected by the lower strips is also higher, thus resulting in statistics errors lower with respect to the ones associated to the upper detectors, due to issues occurred to the upper detectors themselves during data taking (for further details see Sec. 3.1.1).

Moreover, a more pronounced tail on the left part of both single and proton-coincidence distributions seems to appear in the spectra recorded by the upper detectors. This behaviour is likely due to the fact that the incoming $^{32}\mathrm{Ar}^{+}$ nuclei, with an energy of 30 keV, are implanted at the very first thickness of the catcher foil, roughly at (47 ± 14) nm (Mylar) and (21 ± 8) nm (aluminized Mylar), according to SRIM [130]); consequently, the lower detectors record signals from proton traversing only a limited distance inside the catcher, while the upper ones register data associated to protons that traverse a much higher thickness in the Mylar foil. The spectra acquired by the upper detectors suffer than more of the energy straggling of protons inside the catcher, thus resulting in a longer left-hand tail in the peak distributions.

The associated mean proton energy shifts, in case of data recorded by employing the 0.8 μm aluminized Mylar and the 6 μm Mylar catcher foil, are summarized in Table 3.6 and in Table 3.7, respectively. In the tables, the corresponding weighted average, together with their statistical uncertainties [6] and related to each strip in both the hemispheres, is also reported.

	Mean IAS proton energy shift [keV] vs strip n° (AlMylar)				
Silicon detector n°	**1**	**2**	**3**	**4**	**5**
SiDet 1	-	-	-	2.821 ± 0.206	2.541 ± 0.230
SiDet 2	3.976 ± 0.180	-	-	2.718 ± 0.230	-
SiDet 3	4.023 ± 0.175	3.691 ± 0.166	3.208 ± 0.196	3.032 ± 0.221	2.576 ± 0.250
SiDet 4	4.128 ± 0.186	3.575 ± 0.206	3.248 ± 0.250	-	2.556 ± 0.262
Mean (upper SiDet)	4.040 ± 0.104	3.645 ± 0.129	3.223 ± 0.154	2.859 ± 0.126	2.557 ± 0.142
SiDet 5	3.772 ± 0.099	3.652 ± 0.085	3.240 ± 0.089	2.913 ± 0.092	-
SiDet 6	-	-	-	-	-
SiDet 7	4.086 ± 0.088	3.478 ± 0.089	3.178 ± 0.092	2.869 ± 0.097	2.592 ± 0.111
SiDet 8	-	-	-	-	-
Mean (lower SiDet)	3.947 ± 0.066	3.569 ± 0.061	3.210 ± 0.064	2.892 ± 0.067	2.592 ± 0.111

Table 3.6: Summary of the experimental mean energy shifts associated to the IAS proton distributions, computed for each strip of all silicon detectors and related to the runs acquired by employing a 0.8 μm aluminized Mylar foil. Strips are numerically labeled in ascending order according to their spatial disposition, as shown in the CAD drawing and in the final assembly picture in Fig. 2.5. Results are not reported either in case of no data recorded by the strip or in case of a too large energy distribution associated to the IAS peak (σ > 30 keV).

---

[6] If the statistical error bars related to the ensemble of the silicon detectors on which the weighted average is computed do not overlap within 1 σ, the statistical error bars are stretched by a factor $F = \sqrt{\chi^2/NDF}$.

	Mean IAS proton energy shift [keV] vs strip n° (Mylar)				
Silicon detector n°	**1**	**2**	**3**	**4**	**5**
SiDet 1	-	-	-	-	-
SiDet 2	4.061 ± 0.127	3.565 ± 0.120	-	-	-
SiDet 3	4.098 ± 0.139	3.597 ± 0.147	3.026 ± 0.162	2.978 ± 0.186	2.638 ± 0.214
SiDet 4	4.055 ± 0.135	3.795 ± 0.138	3.471 ± 0.150	-	2.678 ± 0.195
Mean (upper SiDet)	4.070 ± 0.077	3.646 ± 0.077	3.266 ± 0.110	2.978 ± 0.186	2.660 ± 0.144
SiDet 5	-	3.577 ± 0.075	3.262 ± 0.076	2.891 ± 0.081	2.651 ± 0.076
SiDet 6	-	-	-	-	-
SiDet 7	3.973 ± 0.078	3.549 ± 0.078	3.204 ± 0.081	2.913 ± 0.083	2.687 ± 0.090
SiDet 8	-	-	-	-	-
Mean (lower SiDet)	3.973 ± 0.078	3.564 ± 0.054	3.235 ± 0.055	2.902 ± 0.058	2.666 ± 0.058

Table 3.7: Summary of the experimental mean energy shifts associated to the IAS proton distributions, computed for each strip of all silicon detectors and related to the runs acquired by employing a 6 μm Mylar foil. Strips are numerically labeled in ascending order according to their spatial disposition, as shown in the CAD drawing and in the final assembly picture in Fig. 2.5. Results are not reported either in case of no data recorded by the strip or in case of a too large energy distribution associated to the IAS peak (σ > 30 keV), or even in case of overlap between the proton IAS peak and the α-peak from ^{148}Gd.

The weighted averages related to each strip in both the hemispheres is clearly showing that the value of the IAS proton shift reduces progressively from strip 1 to strip 5, *i.e.* by moving further away from the z-axis. This tendency can be noticed for both the upper and the lower strips, and remains the same while moving from the aluminized Mylar to the Mylar catcher. A graphics visualization of the weighted average values obtained for each strip is displayed in Fig. 3.15. These values will be directly compared to the associated ones obtained via Geant4 simulations, reproducing precisely both the experimental set-up and the ^{32}Ar radioactive decay.

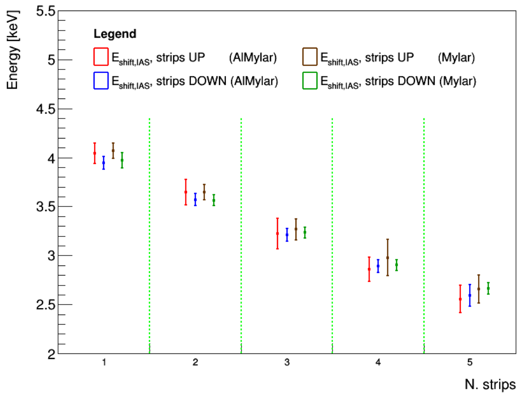

Figure 3.15: Graphics visualization of the experimental mean IAS proton energy shifts as a function of the strips. Results are illustrated for both the hemispheres and both the catcher foils employed during data taking (red and blue for the aluminized one, brown and green for the Mylar one). The vertical error bars correspond to the statistics uncertainties. The vertical dashed green lines are for graphics purpose.

It can be noticed that the highest absolute value of the mean energy shift appears, for both the upper and the lower silicon detectors, in case of proton detection by the strip 1, which is the nearest to the z-axis; a progressively lower value is then observed for the following strips, up to a minimum shift for strip 5. This expected effect is indeed related to the spacial positioning of the strips; effectively, due to kinematics, the average angle between the positron (always detected upwards) and the proton emitted during the decay becomes progressively higher by moving from strip 1 to strip 5, so that the mean energy shift consequently reaches a maximum for the strip nearest to the z-axis (strip 1) and, then, progressively reduces up to a minimum value, obtained for the farther strip with respect to the z-axis (strip 5). At the same time, a progressive reduction in the statistics collected by the strips with higher numerical labels is also visible, mainly due to the spatial confinement of the proton trajectories due to the strong magnetic field.

For completeness, the IAS shifts obtained for each detector and related to each of the five strips are shown in Fig 3.16. As it can be observed, the shifts obtained for the different detectors are in all cases statistically compatible within 1 σ.

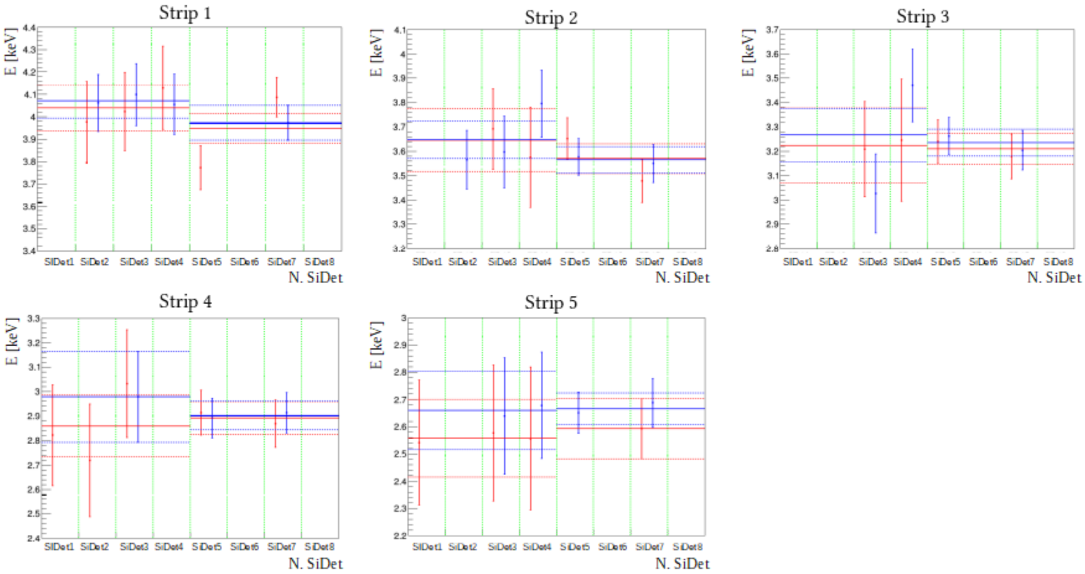

Strip 1

Strip 2

Strip 3

Strip 4

Strip 5

Figure 3.16: Graphics visualization of the experimental IAS proton energy shifts recorded by each silicon detector for strip 1 (top left), strip 2 (top centre), strip 3 (top right), strip 4 (bottom left) and strip 5 (bottom centre). The values reported, summarized in Tab. 3.6 and in Tab. 3.7, are related to the aluminized (red) and to the Mylar (blue) catcher, respectively. The vertical error bars correspond to the statistics uncertainties. The horizontal red and blue lines indicate the weighted average (solid), along with its statistics uncertainty (dashed) for both the upper (SiDet1 to SiDet4) and the lower (SiDet5 to SiDet8) silicon detectors, for the aluminized and the Mylar foil, respectively. The vertical dashed green lines are for graphics purpose.

Chapter 4

Geant4 simulations

In this chapter, the Geant4 simulations related to the data acquired during the experimental campaign on ^{32}Ar performed at the WISArD experiment in October 2021 will be illustrated. In the following, the custom-made code used for the ^{32}Ar decay event generation will be described, the software implementation of the detection set-up and of the magnetic field will be summarized and the numerical methods used for the creation of spectra specular to the ones obtained experimentally will be expounded. Subsequently, the associated overall β-spectra and the β-proton coincident ones will be shown and the values of the mean energy shifts related to the IAS proton group registered by the silicon detectors will be reported.

4.1 ^{32}Ar decay event generator

The WISArD experiment, as explained in Chapter 2, aims to precisely determine the values of the $\tilde{a}_{\beta\nu}$ coefficient for both Fermi and Gamow-Teller transitions via the measurement of the ^{32}Ar proton energy shifts. Specifically, as detailed in Chapter 3, the mean energy shifts between the singles and the β-coincident proton lines measured experimentally can be proven to be linearly proportional to the corresponding theoretical $\tilde{a}_{\beta\nu}$ coefficients; consequently, the values of $\tilde{a}_{\beta\nu}$ can be extracted *a posteriori* from a comparison between the mean proton shifts measured experimentally and the corresponding ones, obtained after varying the value of $\tilde{a}_{\beta\nu}$ in the decay event generator of precise numerical simulations of the experiment, aiming to reproduce both the detection set-up and the ^{32}Ar β-delayed proton decay.
A fairly reliable and complete simulation of the WISArD experiment, capable of implementing the expression of the β-decay rate (see Eq. 1.39) for the generation of the ^{32}Ar decay events, as well as of rightly reproducing the detection set-up and the particle propagation and interaction with matter, represents then a true milestone to precisely determine the $\tilde{a}_{\beta\nu}$ coefficients. For this purpose, a custom-made event generator (CRADLE++), specifically created for

low-energy particle physics, has been exploited in order to generate the information on the decay events and, subsequently, the decay events have been introduced into the WISArD Geant4 simulations.

4.1.1 CRADLE++

The WISArD experiment strongly relies on the realization of accurate numerical simulations, which need to be firstly comprehensive of a precise ^{32}Ar decay event generator. In particular, the open source CRADLE++ (Customizable RAdioactive Decay for Low Energy Particle Physics) [138] has been implemented as an event generator. It is a C++ package aiming to provide a versatile decay event generator for low-energy particle physics in the framework of the electroweak interaction; practically, by manually changing the values of the four dominant coupling constants (vector, axial-vector, scalar and tensor ones) in its configuration file, the related $a_{\beta\nu}$ and b correlation parameters (for further details see Sec. 1.3.4) are computed, and, subsequently, the kinematics of the β-decay is determined[1]. On the basis of the expression of the β-decay rate, shown in Eq. 1.39, and on theoretical calculations on proton emission, the β-proton event decays are then created and, for each particle emitted, the associated momentum and kinetic energy are computed.

More specifically, the general structure of the CRADLE++ program is organized as follows:

- a *INI configuration file*, read in at the start-up to set initial parameters of interest to the decay event simulation. In particular, different options regarding the decay conditions can be specified, *i.e.* the values of the dominant weak interaction coupling constants (C_V, C_A, C_S, C_T), the maximal distance travelled for unstable particle, the maximum state lifetime in correspondence of which stopping the computation of the decay chain, the β-decay mode (either Fermi or Gamow-Teller), the complexity of calculation of the Fermi function (just the approximated Schrödinger solution or the traditional Fermi function) and the Cartesian coordinates of the nuclear polarization of the initial state;

- *Decay Manager*, the main class performing the calculation on the desired amount of event decays to be generated, which can be passed as an additional parameter on the same line launching the program executable file. It keeps the particle stack and factory, and it generates events by calling, in a sequential cascade, the following nested classes (*Particle*, *DecayChannel*, *DecayMode*);

---

[1] As shown in Eq. 1.39, the general expression of the β-decay rate, and so the kinematics of the β-decay, is dependent on both the $a_{\beta\nu}$ and b correlation parameters, which are jointly linked to the $\tilde{a}_{\beta\nu}$ coefficient via Eq. 1.44.

- *Particle*, a class generating objects characterized by information on structure (name, mass, charge, electric charge, number of neutrons, spin) and kinematics (four-momentum array), as well as by an array of eventual decay modes (*DecayChannels*). Each class object corresponds then to a particle created during the physics decay process;

- *DecayChannel*, a class aiming to more precisely describe each decay branch. It sets, depending on the decay channel, the intensity, the parent and daughter excitation energy or the Q-value. The full description of the decay event is completed via a call to its inheriting class (*DecayMode*);

- *DecayMode*, a class aiming to complete the description of the kinematics and dynamics of the specific particle decaying into a particular decay channel. It contains master classes, aiming to analytically describe the decay event and implement the options set into the configuration file (*BetaMinus*, *BetaPlus*, *ConversionElectron*, *Proton*, *Alpha*, *Gamma*), and slave classes (*TwoBodyDecay*, *ThreeBodyDecay*), needed to compute the energy and the four-momentum of the different decay products.

Moreover, as a starting point for the computation of the kinematics associated to the decay, the related Q-values are read from externally provided data listed in the Evaluated Nuclear Structure Data File (ENSDF) [139], as compiled for Geant4 distributions. All decays are first calculated in the rest frame of the mother nucleus and, subsequently, Lorentz-boosted and so reported into the laboratory frame. In the calculations, common natural units are employed ($\hbar = c = m_e = 1$).

The output file is constructed in such a way that each line is associated to a particle created during the decay. In particular, all lines contain the same information, displayed on several columns and organized into a numerical progressive label (event ID), the time of the particle creation (in s), the particle name, its excitation and kinetic energy (in keV) and the associated four-momentum (in keV/c), translated into the laboratory frame. Furthermore, particle emission is calculated into a 4π solid angle and classical momentum and energy conservation laws are implemented.

In the particular case of the simulation of the ^{32}Ar decay, the events are computed as in the experimental conditions, *i.e.* according to the expression of the β-decay rate (see Eq. 1.39) for unpolarized nuclei ($\overrightarrow{I} = \overrightarrow{\sigma} = \overrightarrow{0}$).

4.2 Implementation of the experimental set-up and the data taking conditions

Monte Carlo simulations based on the Geant4 toolkit (version 11.0.2) [140] were performed to reproduce the detection set-up and the experimental conditions occurred during data taking. In particular, as a first step, the CRADLE++ output file related to ^{32}Ar was implemented as decay event generator, in order to precisely create β-delayed proton decay events, with the associated kinematics previously determined from theoretical expressions taking into account the values of the weak interaction coupling constants manually provided by the user.

Subsequently, a realistic replica of the WISArD experimental set-up has been implemented within the simulations. The detection set-up, comprehensive of a plastic scintillator and eight trapezoidal single-sided silicon strip detectors (together with their dead layer), as more extensively detailed in Sec. 2.3, was reproduced, along with its mechanical support structures and associated copper plates, needed to favour the heat exchange with the surrounding cooling system. Moreover, the two-position aluminum arm mounted on one of the two rotatory rods, holding the catcher foil and an eventual 4-α calibration source, has been replicated. Finally, the global structure of the bore of the superconducting magnet, in which the detection set-up is located, has been added.

The geometry of the detection set-up and an illustrative example of a ^{32}Ar β-delayed proton decay, as set out within the simulation code, are shown in Fig. 4.1.

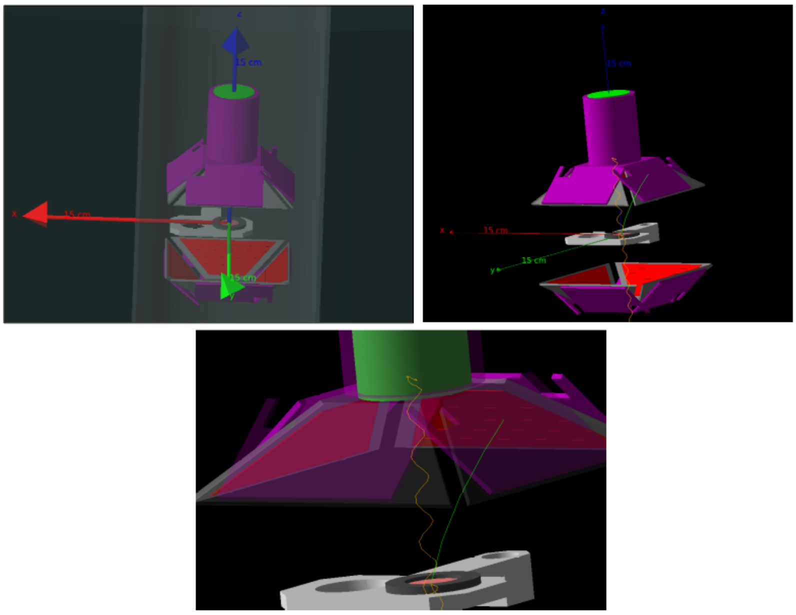

Figure 4.1: Visualization of the WISArD detection set-up as implemented within the Geant4 simulations (top left). The set-up, located in a vacuum tube (semi-transparent grey) in the

bore of the WISArD magnet (dark grey), is comprehensive of a plastic scintillator (green) for β-particle detection and eight single-sided silicon strip detectors for proton detection (together with their dead layer), each of them divided into five trapezoidal strips of equivalent geometrical area (red) and mounted on the respective mechanical support (grey). The silicon detectors are assembled on two truncated pyramid-like structures, mounted symmetrically with respect to the two-position aluminum arm (light grey) containing the catcher foil (magenta), into which the incoming beam is implanted, and an additional hole for the positioning of a calibration source. Further copper plates (magenta), needed to favour the heat exchange with the cooling system, are also represented. On top right, an illustrative example of a ^{32}Ar β-delayed proton decay is shown, with emission of β-particles (orange) and a proton (green); β-particles can be either guided by the magnetic field towards the plastic scintillator or lost in the underneath beam pipe, whereas protons may be slightly deflected towards the silicon detectors. On the bottom, a zoom on the detectors hit, with the frontal elements in transparency.

Furthermore, as explained in Sec. 2.3.1, the incoming $^{32}\mathrm{Ar}^{+}$ nuclei, post-accelerated at an energy of 30 keV, have been estimated to be implanted within the first 47 nm of the Mylar foil and 21 nm of the aluminized catcher, in which the immediately subsequent radioactive decay takes place. Numerically, the experimental beam implantation spot corresponds to the initial position vector into which the decaying particles, simulated by CRADLE++, are first created. Therefore, in order to correctly reproduce the experimental conditions occurred during data taking, the implantation of the $^{32}\mathrm{Ar}^{+}$ beam has been set on the bottom side of the catcher foil, within its first tenths of nanometers in thickness, firstly as point-like and afterwards, more realistically, in a Gaussian concentration distribution (r = 2 mm, σ = 300 μm) Simulations have been performed by varying the catcher foil thickness and material, as well as the correlated coordinates of the implantation point, in order to be consistent with the different data taking conditions (6 μm Mylar and 0.8 μm aluminized Mylar foil).
Subsequently, the decay products, fully described in their physical characteristics and kinematics by the CRADLE++ event generator and already generated inside the Mylar foil, are propagated through the experimental set-up into a 4 T homogeneous magnetic field.

4.3 Numerical methods

The WISArD experiment strongly relies on numerical simulations, not only for the determination of the $\tilde{a}_{\beta\nu}$ coefficient, but also for the estimation of several systematic uncertainties affecting the measurement, the major of which is represented by the β-detection threshold. Consequently, particular attention has been focused to choose a correct algorithm for particle propagation in magnetic field and, moreover, a specific physics simulation package capable of correctly and more precisely tracking and reproducing the interactions of β-particles with matter.

4.3.1 Numerical methods for particle propagation

First, the particle propagation inside the WISArD magnetic field employed for measurements, at an intensity of 4 T, has been replicated. In particular, as more precisely detailed in Sec. B.2, a precise measurement of the magnetic field profile in the region in which the detection set-up is located has been performed in February 2021, in order to quantitatively evaluate the level of field inhomogeneity and its influence on the final systematic error on the $\tilde{a}_{\beta\nu}$ coefficient. By globally mapping the region by means of a translating fluxmeter, it was measured that the relative variation of the magnetic field at 4 T, in a range of ± 100 mm with respect to the central plane, was around $\frac{\Delta B_z}{B_z} \simeq 5\cdot 10^{-5}$ for the axial component and $\Delta B_r \simeq 1\cdot 10^{-3}$ mT for the radial component. The results for all magnetic field strengths are in perfect agreement with the information provided by the manufacturer, thus permitting quantitatively to confirm the previous estimation on the systematic error due to magnetic field homogeneity, evaluated to contribute much less than 1‰ on the global systematic error on the $\tilde{a}_{\beta\nu}$ coefficient for both Fermi and Gamow-Teller transitions.

Though, in the WISArD simulations, the z-directed homogeneous magnetic field used for measurements has been in all cases simulated by using the *G4UniformMagField* class. Specifically, the Runge-Kutta-Nystrom algorithm [141], specifically optimized for second-order initial value differential equations, has been chosen in place of the classical Runge-Kutta fourth-order (RK4) method to numerically solve step-by-step the ordinary differential equations associated to the motion of the particles in a uniform magnetic field. Effectively, in this case the former algorithm is more robust and efficient, since it evaluates the integration error in each step by reusing the field value corresponding to the midpoint of the integration interval, resulting then in only two additional field evaluations per step with respect to the ten field computations required by the general RK4 method.

4.3.2 Numerical methods for particle interaction with matter

The list of all generic physics processes, consisting in particle definitions and radiation and electrically charged-particle interactions with matter, has been then set up from prearranged, standard Geant4 packages that guarantee the usage of well-validated combinations of theoretical and phenomenological physics approaches. Geant4 offers in fact a variety of ready-made models specifically designed to deal with physical processes within different energy ranges, routinely validated and updated at each version release [142]. Moreover, a better general implementation of electron multiple scattering has become throughout the years a fundamental goal to be reached in order to provide the most realistic description possible in the framework of low-energy physics.

Yet, amidst the various possibilities, the *Goudsmit − Saunderson* physics package has been chosen to be implemented within the simulations. Based on *Goudsmit – Saunderson* calculations [143, 144], it is a physics package specifically designed for a precise simulation of electron transport and based on algorithms of the EGSnrc multiple scattering model developed by Kawrakow and Bielajew [145]. In particular, this model, specifically developed to be implemented within Monte Carlo simulations, is based on an approach which combines numerical databases and analytical cross section models to properly take into account different interaction mechanisms due to low-energy and atomic effects, such as Doppler broadening and shell effects. Moreover, previous tests had been performed at LP2I-Bordeaux on the comparison between β-spectra acquired experimentally and the corresponding ones simulated numerically, by varying each time the *PhysicsList* employed for particle tracking and computation of their interactions with matter. According to the test results, presented in Appendix D, the *Goudsmit – Saunderson* model, among the other *PhysicsLists*, proved to be the physics package to better numerically reproduce the low-energy part of different β-spectra. Further information of the difference between the low-energy reproduction implemented within the Geant4 *PhysicsLists* and on the tests performed at LP2I-Bordeaux by means of radioactive sources and a pure mono-energetic electron spectrometer are available in Appendix C.

4.4 Results

In the end, spectra similar to the ones acquired experimentally have been simulated. In particular, the spectra acquired by each strip composing the silicon detectors have been registered, both without any additional condition (singles spectra) and by requiring a coincident β-particle event, recorded concomitantly by the plastic scintillator (β-coincident spectra). In the following, the simulated β-particle and the proton spectra will be shown, and the values related to the simulated mean IAS proton energy shifts will be resumed.

4.4.1 Simulated β-spectrum

The shape of the ^{32}Ar β-spectrum can be inferred from Eq. 1.39 to be proportional to the $\tilde{a}_{\beta\nu}$ coefficient, as follows:

$$\omega(E_e,\Omega_e,\Omega_\nu)dE_e d\Omega_e d\Omega_\nu \propto 1 + \frac{\overrightarrow{p_e}\cdot\overrightarrow{p_\nu}}{E_e E_\nu}a_{\beta\nu} + \frac{m_e}{E_e}b \tag{4.1}$$

In first approximation, b can be considered equal to zero. Afterwards, $\tilde{a}_{\beta\nu}$ will be interpreted as a combination of both the $a_{\beta\nu}$ and the b coefficients, as previously stated in Eq. 1.44.

The value of the $\tilde{a}_{\beta\nu}$ coefficient, by definition, affects then directly the angular distribution of the decay β-spectrum. According to the SM, the value of $a_{\beta\nu}$ for a pure Fermi transition, due to the contribution of a pure vector current to the weak interaction, is expected to be equal to 1, so that the leptons in the β-decay are preferentially emitted in the same direction, with the maximum recoil energy for the daughter nucleus (around 500 eV) and the consequent maximum energy shift between the single and the β-coincident IAS proton lines. On the contrary, in a pure BSM scenario, the only contribution describing the Fermi interaction is given by the scalar current and, consequently, $a_{\beta\nu}$ becomes equal to -1, thus determining the positron and the neutrino to be emitted preferentially in opposite directions, and so determining a minimum recoil energy for the daughter nucleus (around 150 eV) and a consequent minimum energy shift in the mean energy distributions of the IAS protons. In an intermediate case, *e.g.* $a_{\beta\nu} = 0$, the angle between the leptons is distributed isotropically with no preferred direction in the emission.

The most straightforward proof of the direct influence that a variation in the value of the $\tilde{a}_{\beta\nu}$ coefficient has on the overall decay kinematics is represented by the variation in shape of the proton peaks in the corresponding β-coincident proton spectra recorded by the silicon detectors. The distinct shapes in the IAS peak distributions recorded by the lower detectors as a function of different values of the $\tilde{a}_{\beta\nu}$ coefficient are clearly visible in Fig. 4.2.

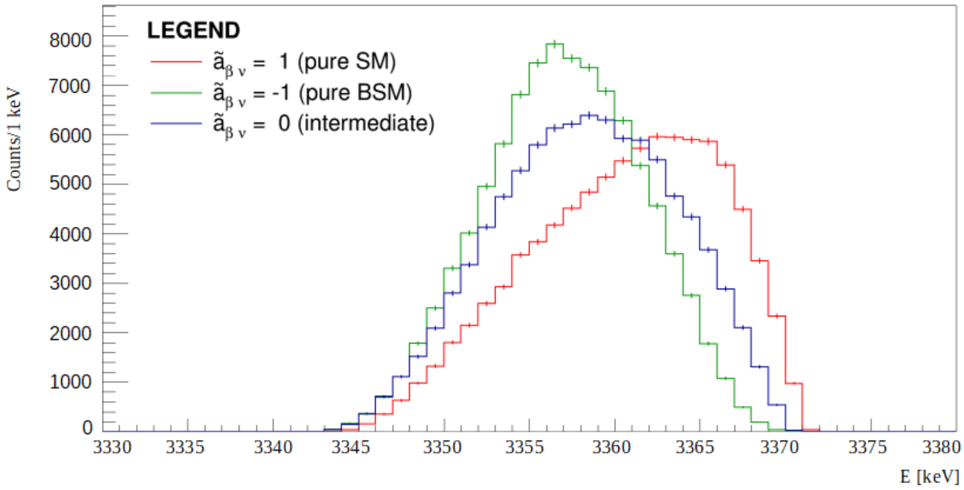

Figure 4.2: superposition of the ^{32}Ar β-coincident proton spectra recorded by the first strip of all lower silicon detectors (zoomed in the IAS peak region) generated with $\tilde{a}_{\beta\nu}$ = -1 (green, pure BSM), $\tilde{a}_{\beta\nu}$ = 0 (blue) and $\tilde{a}_{\beta\nu}$ = 1 (red, pure SM). These scenarios correspond respectively to a minimum energy shift in the mean energy distributions of the IAS protons (BSM), an isotropical distribution with no preferred direction in the emission (intermediate case) and to the maximum proton energy shifts (SM).

Moreover, as more extensively detailed in [119], the overall β-spectrum shape of ^{32}Ar can be decomposed in the sum of more than twenty different either Fermi or Gamow-Teller transitions, each of them contributing with a different intensity and end-point.
For completeness, a full β-spectrum recorded by the plastic scintillator, simulated with a statistics similar to the experimental ones (thirty million events), is shown in Fig. 4.3, together with its component due to a general β-proton coincident detection and to the specific coincident detection with an IAS proton by one silicon detector.

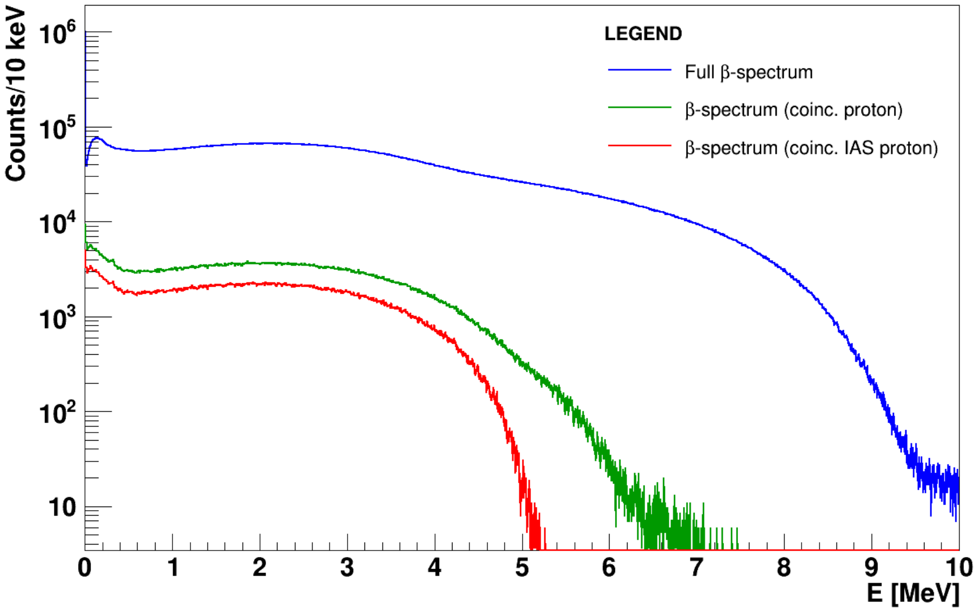

Figure 4.3: Full β-spectrum recorded by the plastic scintillator (blue), generated with 30 million events at $\tilde{a}_{\beta\nu} = 1$. In green, the component associated to a general β-proton detection from one silicon detector; in red, the component associated to a coincident detection with an IAS proton from one silicon detector.

In particular, the overall recorded β-spectrum extends up to its endpoint (Q_{EC} = 11134(2) keV) [119]. On the other hand, the full β-proton coincident one has an endpoint at around 7600 keV. Yet, the known most energetic β-transitions correspond to endpoints equal to, respectively, 7602.9(73) (BR = 0.121(9)%), 7853.5(39) (BR = 0.075(5)%) and 8153.1(133) keV (BR = 0.012(1)%) [119]; consequently, the last two transitions are not here represented due to their limited intensity and will be visible if performing simulations with ten times the statistics (*i.e.* 300 million events). The β-proton coincident spectrum, associated to the detection of an IAS proton, is extending up to its endpoint, at 5046.1(3) keV [119].

4.4.2 Simulated proton spectra and mean proton energy shifts

Spectra specular to the ones collected experimentally have been retrieved for each strip composing the eight silicon detectors. In Fig. 4.4, the superposition of the singles and β-coincident ^{32}Ar decay proton spectrum recorded by one silicon detector (all five strips summed) is shown.

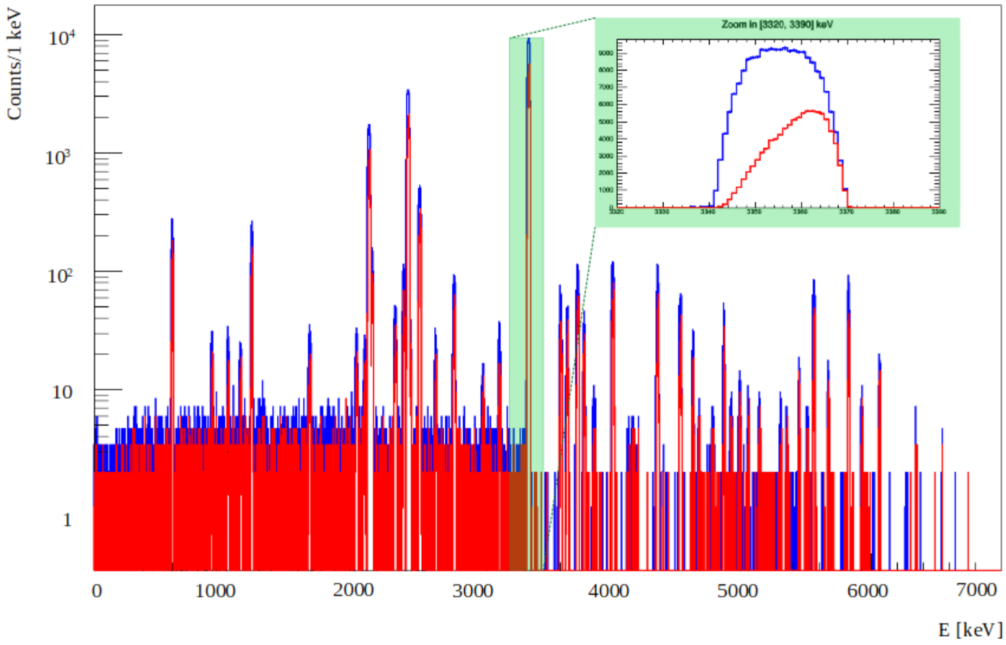

Figure 4.4: Simulated ^{32}Ar decay singles (blue) and β-coincident (red) decay proton spectrum from one silicon detector (SiDet5, all five strips summed) for the Mylar catcher. On top right, a zoom in the IAS proton peak region; the statistics collected in case of a β-proton coincident spectrum is roughly half the one collected in the singles proton spectrum, due to the fact that the intense magnetic field assures the detection of almost exactly 50% (46.6%) of the positrons emitted.

The energy shift towards higher energies for the β-coincident spectrum is clearly visible. Moreover, the peak obtained in the singles proton spectrum appears to be rather wider, due to the larger kinetic-energy broadening occurring while not requiring a coincidence with a β-particle, and so consequently taking into account protons associated to any positron emission angle. The overall statistics collected in case of the β-proton coincident spectrum is roughly half the one collected in the singles proton spectrum, due to the fact the intense magnetic field assures the spatial confinement and detection of almost all the β-particles directed towards the upper hemisphere ($\sim$ 50% of the total emitted), in which the plastic scintillator coupled to the SiPMs array is assembled. The missing fraction is due to β-backscattering in the catcher and to the energy deposited inside the scintillator which is below the β-detection threshold.

Yet, in order to be consistent with the analysis performed for the experimental data and correctly take into account the differences in terms of shifts between different strips, the absolute kinematic shifts have been computed separately for each strip, both for the upper and the lower hemisphere. The data have been then analyzed again by imposing the β-detection threshold at 100 keV; further details on that will be given in Sec. 5.1.

An example of the superposition of the single and the β-coincident proton spectra recorded by all the five strips for two detectors located respectively in the upper and in the lower hemisphere, zoomed in the energy region around the IAS peak, is shown in Fig. 4.5.

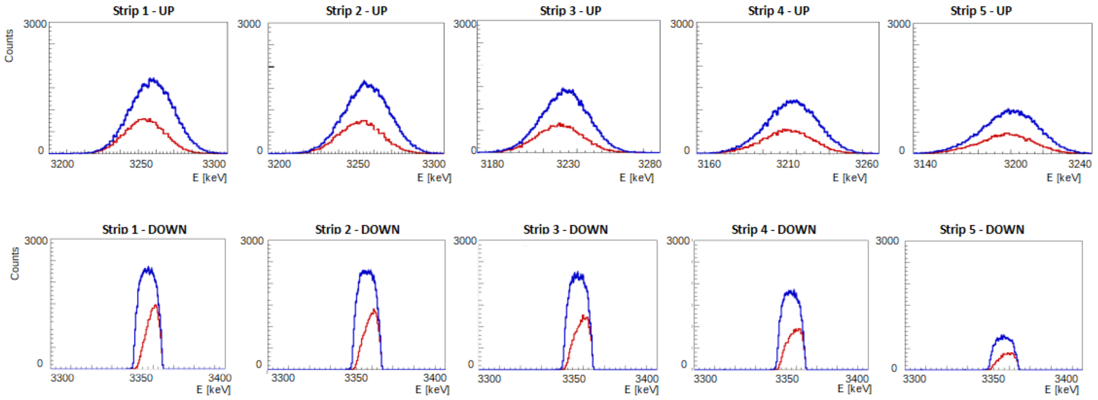

Figure 4.5: Illustrative example showing the superposition of the IAS proton single (blue) and the corresponding β-coincident (red) energy distributions for each of the five strips located on an upper (SiDet3) or lower (SiDet7) silicon detector (Mylar foil). The associated proton energy shifts are calculated as the absolute difference between the means of the proton energy distributions in the energy range around the IAS peak. As expected by kinematics, the shifts are directed towards lower energies for the upper detectors and towards higher energies for the lower ones.

As expected by kinematics, the shifts are directed towards lower energies for the upper silicon detectors and towards higher energies for the lower ones. It can be noted that the proton distributions for the upper detectors are much wider; this is due to the fact that the incoming beam is implanted in the bottom surface of the catcher and, consequently, the protons emitted towards the upper hemisphere have to transverse the whole thickness of the catcher foil before reaching the upper detectors, losing energy in the process and, so, being affected by a more significant energy straggling. Concomitantly, protons interacting with a higher catcher thickness are also more likely to be deviated from the original trajectory; this translates even in a very slightly reduced proton detection by the upper detectors, for which the associated mean energy shifts are therefore affected by a higher statistics uncertainty.

Moreover, as shown in Fig. 2.5, the silicon detectors, both the upper and the lower ones, are assembled on their respective truncated pyramid-like supports in such a way that the five strips are disposed progressively at a higher distance with respect to the z-axis, along which the magnetic field is directed; for convenience, the strips can be then numerically labeled in an ascending order according to their progressive distance to the z-axis, from 1 to 5. Consequently, the highest absolute value of the mean energy shift is expected by kinematics for both upper and lower silicon detectors in case of proton detection by the strip 1, which is the nearest to the z-axis; a progressively lower value is expected to be observed for the following strips, up to a minimum shift for strip 5. Indeed, as expected, the spatial positioning of the strips is directly correlated to the energy shift value; due to kinematics, the mean energy shift reaches a maximum for the strip nearest to the z-axis (strip 1), then progressively reduces up to a minimum value, obtained for the farther strip with respect to the z-axis (strip 5). At the same time, a progressive reduction in the statistics collected by the strips with higher numerical labels is also visible, mainly due to the spatial confinement of the proton trajectories due to the strong magnetic field.

The corresponding mean energy shifts associated to the IAS proton distributions, along with their statistical uncertainties, have been computed for each strip of all silicon detectors by considering a cut on the energy of the coincident electrons, equal to the β-detection threshold value and set at 100 keV (further details on this aspect will be given in Sec. 5.1). The error bars result higher for the detectors located in the upper hemisphere; this is due to the fact that the protons emitted upwards need to traverse a higher thickness of the catcher foil before being detected, thus resulting affected by a more significant energy straggling which enlarges the peak distribution and, consequently, reduce the precision on the mean energy value of the peak. Results are summarized in Table 4.1 and 4.2, for the aluminum and the Mylar foil respectively.

	Mean IAS proton energy shift [keV] vs strip n° (AlMylar)				
Silicon detector n°	**1**	**2**	**3**	**4**	**5**
SiDet 1	4.002 ± 0.040	3.654 ± 0.041	3.232 ± 0.044	2.942 ± 0.047	2.553 ± 0.051
SiDet 2	3.998 ± 0.040	3.594 ± 0.041	3.215 ± 0.044	2.812 ± 0.047	2.541 ± 0.051
SiDet 3	4.042 ± 0.041	3.609 ± 0.041	3.288 ± 0.044	2.888 ± 0.047	2.552 ± 0.051
SiDet 4	4.006 ± 0.040	3.599 ± 0.041	3.167 ± 0.044	2.931 ± 0.047	2.598 ± 0.052
Mean (upper SiDet)	4.011 ± 0.020	3.614 ± 0.021	3.226 ± 0.022	2.893 ± 0.024	2.560 ± 0.026
SiDet 5	3.931 ± 0.032	3.654 ± 0.032	3.186 ± 0.033	2.862 ± 0.036	2.671 ± 0.041
SiDet 6	3.896 ± 0.031	3.542 ± 0.032	3.225 ± 0.033	2.855 ± 0.037	2.536 ± 0.041
SiDet 7	4.032 ± 0.031	3.537 ± 0.032	3.159 ± 0.033	2.898 ± 0.036	2.559 ± 0.040
SiDet 8	3.957 ± 0.032	3.504 ± 0.032	3.193 ± 0.033	2.841 ± 0.037	2.508 ± 0.041
Mean (lower SiDet)	3.954 ± 0.016	3.559 ± 0.016	3.191 ± 0.017	2.864 ± 0.018	2.544 ± 0.020

Table 4.1: Summary of the simulated mean energy shifts, together with their statistical uncertainties, associated to the IAS proton distributions, computed for each strip of all silicon detectors and related to the runs acquired by employing a 0.8 μm aluminized Mylar foil. Strips are numerically labeled in ascending order according to their spatial disposition, as shown in the CAD drawing and in the final assembly picture in Fig. 2.5.

	Mean IAS proton energy shift [keV] vs strip n° (Mylar)				
Silicon detector n°	**1**	**2**	**3**	**4**	**5**
SiDet 1	4.097 ± 0.056	3.668 ± 0.060	3.257 ± 0.067	2.936 ± 0.077	2.620 ± 0.090
SiDet 2	4.093 ± 0.056	3.700 ± 0.060	3.270 ± 0.067	2.940 ± 0.076	2.643 ± 0.090
SiDet 3	4.051 ± 0.056	3.624 ± 0.060	3.315 ± 0.068	2.957 ± 0.078	2.635 ± 0.090
SiDet 4	4.047 ± 0.057	3.710 ± 0.060	3.268 ± 0.067	3.000 ± 0.077	2.693 ± 0.090
Mean (upper SiDet)	4.072 ± 0.028	3.676 ± 0.030	3.278 ± 0.034	2.958 ± 0.038	2.648 ± 0.045
SiDet 5	3.965 ± 0.032	3.606 ± 0.032	3.214 ± 0.034	2.873 ± 0.037	2.642 ± 0.058
SiDet 6	3.932 ± 0.032	3.525 ± 0.032	3.235 ± 0.033	2.850 ± 0.037	2.648 ± 0.058
SiDet 7	4.000 ± 0.032	3.540 ± 0.032	3.163 ± 0.033	2.895 ± 0.037	2.601 ± 0.057
SiDet 8	3.942 ± 0.032	3.550 ± 0.032	3.206 ± 0.033	2.951 ± 0.037	2.603 ± 0.059
Mean (lower SiDet)	3.960 ± 0.016	3.555 ± 0.016	3.204 ± 0.017	2.892 ± 0.019	2.623 ± 0.029

Table 4.2: Summary of the simulated mean energy shifts, together with their statistical uncertainties, associated to the IAS proton distributions, computed for each strip of all silicon detectors and related to the runs acquired by employing a 6 μm Mylar foil. Strips are numerically labeled in ascending order according to their spatial disposition, as shown in the CAD drawing and in the final assembly picture in Fig. 2.5.

A graphics visualization of the weighted average values obtained for each strip is displayed in Fig. 4.6. These values will be compared to the associated ones obtained experimentally, reported in Sec 3.2.5.

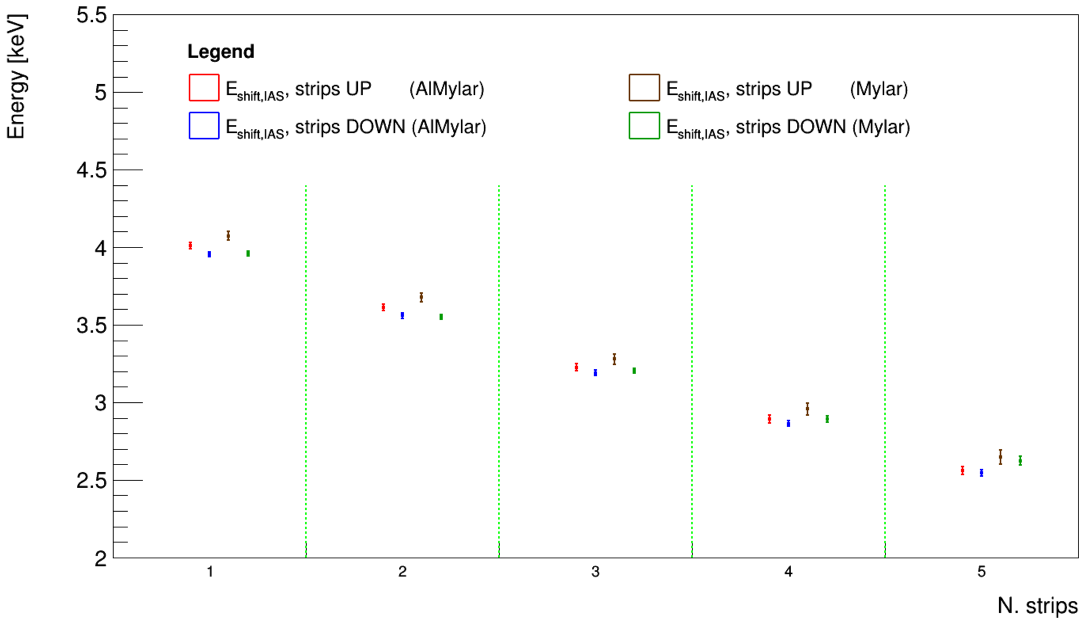

Figure 4.6: Graphics visualization of the simulated mean IAS proton energy shifts as a function of the strips for $\tilde{a}_{\beta\nu} = 1$ ($E_{elCoinc}$ > 100 keV). Results are illustrated for both the hemispheres and both the catcher foils employed during data taking (red and blue for the aluminized one, brown and green for the Mylar one). The vertical error bars correspond to the statistics uncertainties. The vertical dashed green lines are for graphics purpose.

For completeness, the IAS shifts obtained for each detector and related to each of the five strips are shown in Fig 4.7.

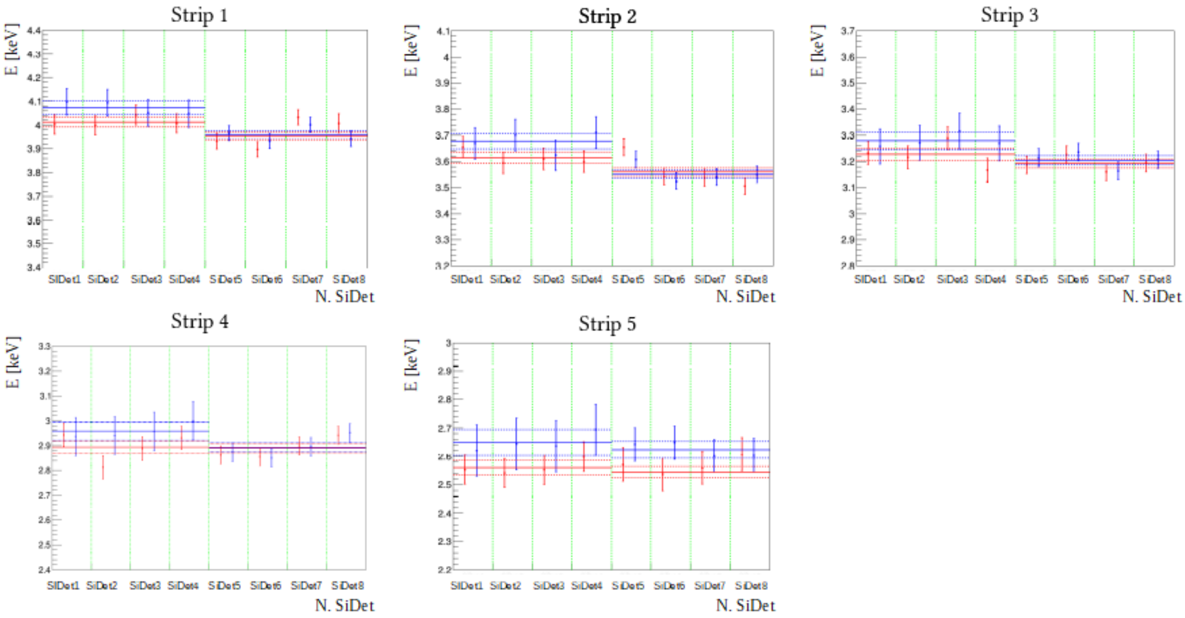
Strip 1
Strip 2
Strip 3
Strip 4
Strip 5

Figure 4.7: Graphics visualization of the simulated IAS proton energy shifts recorded by each silicon detector for strip 1 (top left), strip 2 (top centre), strip 3 (top left), strip 4 (bottom right) and strip 5 (bottom centre) for $\tilde{a}_{\beta\nu}$ = 1 ($E_{elCoinc}$ > 100 keV). The values reported, summarized in Tab. 3.6 and in Tab. 3.7, are related to the aluminized (red) and to the Mylar (blue) catcher, respectively. The vertical error bars correspond to the statistics uncertainties. The horizontal red and blue lines indicate the weighted average (solid), along with its statistics uncertainty (dashed) for both the upper (SiDet1 to SiDet4) and the lower (SiDet5 to SiDet8) silicon detectors, for the aluminized and the Mylar foil, respectively. The vertical dashed green lines are for graphics purpose.

4.4.3 Systematic uncertainties estimation

Comparing the results reported in Table 4.1 and in Table 4.2 with the corresponding experimental ones, no systematic discrepancies between the experimental and the simulated energy shifts appear. Effectively, the shifts computed via the simulations are compatible with the ones obtained from the experiment within 1 σ, already in terms of the only statistical uncertainty. In particular, the results summarized in the previous tables already include the effect of the β-energy threshold for the SiPM cells, set at 100 keV within the simulations. Its value has been quantified with an accurate comparison of the experimental and the simulated β-spectra collected by the SiPM matrix; the procedure followed to achieve this results will be illustrated in the following chapter.

Moreover, in order to study the dependency of the kinematic shift per each strip as a function of the weak interaction coupling constants, different simulations have been performed by varying the value of $\tilde{a}_{\beta\nu}$ as an input parameter within the CRADLE generator and, therefore, in the associated Geant4 simulations, setting it respectively at 1 (pure SM), 0 (intermediate case) and -1 (pure BSM).

Further simulations have been finally performed in order to estimated the systematic uncertainties affecting the final measurement. Particularly, considering in all cases $\tilde{a}_{\beta\nu}$ at 1 (pure SM), various simulations have been performed in order to reproduce possible variation of the experimental and data taking conditions, for both the Mylar and the aluminized Mylar foil:

- the x and y position of implantation of the beam: five simulations have been performed, both for the Mylar and the aluminum foil, considering the (x, y) coordinates for the beam implantation point within the catcher at (-2, 0), (0, -2), (0, 0), (2, 0) and (0, 2) mm, respectively. In this case, the associated z coordinate has not been varied, and its value has been retrieved from SRIM estimations both for the Mylar (47 nm) and the aluminized Mylar foil (21 nm);

- the z position of implantation of the beam from the bottom part of the catcher, varied between three sets of values for both the Mylar (33, 47 and 61 nm) and the aluminum foil (13, 21, 29 nm), respectively. In this case simulations have been performed considering a symmetric implantation ($x = y = 0$ nm), and the z-values for implantation have been varied within 1 σ with respect to the z implantation coordinates estimated via SRIM ((47 ± 14 nm) and (21 ± 8) nm, respectively);

- the silicon detector dead layer, set at 100 nm and at 130 nm, *i.e.* moved between 1 σ with respect to the average dead layer value measured for the silicon detectors at the AIFIRA accelerator (for details see Sec. 2.3.3.1);

- the catcher thickness, assuming a reasonable uncertainty of 2.5% on its value[2]. Simulations have been therefore performed at 6.25 μm (Mylar, with 6 μm nominal thickness) and at 0.82 μm (aluminized foil, with 0.8 μm nominal thickness).

In all cases the corresponding kinematic shifts have been calculated per each strip. Results similar to the ones summarized in Table 4.1 and in Table 4.2 have been obtained. These results will concur to the determination of the systematic uncertainty to the final measurement of the $\tilde{a}_{\beta\nu}$ coefficient. The results obtained are summarized in Table 4.3.

---

[2] A conservative approach has been applied. The percentage uncertainty on the catcher thickness is the same as the one estimated for the 2018 proof-of-principle experiment.

	Systematic uncertainty on mean IAS proton energy shift [keV] vs strip n°					
	AlMylar			Mylar		
Strip n°	**Impl. point**	**Catcher thickness**	**Dead layer**	**Impl. point**	**Catcher thickness**	**Dead layer**
Strip1 (UP)	0.039	0.013	< 0.001	0.035	0.005	< 0.001
Strip2 (UP)	0.046	0.012	< 0.001	0.017	0.005	< 0.001
Strip3 (UP)	0.029	0.002	< 0.001	0.008	0.005	< 0.001
Strip4 (UP)	0.028	0.001	< 0.001	0.070	0.005	< 0.001
Strip5 (UP)	0.036	0.011	< 0.001	0.062	0.004	< 0.001
Strip1 (DW)	0.019	0.007	< 0.001	0.008	0.007	< 0.001
Strip2 (DW)	0.010	0.007	< 0.001	0.022	0.007	< 0.001
Strip3 (DW)	0.007	0.004	< 0.001	0.008	0.007	< 0.001
Strip4 (DW)	0.010	0.004	< 0.001	0.028	0.010	< 0.001
Strip5 (DW)	0.015	0.011	< 0.001	0.016	0.015	< 0.001

Table 4.3: Summary of the systematic uncertainties on the simulated mean energy shifts associated to the IAS proton distributions, computed as the mean value among the different detectors for each strip in the upper (UP) and the in the lower (DW) hemispheres, in case of employment of both the catcher foils. The values are given relatively to the variation of the implantation point, of the catcher thickness and of the silicon detector dead layer.

As attended, the contribution of the systematic uncertainty on the silicon detector dead layer is negligible in all cases, due to its very limited thickness. The dominant systematic uncertainty up to now is given by the beam implantation point inside the catcher foil; however, the values related to this contribution will be recalculated after precise measurements on the beam implantation profile, which will be accomplished in the following months via a dedicated MCPs assembly developed at LPC Caen (for further details see Sec. 5.4.2). Furthermore, the uncertainty related to the source radius will also be estimated[3].

Yet, it can be noticed that the uncertainties reported in Table 4.3 are not simply increasing with the strip number (from 1 to 5), as attended, but rather fluctuating with no repeated scheme correlated to the strip spacial disposition; this can be likely due to the fact that the uncertainty estimation associated to both the implantation point and the catcher thickness are limited by the lack of statistics in the simulations. Nevertheless, the systematic contributions still remain smaller for all strips than the corresponding statistical uncertainties on the kinematic shifts. The results presented here represent just a first estimate; even though the current simulations have already been realized with a higher statistics with respect to the one collected in the experimental data, further simulations with an even higher number of decay events will be required afterwards to estimate both these effects precisely.

A full preliminary comparison between the experimental and the simulated energy shifts will be illustrated in the following chapter.

---

[3] A variation only in the value of σ in the Gaussian distribution of the source, for a given catcher and x, y and z coordinates of implantation point, does not change the energy shift. Simulations have been performed by varying at 100, 200, 300 and 400 μm, showing no difference in the shift values at the permil level and a difference in terms of the statistics collected by the detectors of fairly less than 1‰.

Chapter 5

Discussion

In this chapter, a first preliminary comparison between the experimental data collected during the experimental campaign at ISOLDE in October 2021 and the corresponding numerical simulations will be presented.

In the following, the superposition of the experimental and the simulated spectra acquired by the SiPM matrix, both for the low-gain and the high-gain outputs, will be discussed and the corresponding experimental β-detection threshold will be inferred. Moreover, a preliminary comparison between the experimental and the simulated proton energy shifts related to the IAS peak of ^{32}Ar will be illustrated. As well, an analysis of the systematic uncertainties affecting the final determination of the $\tilde{a}_{\beta\nu}$ coefficient, which is still under investigation, will be described.

5.1 Experimental β-detection energy threshold

Referring to the error budget of the proof-of-principle experiment [111], realized at ISOLDE in November 2018, it comes out that one of the major systematic uncertainties affecting the final determination of the $\tilde{a}_{\beta\nu}$ coefficient is represented by the value of the experimental β-detection energy threshold. Practically, this value can be inferred from a comparison between the experimental and the corresponding simulated β-spectra registered by the SiPM matrix, detected in coincidence with an IAS proton by one of the silicon detectors.

In this specific case, the fact that the SiPM cells had been designed in such a way to provide a dual-range output, resulting both in a low-gain and a high-gain response, turns out to be particularly useful. Indeed, as explained in Sec. 2.3.3.2, the low-gain signals permit to reconstruct the full proton-coincident β-spectrum up to its endpoint, whereas the corresponding high-gain outputs are amplified by a factor of ten in terms of signal amplitude and, consequently, allow to precisely characterize the low-energy part of the spectrum, concerned by the effect of the β-detection threshold. As discussed in Sec. 3.2.2, the LG and the HG spectra acquired with the different SiPM channels have been independently calibrated, at first-order, via a ^{90}Sr radioactive source; subsequently, as illustrated in Sec. 3.2.3, the complete IAS proton-coincident β-spectra have been reconstructed, both for the LG and the HG channels, as a function of all the possible SiPM cell trigger multiplicities. In parallel, as detailed in Sec. 4.4.1, the corresponding IAS proton-coincident β-spectrum acquired by the plastic scintillator has been retrieved from the related Geant4 simulations.

5.1.1 Comparison between the LG and the simulated β-spectrum

A first superposition of the calibrated experimental β-spectra, acquired by the LG channels and reconstructed as a function of all the possible SiPM trigger multiplicities, and the corresponding simulated β-spectrum, convoluted with the response function of the detector, can be performed. In particular, by varying both the linear calibration and the convolution parameters via a gradient descent algorithm, it is possible to define with accuracy the set of parameters which minimizes the χ^2 value between the experimental and the simulated histograms[1]. The result of the comparison between the energy-calibrated LG β-spectra, reconstructed as a function of all the possible multiplicities, and the convoluted simulated spectrum, is shown in Fig. 5.1.

As it can be qualitatively noticed, the simulated spectrum matches rather satisfactorily the reconstructed experimental ones. The only discrepancies appear in the very low-energy region, affected by the β-detection threshold effects. Quantitatively, the relative χ^2 values, computed for each spectrum between 100 and 9000 keV, are reported in Table 5.1.

	LG trigger							
	M1	**M2**	**M3**	**M4**	**M5**	**M6**	**M7**	**M8**
χ^2	2.11	2.12	2.43	2.69	3.06	3.70	5.01	6.98

Table 5.1: Summary of the χ^2 values (computed between 100 and 9000 keV) obtained for the comparison between the experimental energy-calibrated IAS proton-coincident β-spectrum recorded by the SiPM matrix, reconstructed as a function of all the possible LG M_x (x in [1, 9]) SiPM cell cumulative trigger multiplicities, and the corresponding Geant4 convoluted β-spectrum.

---

[1] In particular, the following formula for the energy calibration and resolution have been applied: E [MeV] = $a + b \cdot CH$ and σ [MeV] = $c + d \cdot \sqrt{E}$. A gradient descent algorithm minimizes the χ^2 value between experimental and simulated histograms by iteratively moving in the direction of the steepest descent, defined by the negative of the χ^2-gradient as a function of the four a, b, c and d coefficients. A similar analysis is presented in Sec. D.3.4.2 in Appendix D.

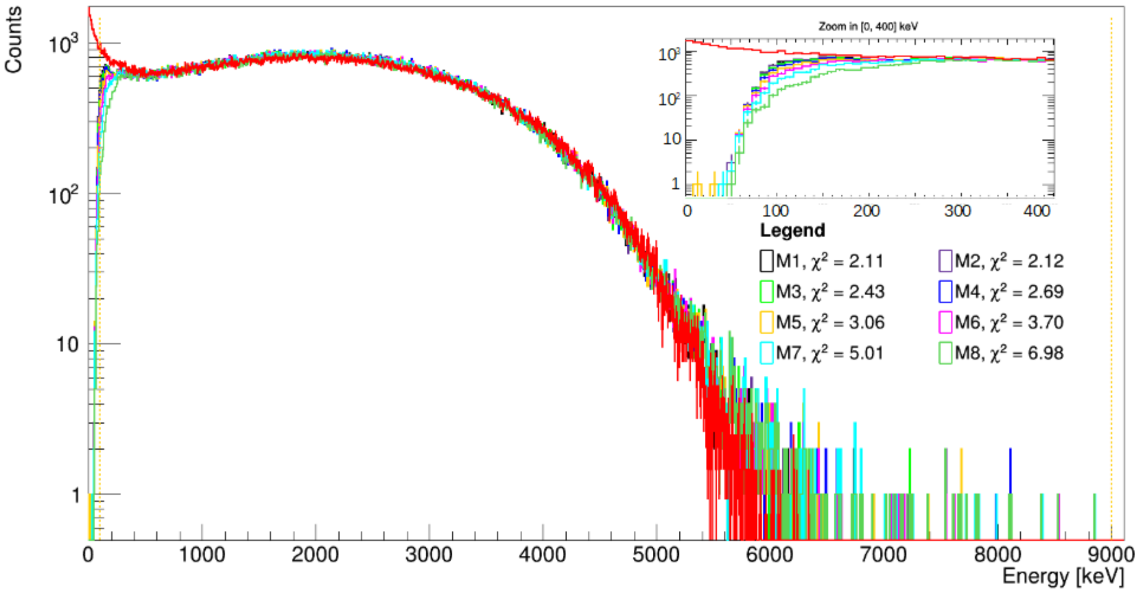

Figure 5.1: Superposition of the LG experimental and the simulated IAS proton-coincident β-spectrum acquired by the SiPM matrix, with a zoom in the low-energy region ([0, 400] keV). The experimental spectra (black, purple, light green, blue, yellow, pink, cyan and green) are reconstructed progressively as a function of all the possible SiPM cell cumulative trigger multiplicities and calibrated in energy at first-order by exploiting the data acquired with a ^{90}Sr radioactive source and, then, according to the parameter minimization operated via a descent gradient algorithm. The simulated spectrum (red) has been convoluted with the detector response function and the related parameters are also determined via the same gradient descent algorithm. The simulated spectrum matches rather satisfactorily the experimental one, as the only discrepancies appear in the very low-energy region, affected by the β-detection threshold effects. The relative χ^2 values, computed for each spectrum between 100 and 9000 keV (indicated by the vertical dashed yellow lines), is reported in the legend. The associated M2 residual plot is shown in Sec. C.5 in Appendix C.

As discussed in Sec. 3.2.3, the trigger multiplicity condition imposed online to reconstruct the β-coincident events can be offline lowered to two cells firing within the same 200 ns window; effectively, in this case the huge amount of signals recorded with multiplicity equal to one and primarily due to noise are still discarded, but, at the same time, a little further amount of exploitable data can be gained back and additionally considered for the analysis. Consequently, referring to Fig. 5.1, the superposition of the convoluted simulated and the energy-calibrated experimental spectrum, reconstructed with the condition of having at least two SiPM cells firing at the same time (*i.e.* the M_2 spectrum), is the one of interest for the derivation of the value of the β-detection energy threshold. In particular, in this case the reduced χ^2 value results equal to 2.12, with significant discrepancies appearing at the level of the experimental curve solely below 150 keV. The experimental β-detection energy threshold can be then inferred as the energy point located roughly at the end of the rising curve characterizing the low-energy part of the experimental spectrum, which is comprised between the energy value corresponding to the first signals acquired (depending on the DAQ thresholds set before the data acquisition, in this case localized at around 40 keV) and the value after which the simulations fairly well reproduce the experimental spectrum (at around 150 keV). So, in principle, the β-detection threshold can be deduced to be between 100 and 200 keV.

In particular, a more precise inference can be performed if considering the superposition of the convoluted simulated spectrum and the corresponding experimental one, reconstructed, this time, at a minimum trigger multiplicity equal to two cells firing at the same time and from the SiPM HG output signals. Effectively, by construction and as verified in Sec. 3.2.2.2, the HG outputs result linearly amplified by a factor of ten in terms of signal amplitude with respect to the corresponding LG ones, thus allowing to precisely characterize the low-energy part of the spectrum, concerned by the effect of the β-detection threshold. Moreover, as resulted from the energy calibration process, the linear amplification regime can be considered as perfectly valid up to a energy of about 1000 keV, after which the HG amplified signal systematically overpasses the shoulder point and constantly reaches the saturation point. The result of the comparison between the experimental HG spectra, reconstructed as a function of all the possible SiPM trigger multiplicities, and the corresponding convoluted simulated one is shown in Fig. 5.2. The related χ^2 values, computed for each spectrum between 100 and 9000 keV, are reported in Table 5.2.

	HG trigger							
	M1	**M2**	**M3**	**M4**	**M5**	**M6**	**M7**	**M8**
χ^2	1.08	1.10	1.11	1.25	1.47	1.61	2.24	3.48

Table 5.2: Summary of the χ^2 values (computed between 100 and 1000 keV) obtained for the comparison between the experimental energy-calibrated IAS proton-coincident β-spectrum recorded by the SiPM matrix, reconstructed as a function of all the possible HG M_x (x in [1, 9]) SiPM cell cumulative trigger multiplicities, and the corresponding Geant4 convoluted β-spectrum.

In all cases, the χ^2 values are significantly low, thus confirming quantitatively the correctness of the Geant4 simulations in reproducing the low-energy part of the spectrum. In particular, for a minimum trigger multiplicity equal to two SiPM HG cells firing at the same time, the corresponding reduced χ^2 is equal to 1.10. Once again, the discrepancies between the simulated and the experimental spectrum appear only in the low-energy region, roughly below 100 keV. The experimental β-detection energy threshold can be hence inferred to be equal to 100 keV, with a reasonable associated uncertainty of around 10 keV.

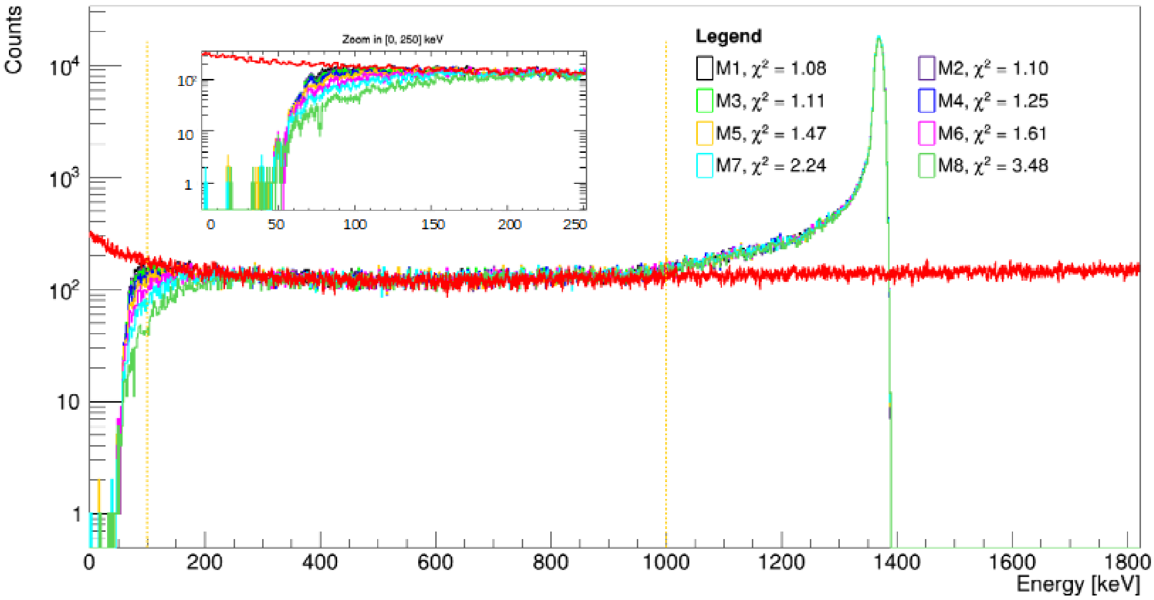

Figure 5.2: Superposition of the HG experimental and the simulated IAS proton-coincident β-spectrum acquired by the SiPM matrix, with a zoom in the low-energy region ([0, 250] keV). The several experimental spectra (black, purple, light green, blue, yellow, pink, cyan and green) are reconstructed progressively as a function of all the possible SiPM cell cumulative trigger multiplicities and linearly amplified by a factor of ten with respect to the corresponding LG spectra; the linear amplification regime, as verified in Sec. 3.2.2.2, is valid up to an energy of about 1000 keV, above which the HG response function begins to reach saturation. The convoluted simulated spectrum (red) is the same as in Fig. 5.1, rescaled for superposition purpose and zoomed in the [0, 1800] keV region. The related χ^2 values, computed for each spectrum between 100 and 1000 keV (indicated by the vertical dashed yellow lines), are reported in the legend. The associated M2 residual plot is shown in Sec. C.5 in Appendix C.

In particular, the value of the β-detection threshold obtained during the 2021 experiment turns out to be approximately three times higher with respect to the one obtained for the SiPM detector in the proof-of-principle experiment in 2018 [111], which was estimated at 25(12) keV, with a conservative 12 keV uncertainty due to low statistics and to a limited knowledge of the detector response function. Specifically, the fact of having this time a higher β-detection threshold, in spite of the employment of a completely new β-detection set-up, is due to the choice of the DAQ threshold settings performed before the start of the experimental campaign. Indeed, the FASTER thresholds were set to rather high values as a precautionary measurement, in order not to have the load of data almost exclusively dominated by the outputs due to noise from the different SiPM cells; however, this choice incidentally influenced the β-detection threshold, causing it to be set at higher values than expected.

Nonetheless, it should be underlined that the β-detection energy threshold, even if it is higher than expected and about ten times larger than the minimum value possibly reachable, is not directly affecting in a dramatic way the determination of the $\tilde{a}_{\beta\nu}$ coefficient. In fact, the existence of the experimental β-energy threshold just implies that a certain amount of data related to the positrons originally emitted in the upward direction and depositing a very low amount of energy inside the scintillator, had not been detected by the SiPM cells. Practically, this means that the β-energy threshold induces a reduction in the statistics collected relatively to the β-coincident events, which directly translates into a tiny systematic effect on the shape of the IAS peak distribution. Consequently, the mean values of the IAS distributions for the β-coincident events can be slightly different and so can be, therefore, for the associated kinematic energy shifts, which are linearly proportional to the $\tilde{a}_{\beta\nu}$ coefficient.

In conclusion, the experimental β-detection threshold does introduce an experimental systematic non-detection of a fraction of the positrons originally emitted towards the scintillator. Yet, in order to correctly reproduce the experimental data, this effect should be included *a posteriori* within the Geant4 simulations of the experiment.

5.1.2 Experimental β-detection threshold in the Geant4 simulations

The results coming from the Geant4 simulations have been then re-analyzed, both in case of employment of the Mylar and the aluminized catcher, by adding the condition of a β-detection threshold. The threshold value has been varied between 90, 100 and 110 keV respectively, in order to estimate the impact of the β-detection threshold estimated in Sec. 5.1, along with its error, on the proton statistics employed for the computation of the IAS energy shifts, and also on the consequent determination of the kinematic shifts themselves.

In Fig. 5.3, an example of superposition of the IAS proton distributions as a function of different cuts on the energy of the positrons registered in coincidence with the IAS protons is shown, respectively for an upper and a lower strip. In Table 5.3 and in Table 5.4, the percentage of statistics registered due to the β-detection threshold at 90, 100 and 110 keV with respect to the case of no thresholds applied (0 keV) is reported, for the aluminized and the Mylar foil respectively.

For the comparison between the experimental and simulated values of the kinematic shifts associated to the IAS peaks, an *a posteriori* β-detection threshold of 100 keV will be applied. The kinematic shifts determined with the other thresholds will be employed for determining the final systematic uncertainty on the measurement associated to the experimental β-detection threshold, for each strips located both in the upper or in the lower hemisphere and for both the catcher foils employed.

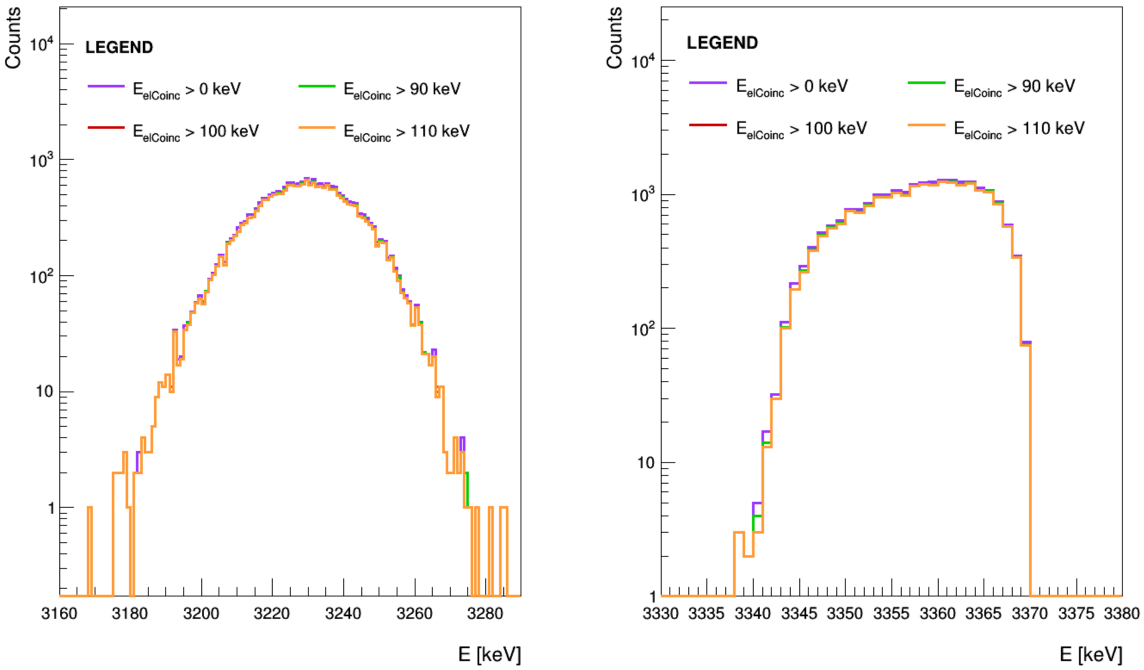

Figure 5.3: superposition of the ^{32}Ar β-coincident IAS proton distributions registered by one strip in the upper hemisphere (left, SiDet3, strip3) and in the lower hemisphere (right, SiDet7, strip3) in case of employment of the Mylar foil as a function of different cuts on the positron energy, at 0 (purple), 90 (green), 100 (red) and 110 keV (orange), respectively.

	Strip n. (AlMylar)				
β-detection threshold [keV]	**1**	**2**	**3**	**4**	**5**
0 (UP coincidence)	100.0(5)	100.0(5)	100.0(5)	100.0(5)	100.0(5)
90 (UP coincidence)	96.1(5)	96.1(5)	96.2(5)	96.2(5)	96.1(5)
100 (UP coincidence)	95.8(5)	95.7(5)	95.8(5)	95.8(5)	95.7(5)
110 (UP coincidence)	95.3(5)	95.3(5)	95.4(5)	95.4(5)	95.4(5)
0 (DOWN coincidence)	100.0(5)	100.0(5)	100.0(5)	100.0(5)	100.0(5)
90 (DOWN coincidence)	96.1(5)	96.2(5)	96.1(5)	96.2(5)	96.1(5)
100 (DOWN coincidence)	95.7(5)	95.9(5)	95.7(5)	95.8(5)	95.7(5)
110 (DOWN coincidence)	95.3(5)	95.5(5)	95.3(5)	95.4(5)	95.3(5)

Table 5.3: Summary of the percentage of the β-coincident events registered by the upper and the lower strips (aluminized Mylar foil) as a function of different β-detection thresholds of 90, 100 and 110 keV, respectively. The associated statistical uncertainties come from the error propagation.

	Strip n. (Mylar)				
β-detection threshold [keV]	**1**	**2**	**3**	**4**	**5**
0 (UP coincidence)	100.0(5)	100.0(5)	100.0(5)	100.0(5)	100.0(5)
90 (UP coincidence)	96.1(5)	96.2(5)	96.2(5)	96.2(5)	96.2(5)
100 (UP coincidence)	95.7(5)	95.8(5)	95.8(5)	95.9(5)	95.8(5)
110 (UP coincidence)	95.4(5)	95.4(5)	95.4(5)	95.5(5)	95.5(5)
0 (DOWN coincidence)	100.0(5)	100.0(5)	100.0(5)	100.0(5)	100.0(5)
90 (DOWN coincidence)	96.1(5)	96.2(5)	96.3(5)	96.3(5)	96.2(5)
100 (DOWN coincidence)	95.7(5)	95.9(5)	95.9(5)	95.9(5)	95.9(5)
110 (DOWN coincidence)	95.3(5)	95.5(5)	95.5(5)	95.5(5)	95.5(5)

Table 5.4: Summary of the percentage of the β-coincident events registered by the upper and the lower strips (Mylar foil) as a function of different β-detection thresholds of 90, 100 and 110 keV, respectively. The associated statistical uncertainties come from the error propagation.

The corresponding systematic uncertainty on the energy shifts associated to the IAS proton peak distribution are summarized in Table 5.5.

	AlMylar	**Mylar**
Strip n°	**Positron energy cut**	**Positron energy cut**
Strip1 (UP)	0.003	0.005
Strip2 (UP)	0.003	0.005
Strip3 (UP)	0.005	0.005
Strip4 (UP)	0.004	0.005
Strip5 (UP)	0.007	0.004
Strip1 (DW)	0.006	0.007
Strip2 (DW)	0.007	0.004
Strip3 (DW)	0.008	0.003
Strip4 (DW)	0.008	0.003
Strip5 (DW)	0.004	0.002

Table 5.5: Summary of the systematic uncertainties on the simulated mean energy shifts associated to the IAS proton distributions, computed as the mean value among the different detectors for each strip in the upper (UP) and the in the lower (DW) hemispheres, in case of employment of both the catcher foils. The values are related to the variation in the shifts as an effect of different energy cuts on the β-coincident events recorded by the SiPMs.

It can be noticed that the systematic uncertainties are not directly and simply increasing with the detector strip number (from 1 to 5), as attended, but rather fluctuating with no repeated scheme correlated to the strip spacial disposition; as already discussed in Sec. 4.4, this can be likely due to the fact that the uncertainty estimation, which still remains for each strip much lower than the corresponding statistical error on the energy shift, is limited by the lack of statistics in the simulations. Further simulations will be performed with a much higher number of decay events to better estimate this effect.

5.2 Comparison between experimental and simulated proton energy shifts

The experimental and the simulated energy shifts related to the IAS proton peak distribution have been computed, as explained in Sec. 3.2.5 and in Sec. 4.4, respectively. Moreover, the systematic uncertainties related to the implantation point, the source radius, the silicon detector dead layer and the catcher thickness have been estimated via different Geant4 simulations, as illustrated in Sec. 4.4.3.

Different simulations have been performed by varying the value of $a_{\beta\nu}$ as an input parameter within the CRADLE event generator, setting it respectively at 1 (pure SM), 0 (intermediate case) and -1 (pure BSM). The comparison between the experimental and the simulated energy shifts (with $a_{\beta\nu}$ = -1, 0 and 1 respectively), is given in Fig. 5.4 and in Fig. 5.5 for the aluminized and the Mylar foil, respectively.

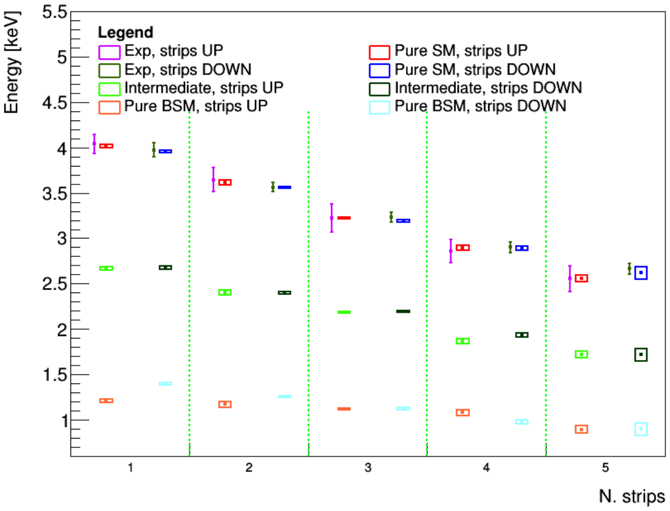

Figure 5.4: Graphics visualization of the mean IAS proton energy shifts as a function of the strips, for the aluminized Mylar foil. Results are illustrated for both the upper and the lower hemispheres, relatively to the values measured experimentally (purple and dark green) and to the ones retrieved via Geant4 simulations, at $a_{\beta\nu}$ = 1 (red and blue), $a_{\beta\nu}$ = 0, (light green and brown), $a_{\beta\nu}$ = -1 (orange and azure). The vertical error bars correspond to the statistics uncertainties; the error boxes indicate the global systematic uncertainties, computed as the sum in quadrature of the single contributions (implantation point, source radius, dead layer and catcher thickness). The vertical dashed green lines are for graphics purpose.

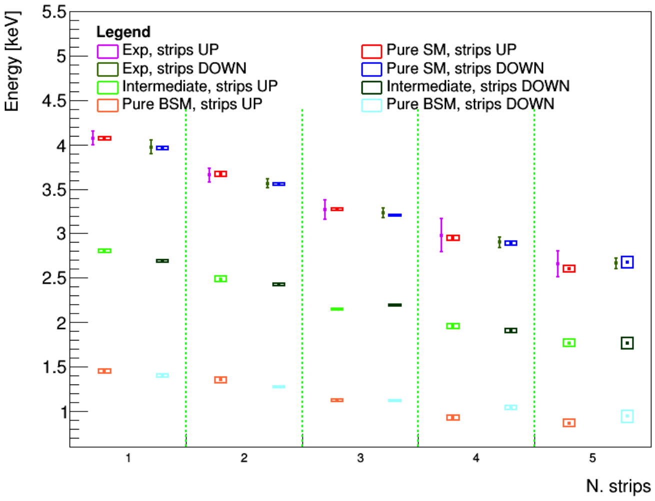

Figure 5.5: Graphics visualization of the mean IAS proton energy shifts as a function of the strips, for the Mylar foil. Results are illustrated for both the upper and the lower hemispheres, relatively to the values measured experimentally (purple and dark green) and to the ones retrieved via Geant4 simulations, at $a_{\beta\nu}$ = 1 (red and blue), $a_{\beta\nu}$ = 0, (light green and brown), $a_{\beta\nu}$ = -1 (orange and azure). The vertical error bars correspond to the statistics uncertainties; the error boxes indicate the global systematic uncertainties, computed as the sum in quadrature of the single contributions (implantation point, source radius, dead layer and catcher thickness). The vertical dashed green lines are for graphics purpose.

Qualitatively, it can be observed that the experimental energy shifts are clearly nearer to the corresponding values obtained from simulations performed at $a_{\beta\nu}$ = 1, *i.e.* accordingly to the pure SM scenario. In particular, all the experimental mean shifts are compatible within 1 σ with the corresponding SM simulated value. Moreover, the vertical error bars indicating the statistical uncertainties on the simulated values are represented, but hardly visible as smaller than the corresponding systematic uncertainties.

Moreover, it can be noted that, for each strip, a progressive reduction in the $a_{\beta\nu}$ value injected within the CRADLE event generator ($a_{\beta\nu}$ varying from 1 to -1) consequently causes an associated reduction in the proton mean energy shift. This outcome, already introduced in Sec. 4.4.1, is due to the fact that, according to the SM, the value of $a_{\beta\nu}$ for a pure Fermi transition is expected to be equal to 1, so that the leptons in the β-decay are preferentially emitted in the same direction, with the maximum recoil energy for the daughter nucleus and, consequently, the maximum energy shift between the single and the β-coincident IAS proton lines. On the contrary, in a pure BSM scenario, the $a_{\beta\nu}$ coefficient is expected to be equal to -1, thus implying that the positron and the neutrino are emitted preferentially in opposite directions; this scenario would imply a minimum recoil energy for the daughter nucleus and, consequently, a minimum energy shift in the mean energy distributions of the IAS protons.

On the other hand, in an intermediate case, *e.g.* $a_{\beta\nu} = 0$, the angle between the leptons is distributed isotropically with no preferred direction in the emission, so that the values of the energy shifts result placed rather symmetrically among the ones obtained for $a_{\beta\nu} = 1$ and $a_{\beta\nu} = -1$.

5.3 Extraction of the $\tilde{a}_{\beta\nu}$ coefficient

By exploiting the results exposed in Fig. 5.4 and in Fig. 5.5, it is possible to extract, strip by strip, the value of $\tilde{a}_{\beta\nu}$ for the pure Fermi transition of ^{32}Ar. Effectively, by plotting the values of the coefficients at which the simulations were performed as a function of the corresponding kinematic energy shifts, it is possible to extract the $\tilde{a}_{\beta\nu}$ value as the intercept between the experimental energy shift and the linear fitting function, obtained from the values retrieved by the simulations performed with different values of the vector and the scalar coupling constants, respectively.

The related values are summarized, strip by strip for both the hemispheres and for both the catcher foils employed, in Table 5.6. The systematic errors are computed as the root sum square of the different contributions computed up to now (implantation point, catcher thickness and cut on the coincident β-particle energy).

	Strip n.				
	1	**2**	**3**	**4**	**5**
UP - A	$1.006(74)_{stat}(29)_{syst}$	$1.023(106)_{stat}(39)_{syst}$	$0.994(146)_{stat}(28)_{syst}$	$1.008(139)_{stat}(31)_{syst}$	$0.998(171)_{stat}(46)_{syst}$
UP - M	$0.991(59)_{stat}(28)_{syst}$	$0.994(66)_{stat}(16)_{syst}$	$1.008(102)_{stat}(9)_{syst}$	$1.022(184)_{stat}(69)_{syst}$	$1.049(165)_{stat}(71)_{syst}$
DW - A	$0.994(52)_{stat}(16)_{syst}$	$1.011(53)_{stat}(12)_{syst}$	$1.007(62)_{stat}(11)_{syst}$	$1.003(70)_{stat}(14)_{syst}$	$0.985(129)_{stat}(22)_{syst}$
DW - M	$1.008(61)_{stat}(10)_{syst}$	$0.990(47)_{stat}(19)_{syst}$	$1.018(53)_{stat}(11)_{syst}$	$0.989(63)_{stat}(32)_{syst}$	$1.004(67)_{stat}(25)_{syst}$

Table 5.6: Summary of the $\tilde{a}_{\beta\nu}$ coefficients for the pure Fermi transition of ^{32}Ar, together with their statistical and systematic uncertainties, strip by strip for both hemispheres (upper and lower, *i.e* 'UP' and 'DW') and both the catcher foils employed (aluminized Mylar and Mylar, *i.e.* 'A' and 'M').

An example of the plots from which the values reported in Table 5.6 have been retrieved is shown in Fig. 5.6 and in Fig. 5.7, for the aluminized and the Mylar catcher foil respectively. In particular, the plots show, strip by strip and for each catcher foil employed, the linear fit on the three couples of points retrieved from the numerical simulations; each couple of point contains, respectively, the information on the $a_{\beta\nu}$ coefficients previously injected into CRADLE++ for the decay event generation and the corresponding mean energy shifts obtained via Geant4 simulations of the decay in the WISArD experimental set-up; the three scenarios correspond to physics purely BSM ($a_{\beta\nu} = -1$), to an intermediate case ($a_{\beta\nu} = 0$) and to the pure SM prediction ($a_{\beta\nu} = 1$). On the top of that, the experimental value is also represented, along with its statistical error bar; by projecting these values on the linear fitting curve, it is therefore possible to extract both the $\tilde{a}_{\beta\nu}$ coefficient and its statistical uncertainty. A similar procedure can be performed by replacing the statistical error bars with the corresponding systematic ones, in order to get the systematic uncertainty on $\tilde{a}_{\beta\nu}$.

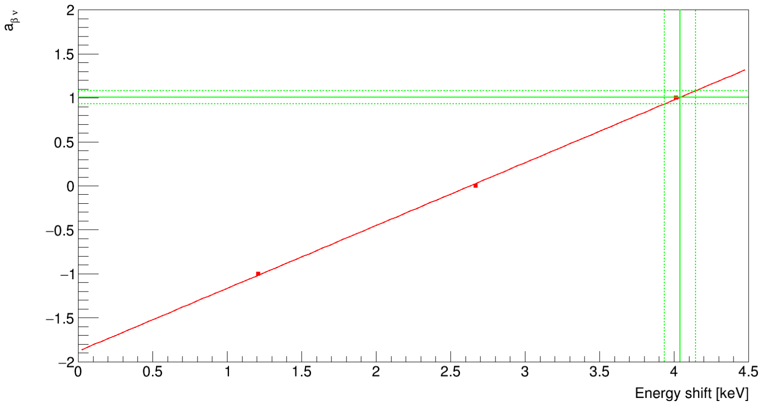

Figure 5.6: Simulated energy shifts (red square) related to the IAS proton peak distribution as a function of different values of the $\tilde{a}_{\beta\nu}$ coefficient for Strip 1 in the upper hemisphere and in case of employment of the aluminized catcher foil, along with the corresponding linear fitting function (red line). The vertical and the horizontal solid lines represent the experimental energy shift and the obtained value for $\tilde{a}_{\beta\nu}$, whereas the associated dashed lines indicate their statistical uncertainties. Similar plots have been realized for the systematic uncertainties.

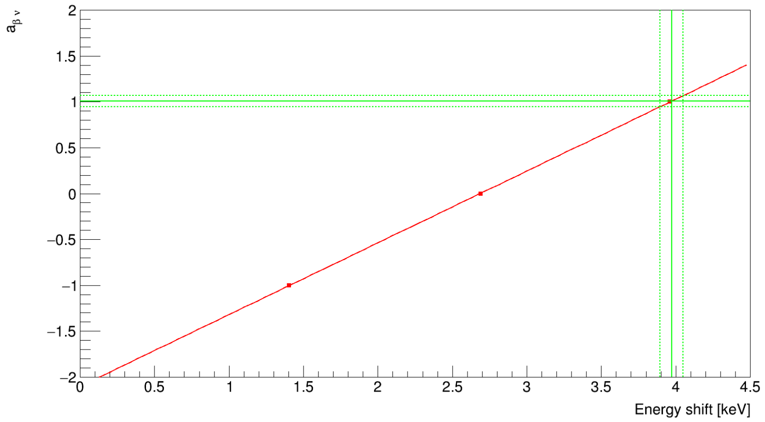

Figure 5.7: Simulated energy shifts (red square) related to the IAS proton peak distribution as a function of different values of the $\tilde{a}_{\beta\nu}$ coefficient for Strip 1 in the lower hemisphere and in case of employment of the Mylar catcher foil, along with the corresponding linear fitting function (red line). The vertical and the horizontal solid lines represent the experimental energy shift and the obtained value for $\tilde{a}_{\beta\nu}$, whereas the associated dashed lines indicate their statistical uncertainties. Similar plots have been realized for the systematic uncertainties.

Looking at the preliminary values reported in Table 5.6, it appears that all of them, as attended, are compatible uniquely within the prediction from the Standard Model.

The final value obtained for the $\tilde{a}_{\beta\nu}$ coefficient for pure Fermi transitions is equal to 1.002 ± 0.017 (stat.). The computation of the global systematic uncertainty will indeed require additional work which will be performed in the following months; in particular, further systematic effects on the determination of the beta-neutrino angular coefficient and associated to the silicon detector calibration of the experimental spectra, as well as to the positron backscattering on both the catcher foil and on the plastic scintillator will be estimated. Furthermore, a precise determination of the real thickness of both the catcher foils employed during the experimental campaign in 2021 is currently foreseen between Winter 2022 and Summer 2023; to this extent, differential measurements will be taken with the WISArD detection apparatus by means of a α-radioactive source, which will be placed, firstly, on the top and, afterwards, underneath the catcher foils. The real thickness of the foils will then be determined by subtracting the mean energy positions of the α-peaks recorded in both cases by the silicon detectors and by retrieving, consequently, the thickness of material associated to the energy lost inside it.

In a similar way, the values related to the $\tilde{a}_{\beta\nu}$ coefficient for pure Gamow-Teller transitions will be extracted from the analysis on the two most intense Gamow-Teller peaks from ^{32}Ar, located at 2121.7(31) and at 2421.8(29) keV, respectively [119].

5.4 Outlooks and perspectives

A proposal for an additional experimental campaign on ^{32}Ar has been submitted and accepted at the INTC (ISOLDE and Neutron Time-of-flight Committee) in February 2022. In particular, the run performed in Autumn 2021, consisting of about ten shifts, allowed to test the completely newly designed mechanical setup, the new particle detectors (both the silicon and the assembly of the plastic scintillator and the SiPMs matrix), as well as the new data acquisition and the control system. Further studies related to the systematic uncertainty contributions to the final measurements and improvement for their reduction are currently under investigation. So far, ten additional shifts have been requested for Summer 2023, in order to dispose again of seven days of full beamtime and complete the related data taking. In this case, the final precision level on the determination of the $\tilde{a}_{\beta\nu}$ coefficient could realistically reach a level below 0.4% (comprehending both the statistical and the overall systematic uncertainty)[2], with the final aim of a precision of 0.1-0.2%, as anticipated in the original proposal, for a longer experimental campaign.

---

[2] By disposing of a longer acquisition time with ^{32}Ar ($\simeq \times 1.5$), a better ion production and transport ($\simeq \times 3$), a better energy resolution ($\simeq \times 2$) and the totality of the silicon detectors working ($\simeq \times 1.5$), the statistics is expected to increase of a factor of roughly 2.5. In the meanwhile, a complete characterization of the systematic errors will be performed.

In the meanwhile, further measurements aiming to precisely characterize the systematic uncertainties will be accomplished. To this extent, in the following, the precise low-energy characterization of the scintillator employed during the experimental campaign last year and additional measurements about the beam implantation profile by means of a dedicated MCP assembly will be discussed. Finally, a further improvement of the mechanical support of the detection set-up, aiming to guarantee a better contact between the detector preamplifiers and the glycol cooling pipes and so a better stability in the detector response function over time, will be illustrated. In parallel, further simulations will be performed by manually changing the value of the b coefficient to non-zero values within the numerical simulations, in order to explore a pure left-handed lepton scenario and determine the sensitivity to the Fierz term achievable with the WISArD experimental set-up.

5.4.1 Low-energy characterization of the scintillator

A low-intensity electron gun has been developed at LPC Caen in order to characterize the response function of the positron detector in the low-energy part of the β-spectrum recorded with the scintillator employed during the 2021 experimental campaign, *i.e.* in the [0, 30] keV energy range. These measurements will likely allow to lower the positron energy threshold below 10 keV and, concomitantly, precisely measure its response function close to the β-detection threshold. Moreover, the systematic error on $\tilde{a}_{\beta\nu}$ directly associated to the β-detection threshold will be reduced down to 0.7×10^{-3}, as a consequence of lowering the thresholds on the individual SiPM cells, registering only signals acquired with at least two cells firing at the same time and a better contact between the β-detector and the cooling system pipes. Lowering the threshold below 10 keV would also permit to reduce the contribution of positron backscattering on the detector down to 0.9×10^{-3}.

5.4.1.1 Experimental set-up

A ^{241}Am radioactive source (A_{tot} = 40 kBq) is placed inside on the bottom side of an aluminum chamber. The α-particles and the ions sputtered from the surface of the source are emitted isotropically. Among all the particles emitted, a certain part results directed towards an aluminum anode, polarized up to -30 kV. Subsequently, after hitting the anode, secondary electrons are emitted out of the anode and then immediately accelerated towards a stainless-steel plate, kept at ground potential, due the strong electric potential difference. After passing through a collimator, the electrons finally reach the scintillator, inside which they deposit their energy. A schematic view of the experimental set-up is reported in Fig. 5.8. Different measurements have been performed so far at 10, 15, 20, 25 and 30 keV, respectively. In particular, it can be underlined that, by means of this device, the energy of the electrons coming out of the anode can be precisely tuned by adjusting the value set on the anode voltage, so that the resulting electron beam directed towards the scintillator will be at any time mono-energetic[3]. Moreover, the electric field is shaped in such a way that only the electrons originally emitted from the central region of the anode are capable of passing through the collimator. At this stage, the cumulative contribution of the *bremsstrahlung* emission and of the diffusion on the collimator, as it can be estimated via the associated Geant4 simulations, is at around 0.1‰; furthermore, even the tail due to the electron backscattering on the scintillator is practically negligible at these low energies.

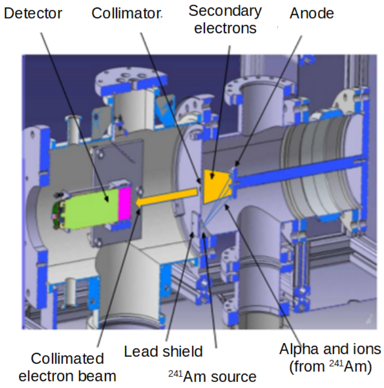

Figure 5.8: Sectional view of the low-intensity electron gun developed at LPC Caen for the low-energy characterization of the scintillator employed during the 2021 experimental campaign.

5.4.1.2 Partial results

The QDC and time-of-flight spectra acquired by a system composed by the EJ204 scintillator employed during the experimental campaign at WISArD in 2021 and a photomultiplier tube from the ET enterprise [146] have been recorded by means of the FASTER acquisition system. In the QDC spectra, as shown in Fig. 5.9 and as expected for the secondary electron production by ion impact on a metal surface, multiple peaks appear beyond the pedestal, progressively less resolved, followed by a continuum. In particular, these peaks correspond to the detection of one, two and three secondary electrons respectively, each of them characterized by an energy of 30 keV.

By subtracting the background, acquired as a unique component in a run without any voltage applied on the anode, is therefore possible to fit the electron spectrum by a convolution of different Gaussian functions in order to reproduce the three visible peaks. By correlating the mean values (in QDC CH) of the peaks to the corresponding energies (in keV), it will be

---

[3] The beam energy dispersion is expected to be very low (in the eV range).

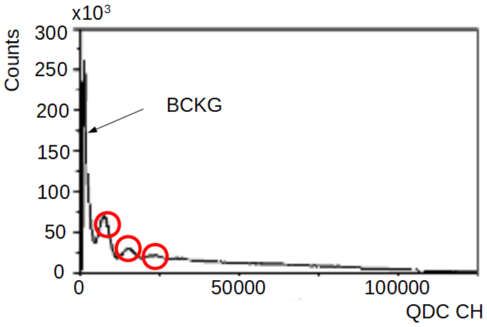

Figure 5.9: QDC spectrum related to the β-spectrum acquired by the plastic scintillator. Beyond the background, three peaks, indicated by the red circles and progressively less resolved, are clearly visible. These peaks correspond to the detection of one, two and three secondary electrons respectively, each of them at an energy of 30 keV.

possible to characterize precisely the low-energy response function of the scintillator, ideally down to 10 keV. Further measurements are still ongoing.

5.4.2 Beam implantation monitoring

The results obtained from the analysis of the data taken in the proof-of-principle experiment have highlighted that, in order to reach the permil precision level on the determination of $\tilde{a}$, the beam implantation profile has to be determined with a spatial precision better than 0.5 mm [111]. For this purpose, a dedicated compact microchannel plate (MCP) position-sensitive detector has been designed at LPC Caen. This custom-made detector, whose assembly is shown in Fig. 5.10(a), globally consists of a 10 mm thick and 25 mm wide detector with an active detection diameter of 15 mm and, for achieving a higher gain, it is indeed composed by three MCPs mounted vertically one on the top of the other (Z-stack configuration) and followed by a square resistive anode made of graphite paint. On the WISArD experiment, the MCP assembly has been mounted on the rotatable rod opposite to the one holding the catcher foil, in such a way that its front face was always perpendicular to the direction of the incoming beam. The rod can be controlled from outside the magnet so that the MCPs, mounted just a few mm below the catcher, can be inserted to measure the beam spatial profile directly at the implantation point.
The detection principle is such that, after the impact of an incoming ion, the electron avalanche emitted by the back MCP is collected by the resistive anode, which then provides information on the impact position through the measurement of the charge shared between its four corners. Moreover, a 0.5 mm thick stainless steal calibration mask composed of 1.2×1.2 mm^2 square holes with a pitch of 2 mm is permanently mounted in front of the MCPs to provide high accuracy in terms of position calibration. In Fig. 5.10(b), the distribution of the charge

ratios R_X and R_Y obtained when irradiating the detector with α-particles emitted by a ^{241}Am source located 80 mm away from the mask is shown. In particular, the R_X (R_Y) coordinates are here directly inferred from the difference between the charges collected on the right (up) corners and the left (down) corners, divided by the sum of charges. However, the distortions due to the square shape of the anode and to inhomogeneities in the graphite paint thickness require the use of an additional numerical treatment. Polynomial functions depending on R_X and R_Y are thus used to reconstruct a realistic position in X and Y matching the mask dimensions. In Fig. 5.10(c), an example of such a reconstruction obtained with fifth-degree polynomial functions, resulting from a multi-dimensional fit of the mask image, is visible.
A detailed analysis of the reconstructed image has demonstrated that, for the central part of the detector (within a 8 mm diameter circle), the spatial resolution (FWHM) in X and Y is better than 0.25 mm and the related accuracy better than 0.1 mm. These results fulfill the needs for beam monitoring, but additional tests will need to be performed on site. Effectively, it is known that the MCPs are slightly sensitive to a strong magnetic field, as the trajectories of the avalanche electrons inside the micro-channels are deviated by the field itself. In particular, strong magnetic fields directed along with the channel axis, as in case of the one employed in the WISArD experiment, can decrease the overall gain of the MCPs.
These calibrations will thus have to be completed directly at ISOLDE, within the WISArD magnet bore and by ramping up the magnetic field to 4 T, corresponding to the intensity used during the data taking in October 2021. A thin 10% transmission mesh will also be inserted right behind the calibration mask in order to both attenuate the ion beam intensity before hitting the front MCP and serve as a Faraday cup for beam current measurement.

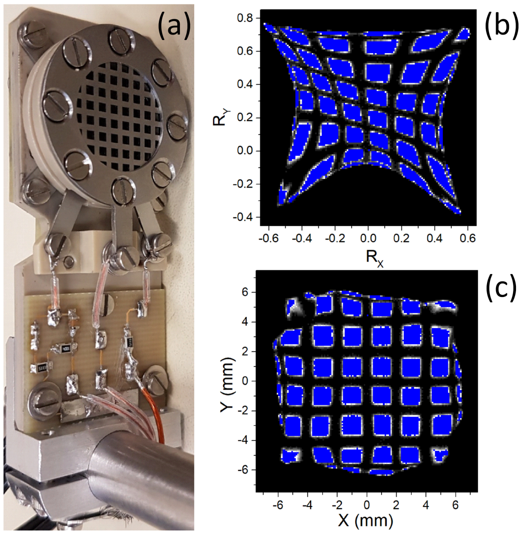

Figure 5.10: Picture of the MCP detector assembly (a), mask image reconstruction using charge-sharing ratios (b) and after an additional numerical treatment (c).

5.4.3 Further improvement of the mechanical support

In order to both reduce the statistics and systematic uncertainties on the final measurement, a new mechanical support holding the detection set-up has been designed and manufactured. An global view of the novel end-part structure to be inserted in the magnet bore is shown in Fig. 5.11.

In this way, the incoming ^{32}Ar beam is directed through a collimator (possible radius of 2, 5 and 10 mm) before being implanted inside the catcher foil. The beam profile can be monitored via the dedicated MCP detector, described in Sec. 5.4.2, and further calibration measurements are still possible by mounting a radioactive source into the adjacent hole of the two-arm aluminum support. The silicon detectors can be mounted again onto two pyramid-like structures; the assembling procedure is now made easier and the pyramids can be adjusted at roughly half the actual distance, in order to be closer one to each other and thus improve the proton detection solid angle and so the overall statistics collected. The silicon detectors and the preamplifiers (for both the SiPM and the silicon detectors) are now tightly fixed on the newly designed low-end part of the WISArD tower, improving the contact with the cooling system pipes; a better heat exchange and reduction in the energy resolution is then attended for both the β-particle and the proton detectors.

Moreover, a new catcher foil, characterized by a very limited thickness, reduced roughly of a factor of ten with respect to the one used in 2021, will be employed. In this way, the systematic effects associated to the β-backscattering inside the catcher foil will be almost directly and linearly reduced and, at the same time, the resolution on the proton energy shifts for the upper silicon detectors will consequently increase.

Further tests of the overall mechanical assembly and of all the detectors are currently scheduled for December 2022, whilst an additional experimental campaign with the ^{32}Ar beam is foreseen for Summer 2023.

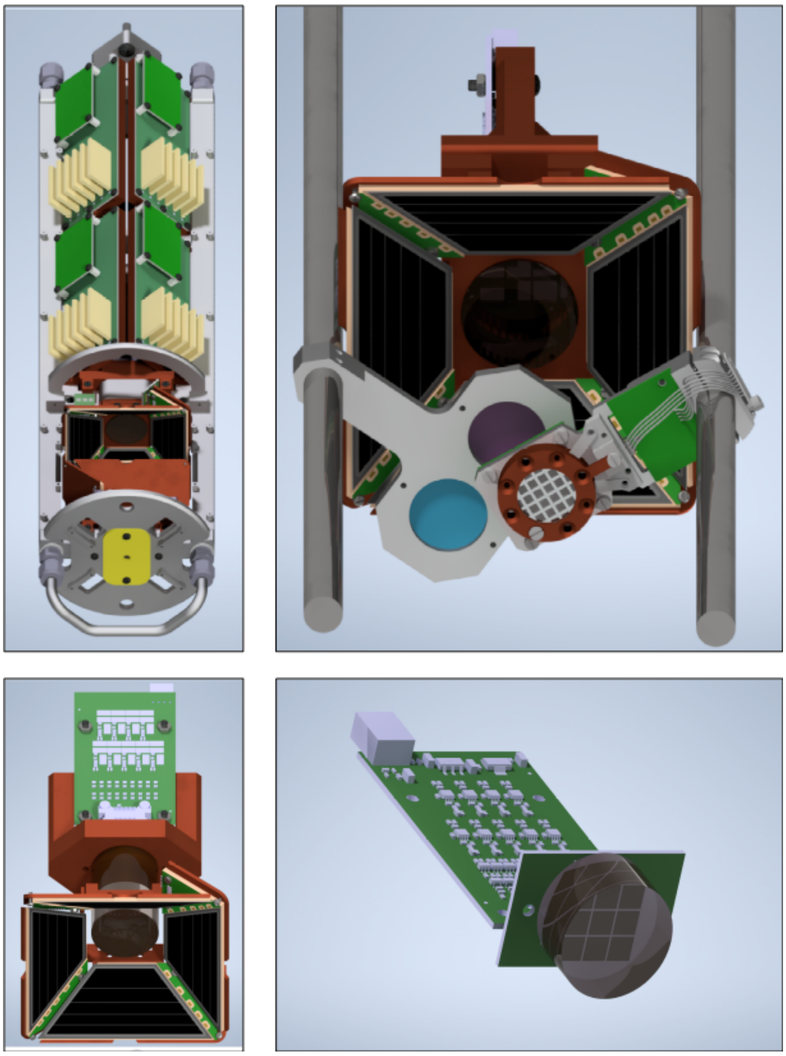

Figure 5.11: CAD drawing of the newly designed end-part mechanical structure on which the detection set-up is assembled (top left), with a zoom in its central part (top right). The incoming beam, after traversing a collimator (dark yellow), is implanted inside the catcher foil (magenta), where the decay takes place; the beam implantation profile can be monitored via a dedicated MCP detector and calibration measurements can be performed with sources placed in the adjacent hole (cyan) on the two-arm aluminum support. The silicon detectors (black) are yet tightly assembled onto two copper pyramid-like structures (brown), which can be now moved closer one to each other to enhance the solid angle coverage. The contact of the preamplifier boards (green) and the pyramids to the lateral cooling system pipes (grey) is also improved. On the bottom, the assembling of the plastic scintillator (transparent) and the SiPM preamplifier board (green) on the upper truncated pyramid-like structure is shown (bottom left); the β-detection set-up is visible (bottom right), along with its SiPMs 3×3 cell matrix (black). Connecting cables from the preamplifiers to the detectors are not shown for graphics purpose.

Chapter 6

Conclusions

The Standard Model of particle physics has represented for more than half a century a remarkably successful theory in describing elementary particles and their interactions, withstanding decades of precision tests at both the low-energy scale, notably via nuclear β-decay, and at the high-energy scenario, with particle collisions at particle accelerators.
In recent years, a significant effort has been put on the realization of low-energy physics experiments, which demonstrated to be a powerful tool to precisely test discrete symmetries and search for the possible existence of exotic interactions not included in the original formulation of the V-A theory, describing the electroweak interaction within the Standard Model. Particularly, the experimental determination of the $\tilde{a}_{\beta\nu}$ coefficient, function of both the β-neutrino angular coefficient ($a_{\beta\nu}$) and the Fierz term (b) for both Fermi and Gamow-Teller transitions directly allows to set new limits on the existence of the scalar and the tensor contributions to the weak interaction, respectively.
In this framework, after the realization of a successful proof-of-principle experiment in 2018 (already leading to the third best measurement of $\tilde{a}_{\beta\nu}$ for Fermi transitions), a further experimental campaign with ^{32}Ar has been performed at the WISArD experiment, permanently installed at ISOLDE/CERN, in October 2021. In the previous chapters, the data taking conditions and the experimental detection set-up have been described. Furthermore, the related data analysis and the associated Geant4 simulations have been illustrated and the comparison between the experimental and the simulated proton single and β-coincident spectra for the most intense Fermi transition has been presented. The final value extracted for the $\tilde{a}_{\beta\nu}$ coefficient for Fermi transition (1.002 ± 0.017 (stat.)) is in agreement with the Standard Model prediction, thus confirming the vector contribution as the dominant one in the description of Fermi interaction. In the end, in spite of the very limited acquisition time and degraded detection conditions (problems at the level of ion production and transport to the implantation point for most of the beamtime, a certain number of detectors showing bad

energy resolution or even not working and employment of a thick Mylar catcher), this measure still represents a reduction of a factor of roughly 1.8 in terms of the statistical uncertainty with respect to the previous proof-of-principle experiment [111]. A complete study on the systematic uncertainty is currently ongoing and will be accomplished in the following months; in particular, the systematic uncertainties associated to the calibration of the proton spectra will be estimated, as well as the ones associated to positron backscattering on the scintillator and on the thickness of both the catcher foils employed during the experimental campaign. An additional experimental campaign on ^{32}Ar, consisting in a week of beamtime, has already been accepted by the INTC (ISOLDE and Neutron Time-of-flight Committee) in February 2022. In particular, the run performed in Autumn 2021, consisting of about ten shifts, allowed to test the completely newly designed mechanical setup, the new particle detectors (both the silicon and the assembly of the plastic scintillator and the SiPMs matrix), as well as the new data acquisition and the control system. The data taking will be then completed in Summer 2023, after a precise characterization of the systematic uncertainties. In this case, the final precision level on the determination of the $\tilde{a}_{\beta\nu}$ coefficient will realistically reach a value below 0.4%, whereas a further extensive experimental campaign will permit finally to achieve the precision level of the order of 0.1-0.2%, as anticipated in the original proposal.

Appendix A

Complements to the theory of electroweak interaction

A.1 β-decay transitions and selection rules

In β-decay, the angular momentum conservation requires that:

$$\vec{J_P} = \vec{J_D} + \vec{L} + \vec{S} \tag{A.1}$$

where $\vec{J_P}$ and $\vec{J_D}$ are the spin vectors associated to the parent and daughter nuclei respectively, $\vec{L}$ (= $\vec{L_e}$ + $\vec{L_\nu}$) is the orbital angular momentum and $\vec{S}$ (= $\vec{S_e}$ + $\vec{S_\nu}$) is the spin associated to the leptons emitted in the decay. In the semiclassical approximation, the lepton orbital angular momentum is given by:

$$L = \hbar \sqrt{\ell(\ell + 1)} = pb \leq pR \tag{A.2}$$

where b is the transverse impact parameter and R the nuclear radius. Consequently:

$$\sqrt{\ell(\ell + 1)} \leq \frac{p_e R}{\hbar} \approx 10^{-2} << 1 \Rightarrow \ell = 0 \tag{A.3}$$

since p_e is at most on the order of few $\frac{MeV}{c}$ and R is on the order of some fm.
Therefore, β-decays related to $\ell = 0$ have been historically called *allowed*, while those characterized by $\ell > 0$ have been named *forbidden*, even if they are only probabilistically unfavoured. Effectively, both electron and neutrino can be seen as free particles after being created during the weak interaction process and, so, the associated wavefunctions can be approximated via a Taylor-series expansion in terms of the quantum number ℓ:

$$\psi_{e,\nu}(\vec{r}) \;=\; \frac{1}{\sqrt{V}}\, e^{\frac{i}{\hbar}\vec{p}\cdot\vec{r}} \;\approx\; \frac{1}{\sqrt{V}}\left[1 + \frac{i}{\hbar}\vec{p}\cdot\vec{r} + o((\frac{\vec{p}\cdot\vec{r}}{\hbar})^n)\right] \tag{A.4}$$

where the product $\frac{pr}{\hbar}$ is of the order of 10^{-2}, so that the terms in the Taylor series become progressively smaller. Moreover, the value of ft depends quadratically on the module of the nuclear matrix element M_{if}, so that each unit of ℓ directly brings a factor of suppression in the decay rate on the order of $10^{-3} \div 10^{-4}$.

Moreover, considering Eq. A.4, it consequently follows that for allowed transitions ($\ell = 0$) the parity of the nucleus should be immutated. Indeed, the nuclear matrix element at first order would become zero if the parity of the nucleus changes:

$$M_{if}^{\ell=0} \;=\; \int \psi_D^*(\vec{r})\,\psi_P(\vec{r})\,d\vec{r} \;=\; 0 \qquad if \quad \Pi_f \neq \Pi_i \tag{A.5}$$

Transitions with nuclear parity change should then be described by the higher-order terms in the Taylor series, corresponding to the *forbidden* transitions:

$$M_{if}^{\ell>0} = \frac{i}{\hbar}\int \psi_D^*(\vec{r})\,(\vec{p}\cdot\vec{r})\,\psi_P(\vec{r})\,d\vec{r} \;-\; \frac{1}{2\,\hbar^2}\int \psi_D^*(\vec{r})\,(\vec{p}\cdot\vec{r})^2\,\psi_P(\vec{r})\,d\vec{r} \;+\;\cdots \tag{A.6}$$

A summary resuming the β-decay selections rules is shown in Table A.1.

Decay type	ΔJ	ΔI	$\Delta\pi$	$\log_{10}\mathcal{F}t$
Superallowed	$0^+ \longrightarrow 0^+$	0	no	3.1 - 3.6
Allowed	0, 1	0, 1	no	2.9 - 10.0
First forbidden	0, 1, 2	0, 1	yes	5- 19
Second forbidden	1, 2, 3	0, 1	no	10- 18
Third forbidden	2, 3, 4	0, 1	yes	17- 22
Fourth forbidden	3, 4, 5	0, 1	no	22 - 24

Table A.1: Summary of the β-decay selection rules.

A.2 Coupling constants in the $V-A$ theory

Nuclear β-decay indeed represents a powerful tool complementary to high-energy particle collision experiments in the search for physics beyond the Standard Model. In theory, the bridgehead between the two worlds is represented by the Effective Field Theory (EFT), which permits to relate the low-energy hadronic description of the β-decay Hamiltonian to the high-energy quark-level Lagrangian. In particular, calculations show that the ten different coupling constants C_i and $C_i^{'}$ (reported in Eq. 1.38) can be expressed as directly proportional to the Wilson coefficients $\varepsilon_{\mathcal{X}}$ and $\tilde{\varepsilon}_{\mathcal{X}}$ (outlined in Eq. 1.47) via $g_{\mathcal{X}}$ constants ($\mathcal{X}$ = V, A, S, T, P) that have to be determined from lattice field theory or other theoretical models.

Specifically, by separating the left-handed (via $C^{+}_{\mathcal{X}}$) and the right-handed (via $C^{-}_{\mathcal{X}}$) neutrino coupling constants and by subsequently rewriting $C_{\mathcal{X}} \equiv \frac{C^{+}_{\mathcal{X}}+C^{-}_{\mathcal{X}}}{2}$ and $C^{'}_{\mathcal{X}} \equiv \frac{C^{+}_{\mathcal{X}}-C^{-}_{\mathcal{X}}}{2}$, one has:

$$\begin{aligned}
C^{+}_{V} &= +\frac{V_{ud}}{v^2}\, g_V\, \sqrt{1+\Delta^{V}_{R}}\,(1+\varepsilon_L+\varepsilon_R) & C^{-}_{V} &= +\frac{V_{ud}}{v^2}\, g_V\, \sqrt{1+\Delta^{V}_{R}}\,(\tilde{\varepsilon}_L+\tilde{\varepsilon}_R)\\
C^{+}_{A} &= -\frac{V_{ud}}{v^2}\, g_A\, \sqrt{1+\Delta^{A}_{R}}\,(1+\varepsilon_L-\varepsilon_R) & C^{-}_{A} &= +\frac{V_{ud}}{v^2}\, g_A\, \sqrt{1+\Delta^{A}_{R}}\,(\tilde{\varepsilon}_L-\tilde{\varepsilon}_R)\\
C^{+}_{S} &= +\frac{V_{ud}}{v^2}\, g_S\, \varepsilon_S & C^{-}_{S} &= +\frac{V_{ud}}{v^2}\, g_S\, \tilde{\varepsilon}_S\\
C^{+}_{T} &= +\frac{V_{ud}}{v^2}\, g_T\, \varepsilon_T & C^{-}_{T} &= +\frac{V_{ud}}{v^2}\, g_T\, \tilde{\varepsilon}_T\\
C^{+}_{P} &= +\frac{V_{ud}}{v^2}\, g_P\, \varepsilon_P & C^{-}_{P} &= +\frac{V_{ud}}{v^2}\, g_P\, \tilde{\varepsilon}_P
\end{aligned} \tag{A.7}$$

where V_{ud} is the first CKM matrix element, $v = \sqrt{\frac{1}{\sqrt{2}G_F}} \sim 246.22$ GeV, $\Delta^{V,A}_{R}$ are the short-distance radiative corrections and $g_V = 1$ (universal according to the CVC hypothesis, verified apart from negligible quadratic corrections coming from isospin-symmetry breaking), $g_A = 1.251(33)$, $g_S = 1.022(100)$, $g_T = 0.989(33)$ and $g_P = 349(9)$ [147]. Normally, the pseudoscalar contribution has always been neglected in nuclear β-decay as the semileptonic pion decay $\pi \longrightarrow e\nu$ offers higher order of magnitudes of sensitivity in setting limits to this exotic contribution [49] and no contribution from its part has been found up to date.

A.3 Angular correlation coefficients in nuclear β-decay

The angular correlation coefficients reported in Eq. 1.39 do have the following extensive expressions:

- $\alpha_{\beta\nu}$, **angular correlation coefficient**:

$$\begin{aligned}
a_{\beta\nu}\xi &= |\mathcal{M}_F|^2 \left[-|C_S|^2 + |C_V|^2 - |C^{'}_S|^2 + |C^{'}_V|^2 \mp 2\,\frac{\alpha Z m}{p_e}\, Im\left(C_S\, C^{*}_V + C^{'}_S\, C^{'*}_V\right)\right]\\
&+ \frac{|\mathcal{M}_{GT}|^2}{3} \left[|C_T|^2 - |C_A|^2 + |C^{'}_T|^2 - |C^{'}_A|^2 \pm 2\,\frac{\alpha Z m}{p_e}\, Im\left(C_T\, C^{*}_A + C^{'}_T\, C^{'*}_A\right)\right]
\end{aligned} \tag{A.8}$$

- b, **Fierz term:**

$$b\xi \;=\; \pm 2\Gamma Re\left[|\mathcal{M}_F|^2\left(C_S\,C_V^{*} + C_S^{'}\,C_V^{'*}\right) \;+\; |\mathcal{M}_{GT}|^2\left(C_T\,C_A^{*} + C_T^{'}C_A^{'*}\right)\right] \tag{A.9}$$

- A, **β-asymmetry parameter:**

$$\begin{aligned}
A\xi \;=\;& |M_{GT}|^2\,\lambda_{I'I}\left[\pm 2\,Re(C_T\,C_T^{'*} - C_A\,C_A^{'*}) + 2\,\frac{\alpha Z m_e}{p_e}\,Im(C_T\,C_A^{'*} + C_T^{'}\,C_A^{*})\right]\\
&+\delta_{I'I}\,M_F\,M_{GT}\,\sqrt{\frac{I}{I+1}}\;\times\;\left[2\,Re(C_S\,C_T^{'*} + C_S^{'}\,C_T^{*} - C_V\,C_A^{'*} - C_V^{'}\,C_A^{*})\right.\\
&\pm 2\,\frac{\alpha Z m_e}{p_e}\,Im(C_S\,C_A^{'*} + C_S^{'}\,C_A^{*} - C_V\,C_T^{'*} - C_V^{'}\,C_T^{*})
\end{aligned} \tag{A.10}$$

- B, **ν-asymmetry parameter:**

$$\begin{aligned}
B\xi \;=\;& 2\,Re\left\{|M_{GT}|^2\,\lambda_{I'I}\;\times\;\left[\frac{\Gamma m_e}{E_e}\,(C_T\,C_A^{'*} + C_T^{'}\,C_A^{*}) \pm (C_T\,C_T^{'*} + C_A\,C_A^{'*})\right]\right.\\
&-\delta_{I'I}\,M_F\,M_{GT}\,\sqrt{\frac{I}{I+1}}\;\times\;\left[(C_S\,C_T^{'*} + C_S^{'}C_T^{*} + C_V\,C_A^{'*} + C_V^{'}\,C_A^{*})\right.\\
&\left.\left.\pm\,\frac{\Gamma m_e}{p_e}\,(C_S\,C_A^{'*} + C_S^{'}\,C_A^{*} + C_V\,C_T^{'*} + C_V^{'}\,C_T^{*})\right]\right\}
\end{aligned} \tag{A.11}$$

- D, **D-triple coefficient:**

$$\begin{aligned}
D\xi \;=\;& \delta_{I'I}\,M_F\,M_{GT}\sqrt{\frac{I}{I+1}}\,\left[2\,Im(C_S\,C_T^{*} - C_V\,C_A^{*} + C_S^{'}\,C_T^{'*} - C_V^{'}\,C_A^{'*})\right.\\
&\left.\mp 2\,\frac{\alpha Z m_e}{p_e}\,Re(C_S\,C_A^{*} - C_V\,C_T^{*} + C_S^{'}\,C_A^{'*} - C_V^{'}\,C_T^{'*})\right]
\end{aligned} \tag{A.12}$$

- G, **longitudinal β-polarization:**

$$\begin{aligned}
G\xi \;=\;& |M_F|^2\,\left[\pm 2\,Re(C_S\,C_S^{'*} - C_V\,C_V^{'*}) \;+\; 2\,\frac{\alpha Z m_e}{p_e}\,Im(C_S\,C_V^{'*} + C_S^{'}\,C_V^{*})\right]\\
&+|M_{GT}|^2\,\left[\pm 2\,Re(C_T\,C_T^{'*} - C_A\,C_A^{'*}) \;+\; 2\,\frac{\alpha Z m_e}{p_e}\,Im(C_T\,C_A^{'*} + C_T^{'}\,C_A^{*})\right]
\end{aligned} \tag{A.13}$$

- ***R*, *R*-triple coefficient:**

$$\begin{aligned} R\xi \;=\; & |M_{GT}|^2\, \lambda_{I^{'}I} \left[\pm\, 2\, Im(C_T\, C_A^{'*} \,+\, C_T^{'}\, C_A^{*}) \,-\, 2\, \frac{\alpha Z m_e}{p_e}\, Re(C_T\, C_T^{'*} \,-\, C_A\, C_A^{'*}) \right] \\ & +\, \delta_{I^{'}I}\, M_F\, M_{GT}\, \sqrt{\frac{I}{I+1}} \,\times\, \left[2\, Im(C_S\, C_A^{'*} \,+\, C_S^{'}\, C_A^{*} \,-\, C_V\, C_T^{'*} \,-\, C_V^{'}\, C_T^{*}) \right. \\ & \left. \mp\, 2\, \frac{\alpha Z m_e}{p_e}\, Re(C_S\, C_T^{'*} \,+\, C_S^{'}\, C_T^{*} \,-\, C_V\, C_A^{'*} \,-\, C_V^{'}\, C_A^{*}) \right] \end{aligned} \tag{A.14}$$

where the ξ and Γ coefficients are equal to:

$$\begin{cases} \xi \;=\; & |\mathcal{M}_F|^2 \;\left(|C_S|^2 + |C_V|^2 + |C_S^{'}|^2 + |C_V^{'}|^2 \right) \\ & +\, |\mathcal{M}_{GT}|^2 \left(|C_T|^2 + |C_A|^2 + |C_T^{'}|^2 + |C_A^{'}|^2 \right) \\ \Gamma & =\, \sqrt{1 - \alpha^2 Z^2} \end{cases}$$

where α is the fine structure constant and Z is the atomic number of the daughter nucleus. Moreover:

$$\lambda_{I^{'}I} = \begin{cases} 1, & \text{for } I \longrightarrow I^{'} = I \text{ - } 1 \\ \frac{1}{I+1}, & \text{for } I \longrightarrow I^{'} = I \\ -\frac{I}{I+1}, & \text{for } I \longrightarrow I^{'} = I + 1 \end{cases} \tag{A.15}$$

and $\delta_{I^{'}I}$ indicates the Kronecker delta symbol applied on I and $I^{'}$, which are the angular momenta of the original and final nuclei, respectively.

Appendix B

The WISArD beamline and its offline ion source

This Appendix is dedicated to the description of the WISArD beamline and of its offline stable ion source, permanently installed at the low-energy radioactive ion beam facility ISOLDE at CERN.

B.1 The WISArD beamline

As presented in Chapter 2, the WISArD experiment is located on an experimental platform nearly at the centre of the ISOLDE experimental hall at CERN. The ISOLDE (ISotope OnLine DEvice) facility [148, 125] receives protons at 1.4 GeV energy from the Proton Synchrotron Booster (PSB) [149, 150], coming in bunches with a time separation of 1.2 s and an average intensity up to 2 μA. Subsequently, these protons impinge on a thick (up to a few 100g/cm^2) target material, from which a mixture of radioactive elements is created via spallation, fission or fragmentation reaction processes [151]. The radioactive beam formed by the species of interest is then extracted by heating the target and by subsequently ionizing the nuclides in this mixture by surface ionization, laser ionization or electron impact in a plasma. Over the past decades, ISOLDE has pursued studies on different target-ion source combinations, allowing for production of radioisotopes from more than 60 different elements, ranging from $^{6}_{2}$He to $^{231}_{88}$Ra, with intensities up to 10^{11} atoms per μA proton beam [152]. Specifically, in the current experiment, the ^{32}Ar atoms diffuse out from the hot nano-CaO target ($\sim$ 750° C) [129] via a cooled Cu transfer line to the Versatile Discharge Ion Source (VADIS/VD7) [153], where the ion beam is produced. After the extraction and the mass separation operated by the General Purpose Separation (GPS), the beam is post-accelerated at 30 keV and sent to the Penning trap system of ISOLDE-REXTRAP [154] which finally, set into a continuous transmission operating mode, delivers the beam to the WISArD ion beam transport system.

The purpose of the WISArD beamline, comprehensive as well of a stable potassium ion source used for offline beam transmission studies, is uniquely to transport the ion beam from REXTRAP up to the implantation catcher foil, located together with the detection set-up inside the superconducting Oxford Instruments magnet. Up to this end, the beamline is divided into two sections, the horizontal beamline (HBL) and the vertical beamline (VBL). A schematic sectional drawing of the overall WISArD beamline is reported in Fig. B.1.

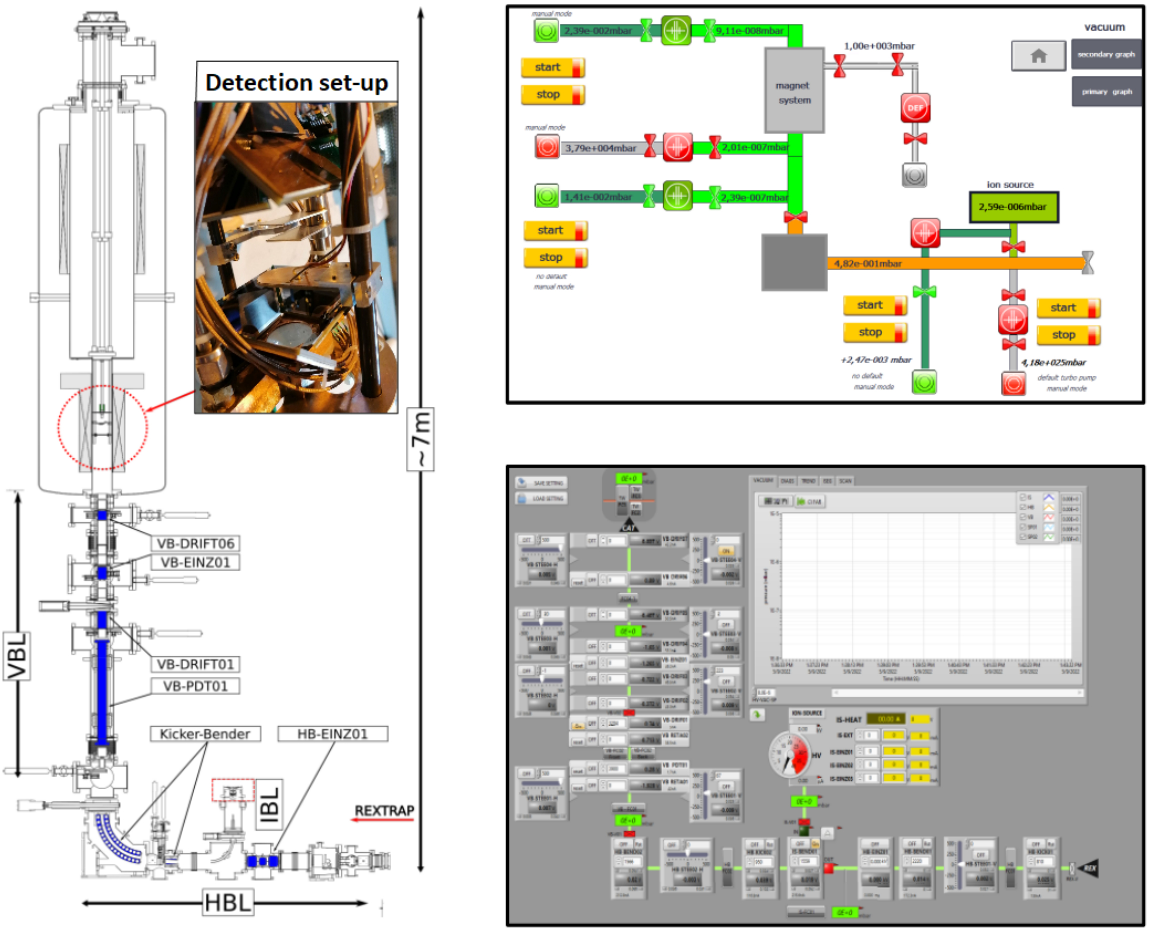

Figure B.1: Left: schematic sectional drawing of the WISArD ion beam transport horizontal (HBL) and vertical (VBL) beamline, ending in the superconducting magnet in which the detection set-up is installed. Top right: layout of the PLC touch panel permitting to visualize the vacuum system status over the beamline and inside the magnet. Bottom right: LabVIEW interface permitting to remotely apply and monitor the voltage power on the different electrostatic components of both the HBL and the VBL. Further details are reported in Sec. B.1.1 and B.1.2.

Overall, a SIMATIC touch panel connected to a Programmable Logic Controller (PLC) is employed to visualize the vacuum system status and remotely perform operations related to the vacuum system, *i.e.* starting/stopping primary scroll and turbo-molecular pumps and opening/closing the vacuum valves (UHVs) between different sectors. Additional safety procedures regarding the automatic closure of UHV valves in case of pressure not sustainable for a working regime of a turbo-molecular pump ($< 0.5 \cdot 10^{-3}$ mbar) are already implemented in the PLC logic. Furthermore, a tailor-made LabVIEW [155] interface is also implemented to remotely monitor and apply voltage power on the different electrostatic components of both the HBL and the VBL. The PLC layout of the vacuum system and the LabVIEW interface used to control the elements of the WISArD beamline are also shown in Fig. B.1.

B.1.1 Horizontal beamline

The HBL extends from the last REXTRAP outlet valve (UHV) to the second 90° bender of the WISArD experiment (HBBEND02 in Fig. B.2). This sector was designed to have a length sufficiently high to guarantee the transport of the ion beam just below the superconducting magnet, which is located at nearly 6 m with respect to REXTRAP, *i.e.* at the minimum spatial distance required in order to avoid possible interference to nearby experiments due to the high magnetic field used in the WISArD experiment (nominally 4 T, it can be set up to a maximum of 9 T). A schematic view of the HBL is reported in Fig. B.2.

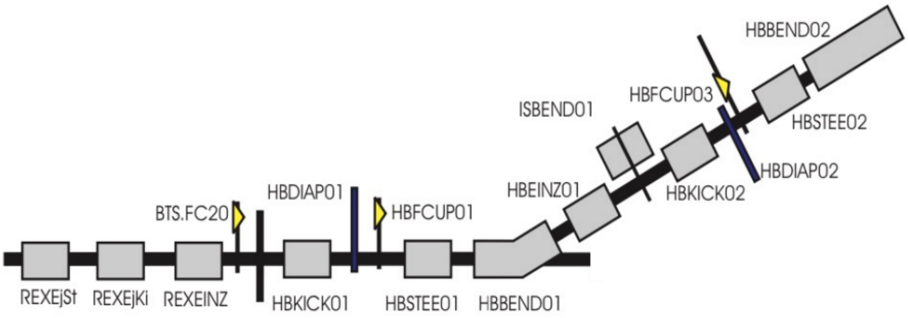

Figure B.2: Schematic view of the electrode layout in the horizontal beamline (HBL) used to assure the incoming ion beam transmission to the following vertical beamline sector. A list of the commonly used abbreviations in the labels related to the different WISArD beamline components is reported in Table B.1.

The horizontal beamline consists of various electrostatic components and diagnostic tools employed to adjust and maximize the ion beam transport to the following VBL sector. Specifically, the most delicate operation that permits to reach an optimal beam transmission through the whole HBL is represented by a fine tuning of two kicker-bender assemblies and a high-voltage Einzel lens.

The electrostatic kicker-assemblies (HBKICK01 and HBKICK02) consist in two parallel deflection plates each ($60 \times 60\ mm^2$, gap of 3 cm) tilted over an angle of 3.75° with respect to the beam axis, in order to slightly deflect the incoming ions towards the following bender electrodes.

The bender assemblies are composed each of two spherical electrodes (385 mm and 415 mm inner and outer radius, respectively), which permit to bend the trajectory of the incoming ion beam respectively by 29° (HBBEND01) and by 90°, in a radius of 400 mm (HBBEND02). The electrode HBBEND02 is used to transmit the beam from the HBL and the VBL. A third bender (ISBEND01), located between HBBEND01 and HBBEND02, can be also mechanically inserted into the HBL to perform offline transmission tests with stable beam from the offline ion source (IS). Yet, the main challenge in the HBL is to steer the beam efficiently through both the 29° and 90° kicker-bender electrodes; in order to simplify this task and try to achieve the maximum transmission efficiently throughout the HBL, further steerer plates (HBSTEE01 and HBSTEE02) are used to correct the beam trajectory horizontally with respect to the beam axis and an Einzel lens was installed to be able to better focus the beam before it enters the 90° bender.

The Einzel lens is placed between the entrance and exit of both kicker-bender assemblies and it is formed by three metal electrodes arranged coaxially in a row. In particular, the two outer electrodes are set to ground potential, while the central electrode is set to high-voltage, typically at a value around 12 kV to assure the maximal beam transmission for an incoming beam at an energy of 30 keV.

A list of the commonly used abbreviations in the labels related to the different WISArD beamline components is reported in Table B.1.

Label	Definition	Label	Definition
HB	Horizontal beamline	STEE	Steerer
VB	Vertical beamline	BEND	Bender
IS	Offline stable ion source	EINZ	Einzel lens
KICK	Kicker	RETA	Retardation electrode
DIAP	Diaphragm	PDT	Pulse drift tube
FCUP	Faraday cup	DRIF	Drift electrode

Table B.1: Summary of the correspondence between the abbreviations employed in labels shown in Fig. B.2 and B.3 and their extended reference to the different WISArD beamline components.

B.1.2 Vertical beamline

The VBL is connected to the HBL by means of the 90° bender (HBBEND02) and finally permits to control and optimize the ion beam transmission up to the catcher foil, situated inside the superconducting magnet. A schematic view of the VBL components is shown in Fig. B.3.

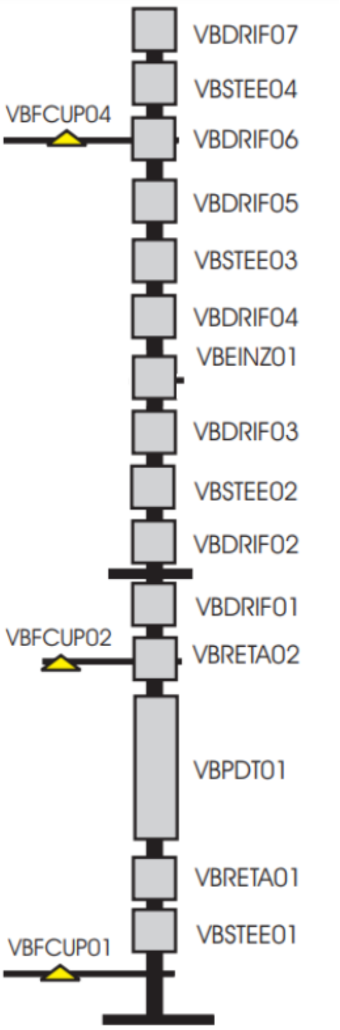

Figure B.3: Schematic view of the electrode layout in the vertical beamline (VBL) employed to optimize the ion beam transmission up to the implantation point, located inside the WISArD magnet. A list of the commonly used abbreviations in the labels related to the different VBL components is reported in Table B.1.

The VBL is composed by different stainless steel cylindrical electrodes with an internal diameter of 60 mm, used specifically to focus the incoming beam and subsequently inject it into the magnet section.

In its lower part, the VBL comprises a 78 cm long cylindrical electrode (VBPDT01), which was used in the former WITCH experiment [76–78] to slow down the energy of the ion beam from 30 keV to 1.5 keV. However, in the current implementation the ion beam does not need to be slowed down, so that the PDT is exploited uniquely to create a regular drift region useful to adjust the beam trajectory with respect to the vertical axis. Concomitantly, four doublets of X-Y steerer plates (VBSTEE01, VBSTEE02, VBSTEE03, VBSTEE04) allow to correct the beam trajectory for slight shifts in a perpendicular plane with respect to the vertical axis. The second part of the VBL is composed by multiple shorter electrodes, which concur to assure flexibility during the ion beam manipulation. In particular, the Einzel lens electrodes are used to tightly focus the beam trajectory to be as parallel as possible to the magnetic field lines generated by the superconducting magnet in the downstream section.

In analogy to the HB, also in the VB several diagnostic elements (Faraday cups and collimator strip systems) permit to measure the intensity of the incoming beam and to focus it as much as possible in a small geometrical spot, ideally symmetrically distributed around the vertical axis, in order to try to reach the most optimal conditions for the implantation inside the catcher foil. In particular, on the same arm holding the first Faraday cup (VBFCUP01), three 10% attenuation grids have been mounted vertically one on the top of the other and can be manually inserted, by adjusting the horizontal position of the arm, in order to reduce the beam intensity delivered to the MCPs in case of beam profile measurements (for further details on the MCPs see Sec. 5.4.2).

B.1.3 Offline ion source

On the top of the horizontal beamline, just above ISBEND01, a surface-ionization ion source (^{39}K) permits to perform offline tests on the ion beam transmission through the WISArD beamline.

The ion source is composed of a small metallic cavity filled with small pieces of potassium pellets, from which the ^{39}K ions can be created via surface ionization just by being in contact with heated walls of the ion source cavity. The production efficiency in this case is known to be fairly optimal, as the alkali metals are characterized by a low work function and therefore are easily extracted as singly-charged ions; however, the rate of production is known to be variable as a function of the heating temperature applied on the walls of the ion source itself. Right after the ion creation, an Einzel lens, consisting in the classical three cylindrical-shaped electrodes, is used to extract the beam and focus it towards the ion source bender (ISBEND01), from which the beam is directly transmitted to the HB. The values of the high voltage applied on the heating electrode, on the Einzel lens components and on the bender can be set remotely via a dedicated LabVIEW interface. For safety purpose, the value of the ion source extraction current can be set as increasing with a certain amplitude step function in a specific time interval; by default, it increases by 1 A every 10 s after the application of the high voltage on the heating electrode.

Offline tests performed with the potassium source allowed to study the variation of the beam transmission efficiency in the WISArD beamline with respect to the proof-of-principle experiment performed in 2018, right after the upgrade of the beamline performed in the past three years. In conclusion, a sensible improvement has been achieved, passing from $\sim 12\%$ transmission efficiency reached in 2018 to a maximum of 85% in 2021 [156].

A picture of the WISARD offline ion source, together with the LabVIEW interface used to control the high voltages applied on it, is shown in Fig. B.1.

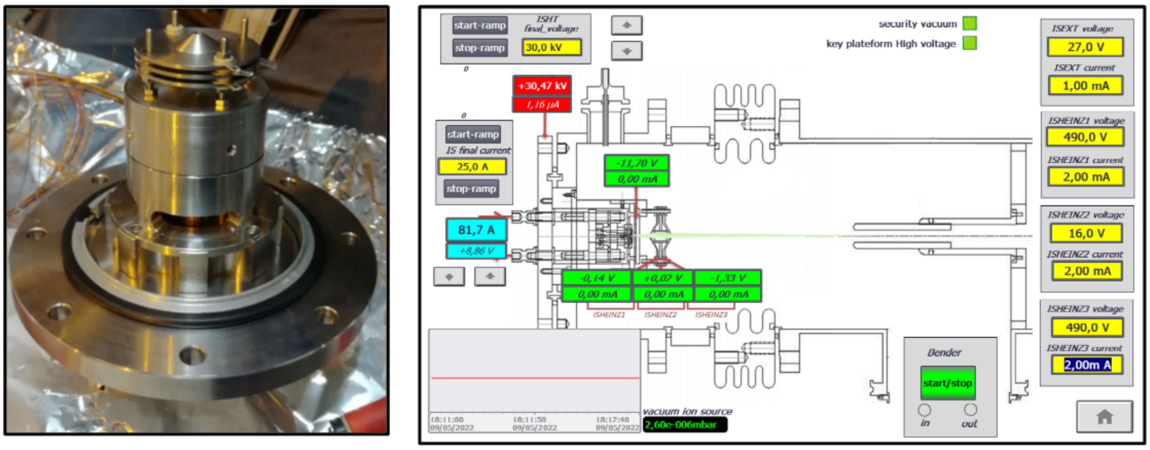

ISHT final_voltage: 30,0 kV

+30,47 kV
1,16 µA

IS final current: 25,0 A

81,7 A
+8,86 V

-11,70 V
0,00 mA

-0,14 V 0,00 mA
+0,02 V 0,00 mA
-1,33 V 0,00 mA

ISEXT voltage: 27,0 V
ISEXT current: 1,00 mA
ISHEINZ1 voltage: 490,0 V
ISHEINZ1 current: 2,00 mA
ISHEINZ2 voltage: 16,0 V
ISHEINZ2 current: 2,00 mA
ISHEINZ3 voltage: 490,0 V
ISHEINZ3 current: 2,00m A

vacuum ion source: 2,60e-006mbar

Figure B.4: On the left, picture of the WISArD offline ion source; on the top, the three equally spaced electrodes composing the Einzel lens are visible. On the right, layout of the LabVIEW interface allowing to set high voltages on the heating and extraction electrodes composing the ion source, as well as on the three electrodes composing the Einzel lens.

B.2 Magnet section and field profile measurement

The last section of the WISArD beamline is composed of a superconducting magnet system manufactured by Oxford Instruments, which is capable of producing magnetic fields with an intensity up to 9 T. The magnet, formerly used for the WITCH experiment [76–78] has two primary coil windings designed to produce independent homogeneous magnetic fields at two different locations, with a maximum strength of 9 T in the lower part and 0.2 T at the centre of the upper magnet section, respectively. This particular configuration was thought in such a way that the recoiling ions studied in the former WITCH experiment, escaping the lower decay trap region after β-decay, were gently guided into the central spectrometer region by their cyclotron motion along the magnetic field lines. On their way from the high magnetic field in the decay trap to the low magnetic region in the center of the spectrometer, the magnetic gradient force was acting to convert almost completely their cyclotron energy into longitudinal motion. Subsequently, the recoil ions were pulled off the magnetic field lines by applying a high negative high voltage on a retardation electrode; the ions were then finally focused onto a MCP detector by means of an Einzel lens electrode and two drift electrodes for energy measurement.

However, in the WISArD experiment the weaker field coil is not used anymore, and only the uniform 9 T magnetic region is employed for the measurements. This section surrounds a cylindrical vacuum bore tube, which is characterized by an inner diameter of 185 mm and an outer diameter of 130 mm, and by a height of 482 mm. In order to access this volume and place the detection set-up inside it, a unique access is guaranteed by an opening at the top of the cryostat system, at roughly 2.5 m above. In particular, the detection set-up, comprehensive of all detectors and their respective preamplifiers, is mounted at the very bottom of a taylor-made mechanical structure, normally referred to as the WISArD tower. The tower is then vertically placed inside the magnet, such that the detection set-up results located inside the high-intensity magnetic field region. A picture of the assembled WISArD tower outside vacuum is reported in Fig. B.5.

Moreover, the inner walls of the magnet bore are physically connected to the magnet cryogenic vessels, containing liquid helium; once thermalized, the bore is then cooled by contact with the cryogenic vessels at a temperature of roughly -30°C.

Figure B.5: On the top, picture of the upper part of the nearly 2.5 m long WISArD tower, which is vertically inserted inside the magnet section from the opening at the top of the cryostat system. At the bottom, a picture of the lower part of the tower, with an orange ellipse showing the zone in which the detection set-up, comprehensive of all the detectors and their respective preamplifiers, is located.

As it comes out from the error budget of the proof-of-principle experiment [111], one of the less significant contribution to the overall systematic errors in the determination of the $\tilde{a}_{\beta\nu}$ coefficient is given by the uncertainty on the homogeneity of the magnetic field used during the experiment. Nevertheless, a precise measurement of the magnetic field profile in the 9 T region has been performed in February 2021, in order to quantitatively evaluate the level of field inhomogeneity and its influence on the final systematic error. In total, three global mapping measurements based on a translating fluxmeter [157] have been performed; in particular, a single measurement was performed at a steady state and ramping-up and ramping-down the current in the primary coil, while in parallel moving the fluxmeter back and forth in the available travel range (almost the total length of the magnet bore) while the related Faster Digital Integrators (FDIs) were acquiring signals at 500 kHz from the induction coils. In conclusion, the relative variation of the magnetic field at 4 T, in a range of $\pm$ 100 mm with respect to the central plane, were evaluated to be $\frac{\Delta B_z}{B_z} \simeq 5 \cdot 10^{-5}$ for the axial component and $\Delta \mathrm{B}_r \simeq 1 \cdot 10^{-3}$ mT for the radial component. The results for all magnetic field strengths are in perfect agreement with the information provided by the manufacturer, thus permitting quantitatively to confirm the previous estimation on the systematic error due to magnetic field homogeneity, evaluated to contribute less than $1‰$ on the global systematic error on the $\tilde{a}_{\beta\nu}$ coefficient for both Fermi and Gamow-Teller transitions. Further details on the magnetic field profile measurements are reported in [156].

Appendix C

Further information on data analysis and simulations

C.1 Estimated ^{32}Ar^{+} production yield and implantation rate

During data taking, the estimated ^{32}Ar^{+} production yield at the ISOLDE target has been estimated from the data recorded by the silicon detectors composing the WISArD experimental set-up. In particular, after performing a rough preliminary energy calibration on all strips and back-sides of the eight silicon detector, the temporal rate of protons in the region around the IAS peak ([3320, 3400] keV) has been employed for the estimation of the total ^{32}Ar^{+} implantation rate inside the WISArD magnet. The total implantation rate has been then multiplied by the transmission efficiencies towards both the WISArD beamline and the REX set-up, in order to backwards estimate the ^{32}Ar production yield.
Specifically, the following formula has been employed:

$$\mathcal{N}_{tot}[pps/\mu A] = \frac{\sum_{i=1}^{8} N_{IAS,i}}{BR_{IAS} \cdot \Delta t_{acq} \cdot \varepsilon_{geom} \cdot \varepsilon_{wis} \cdot \varepsilon_{rex} \cdot I_p} \tag{C.1}$$

where:

- $\mathcal{N}_{tot}$ is the estimated ^{32}Ar^{+} production yield (in pps/μA);
- $N_{IAS,i}$ is the amount of protons in the IAS region registered by the i-th silicon detector (i = 1, ... ,8);
- BR_{IAS} is the branching ratio of the IAS proton line (22.63(25)% [119]);
- Δt_{acq} is the acquisition time (in s);

- ε_{geom} is the WISArD detector geometrical efficiency (estimated from Geant4 simulations to be around 57%);
- ε_{wis} is the estimated beam transmission efficiency through the WISArD beamline ($\simeq$ 50%);
- ε_{rex} is the estimated beam transmission efficiency through the REX set-up located before the WISArD beamline ($\simeq$ 50%);
- I_p is the proton current delivered to the target from the PS Booster (up to 2 μA).

The initial average ^{32}Ar^{+} production yield was estimated to be $\simeq$ 500 pps, more than a factor five below the ISOLDE standard capability [129], thus determining a loss in statistics in the first runs acquired. However, after retuning the beam through the REX set-up and performing a joint scan of the proton distribution hitting the target and the target heating (target current was increased from 245 to 252 A), a factor three in terms of beam production was immediately gained, thus leading to an estimated ^{32}Ar^{+} production yield of roughly 1500 pps, right after the first few hours of data taking. The percentages of beam transmission through the REX-ISOLDE set-up and the WISArD beamline were estimated to be both around 50%, resulting in a total implantation rate of roughly 360 pp. For further details on the conditions of data taking see Sec. 3.1.1.

C.2 Silicon detector energy calibration with ^{33}Ar

As explained in Sec. 3.1.1, a few hours of data taking were dedicated to the collection of data relatively to the β-delayed proton decay of ^{33}Ar. In particular, according to the ISOLDE Yield Database [152], the production yield out of a nanostructured calcium oxide (CaO) powder target for ^{33}Ar appears to be at around 120000 pps, thus more than forty times higher with respect to the production rate of ^{32}Ar, estimated to roughly 2600 pps. Consequently, in principle, the acquisition of data from the ^{33}Ar decay for a limited amount of time for both the catchers employed (6 μm Mylar and 0.8 μm aluminized Mylar foil) should allow to collect sufficient statistics to independently calibrate in energy all the silicon detectors and, subsequently, exploit the newly determined fitting function to calibrate the spectra collected in both cases with ^{32}Ar.

Specifically, the energy calibration can be performed independently for each of the five strips located either in the upper or in the lower hemisphere by correlating the ADC values corresponding to the two most intense peaks of ^{33}Ar to the corresponding energy values. The energy values of these two peaks, located respectively at 2100(3) and at 3173(3) keV [158], need to be first corrected for the energy lost by the protons before reaching the active part of the silicon detectors, both in the catcher foil and within the silicon detector dead layer. In particular, corrections do depend both on the initial kinetic energy of the protons and on the real thickness traversed inside the catcher foil and the dead layer, which turns out to be different for each strip due to the diverse bending effect on the particle trajectory induced by the magnetic field. Furthermore, the corrections for the energy lost inside the catcher foil, at a given energy, result asymmetric between the strips located in the upper and in the lower hemisphere; effectively, as it can be estimated via SRIM [130] calculations, the implantation point of the incoming ^{33}Ar^{+} ions, post-accelerated at 30 keV, is not located at the centre of the catcher foil, but rather in its very bottom part, at (47 $\pm$ 14) nm and at (21 $\pm$ 8) nm for the Mylar and the aluminized Mylar, respectively. All these corrections can be automatically estimated for the data acquired with both the catcher foils via precise Geant4 simulations reproducing the WISArD detection set-up and the data taking conditions.

However, in the end the statistics collected with ^{33}Ar during the experimental campaign appeared not to be sufficient to calibrate with precision the spectra collected by the different strips. As illustrated with more detail in Sec. 3.2.1, the silicon detectors were finally calibrated by exploiting the two most intense peaks of ^{32}Ar, corrected for the energy lost by the protons before impacting on the detectors, estimated in a similar way from Geant4 simulations.

For completeness, results related to the corrections to the energy calibration of the two most intense peaks of ^{33}Ar are reported in Table C.2 and in Table C.1, related to the aluminized Mylar and the Mylar catcher foil respectively.

	^{33}Ar corrected proton energy [keV] vs strip n° (AlMylar)				
Information	**1**	**2**	**3**	**4**	**5**
E_{th} [keV]	2100(3)	2100(3)	2100(3)	2100(3)	2100(3)
$\Delta E_{catcher}$ ($s_{c,up}$) [keV]	41.9(2)	46.1(2)	51.5(2)	57.6(2)	65.0(2)
$\Delta E_{deadLayer}$ ($s_{dL,up}$) [keV]	2.72(2)	2.71(2)	2.75(2)	2.81(2)	2.92(2)
$E_{cal,up}$ ($s_{c,up}$, $s_{dL,up}$) [keV]	2055.38(322)	2051.19(322)	2045.75(322)	2039.59(322)	2032.08(322)
E_{th} [keV]	2100(3)	2100(3)	2100(3)	2100(3)	2100(3)
$\Delta E_{catcher}$ ($s_{c,down}$) [keV]	1.10(1)	1.23(1)	1.38(1)	1.53(1)	1.65(1)
$\Delta E_{deadLayer}$ ($s_{dL,down}$) [keV]	2.69(2)	2.67(2)	2.69(2)	2.75(2)	2.84(2)
$E_{cal,down}$ ($s_{c,down}$, $s_{dL,down}$) [keV]	2096.21(303)	2096.10(303)	2095.93(303)	2095.72(303)	2095.51(303)
E_{th} [keV]	3173(3)	3173(3)	3173(3)	3173(3)	3173(3)
$\Delta E_{catcher}$ ($s_{c,up}$) [keV]	29.9(2)	32.8(2)	36.7(2)	41.1(2)	46.2(2)
$\Delta E_{deadLayer}$ ($s_{dL,up}$) [keV]	1.97(2)	1.95(2)	1.97(2)	2.01(2)	2.06(2)
$E_{cal,up}$ ($s_{c,up}$, $s_{dL,up}$) [keV]	3141.13(322)	3138.25(322)	3134.33(322)	3129.89(322)	3124.74(322)
E_{th} [keV]	3173(3)	3173(3)	3173(3)	3173(3)	3173(3)
$\Delta E_{catcher}$ ($s_{c,down}$) [keV]	0.81(1)	0.91(1)	1.01(1)	1.12(1)	1.21(1)
$\Delta E_{deadLayer}$ ($s_{dL,down}$) [keV]	1.96(2)	1.95(2)	1.97(2)	1.99(2)	2.05(2)
$E_{cal,down}$ ($s_{c,down}$, $s_{dL,down}$) [keV]	3170.23(303)	3170.14(303)	3170.02(303)	3169.89(303)	3169.74(303)

Table C.1: Summary of the corrections to the energy calibration relatively to the two most intense proton energy peak lines of ^{33}Ar, at 2100(3) and 3173(3) keV respectively [158]. Corrections for the energy lost inside the catcher foil and in the silicon detector dead layer have been retrieved via Geant4 simulations of the WISArD detection set-up, by generating mono-energetic protons at 2100 and 3173 keV implanted, concerning the x and y coordinates, at the centre of a 0.8 μm aluminized Mylar foil and, regarding the z coordinate, at 21 nm with respect to the bottom part of the catcher. Simulations have been performed assuming an initial proton Gaussian distribution around the implantation point (r = 2 mm, σ = 300 μm).

	^{33}Ar corrected proton energy [keV] vs strip n° (Mylar)				
Information	**1**	**2**	**3**	**4**	**5**
E_{th} [keV]	2100(3)	2100(3)	2100(3)	2100(3)	2100(3)
$\Delta E_{catcher}$ ($s_{c,up}$) [keV]	142.8(2)	160.5(2)	179.9(2)	202.0(2)	228.7(2)
$\Delta E_{deadLayer}$ ($s_{dL,up}$) [keV]	2.85(2)	3.00(2)	3.00(2)	3.03(2)	3.15(2)
$E_{cal,up}$ ($s_{c,up}$, $s_{dL,up}$) [keV]	1954.35(322)	1936.50(322)	1917.10(322)	1895.00(322)	1868.15(322)
E_{th} [keV]	2100(3)	2100(3)	2100(3)	2100(3)	2100(3)
$\Delta E_{catcher}$ ($s_{c,down}$) [keV]	1.10(1)	1.23(1)	1.38(1)	1.53(1)	1.62(1)
$\Delta E_{deadLayer}$ ($s_{dL,down}$) [keV]	2.67(2)	2.66(2)	2.70(2)	2.75(2)	2.83(2)
$E_{cal,down}$ ($s_{c,down}$, $s_{dL,down}$) [keV]	2096.23(303)	2096.11(303)	2095.92(303)	2095.72(303)	2095.55(303)
E_{th} [keV]	3173(3)	3173(3)	3173(3)	3173(3)	3173(3)
$\Delta E_{catcher}$ ($s_{c,up}$) [keV]	102.5(2)	114.7(2)	128.4(2)	143.7(2)	162.0(2)
$\Delta E_{deadLayer}$ ($s_{dL,up}$) [keV]	2.02(2)	2.00(2)	2.02(2)	2.05(2)	2.13(2)
$E_{cal,up}$ ($s_{c,up}$, $s_{dL,up}$) [keV]	3068.48(322)	3056.30(322)	3042.58(322)	3027.25(322)	3008.87(322)
E_{th} [keV]	3173(3)	3173(3)	3173(3)	3173(3)	3173(3)
$\Delta E_{catcher}$ ($s_{c,down}$) [keV]	0.80(1)	0.90(1)	1.00(1)	1.12(1)	1.19(1)
$\Delta E_{deadLayer}$ ($s_{dL,down}$) [keV]	1.96(2)	1.95(2)	1.98(2)	2.01(2)	2.03(2)
$E_{cal,down}$ ($s_{c,down}$, $s_{dL,down}$) [keV]	3170.24(303)	3170.15(303)	3170.02(303)	3169.87(303)	3169.78(303)

Table C.2: Summary of the corrections to the energy calibration relatively to the two most intense proton energy peak lines of ^{33}Ar, at 2100(3) and 3173(3) keV respectively [158]. Corrections for the energy lost inside the catcher foil and in the silicon detector dead layer have been retrieved via Geant4 simulations of the WISArD detection set-up, by generating mono-energetic protons at 2100 and 3173 keV implanted, concerning the x and y coordinates, at the centre of a 6.0 μm Mylar foil and, regarding the z coordinate, at 47 nm with respect to the bottom part of the catcher. Simulations have been performed assuming an initial proton Gaussian distribution around the implantation point (r = 2 mm, σ = 300 μm).

C.3 Statistics error on the mean proton energy shift

The mean proton energy shift has been defined in Chapter 3 as the absolute value of the difference between the means of the single and coincident proton energy peaks, so as:

$$\bar{E}_{shift} = \mid \bar{E}_{coinc} - \bar{E}_{sing} \mid \tag{C.2}$$

where $\bar{E}_{coinc}$ and $\bar{E}_{sing}$ are not statistically independent, as the events used to determine $\bar{E}_{coinc}$ are also part of the set of events used to determine $\bar{E}_{sing}$. It is thus needed to express the mean energy shift in a different way, by using only statistically independent data. The previous equation can be reformulated as follows:

$$\begin{aligned} \bar{E}_{shift} &= \left| \bar{E}_{coinc} - \left(\frac{N_{coinc} \cdot \bar{E}_{coinc} + N_{nonCoinc} \cdot \bar{E}_{nonCoinc}}{N_{sing}} \right) \right| \\ &= \left| (\bar{E}_{coinc} - \bar{E}_{nonCoinc}) \cdot \left(1 - \frac{N_{coinc}}{N_{sing}} \right) \right| \end{aligned} \tag{C.3}$$

where N_{sing}, N_{coinc} and $N_{nonCoinc}$ indicate, respectively, the total number of counts in the single energy peak (corresponding to silicon signals acquired with and without a coincident signal from a β-particle in the SiPM), the number of counts in the corresponding β-coincident proton peak and the number of counts in the proton peak in case of no associated β-coincident events. Consequently, by definition:

$$N_{sing} = N_{coinc} + N_{nonCoinc} \tag{C.4}$$

and, due to the employment of a high magnetic field and to the symmetric disposition of the detection set-up around the implantation foil (for further details see Sec. 2):

$$N_{coinc} \simeq \frac{N_{sing}}{2} \implies N_{coinc} \simeq N_{nonCoinc} \simeq \frac{N_{sing}}{2} \tag{C.5}$$

The error associated to the mean energy shift can then be derived by propagation of the uncertainty on its four independent composing variables ($\bar{E}_{coinc}$, $\bar{E}_{nonCoinc}$, N_{coinc} and $N_{nonCoinc}$). Its value can be determined as follows:

$$\begin{aligned} \sigma_{\bar{E}_{shift}} &= \left[\left(\frac{\partial \bar{E}_{shift}}{\partial \bar{E}_{coinc}} \right)^2 \cdot \sigma^2_{\bar{E}_{coinc}} + \left(\frac{\partial \bar{E}_{shift}}{\partial \bar{E}_{nonCoinc}} \right)^2 \cdot \sigma^2_{\bar{E}_{nonCoinc}} \right. \\ &\left. + \left(\frac{\partial \bar{E}_{shift}}{\partial N_{Coinc}} \right)^2 \cdot \sigma^2_{N_{coinc}} + \left(\frac{\partial \bar{E}_{shift}}{\partial N_{nonCoinc}} \right)^2 \cdot \sigma^2_{N_{nonCoinc}} \right]^{1/2} \end{aligned} \tag{C.6}$$

where $\sigma_{\bar{E}_{coinc}}$ is the root mean square of the β-proton coincident distribution divided by the square root of N_{coinc} and $\sigma_{\bar{E}_{nonCoinc}} \sim \sigma_{\bar{E}_{coinc}}$. Furthermore, $\sigma_{N_{coinc}} \equiv \sqrt{N_{coinc}}$ and $\sigma_{N_{nonCoinc}} \sim \sigma_{N_{coinc}}$. By combining Eq. C.4 and the approximations reported in Eq. C.5, it can be found:

$$\begin{aligned}
&\bullet \quad \frac{\partial\,\bar{E}_{shift}}{\partial\,\bar{E}_{coinc}} = 1 - \frac{N_{coinc}}{N_{sing}} \simeq \frac{1}{2} \\
&\bullet \quad \frac{\partial\,\bar{E}_{shift}}{\partial\,\bar{E}_{nonCoinc}} = -\left(1 - \frac{N_{coinc}}{N_{sing}}\right) \simeq -\frac{1}{2} \\
&\bullet \quad \frac{\partial\,\bar{E}_{shift}}{\partial\,N_{coinc}} = \left(\bar{E}_{coinc} - \bar{E}_{nonCoinc}\right) \frac{\partial}{\partial\,N_{coinc}} \left(1 - \frac{N_{coinc}}{N_{sing}}\right) \simeq -\frac{\bar{E}_{shift}}{N_{sing}} \\
&\bullet \quad \frac{\partial\,\bar{E}_{shift}}{\partial\,N_{nonCoinc}} = \left(\bar{E}_{coinc} - \bar{E}_{nonCoinc}\right) \frac{\partial}{\partial\,N_{nonCoinc}} \left(1 \frac{N_{coinc}}{N_{sing}}\right) \simeq +\frac{\bar{E}_{shift}}{N_{sing}}
\end{aligned} \tag{C.7}$$

By replacing the partial derivatives computed in Eq. C.7 into Eq. C.6, the error associated to the mean proton energy shift assumes the final following form:

$$\sigma_{\bar{E}_{shift}} = \sqrt{\frac{1}{2}\,\sigma^2_{\bar{E}_{coinc}} + \frac{1}{N_{sing}}\,\bar{E}^2_{shift}} \tag{C.8}$$

In particular, $\bar{E}_{coinc}$, N_{sing} and $\bar{E}_{shift}$ can be directly inferred from both the proton experimental and simulated spectra.

C.4 Physics package available in Geant4

As systematically found out in the studies on the numerical reproduction of β-spectra performed at LP2I-Bordeaux (see Appendix D), all experimental runs have been globally better reproduced by simulations making use of the *Goudsmit-Saunderson* and the *Penelope PhysicsLists*, which both provide a fairly precise replica of the experimental spectra down to an energy of about 150 keV. Indeed, the main discrepancies between simulations performed with different *PhysicsLists* appear to be clearly visible in the low-energy region of the spectra ($0 < E_e < 150$ keV) and are mainly due to the different implementation of algorithms treating β-particle multiple Coulomb scattering inside materials.

C.4.1 Physics packages specific for β-particle reproduction

Effectively, charged particles traversing a finite thickness of matter undergo a very large number of single collisions with atomic electrons, whose cumulative effects result in a net deflection from the original particle direction and both a longitudinal and lateral displacement with respect to the collision point. Traditionally modeled by using Molière's theory [159], multiple Coulomb scattering (MSC) is currently implemented by default into Geant4 under the form stated by Lewis theory [160], which permits to quantitatively determine most of the main properties characterizing MSC (deflection angle, geometrical path length, mean lateral displacement and correlated energy deposition) by implementing the transport equations for charged particles and making use of the particle average first and second transport mean free paths, both fairly well estimated several decades ago [161]. In particular, the Urban MSC model satisfies general requirements for many experiments related to both low and high energy physics and its correctness has been independently confirmed via different independent sets of simulations (see for example [162–164]). However, in spite of the already valuable numerical reproductions provided by the Urban MSC model, an even better general implementation of the electron multiple scattering has become throughout the years a fundamental goal to be reached in order to provide a more realistic description of the low-energy physics inside Geant4 and to be as well competitive with the better accuracy achievable by using other condensed simulation codes or mixed algorithms, such as EGSnrc or Penelope respectively.

In order to finally improve the low-energy physics description in Geant4, two newly developed *PhysicsLists* have been made available since version 9.3. The first physics package is $Goudsmit-Saunderson$, which is based on $Goudsmit-Saunderson$ calculations [143, 144] and specifically designed for a precise simulation of electron transport; moreover, it is based on algorithms of the EGSnrc multiple scattering model developed by Kawrakow and Bielajew [145]. The second physics package is the new version of *Penelope*, based on the PENELOPE code of transport (version 2008) [165], released in order to replicate PENELOPE-based algorithms; specifically, it is based on simulations of elastic electron collisions, performed by using relativistic (Dirac) partial-wave differential cross sections generated via the computer code ELSEPA [166] to better reproduce the electron transport at low energies. In particular, both these models, specifically developed to be implemented within Monte Carlo simulations, are based on an approach which combines numerical databases and analytical cross section models to properly take into account different interaction mechanisms due to low-energy and atomic effects, such as Doppler broadening and shell effects.
Goudsmit-Saunderson and *Penelope*, as peculiarly accomplished to precisely reproduce low-energy physics, result then the best *PhysicsLists* to numerically reproduce experimental spectra of β-particles. The results obtained from tests performed at LP2I-Bordeaux in different experimental conditions (mono-energetic beam from an electron spectrometer and radioactive sources) are in agreement and quantitatively support these general assumptions.

C.4.2 Further packages for electromagnetic physics reproduction

Furthermore, other more general electromagnetic packages have been introduced and are available in Geant4 to simulate electromagnetic interactions related to many different particles and at many different energy scales: Standard Package [167], Low Energy Package based on Livermore data libraries [168–170] and an additional Low Energy Package based also partially on the Penelope analytical approach [171], introduced in the previous paragraph. However, as it appears from the tests performed at LP2I-Bordeaux, these further packages lead to the generation of numerical spectra that systematically overestimated the experimental ones in the low-energy region. These differences between simulated and experimental spectra reflect the different way in which the Geant4 *PhysicsLists* handle the electromagnetic interactions of charged particles, concerning particularly the treatment of multiple scattering, Compton scattering and Auger effect.

C.4.2.1 The Standard package

The Standard Package provides a plethora of models (*e.g. emstandard_opt4*) based on an analytical approach capable of describing interactions of β-particles, photons and charged hadrons in an energy range between 1 keV and 100 TeV. All these models, while treating inter-atomic interactions, consider atomic electrons as quasi-free, neglecting in all cases, except for photoelectric effect, the atomic electron binding energy; additionally, they assume the atomic nucleus as fixed, neglecting always its recoil momentum. Such low-energy approximations, even though not completely acceptable for low-energy physics reproduction, are pretty reasonable if considering that the Standard Package, indeed owing to its possibility to simulate varieties of particles at all energy-scales, was specifically conceived rather for high energy physics purpose.

Yet, simulations performed by using *emstandard_opt4* already replicate fairly well the experimental runs, but unsurprisingly hugely differ in the very low energy region ($0 < E_e <$ 0.05 MeV) due to the implementation of grosser algorithms for the treatment of inter-atomic electron interactions.

C.4.2.2 The Low Energy Physics package

The Low Energy Package based on Livermore data libraries, consisting in the *Livermore* and *LowEMEnergyPhysics PhysicsLists*, extends the range of accuracy of electromagnetic interactions down to lower energies with respect to the Standard Package. In fact, both these models make use of different evaluated data libraries (EPDL97 [172], EEDL [173], EADL [174]) in order to compute and implement cross-sections in step-by-step tracking to properly model photon and β-particle interactions with matter down to an energy of 250 eV. However, the two *PhysicsLists*, even if belonging to the same package, greatly differ in the way of treating both multiple Coulomb and bound atomic electron Compton scattering. In particular, *Livermore* handles MCS by implementing a combination of the GS model at lower energies (E_e < 1 MeV) and WentzelVI together with Single Coulomb Scattering (SCS) algorithms at higher energies, and implements Compton scattering by using the Ribberfors scattering model, which computes double differential Compton scattering cross sections by using the Relativistic Impulse Approximation [175]. On the contrary, *LowEMEnergyPhysics* allows to simulate electron multiple scattering by using uniquely the WentzelVI model and reproduces Compton scattering via an alternative computational model, developed by the Monash University, up to 20 MeV and by the Klein-Nishina model above 20 MeV.

In this case the main differences between *Livermore* and *LowEMEnergyPhysics* come from the different implementation of algorithms to properly treat Compton scattering; effectively, if looking at comparisons between simulated and experimental runs acquired in a previous campaign by means of a pure electron spectrometer at LP2I-Bordeaux (for details see Appendix D), the low-energy regions in the β-spectra, corresponding to the backscattering continuum and mainly influenced by the MSC coding, appear well reproduced by both *PhysicsLists*. In case of runs analyzed for the 2019 WISArD experimental campaign with β-calibration sources, differences in physics reproduction, concerning both β-particles and photons detection, are evident, especially if considering the continuum at low energies, given by the contributions of both MSC and Compton effect. The fact that *Livermore* systematically better reproduces experimental results can be ascribed to the fact that, differently from the limited computational model implemented in *LowEMEnergyPhysics*, it implements with better accuracy the calculation of the polar ejection angle and direction of the Compton electron, with a direct impact on the determination of the energy deposited by each Compton electron inside the detector [176].

C.5 Further information on the comparison between the experimental and the simulated β-spectra

The comparison between the LG and HG energy-calibrated experimental β-spectrum in coincidence with an IAS proton (acquired with at least two cells firing at the same time) and the corresponding simulated ones (convoluted with the response function of the β-detector) are shown in Fig. C.1 and in Fig. C.2, respectively. In addition to the discussion presented in Sec. 5.1.1, in the figures the bin-per-bin difference between the calibrated experimental and the smeared simulated spectra, normalized to half the sum of their respective bin contents, are shown, along with the x-axis projection of the normalized bin-per-bin difference between the cutting thresholds for the computation of the χ^2-value. The normalized bin-per-bin difference is clearly fluctuating around zero in both cases, and its x-axis projection result in both cases in a Gaussian distribution centered on the zero value, thus indicating, together with a fairly low χ^2-value, a rather good quality in the numerical reproduction of the experimental spectrum.

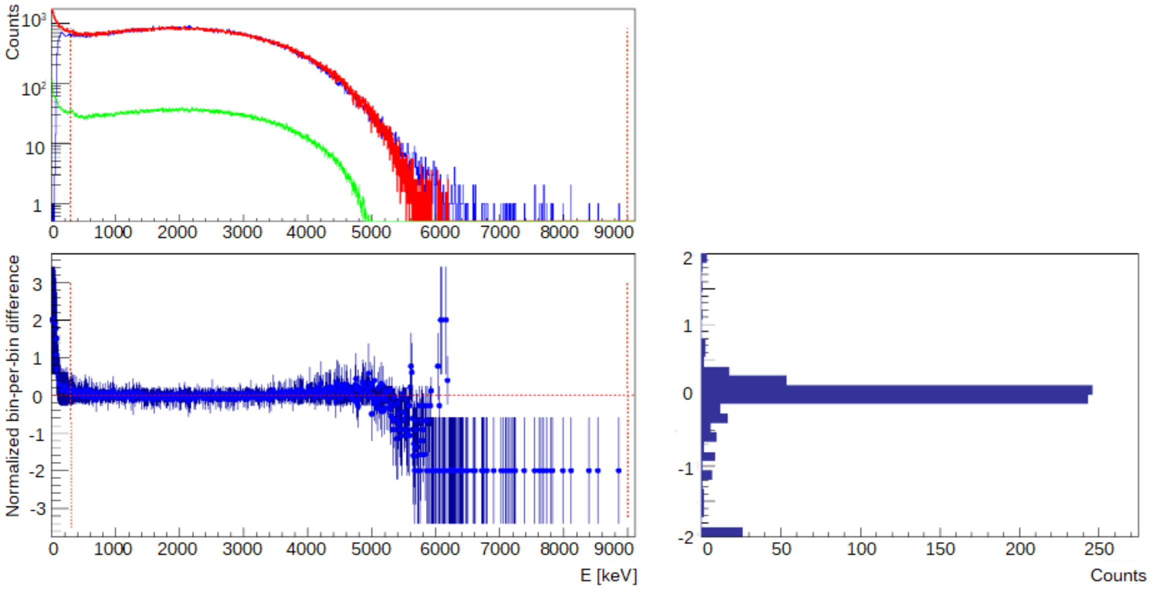

Figure C.1: Top left: superimposed experimental energy-calibrated LG β-spectrum, recorded in coincidence with an IAS proton and with at least two cells firing at the same time (blue), and the corresponding smeared Geant4 spectrum (red); the pure Geant4 spectrum (green, rescaled for graphics purpose), with cutting thresholds (vertical dashed orange lines) delimiting the energy region for the computation of the χ^2, is also represented (χ^2 = 2.12). Bottom left: the bin-per-bin difference between the calibrated experimental and the smeared simulated spectra, normalized to half the sum of their respective bin contents. Bottom right: the x-axis projection of the normalized bin-per-bin difference between the cutting thresholds.

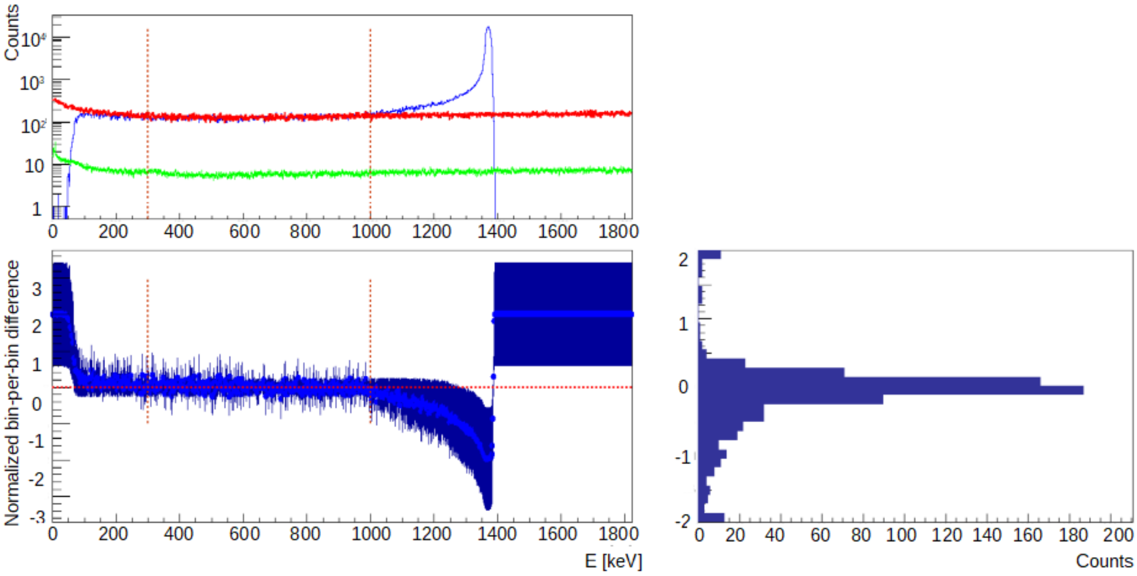

Figure C.2: Top left: superimposed experimental energy-calibrated HG β-spectrum, recorded in coincidence with an IAS proton and with at least two cells firing at the same time (blue), and the corresponding smeared Geant4 spectrum (red); the pure Geant4 spectrum (green, rescaled for graphics purpose), with cutting thresholds (vertical dashed orange lines) delimiting the energy region for the computation of the χ^2, is also represented ($\chi^2 = 1.10$). Bottom left: the bin-per-bin difference between the calibrated experimental and the smeared simulated spectra, normalized to half the sum of their respective bin contents. Bottom right: the x-axis projection of the normalized bin-per-bin difference between the cutting thresholds.

Appendix D

β-backscattering measurements and further tests

D.1 Physics motivation

A proof-of-principle experiment of WISArD has been performed at ISOLDE in November 2018 by means of equipment and detectors readily available at CENBG and the acquisition system provided by LPC Caen. In spite of the employment of a rather rudimental set-up, a fairly short beam time allocated for the experiment and a rigid limitation at the level of ion transmission due to the meagre existing beam optics, the collected data permitted to perform the third and fourth most precise measurement of $\tilde{a}_{\beta\nu}$ for a pure Fermi and a pure Gamow-Teller transition, corresponding to $\tilde{a}_{\beta\nu}$ = 1.007(32)$_{stat}$(25)$_{syst}$ and $\tilde{a}_{\beta\nu}$ = -0.222(86)$_{stat}$(16)$_{syst}$ respectively [111]. The related error budget, comprehensive of the systematic error contributions as well as their relative uncertainties and cumulative uncertainties on $\tilde{a}_{\beta\nu}$ for both Fermi and Gamow-Teller transitions, is reported in Table D.1.

Yet, in order to reach the challenging level of precision of 0.1% on the determination of $\tilde{a}_{\beta\nu}$ in the final experiment, both the statistical and systematic uncertainties need to be reduced by at least an order of magnitude. In particular, in the end statistical uncertainties are realistically expected to be lowered no less than a factor of fifty as an overall consequence of a cumulative longer two-week beam time (almost ten times higher with respect to the proof-of-principle experiment), a considerable increase in ^{32}Ar^{+} beam transmission (more than five times higher) and a relevant upgrade in the experimental set-up dedicated to proton detection, which will consist of new silicon detectors characterized by higher resolution (between 5 and 10 keV) and a thinner dead layer ((100.0 ± 39.2) nm), disposed in a geometrical configuration capable of providing a three times higher detection solid angle.

As well, all systematic errors should be minimized to reach an overall contribution at the 10^{-3} level; although this is indeed a demanding challenge, all present efforts are actually addressed to finally achieve this ambitious objective.

Syst. contribution	**Error source**	**Uncertainty**	$\Delta\tilde{a}_F$ (‰)	$\Delta\tilde{a}_{GT}$ (‰)
background	false coincidences	8%	< 1	2
protons	detector calibration	0.2%	9	6
	detector position	1 mm	< 1	1
	source position	3 mm	3	2
	source radius	3 mm	1	1
	B field	1%	< 1	< 1
	silicon dead layer	0.3 μm	5	7
	Mylar thickness	0.15 μm	2	3
positrons	detector backscattering	15%	2	1
	catcher backscattering	15%	21	11
	detection threshold	12 keV	8	4
Total			**25**	**16**

Table D.1: Error budget of the proof-of-principle of the WISArD experiment realized at ISOLDE in November 2018, comprehensive of sources of systematic errors, uncertainties on the source of errors and related uncertainties on $\tilde{a}_{\beta\nu}$ for both Fermi and Gamow-Teller transitions [111].

In particular, all the systematic uncertainties related to a limited knowledge of the detection system (silicon detector calibration, detector and source relative positions, source radius at the implantation, magnetic field homogeneity and silicon detector dead layer) will be brought down by a factor of around five, as a result of different dedicated experimental campaigns aiming to precisely measure the transverse profile of the ion beam at the implantation inside the catcher, as well as to accurately characterize both the new silicon detectors and the homogeneity of the magnetic field in order to definitely test out and possibly constraint the respective technical characteristics furnished by the manufacturers. In parallel, the actual Mylar catcher foil, used for the implantation of the ion beam, will be replaced by a commercial 500 nm thick Mylar foil, which will straightforwardly pull down the effect of the β-particle backscattering inside the catcher by a factor of about thirteen, directly proportional to the reduction in thickness of the catcher foil itself, presently with a thickness of 6.5 μm.

Yet, one of the major contributions to the systematic uncertainty on the determination of the $\tilde{a}_{\beta\nu}$ parameter is still be represented by the backscattering of the positrons inside the catcher foil and on the plastic scintillator. This contribution, which cannot be directly reduced or constrained, leads in both cases to a non-detection of a fraction of the positrons originally emitted in the upward direction. In order to globally reduce the overall uncertainty related to positron backscattering, different sets of measurements have been performed by means of an electron spectrometer and radioactive sources with diverse dedicated experimental set-ups, installed at LP2I-Bordeaux, with the final aim to explicitly characterize β-particle backscattering inside the plastic scintillator and simultaneously constraint the corresponding Geant4 simulations. In this way, it has been therefore possible to verify the accuracy in the numerical reproduction of the collected β-spectra, with particular care to the low-energy region corresponding experimentally to the area located close to the β-detection threshold. Additionally, a low intensity electron emitter, presently under development at LPC-Caen, will be employed to finely determine the response function of the positron detector in the energy range between 0 and 30 keV, with the ultimate goal to study the detector energy threshold specifically below 10 keV and pull down as well its uncertainty to about 1 keV. In such a scenario, the systematic errors on $\tilde{a}_{\beta\nu}$ related to the detector backscattering and detector threshold are projected to be reduced to a contribution of 0.9×10^{-3} and 0.7×10^{-3}, respectively.

In the following, the different experimental campaigns specifically devoted to the precise study of the backscattering of β-particles inside the plastic scintillator, conducted at ISOLDE and LP2I-Bordeaux between 2019 and 2021, will be presented and the data analysis and comparison to Geant4 simulations will be discussed.

D.2 Tests with a high-energy resolution electron beam spectrometer

First tests aiming to precisely characterize the β-backscattering contribution to the low-energy region of the β-spectra were conducted by means of the high-energy resolution electron beam spectrometer available at CENBG during Spring 2019.

Set up on the base of the technical drawings relative to the one available at the *Institut Pluridisciplinaire Hubert Curien* (IPHC) in Strasbourg, the electron beam spectrometer [177], originally developed for the characterization of the scintillating counters in the MeV-range employed for the SuperNEMO experiment [178], is capable of providing collimated mono energetic electron beams characterized at the same time by high intensity and high-energy resolution. The electron beam is produced from a ^{90}Sr source (Q_β = 0.546 MeV, half-life = 29 y), that decays into ^{90}Y, which is in turn a β-emitter with a Q_β of 2.282 MeV and a half-life of 64 hours. The electrons emitted are then extracted and enter into a region in which a nearly uniform magnetic field, created by a pair of Helmoltz coils symmetrically placed on each side of the area, is applied. Hence, the magnetic field, whose intensity can be set

directly by the user via the software program connected to the spectrometer electronic control boards, makes the electrons gently bending into a curved path inside the spectrometer, with a radius strictly dependent on their kinetic energies, and permits consequently the selection of an outcoming pure mono energetic electron beam. The beam is then directed towards a vertical 2 mm radius collimator and, after traversing sequentially a 12.5 μm thick Mylar foil and a 14.5 μm thick black polycarbonate sheet, finally enters into the light-tight chamber containing the detection set-up. In particular, the Mylar foil serves as a separation between the primary vacuum made inside the spectrometer and the atmospheric pressure kept inside the external chamber, whereas the polycarbonate film, owing to its well-known property of highly efficient light transmission, has been introduced to guarantee the dark state operational condition required by the overhanging detectors.
A schematic representation of the transverse section of the electron spectrometer is reported in Fig. D.1.

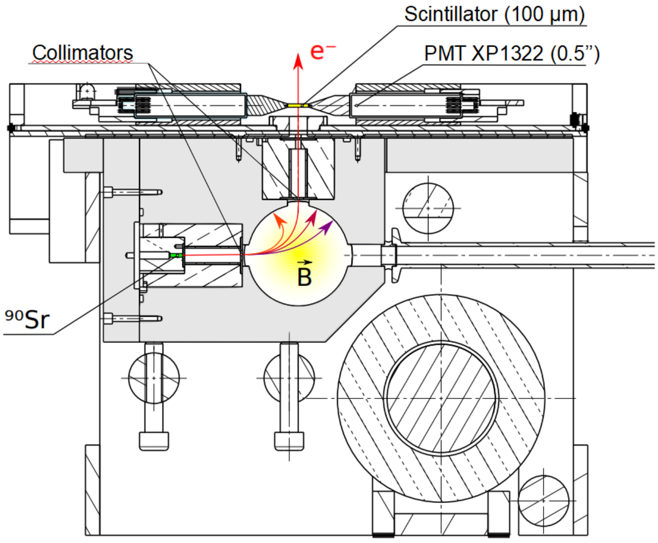

Figure D.1: Schematic sectional view of the electron beam spectrometer available at LP2I Bordeaux. Electrons, produced continuously in the β-decay of a ^{90}Sr source, are extracted and then selected in energy within a nearly uniform magnetic field region. The newly formed mono energetic electron beam is then collimated towards a light-tight box containing both the trigger module, composed of a 100 μm thick plastic scintillator coupled to two PMTs, and the thicker plastic scintillator (R = 1 cm, L = 5 cm), placed 2.5 cm above, used to collect the β-spectra.

As schematically shown in Fig. D.2, the lightproof box contains the detection set-up, composed of a system consisting in a trigger module and a plastic scintillator, explicitly conceived for the exclusive detection of spectra from the incoming mono energetic electron beam.

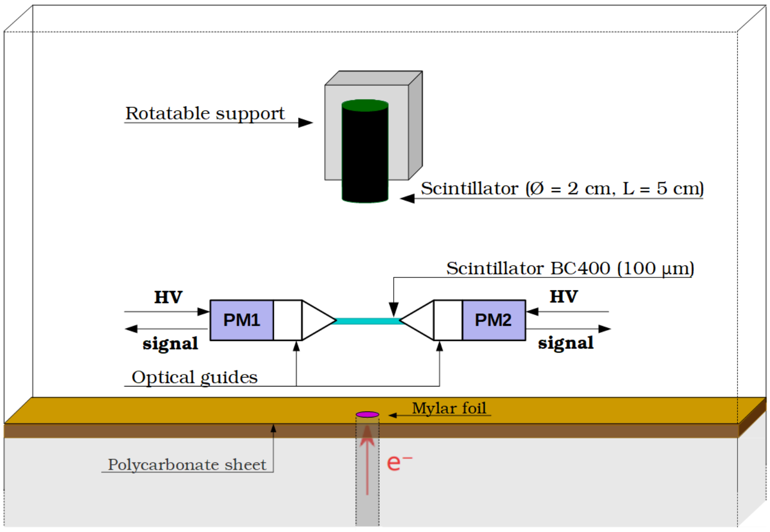

Figure D.2: Schematic sectional view of the experimental set-up coupled to the electron beam spectrometer. The primary mono energetic electron beam, coming out of the vacuum vertical collimator (dark grey) located at the very end of the electron spectrometer, first traverses sequentially a 12.5 μm Mylar foil (magenta) and the 12.5 μm polycarbonate sheet (light brown) placed at the entrance of the light-tight detection chamber (dark brown) containing the detection set-up, kept at atmospheric pressure. Successively, after eventually losing part of their energies in collisions with the molecules of air, electrons mainly pass through the trigger module, composed of a thin plastic scintillator (cyan) connected via optical guides (white) to two photomultiplier tubes (PMTs, blue), and are then finally detected by a thicker plastic scintillator (green), wrapped into a few mm layer of insulation tape (black), placed on a rotatable support (grey) and connected to a PMT.

Specifically, the trigger module comprehends a thin rectangular BC-400 100 μm thickness plastic scintillator, placed 1.1 cm above the polycarbonate film and coupled at each of its extremities to a Hamamatsu R9880U-100 photomultiplier tube (PMT) by means of the EJ-550 Optical Grade Silicone Grease, characterized by excellent optical transmission properties into the near-ultraviolet region, which corresponds precisely to the average wavelength of the scintillation photons created inside the thin plastic scintillator as a consequence of the energy lost by the incoming electrons. The analogical output signals produced by the PMTs of the trigger module are then dispatched to the FASTER acquisition system; subsequently, if both above their respective discrimination thresholds and collected within the same time integration window, they constitute the trigger for the acquisition of the thicker detector placed 2.45 cm above, made again of plastic scintillator with radius of 1 cm and length of 5 cm. The scintillator is coupled to a ET HV2520CP photomultiplier tube, which finally consents the collect the electron energy spectra. Moreover, the scintillator is wrapped on its lateral side into a few mm layer of commercial black polyvinyl chloride insulation tape, which improves the effectiveness of light detection and ensures as well an even further external light-tightness, and is mounted on a mechanical support that can be rotated up to 60° in order to allow the collection of energy spectra with different relative incident angles between the incoming electron beam and the detector base surface.

The experimental set-up, as assembled at LP2I-Bordeaux during Spring 2019, is shown in Fig. D.3.

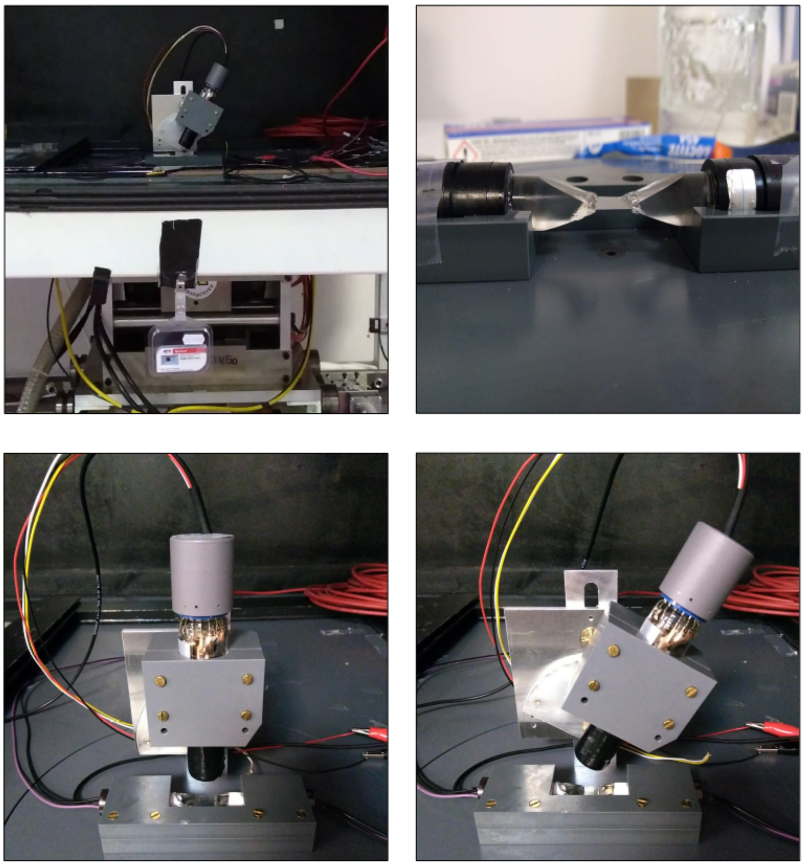

Figure D.3: Experimental set-up used for the measurements on the variation of the β-backscattering coefficient as a function of the relative incident angle between the incoming electron beam and the detector base surface. Top left: general view of the set-up; the mono energetic electron beam, after leaving the vertical spectrometer collimator, enters into the light-tight chamber kept at atmospheric pressure. Top right: trigger module placed above the spectrometer collimator, composed of a thin plastic scintillator held by two optical guides coupled to the respective PMTs. Bottom left: plastic scintillator, placed at $\theta = 0°$ above the trigger module in its rotatable support, coupled to its PMT. Bottom right: plastic scintillator rotated at $\theta = 40°$ with respect to the incoming beam direction.

All the experimental set-up is kept at atmospheric pressure; consequently, the collected β-energy spectra will systematically suffer of a broadening of the primary electron energy spectrum due to the energy loss due to straggling in air. Effectively, the primary electron beam, as soon as it leaves the vertical collimator still placed in a primary vacuum, comes across the air and then stochastically loses energy by both elastic and inelastic collisions with the air molecules or cluster of atoms acting as a unit, inducing then mainly excitations and dissociations of the air species with associated sporadic creation of energetic secondary electrons and resulting globally into a non-negligible energy degradation and mean angular deviation with respect to the original straight path hounded in vacuum.

Basically, this experimental set-up aims to partially reproduce the scenario depicted in WISArD, where the positrons emitted from the ^{32}Ar spiral along the magnetic field lines and consequently enter into the plastic scintillator, specifically conceived for β-particle detection, with different incident angles which, in this case, depend on the orientation of their initial velocity with respect to the magnetic field vector. A dedicated experimental campaign making use of the aforementioned experimental set-up, along with the corresponding data analysis and comparison to the related Geant4 simulations, will then permit to verify independently the accuracy of Geant4 in its replication of the β-spectra collected by a plastic scintillator; in particular, specific attention will be held to the reproduction of the electron low-energy regions, which correspond experimentally to the pool of data located around the β-detector threshold and whose numerical simulation is known to be strongly dependent on the different algorithms adopted for treating the multiple Coulomb scattering, implemented within the Geant4 code itself.
In the following, the experimental campaign specifically devoted to the precise study of the electron backscattering inside the thicker plastic scintillator will be presented and an overall discussion on the comparison with the related Geant4 simulations will be illustrated.

D.2.1 Data taking

Several runs were acquired by varying both the energy of the incoming electron beam and the inclination of the rotatable holder supporting the thick plastic scintillator, *i.e.* the relative incident angle between the incoming electrons and the normal to the detector base surface. Namely, the electron beam energies were varied from a minimum of 0.7 up to 1.4 MeV and three different angle positions were tested, displacing the upper β-detector at 0°, 20° and 40° with respect to the axis of the spectrometer vertical collimator. The correspondence between run numbers, primary electron beam energies and relative incident angles between the β-detector and the incoming beam finally considered for further analysis is summarized in Table D.2.

Run number	E_e **[MeV]**	θ **[°]**
4	1.0	0
5	1.2	
6	0.8	
8	0.7	
13	1.0	20
15	0.8	
17	0.7	
18	1.2	
19	1.4	
29	1.2	40
30	0.8	
31	1.4	
32	0.7	

Table D.2: Summary of the correspondence between run numbers, primary electron beam energies and relative incident angles between the β-detector and the incoming beam related to the runs selected for the further data analysis. Some runs have been discarded as acquired at the same beam energy and detector geometrical configuration, or as a consequence of the severe energy degradation in the collected spectra due to the progressive optical grease softening and evaporation during data taking. Detection thresholds have been lowered for the two PMTs of the trigger module and instead increased for the β-detector between run 8 and run 13.

D.2.2 Data analysis

The analogical output signals produced by the three PMTs have been all amplified, converted into digital values via an ADC module and finally dispatched to a common FASTER acquisition system.

In particular, the signals coming out of the two PMTs composing the trigger module, if both above their respective discrimination thresholds and collected within the same time integration window, constitute the trigger to start the acquisition of the β-detector placed above. Effectively, the probability of interaction of the few *bremsstrahlung* photons originated by the incoming electron beam in collisions with the materials surrounding the spectrometer is fairly negligible inside the 100 μm thick plastic scintillator of the trigger module, whereas the average energy lost inside it by the incoming electrons is around 20 keV; the trigger module permits therefore to start the acquisition of the β-detector by discriminating on the signals created almost entirely by the passage of electrons inside it or, with a significantly smaller contribution, by high-energy cosmic rays. All the three signal outputs, in case of a detection in coincidence triggered by the two PMTs of the trigger module, are then registered into three distinct *TLeaves* and so considered as a new grouped entry in the related *TTree* generated inside the newly created ROOT file referred to the particular experimental run currently under data taking.

An example of the signals recorded by the two PMTs composing the trigger module, namely PM1 and PM2, and consequently by the β-detector placed above is reported in Fig. D.4.

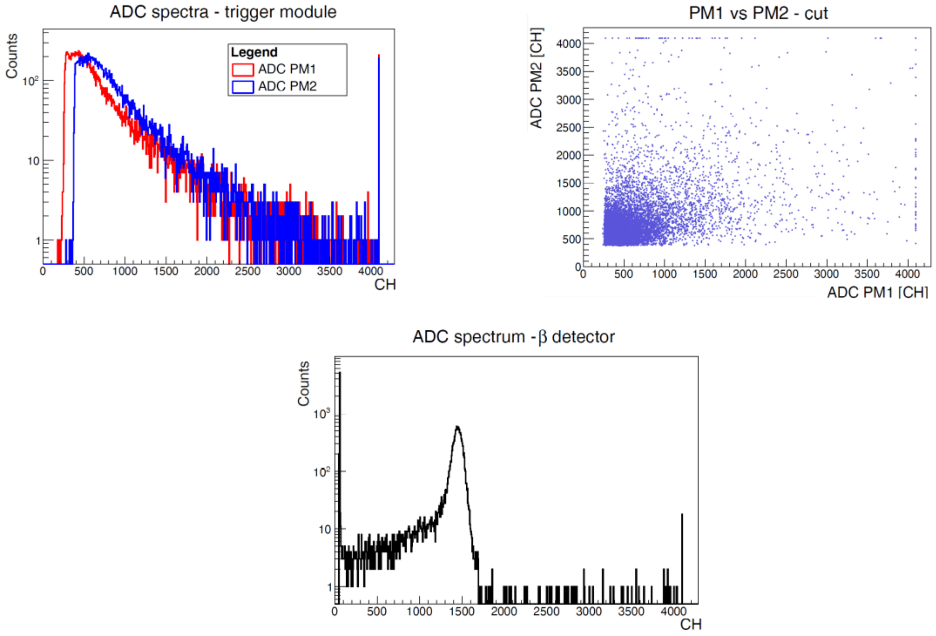

Figure D.4: ADC spectra acquired for run 4 (E_e = 1.0 MeV, $\theta = 0°$) without any cut applied. Top left: raw spectra from the two PMTs composing the trigger module. Top right: 2-D histogram reporting the PM1 spectrum as a function of the PM2 one. Bottom: spectrum recorded by the β-detector placed above the trigger module, once coincidences have been detected by the trigger module.

Primarily, a customary routine has been applied systematically to all runs in order to get rid of the very low-energy events originated mainly from the electronic noise of the PMTs of the trigger module, with the final aim to discard the fake events which are indeed recorded as a coincidence by the trigger module but are in fact not due to a real energy deposition of the incoming beam electrons inside it. In practice, a methodical cut on the sum of the signals coming from the trigger has been applied as a condition to fill in the corresponding β-detector spectrum; specifically, as both the PM1 and PM2 triggering thresholds have been set for all runs to a voltage corresponding to ADC channels comprised between 300 and 500, the β-detector spectra have been replenished only whether the sum of the PM1 and PM2

ADC values related to each entry of the *TTrees* stored in the ROOT files associated to the diverse experimental runs was in all cases superior to channel 1000 (runs taken at θ = 0°) or to channel 600 (runs taken at θ = 20° and 40°, right after a lowering of the PMTs thresholds during data taking).

An example of the cuts applied on the signals recorded by the two PMTs composing the trigger module and consequently on the β-detector spectrum is reported in Fig. D.5.

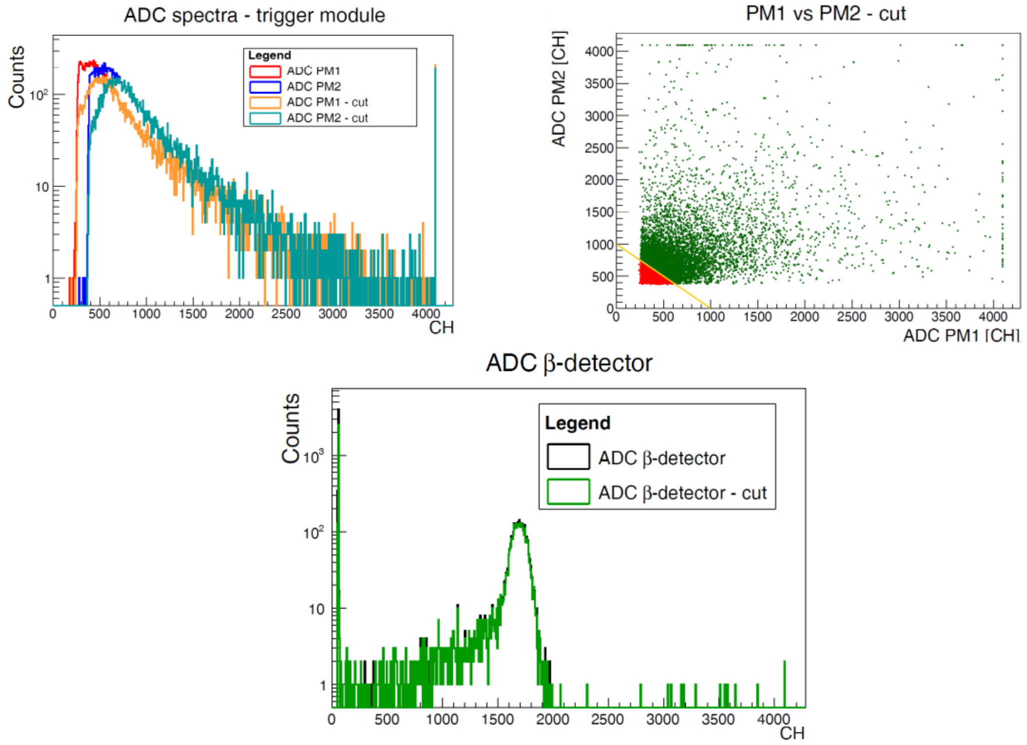

Figure D.5: Raw and cut ADC spectra acquired for run 4 (E_e = 1.0 MeV, $\theta = 0°$). Top left: raw (red and blue) and cut (orange and aqua) spectra from the two PMTs composing the trigger module. Top right: 2-D histogram reporting the PM1 spectrum as a function of the PM2 one, divided obliquely by the line corresponding to the cut applied (orange) into two regions, respectively the cut one (red) and the one considered for the further analysis (dark green). Bottom: raw (black) and cut (light green) spectrum recorded by the β-detector.

In particular, the effects of the cuts on the acquired β-detector spectra have been quantified in terms of the percentage of events present in the newly filled β-spectra with respect to the initial total number of events reported in the raw, not-cut β-detector ADC spectra. The corresponding values, computed for all runs and related to both the total spectrum and the signal energy region, are recorded in Table D.3.

Run number	E_e **[MeV]**	θ [°]	$N_{entries}$ **after cut [%]**	
			Total integral	**Integral after noise peak**
4	1.0	0	77.8	94.2
5	1.2		49.6	94.3
6	0.8		85.7	94.6
8	0.7		78.2	94.7
13	1.0	20	94.6	95.9
15	0.8		95.7	96.4
17	0.7		95.0	96.7
18	1.2		59.1	96.3
19	1.4		73.3	96.2
29	1.2	40	93.4	95.5
30	0.8		93.6	95.6
31	1.4		93.6	95.3
32	0.7		93.8	95.5

Table D.3: Summary of the correspondence between run numbers, primary electron beam energies, relative incident angles between the β-detector and the incoming beam and the percentages of events present in the β-spectra after the application of the cut selection on the signals coming out of PM1 and PM2. Percentages have been computed for all runs both as the ratio between the total number of entries in the collected ADC spectra (before and after the application of the cut) and as the ratio of the integral of the spectra after channel 300, so surely after the peak mainly related to the PMT electronic noise (before and after the application of the cut).

The percentages of events present in the β-spectra after the application of the cut selection on the signals coming out of PM1 and PM2, reported in Table D.3, have been computed for all runs in two different ways, respectively as the percentage ratio between the total integral of each ADC spectrum before and after the application of the cut and as the ratio between the integral of the region located after the noise peak ($\sim$ 300 CH for all runs) indeed before and after the cut selection. Thereby, the first value permits to evaluate the overall effect of the cut on the final β-spectra in both the noise and the signal regions, corresponding respectively for all runs to the areas before and after channel 300; on the contrary, the second value allows to estimate the cut repercussions on the β-detector ADC spectra in the region surely above the noise peak, corresponding then to the signals associated to a non-negligible energy deposit within all the detectors, due to a coincident passage principally of β-particles, and to a minor extent of high-energy cosmic rays, sequentially inside the thin scintillator of the trigger module and, afterwards, in the β-detector placed above.

As shown in Table D.3, all the percentages related to the ratio between the total integral of the spectra before and after the cut selection result systematically lower with respect to the corresponding values computed as the ratio between the non-cut and the cut signal region

(CH > 300); this characteristics, particularly evident for all runs acquired at $\theta = 0^\circ$ and less pronounced for the remaining runs collected at $\theta = 20^\circ$ and $\theta = 40^\circ$ as a consequence of the higher β-detector threshold set for these runs during data taking, indicates quantitatively that the cut procedure has been applied in all cases fairly correctly, resulting for all runs in a systematic discard of the entries related to the very low energetic coincidences recorded by the PMTs of the trigger module, which are principally associated to the electronic noise and indeed not to a passage of energetic electrons inside it. In parallel, as well, the fact that the percentage ratios related to the cut effects on the electron signal regions are all stable at around 95% indicates that the large majority of events detected as a coincidence by the trigger module and indeed related to the energy deposit of β-particles inside the thick plastic scintillator are generally preserved after the application of the cut itself.

A common energy calibration is therefore required in order to provide a universal energy-referenced scale and allow later on a comparison of the collected experimental data with the related Geant4 simulated spectra. Each peak present in the ADC spectra, corresponding in terms of energy to the difference between the selected energy of the incoming electron beam for the given run under analysis and the average energy lost by these mono-energetic electrons inside the thin plastic scintillator of the trigger module, has been therefore fitted via a pure Gaussian function; each electron peak energy has then been plotted, independently for runs taken at $\theta = 0^\circ$, 20° and 40°, as a function of the corresponding channel mean value returned by the related Gaussian fit and, subsequently, the three associated linear energy calibration functions, different for each angle configuration, have yet been determined as a result of the interpolation of all the plotted energy-channel peak correspondences.

An example of a Gaussian fit applied on a raw ADC spectrum after the application of the cut selection, as well as the different linear energy calibration functions and corresponding energy resolution functions determined for runs at $\theta = 0^\circ$, 20° and 40° are reported in Fig. D.6.

As shown in Fig. D.6, all the three linear calibration functions perfectly fit the corresponding data points; in particular, the function related to the runs taken at $\theta = 0^\circ$ is characterized by a lower angular coefficient, whereas the functions associated to the runs at $\theta = 20^\circ$ and 40° respectively, which are perfectly superposed but reported as slightly vertically shifted for a better graphics visualisation, are identified by a more pronounced slope.

Furthermore, the correlated energy resolution functions, determined as the linear interpolation of the widths returned by the Gaussian fits as a function of the corresponding square root of the electron energy peaks, result as well perfectly adapted to the experimental data. In principle, a progressive degradation of the energy resolution is attended to take place between runs acquired at steadily higher inclinations of the β-detector with respect to the direction of

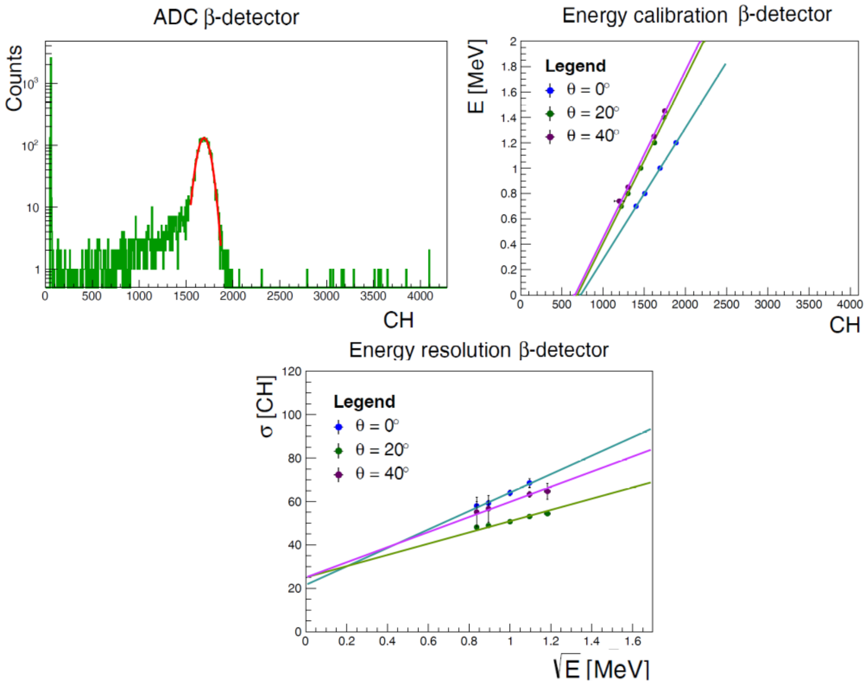

Figure D.6: Extrapolation of the linear energy calibration functions. Top left: Gaussian fit (red) applied on the cut spectrum of the β-detector for run 4 (E_E = 1.0 MeV, θ = 0°). Top right: linear energy calibration functions for runs at θ = 0° (blue), 20° (green) and 40° (purple); purple points and the corresponding calibration line are slightly vertically shifted for graphics purpose. Bottom: corresponding energy resolution functions. The intercept should normally be much closer to zero if the resolution was dominated by the statistics of photons. In this case, at low energy, contributions from the trigger scintillator and from straggling in the air play a significant role.

the incoming electron beam, as a combined consequence of the different spread in terms of the energy lost by the incoming β-particles travelling through a diverse longitudinal breadth of air before reaching the detector base and also because of the more pronounced spread in energy due to the related incremented probability of being backscattered on the detector itself. Practically, the degradation in the detector energy resolution, is clearly visible for the runs acquired in configurations with the detector inclined with respect to the ones recorded with the detector placed on the longitudinal axis of the incoming beam. Such anomaly is potentially due to the fact that the central runs ($13 < N_{run} < 29$) have been recorded precisely during the severe heat wave that stroke Bordeaux, which caused repeated problems of progressive softening and evaporation of the optical grease used to couple the plastic scintillators to their respective PMTs, yet resulting in a non perfect optical coupling and so in a systematic loss in resolution in the recorded β-spectra.

The superposed energy-converted experimental spectra are shown in Fig. D.7.

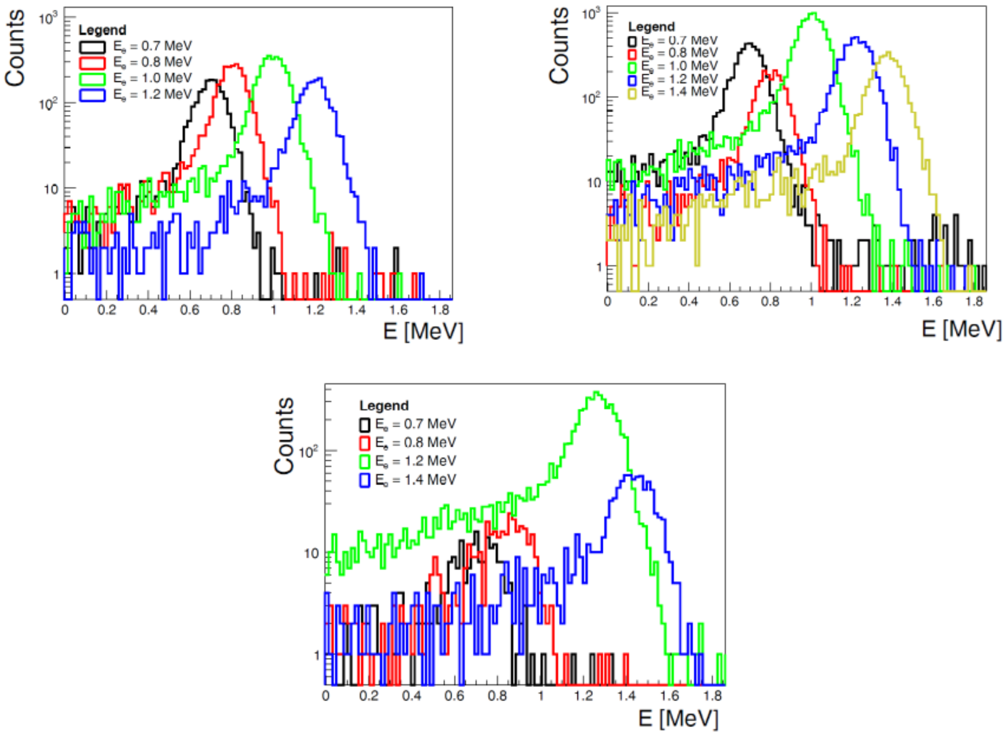

Figure D.7: Superposition of the calibrated experimental spectra at $\theta = 0^\circ$ (top left), $\theta = 20^\circ$ (top right) and $\theta = 40^\circ$ (bottom).

D.2.3 Geant4 simulations

Monte Carlo simulations based on the Geant4 toolkit (version 10.5.p01) were performed to re-produce all the runs taken with the mono energetic electron spectrometer (details reported in Table D.2). First, a realistic replica of the experimental set-up has been implemented in the simulations. The geometry of the detection set-up, as schematically sketched in Fig. D.2, comprehensive of the reproduction of the incoming electron beam is shown in Fig. D.8. The list of all generic physics processes, consisting in particle definitions, radiation and electrically charged-particle interactions with matter, has been set up from prearranged, standard packages that guarantee the employment of well-validated combinations of theoretical and phenomenological physics approaches. Geant4 offers in fact a variety of ready-made models specifically designed to deal with physical processes within different energy ranges, routinely validated and updated at each version release [140].

All the acquired experimental runs, whose details are reported in Table D.2, have been simulated. In particular, each run has been reproduced independently seven times, every time varying the implementation of the *PhysicsList*, the dedicated class comprehensive of the algorithms entailed to model in different ways the electromagnetic interactions with matter.

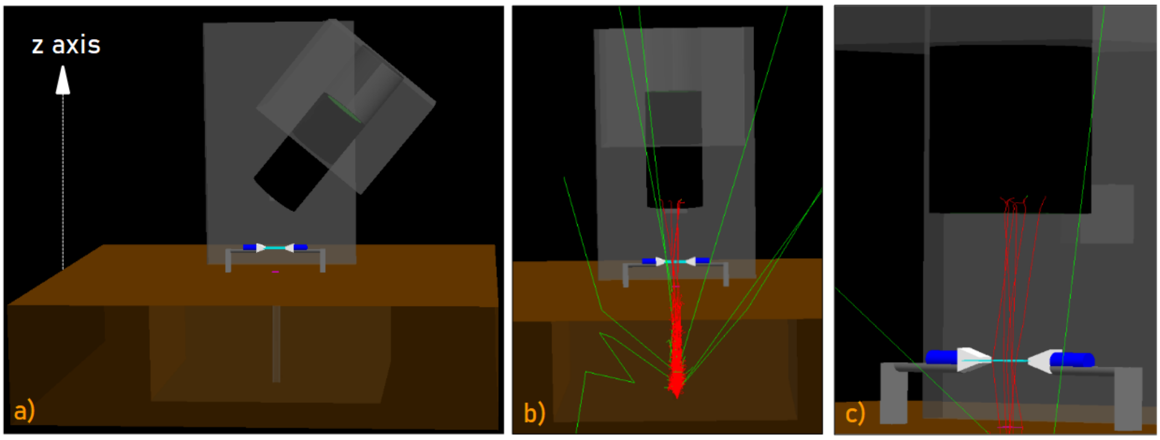

Figure D.8: Visualization of the geometric configuration of the electron spectrometer and detection set-up as implemented within the Geant4 simulations. The primary mono energetic electron beam, coming out of the vacuum vertical collimator (dark grey) located at the very end of the electron spectrometer, traverses sequentially a Mylar foil (magenta) and a polycarbonate sheet (light brown) located at the entrance of the light-tight box kept at atmospheric pressure; then, after eventually losing energy in collisions with the molecules of air, mainly passes through the trigger module, composed of a thin plastic scintillator (cyan) connected via optical guides (white) to two photomultiplier tubes (PMTs, blue) placed on their mechanical supports (light grey) and are then finally detected by a thicker plastic scintillator (green), wrapped into a few mm layer of insulation tape (black) and placed in a rotatable support (grey). An overall view of the set-up, as well as a simulation of the incoming beam (electrons in red and *bremsstrahlung* photons in green) and the corresponding zoom on the detection area are shown in fig. a), b) and c), respectively.

Specifically, the diverse physics models provided by Geant4, nevertheless all quantitatively validated in common case studies and capable of generating global results in excellent agreement with the reference data of the United States National Institute of Standards and Technologies (NIST, [179, 180]) [181, 182], indeed largely differ from each other at the level of the algorithms implemented to replicate the transport and the interactions of the electrons with matter and, particularly, in the description of both electron single (SS) and multiple Coulomb scattering (MCS). Therefore, in order to quantitatively evaluate afterwards the differences between the β-spectra reproductions provided by the diverse algorithms implemented within the *PhysicsList*, all the experimental runs have been reproduced by using the following *PhysicsLists*:

- *Single – Scattering*, entirely based on the original Wentzel analytical derivation of the electron scattering functions [183]. Highly accurate and reliable, it traditionally provides a physics benchmark for all the other MCS-based models, but at the cost of sensibly longer computation time;

- $Wentzel - VI$, based on a combination of single scattering and multiple scattering models, where larger scattering angles are modeled from the original Wentzel single scattering model [183] and smaller angles are derived by a modified multiple scattering approach [164];

- $Goudsmit - Saunderson$, implementing uniquely the Goudsmit-Saunderson model [143, 144] to treat β-particles at all energies;

- *emstandard_opt4* : for β-particles, multiple Coulomb scattering is handled by the Goudsmit-Saunderson model ($0 < E_e < 100$ MeV) combined with the single Coulomb scattering model, applied for larger scattering angles;

- *Livermore*: for β-particles, multiple Coulomb scattering is handled by the Goudsmit-Saunderson model at low energy ($E_e \leq 1$ MeV) and by the WentzelVI model at higher energies, together with the single Coulomb scattering model, which is applied indeed again for large scattering angles;

- $Penelope$: taylor-made low-energy models are used for γ-rays and β-particles below 1 GeV and are in both cases based on algorithms originally implemented in PENELOPE (Penetration and ENErgy LOss of Positrons and Electrons) [184], a general-purpose Monte Carlo code system alternative to Geant4 used for simulation of electron and photon transport and interactions in arbitrary materials. Above 1 GeV and for all other charged particles the algorithms are the same implemented in *emstandard_opt4* ;

- *LowEMEnergyPhysics*: allows to simulate electron multiple scattering by using data-driven algorithms based on the Livermore data libraries [168–170]. Additionally, it reproduces Compton scattering via an alternative computational model specifically developed by the Monash University.

Simulated runs have been analyzed in the same way of the experimental ADC spectra. Details related to the analysis and comparisons between the simulated and the experimental spectra will be discussed in Sec. D.2.4.

D.2.4 Comparison between experimental data and Geant4 simulations

Systematic studies on all the acquired runs have been performed in order to determine the variation of the experimental β-backscattering coefficient as a function of both the kinetic energy and the relative incident angle of the incoming electron beam with respect to the base surface of the thick plastic scintillator. In parallel, comparisons between the experimental and the simulated β-spectra collected by the thick plastic scintillator will permit to quantitatively ascertain the differences among the diverse implemented *PhysicsLists* concerning the reproduction of the low-energy β-spectrum, which is almost entirely determined by the backscattering of β-particles on the thick plastic scintillator.

In particular, the replicated β-spectra collected by the thick plastic scintillator, each of them related to a given experimental configuration and simulated by means of seven different *PhysicsLists*, have all been replenished only whether the incoming particles had previously deposited energy within the thin plastic scintillator of the trigger module. Moreover, as detailed in Sec. D.2.2, both the energy calibration and the energy resolution functions have been retrieved for all the three tested angle configurations from an interpolation of the positions and widths of their respective Gaussian fits to the electron peaks in the ADC spectra. Depending each on two parameters, these two functions assume respectively the following forms:

$$E[MeV] = a + b \cdot CH \tag{D.1}$$

$$\sigma[MeV] = c + d \cdot \sqrt{E} \tag{D.2}$$

where a, b, c and d are the coefficients obtained from the respective linear regressions.

In particular, the former formula has been used to convert the experimental ADC spectra into the corresponding energy spectra, while the latter has been used to smear the simulated spectra with the energy resolution of the plastic scintillator.

Therefore, for all the considered experimental configurations, the seven related simulated β-spectra have then been scaled and superimposed to the corresponding experimental β-spectrum, previously cut with respect to the sum of the signals coming from the two PMTs of the trigger module, in order to directly provide a qualitative juxtaposition and yet allow, subsequently, a quantitative comparison on the β-backscattering reproduction by the different numerical algorithms implemented within the diverse *PhysicsList*. Nevertheless, it should be remarked that the values of a, b, c and d coefficients extracted from the different linear function shown in Eq. D.1 and in Eq. D.2 do not represent directly the parameter values allowing the maximal agreement between experiment and simulation, but rather a good starting point to finally retrieve them. Effectively, the only method guaranteed to converge to the global minimum of this optimisation problem is given by a complete exploration of the parameter space; this can be done by using as departure points the coefficient values obtained by the linear fits on the experimental runs and then by applying a gradient descend, an optimization algorithm specifically implemented to find the set of a, b, c and d parameters that minimizes the χ^2 value between experimental and simulated histograms by iteratively moving in the direction of steepest descent as defined by the negative of the χ^2-gradient as a function of these five coefficients. Moreover, as a complete scan of the continuous parameter space is not possible, the gradient descent algorithm can be applied to define a smaller subspace of discrete parameter value changes such that an adequately sampled grid search may be defined. In particular, each coefficient has been varied in the range [-2σ_{err}, 2σ_{err}] around the initial value, with σ_{err} representing the respective coefficient errors coming from initial data fits, and combinations with different parameter values have been computed. Finally, the set of a, b, c and d parameters corresponding to the minimum χ^2 value has been applied on both experimental and simulated spectra for a given run to respectively describe and reproduce in the most precise way possible the experimental β-detector characteristics, as well as to allow later on quantitative conclusions on the accuracy with which Geant4 can reproduce the collected experimental β-energy spectra.

An example of simulated spectra computed with different *PhysicsLists*, each of them smeared with the corresponding experimental one by using the same pool of parameters and superimposed to the corresponding experimental spectrum, is reported in Fig. D.9.

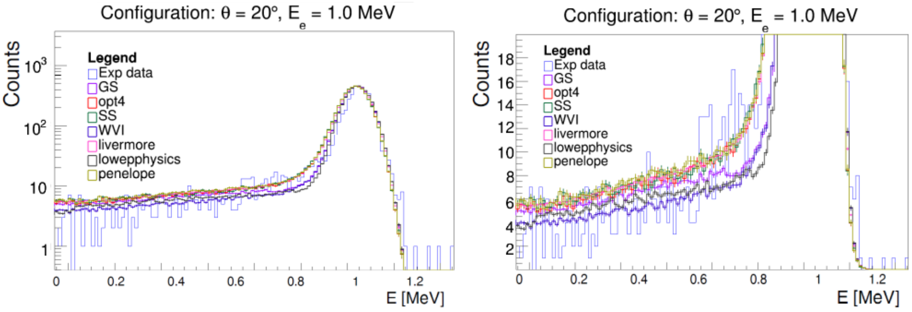

Figure D.9: Comparison between experimental and simulated spectra reproduced with different *PhysicsLists* for run 13 (measurement at E_e = 1.0 MeV and θ = 20°). Superimposed calibrated experimental β-spectrum (light blue) and smeared Geant4 spectra simulated with *GoudsmitSaunderson* (GS, purple), *emstandard_opt4* (opt4, red), *Single-Scattering* (SS, green), Wentzel-VI (WVI, dark blue), *Livermore* (pink), *LowEMEnergyPhysics* (lowwpphysics, gray) and *Penelope* (yellow) *PhysicsLists* are shown, respectively, for the overall spectrum (left) and zoomed in the low-energy region (right).

Subsequently, a quantitative comparison on the reproduction of the low-energy region of the collected electron spectra performed by the different *PhysicsLists*, which is almost entirely affected by the backscattering of β-particles, has been accomplished. Effectively, as the kinetic energy of the incoming electron beam had been preset for each run via the software program connected to the spectrometer electronic control boards, all the incoming β-particles are expected to lose the same amount of energy inside the thick plastic scintillator, specifically equal to the difference between their initial kinetic energy and the energy lost inside the thin plastic scintillator of the trigger module (around 20 keV), and, therefore, they are expected to be reported as counts located roughly at the same channel in the corresponding β-detector ADC spectrum. Nevertheless, mainly owing to the β-backscattering and to a much less extent to the broadening of the incoming energy distribution consequent to the multiple electron scattering in air, electrons have a certain probability of being ejected by the plastic scintillator once just got in, depositing so only a certain fraction of their original kinetic energy within the β-detector.

Practically, these probabilities, commonly referred to as β-backscattering ratios, have been computed for all runs for both the experimental and the seven simulated spectra related to the energy collection of the thick plastic scintillator. In particular, each coefficient has been obtained as the ratio between the integral of the background continuum region (from 0 MeV up to left inflection point beyond which the Gaussian peak is located) and the total integral of the corresponding β-spectrum; the statistic errors were propagated and studies by varying ten times the integral ranges on each background region were performed, thus allowing for an estimation of the systematic uncertainties.

In particular, β-backscattering coefficients computed on both the experimental and all the simulated collected electron spectra characterized by the highest statistics for the three tested angle configurations (runs 4, 13 and 31 for $\theta = 0°$, $\theta = 20°$ and $\theta = 40°$ respectively, details in Tab. D.2), along with their relative statistic and systematic uncertainties, are reported in Table D.4. From Table D.4, it can be noticed that the *PhysicsLists* systematically better reproducing the experimental results are *Penelope* and *Goudsmit Saunderson*, which had been effectively developed to treat with the highest precision possible the numerical reproduction of the low-energy β-particle interaction with matter. Further studies performed to independently crosscheck these observations will be detailed in the following.

Configuration	Type	Backscattering coefficient [%]
E = 1.0 MeV, θ = 0°	Experimental	8.58 ± 0.45 (stat.) ± 0.51 (syst.)
	Penelope	9.05 ± 0.05 (stat.) ± 0.40 (syst.)
	GS	8.86 ± 0.04 (stat.) ± 0.49 (syst.)
	opt4	8.88 ± 0.05 (stat.) ± 0.41 (syst.)
	Livermore	8.86 ± 0.05 (stat.) ± 0.40 (syst.)
	LowEMEnPhysics	6.84 ± 0.03 (stat.) ± 0.57 (syst.)
	SS	9.17 ± 0.05 (stat.) ± 0.40 (syst.)
	WVI	6.40 ± 0.03 (stat.) ± 0.61 (syst.)
E = 1.0 MeV, θ = 20°	Experimental	9.87 ± 0.48 (stat.) ± 0.44 (syst.)
	Penelope	10.12 ± 0.06 (stat.) ± 0.34 (syst.)
	GS	9.53 ± 0.04 (stat.) ± 0.32 (syst.)
	opt4	10.48 ± 0.06 (stat.) ± 0.35 (syst.)
	Livermore	10.32 ± 0.05 (stat.) ± 0.34 (syst.)
	LowEMEnPhysics	8.39 ± 0.04 (stat.) ± 0.47 (syst.)
	SS	10.67 ± 0.06 (stat.) ± 0.34 (syst.)
	WVI	7.82 ± 0.04 (stat.) ± 0.50 (syst.)
E = 1.4 MeV, θ = 40°	Experimental	17.14 ± 1.40 (stat.) ± 1.14 (syst.)
	Penelope	15.23 ± 0.06 (stat.) ± 1.19 (syst.)
	GS	16.75 ± 0.05 (stat.) ± 1.38 (syst.)
	opt4	15.14 ± 0.06 (stat.) ± 1.20 (syst.)
	Livermore	15.10 ± 0.05 (stat.) ± 1.22 (syst.)
	LowEMEnPhysics	12.89 ± 0.05 (stat.) ± 1.50 (syst.)
	SS	15.12 ± 0.06 (stat.) ± 1.20 (syst.)
	WVI	11.93 ± 0.04 (stat.) ± 1.62 (syst.)

Table D.4: Summary of the correspondence between the experimental configuration (energy of the electron beam and relative beam incident angle with respect to the detector), experimental or *PhysicLists* implemented within the simulations and corresponding β-backscattering coefficients, along with their relative statistic and systematic uncertainties. Only values related to the runs acquired with the highest statistics for each angle configuration (θ = 0°, 20° and 40°) are reported.

D.3 Tests with radioactive sources with the WISArD 2019 detection set-up

By employing the detection set-up formerly used for the WISArD proof-of-principle experiment in 2019 (for more details see Sec. 2.3.2), a further additional campaign has been performed at the WISArD experiment.

D.3.1 Data taking

From the 1^{st} of July to the 10^{th} of July 2019 ($\sim$ 130 h of data acquisition) a total of 36 runs were collected, each of them characterized by the employment of different radioactive sources and magnetic field intensities. The set of measurements has been organized as follows:

- 13 runs with a ^{207}Bi source (A = 20.9 kBq): it disintegrates mainly by electron capture to excited states of ^{207}Pb, which can then return to the ground state either by emitting γ-rays or conversion electrons, mainly at 481, 583 keV, 975 and 1048 keV. Experimentally, with a β-detector resolution higher than a few tenths of keV, only a mixing of the former two and the last two energy peaks can be observed. A weak transition by β^+-decay has also been reported;
- 8 runs with a ^{137}Cs source (A = 36.8 kBq): it disintegrates via β^--emission to the ground state of ^{137}Ba (5.6%) or to an excited state of ^{137}Ba (94.7%), which can return to stability either by emitting a γ-ray of 662 keV (85.1%) or through internal conversion (9.6%). The conversion electron energy is indeed lower than the γ-energy depending on the binding energy of the shell from which the electron is emitted;
- 7 runs with a multiple α-source (A_{total} = 4.6 kBq): it is made of ^{148}Gd, ^{239}Pu, ^{241}Am and ^{244}Cm, which decay emitting α-particles at main energies of respectively 3.271, 5.156, 5.486 and 5.805 MeV;
- 8 runs with a ^{133}Ba source (A = 592.8 kBq): it disintegrates primarily by electron capture to two excited levels of ^{133}Cs at 437 keV (85.4%) and 383 keV (14.5%), with three significantly minor branches to the 160 and 81 keV excited levels and to the ground state. Due to the β-detector resolution, a unique wide energy peak resulting from the mixing of all the electron capture peaks is visible.

During the online data monitoring, four runs (one for ^{207}Bi and three for ^{137}Cs) were identified as not valid due to an excessive noise in the SiPM output and so rejected from the forthcoming data analysis. The correspondence between runs and magnetic field intensities are summarized in Table D.5.

Source	**Run number**	**B (T)**
^{207}Bi	1, 2, 3, 4, **5**, 6, 7, 8, 9, 10, 11, 12, 13	0, 4, 6, 0.3, **0.4**, 1, 2, 1.5, 1, 0.5, 0.2, 0.1, 0
^{137}Cs	**14**, **15**, **16**, 17, 18, 19, 20, 21	**4**, **4**, **0**, 2, 0, 1, 0.5, 0
4-α	22, 23, 24, 25, 26, 27, 28	0, 6, 4, 2, 1, 0.5, 0
^{133}Ba	29, 30, 31, 32, 33, 34, 35, 36	0, 0, 6, 4, 2, 1, 0.5, 0

Table D.5 Summary of the correspondence between radioactive sources, run numbers and magnetic field values at which the runs were acquired. In some cases measurements at the same B field were repeated. In bold, the runs excluded from the data analysis.

D.3.2 Data analysis

In the following, the data analysis related to the spectra acquired with the multiple α-source and the conversion electron sources will be illustrated.

D.3.2.1 Multiple α-source

Each run acquired with the multiple α-source consists of seven ADC spectra corresponding to the seven silicon detectors active at the moment of the data acquisition (Si4D was disconnected and non operative). In all cases the four energy peaks coming from the decay of the four source components are clearly visible and well separated.

First, a procedure of energy calibration is needed for all detectors and all runs in order to provide a common energy-referenced scale and allow later on a comparison with the related Geant4 simulated spectra. Each ADC spectrum has then been converted into the correspondent energy spectrum through the application of a linear energy calibration function, obtained by interpolating the precisely known energy values corresponding to the α-peaks as a function of the mean values of the Gaussian fits on the energy peaks in the raw channel-based spectra. An example of a linear calibration function, with a raw and a calibrated ADC spectrum, is reported in Fig. D.10.
Then, in order to quantitatively compare the calibrated ADC spectra at different magnetic field intensities, the detection efficiency for each peak in each run has been computed. Each detection efficiency has been determined, for each run, as the integral of counts recorded by the detector at a given peak (N_p) corrected by the data acquisition time (Δt), as follows:

$$\varepsilon_p^{det,run} = \frac{N_p^{det,run}}{\Delta t_{run}} \tag{D.3}$$

Since the four energy peaks are clearly separated and do not give rise in any case to peak overlaps, integration windows for the determination of N_p have been fixed for all detectors and runs. The correspondence between α-particle energies and integration limits applied for the calculus are detailed in Table D.6.

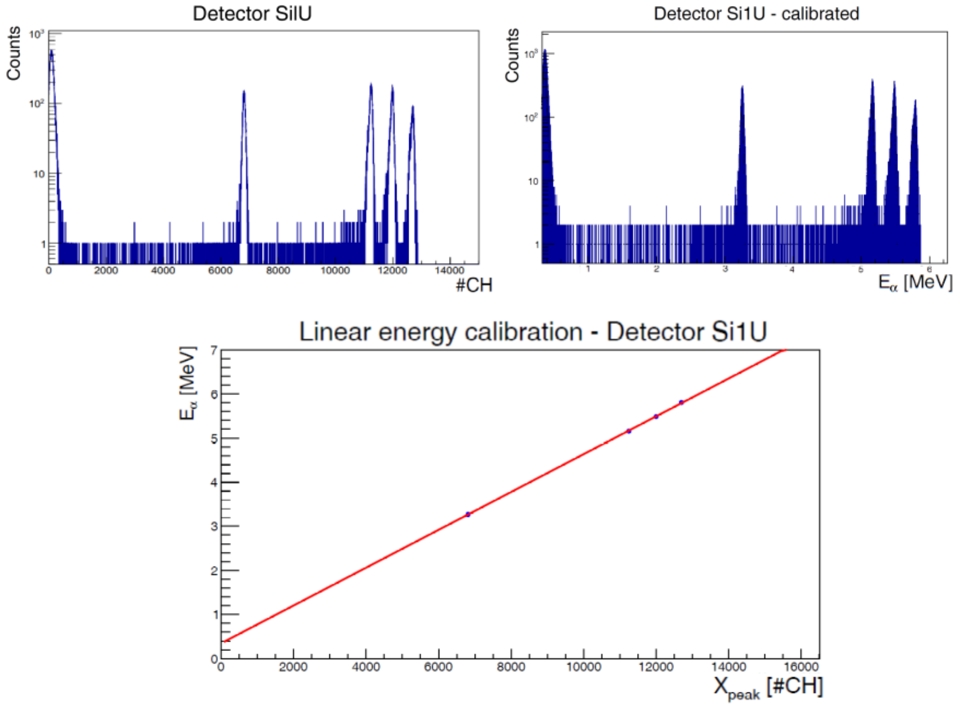

Figure D.10: Raw (top left) and calibrated (top right) QDC spectrum related to detector Si1U for run 22 (measurement at B = 0 T). The related linear energy calibration function is shown at the bottom.

Peak n.	Source	Energy [MeV]	Lower limit [MeV]	Upper limit [MeV]
1	^{148}Gd	3.271	3.100	3.400
2	^{239}Pu	5.156	5.000	5.300
3	^{241}Am	5.486	5.300	5.600
4	^{244}Cm	5.805	5.600	5.950

Table D.6: Summary of the correspondence between α-particle main peak energies and the lower and upper integration limits used for the determination of the detection efficiencies.

All the detection efficiencies have then been computed. Moreover, in order to have a common reference to compare the results at different magnetic field intensities, all the efficiencies related to each detector have been normalized to the correspondent value at B = 0 T.
In particular, between the two runs acquired in absence of magnetic field (see Table D.5), the second one (*i.e.* run 28) was singled out to be the reference at B = 0 T, both due to its higher statistics and to the fact that it was collected reasonably longer after the replacement of the source of ^{137}Cs with the multiple-α source ($\Delta t \sim 16$h), so certainly after the end of the cooling of the experimental set-up and therefore in stable experimental conditions.

Plots reporting the normalized detection efficiencies for all detectors as a function of the magnetic field are presented in Fig. D.11.

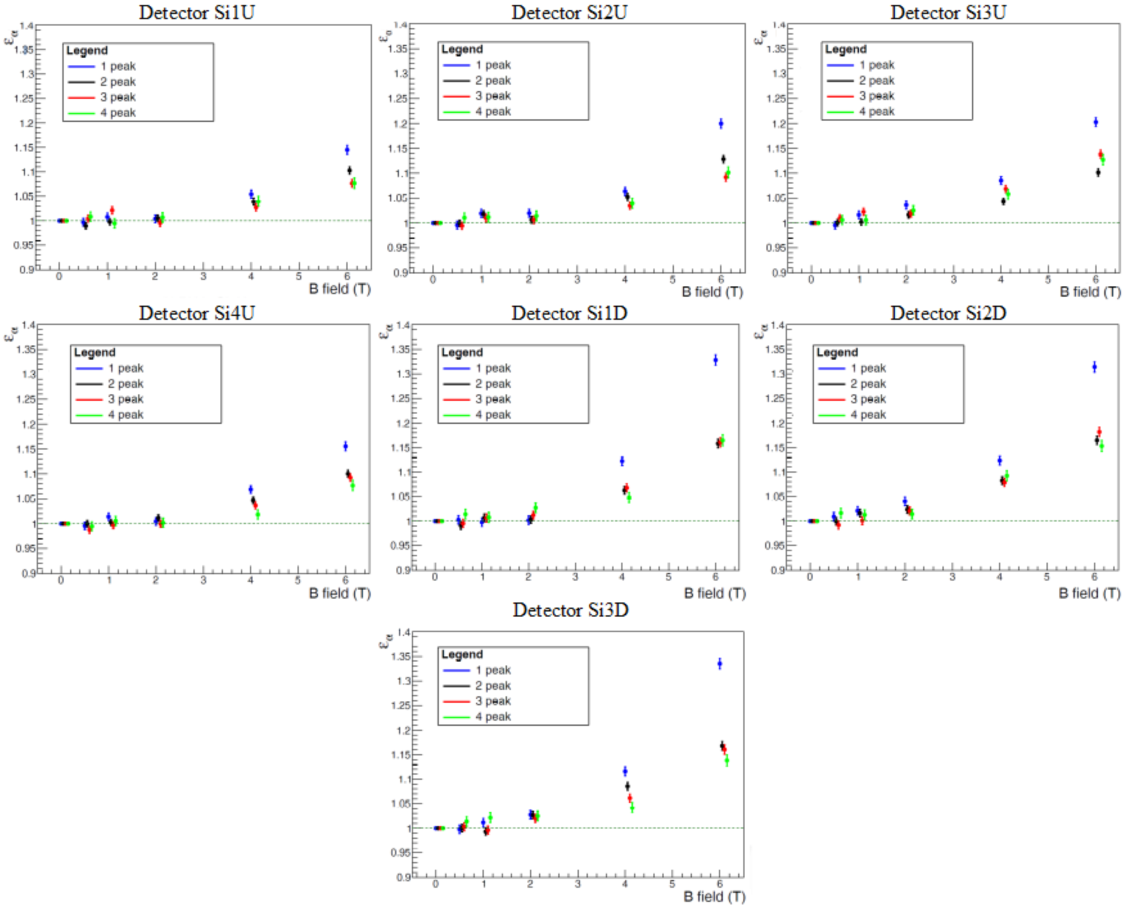

Figure D.11: Normalized experimental detection efficiencies for all silicon detectors as a function of the magnetic field intensity. In each plot, results are presented for all the α-energy peaks (^{148}Gd in blue, ^{239}Pu in black, ^{241}Am in red and ^{244}Cm in green, respectively). Values are slightly separated for visualisation purpose. The dashed green line at unity shows the reference of normalization at B = 0 T.

In all cases, as expected, the detection efficiencies increase with the magnetic field. The effect appears to be even more noticeable if considering less energetic α-particles for which, owing indeed to their lower kinetic energy, the pitch of the helical path of the particle in the magnetic field is slightly more affected by different field intensities.
Systematic differences between the efficiencies of the upper and lower detectors can be attributed to a lack of determination in the knowledge of the exact position of the radioactive source during data taking, which may not have been placed perfectly symmetrical with respect to the detection planes but rather a few mm upwards with respect to the centre of the detection set-up.

Experimental detection efficiencies can then be compared to the corresponding values obtained via Geant4-based simulations of the WISArD set-up. The level of agreement between experimental and simulated results will represent a crystalline and quantitative indicator to validate the WISArD Geant4 simulations, particularly concerning the accuracy of radioactive source reproduction and numerical calculations related to particle transportation within the magnetic field.

D.3.2.2 Conversion electron sources

Each run acquired with the different conversion electron sources consists of three QDC spectra, whose integration windows are [-10, 250], [-10, 50] and [-10, 1200] ns respectively. Further details on the correspondence between sources, run numbers and magnetic field intensities at which the measurements were performed are summed up in Table D.5.

Practically, as far as a β-particle hits the plastic scintillator, it releases its energy inside the material, resulting in a local excitation of the electrons in the crystal; excited electrons then rapidly decay, causing almost immediately ($\tau \simeq 2 \div 3$ ns) the emission of a certain amount of photons ($N_\gamma \simeq 10^4 \ \frac{photons}{MeV}$) which are then reflected inside the scintillator itself, a part of which finally hits the Geiger-mode avalanche photodiodes (APDs) that constitute the SiPM, triggering an electron avalanche that generates the current pulse detected by the DAQ and then reported in the QDC spectrum. During breakdown in an APD, a large number of carriers are then generated in the Geiger discharge; whilst most of the carriers move freely towards their respective electrodes and lead to the formation of the main current pulse, some of them may be trapped in metastable traps present in the intrinsic defects of the silicon, being subsequently released ($\tau_{delay} \simeq 10 \ \nabla\cdot \ 40$ ns) and potentially initiating additional secondary avalanches resulting in additional pulses which contribute to the observed signal as a part of the noise. In particular, shortly-delayed afterpulses which take place during the recovery time of an APD do normally have little effect, since the photodiode is still not fully charged; yet, longer delay afterpulses can alter measurements with the SiPM, with an effect that becomes more pronounced as the count rate increases. The stochastic nature of this process affects the performance of the photodetector as well as, consequently, the overall quality of the collected QDC spectra; however, since this is inevitable, one way to reduce its final impact is represented by choosing an appropriate QDC integration window, which should be reasonably wide to contain a complete current pulse generated by an electron avalanche in one of the APDs that compose the SiPM, but at the same time not too large to avoid integrating over more than one main pulse or over afterpulses created as a consequence of secondary effects in the APDs themselves.

In the following, among the three different QDC spectra acquired in different integration windows, only QDC spectra acquired in range [-10, 250] ns have been considered for the analysis.

First, spectra have been normalized to their respective acquisition times and then corrected for their respective source activity. Plots showing the superimposed normalized QDC spectra acquired per each radioactive source are shown in Fig. D.12.

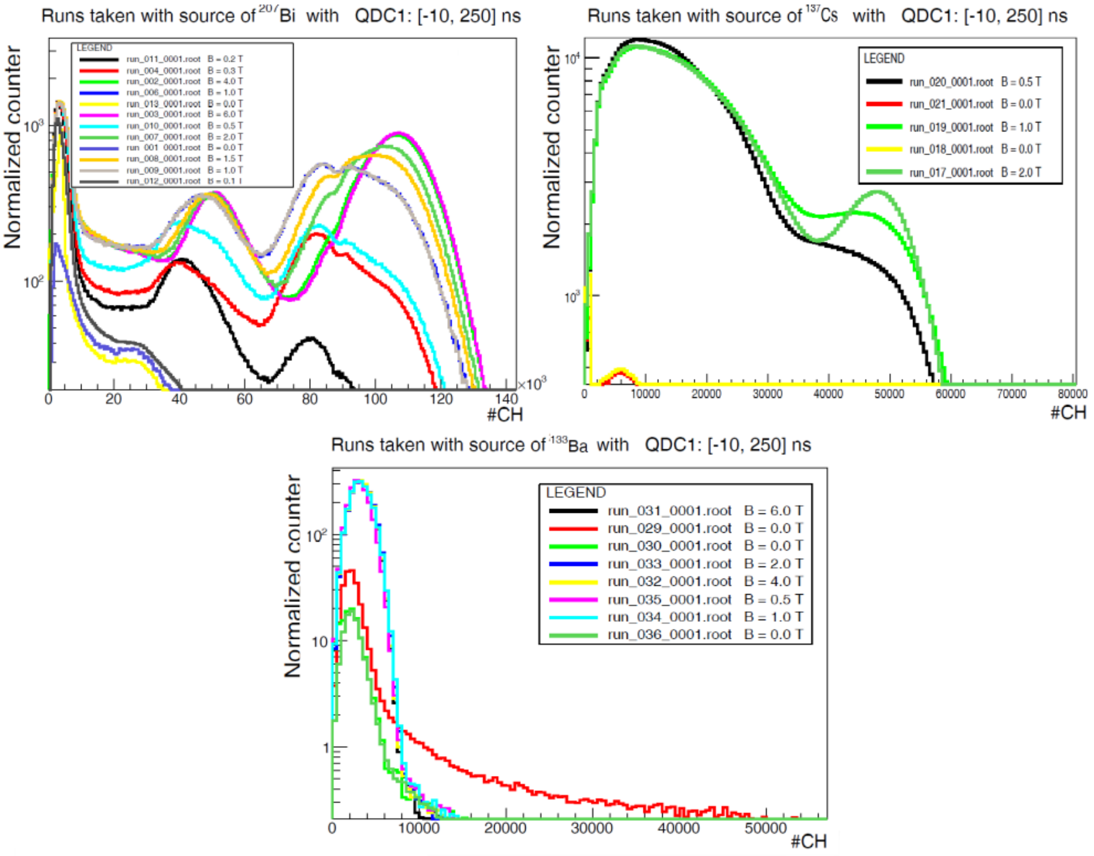

Figure D.12: Superimposed QDC spectra acquired for the ^{207}Bi (top left), the ^{137}Cs (top right) and the ^{133}Ba (bottom) source. Spectra have been normalized to their respective acquisition time and corrected for their respective source activity.

As mentioned in Sec. D.3.1, all β-sources disintegrate either by β-decay or electron capture to an excited state of the respective daughter nucleus, which can then indeed return to the ground state either by γ or conversion electron emission. In measurements with a magnetic field, as the detector set-up consists of a unique plastic scintillator coupled to a SiPM, the electron detection efficiency is expected to go up to a maximum of 50%, while the contribution to the energy spectra coming from photons, which are indeed not affected by the magnetic field, remains on the order of about 1.5%, as inferred from a geometric solid-angle efficiency calculation; in measurements with the magnetic field, the contribution of the photons to the final energy spectrum could then be considered as rather negligible. Nevertheless, since the final goal will be to study the accuracy of Geant4 simulations in reproducing experimental β-spectra, only the β-contribution should be taken into account in the QDC spectra; then, since the γ-contribution is constant at all magnetic field values, a bin-per-bin subtraction between the spectra taken at different magnetic field intensities and the respective spectrum taken at B = 0 T should be done for all runs and all radioactive sources.

In particular, as reported in Table D.5, different runs were acquired for each source at B = 0 T. Referring to Fig. D.12, the QDC spectra associated to B = 0 T are shown respectively in violet and yellow (^{207}Bi, top left), yellow and red (^{137}Cs, top right), and red, light and dark green (^{133}Ba, bottom). Apparently, only runs for the ^{137}Cs source seem to be compatible at B = 0 T; on the contrary, slight differences are visible for ^{207}Bi if comparing runs 1 (violet) and 13 (yellow), and even more pronounced disparity in the overall β-spectrum shape are evident for the three spectra of ^{133}Ba in absence of magnetic field, corresponding respectively to run 29 (red), run 30 (light green) and run 36 (dark green). Differences between these runs for each radioactive source can be attributed to the different chronological order in which these runs were acquired; effectively, while run 1 and run 29 were collected soon after the insertion of the radioactive source inside the WISArD superconducting magnet ($t \simeq 8$ h), run 13 and run 36 were recorded much later ($t \simeq 18$ h), after all the other measurements at B $\neq$ 0 T, and so certainly after the end of the cool-down of the experimental set-up and then in more stable conditions in which fluctuations of the SiPM board temperature, that can normally greatly influence its output reply, no longer occurred. Moreover, the effects of the different circumstances of data taking are reflected in the presence of much less noise in the spectra related to run 13 and 36 with respect to the correspondent spectra at run 1 and 29.

In order to single out a unique reference run in absence of magnetic field for each β-source, the criterion of considering only the spectra with a noise contribution as little as possible, consequence of more stable experimental conditions in data taking, was taken into account. Then, runs 13, 21 and 36 were considered to be the reference runs at B = 0 T for ^{207}Bi, ^{137}Cs and ^{133}Ba respectively.

A bin-per-bin subtraction between the spectra taken at different magnetic field intensities and the respective reference spectrum taken at B = 0 T was then performed for all runs and all radioactive sources. Results of subtraction are displayed in Fig. D.13.

Referring to Fig. D.13, a systematic shift of all spectra towards higher QDC channels with increasing magnetic field intensities is clearly visible for all radioactive sources, being particularly noticeable for ^{207}Bi and ^{137}Cs and less pronounced for ^{133}Ba. Furthermore, it can be noticed that the total integral of each QDC spectrum at a given β-source, already

normalized to both the source activity and the acquisition time, steadily rises with increasing magnetic field intensities; in particular, this feature becomes fairly prominent for the sharp peaks corresponding to the internally converted electrons of ^{207}Bi and ^{137}Cs.
Both these aspects represent an evident sign that the magnetic field directly affects the QDC spectra, influencing the amount of detected β-particles with a more remarkable effect on higher end-point energy β-spectra ($Q(^{207}\text{Bi})$ = 2398.8 keV, $Q(^{137}\text{Cs})$ = 1175.63 keV and $Q(^{133}\text{Ba})$ = 517.4 keV). Specifically, the progressive upward shift of the normalized spectra is due to the fact that increasingly higher magnetic fields gradually reduce the pitch of the helical path of the particles spiraling along the field lines, making then steadily more and more electrons to converge on the plastic scintillator and resulting finally in higher QDC counts.

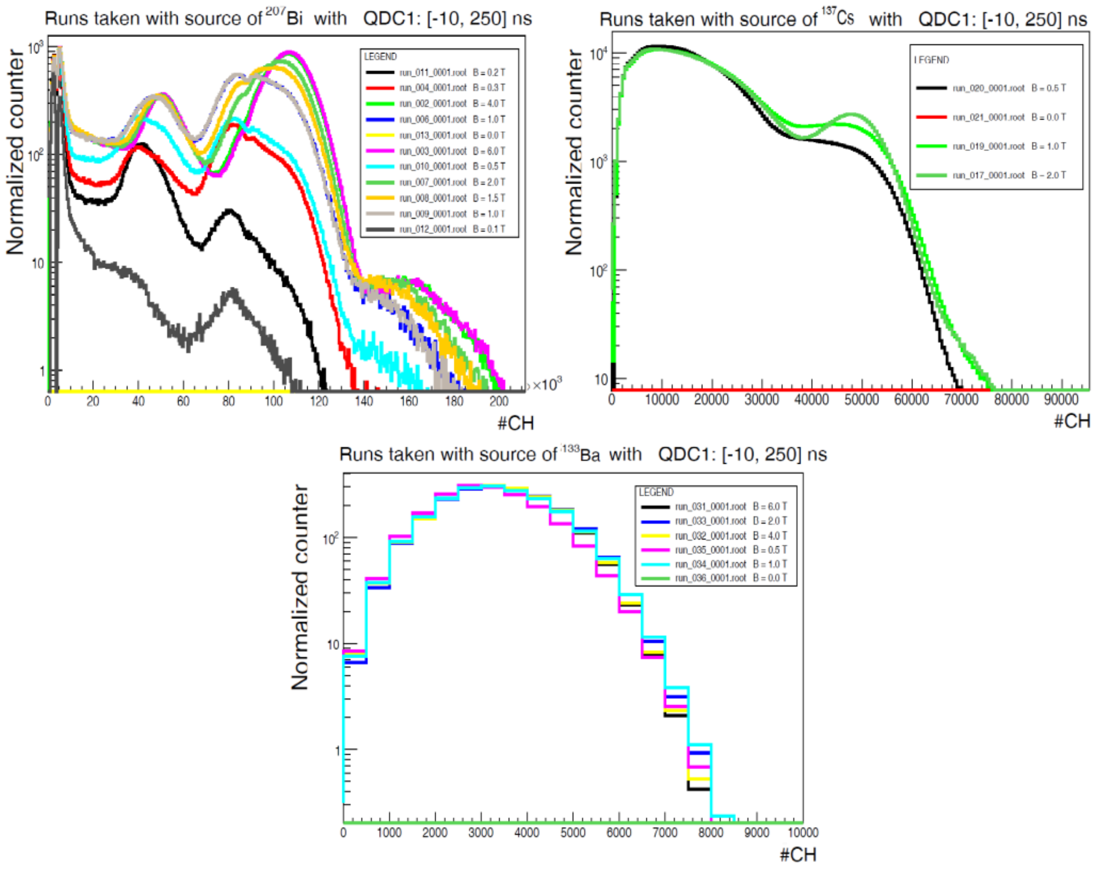

Figure D.13: Superimposed QDC spectra acquired for the ^{207}Bi (top left), the ^{137}Cs (top right) and the ^{133}Ba (bottom) source. Spectra have been normalized to their respective acquisition time and corrected for their respective source activity. Subtraction with reference runs at B = 0 T (runs 13, 21 and 36 respectively) has been performed for all spectra.

Moreover, concerning the ^{207}Bi runs, it can be observed that the first conversion peak (20000 CH < x < 60000 CH) still maintains its Gaussian shape with increasing magnetic field, while the second conversion peak (70000 CH < x < 140000 CH) presents a double-structure which becomes progressively less pronounced with increasing magnetic fields to finally disappear at higher intensities. This characteristic shape is due to the process of electron internal conversion itself, which for both peaks mainly involves the ejection of electrons from the K and L electronic shells, corresponding respectively to 482 and 554 keV in the former case (intensity of 1.52% and 0.44 %) and to 976 and 1048 keV in the latter (intensity of 7.03% and 1.84 %); whilst the first peak appears in all cases composed by an indistinguishable mix of the two conversion electron energies, assuming always a Gaussian shape, the second peak is visibly formed by the sum of the two non-completely resolved K-shell and L-shell conversion peaks, with a difference between them that progressively vanishes at higher magnetic fields. Additionally, a weakly converted third peak (140000 CH < x < 200000 CH), corresponding to the emission of a higher-energy K-shell electron (E_e = 1684 keV, intensity of 0.02 %), together with the main conversion electron sum peak, which is the result of the increasing signal pile-up, is barely visible at B $\geq$ 1 T.

In the case of ^{137}Cs, the main noticeable characteristic is represented by the only peak (40000 CH < x < 60000 CH) resulting from a combination of the K-shell (E_e = 624 keV, intensity of 7.62 %) and the L-shell conversion electron (E_e = 656 keV, intensity of 1.42 %), which becomes more prominent over the β-decay continuum with increasing magnetic fields.
In the case of ^{133}Ba, since the differences in energies between the main converted electrons (E_e = 238, 266, 319 and 349 keV) are fairly below a typical plastic scintillator energy resolution, a unique broad peak incorporating many smaller weakly-converted transitions is visible. Therefore, since the final goal of the analysis will be the study of the quality of the reproduction of β-spectrum shapes in magnetic fields via Geant4 simulations, the measurements taken with the ^{133}Ba can be neglected from further studies due to a lack of reference energy peaks, whose presence is instead of fundamental importance to allow comparisons between experimental and simulation results.

Finally, by calculating the pitch of the helical path of electrons moving in a uniform magnetic field, it results that the minimum intensity of magnetic field needed to make all β-particles, even the most energetic conversion electrons of ^{207}Bi (E_e = 1684 keV), to converge to the plastic scintillator should be roughly $\sim$ 2 T. This means that the β-emission cone, whose angle progressively reduces with increasing magnetic field, starts to be fully contained inside the detection solid angle at least from B = 2 T, leading to a saturation in the detection efficiency which reaches its maximal value of 50 %, correspondent to the detection of all the electrons emitted in the hemisphere in which the β-detector is placed. The fact that no changes in β-spectrum shapes occur only for measurements with B $\geq$ 2 T is then attended by kinematics.

Subsequently, a procedure of energy calibration is needed for all runs in order to provide a common energy-referenced scale and allow later on a comparison with the Geant4 simulated spectra.

Each QDC spectrum has then been converted into the corresponding energy spectrum. Specifically, the energy regions around the two main conversion electron peaks were interpolated with different Gaussian functions convoluted with an exponential background; then, the mean values of the respective Gaussian convoluted fits were reported as a function of the known energies at which the electron conversion peaks appear, and parabolic energy calibration functions were determined in order to convert the raw channel-based spectra into the respective energy spectra. In particular, since all conversion peaks result of a combination of K and L-shell electrons, the energy values used for interpolation have been computed as the weighted average between the characteristic electron emission energies from the different shells and their relative transition intensities; additionally, in order to provide a supplemental point to compute the calibration functions, a further Gaussian fit has been performed on the pedestal (0 CH < x < 10000 CH) of the ^{207}Bi and on the left side of the prominent β-decay peak (0 CH < x < 4000 CH), which both correspond almost entirely to the noise contribution to the QDC spectra.

As pointed out in the precedent discussion, a steady right shift of the spectra with the magnetic field is clearly visible for both ^{207}Bi and ^{137}Cs measurement series; therefore, since the reference conversion peaks are moving towards higher QDC channels due to the different charge collection as a function of the magnetic field intensity, this effect implies that *ad hoc* energy calibration functions should be adopted for each run.

All raw QDC spectra acquired with the different β-sources at different magnetic field intensities have been transformed via the respective energy calibration functions into the corresponding energy spectra. Experimental energy spectra will then be compared to the Geant4 simulated spectra.

D.3.3 Geant4 simulations

Monte Carlo simulations based on the Geant4 toolkit (version 10.5.p01) were performed to reproduce all the runs taken with the multiple-α and the different β-sources (for details see Table D.5), with the final aim to determine the accuracy that can be achieved by using simulations as a complementary tool to describe and predict experimental β energy spectra.

First, a realistic replica of the WISArD experimental set-up has been implemented in the simulations. The geometry of the detection set-up and illustrative examples of radioactive decays, as set out within the simulation code, are shown in Fig. D.14. All the acquired experimental runs, whose details are reported in Table D.5, have then been simulated.

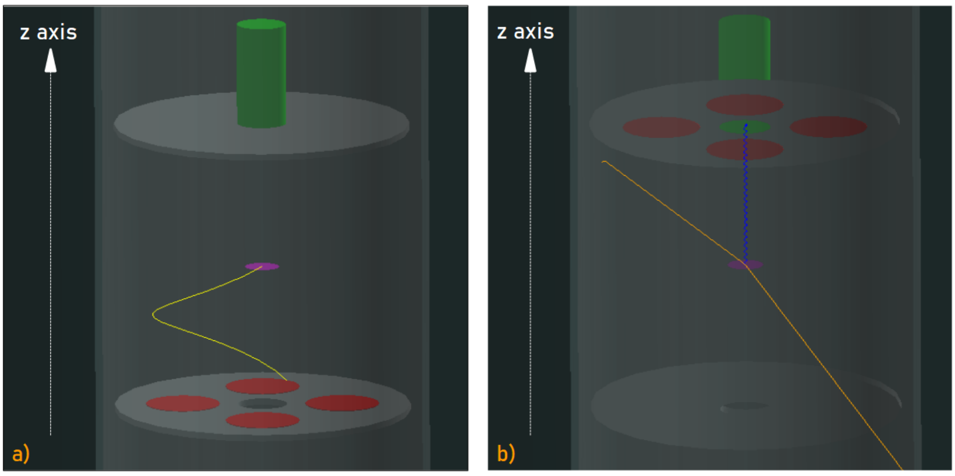

Figure D.14: Visualization of the geometric configuration used in the GEANT4 simulations. The set-up is located in a vacuum tube (semi-transparent grey) in the bore of the WISArD magnet (dark grey) and it is comprehensive of two detection planes containing the scintillator (green) and the eight silicon detectors (red). Examples of radioactive decays of point-like sources deposited on a mylar foil (magenta), namely ^{148}Gd with emission of α-particle (yellow) and ^{207}Bi with emission of electron (blue) and photons (orange), are shown in fig. a) and b), respectively.

D.3.3.1 Multiple α-source

All runs acquired with the multiple α-source have been simulated. In particular, distinct simulations for each of the four nuclides composing the multiple α-source have been performed at all magnetic field intensities investigated experimentally; then, all simulated spectra detected at a given magnetic field value have been summed up for each detector in order to build overall simulated runs perfectly specular to the corresponding experimental ones.

Specifically, each radioactive source has been coded in the form of a very thin and uniform circular spot of 1 mm radius deposited on a 7 μm mylar foil; each simulation, for all magnetic field intensities tested, has then been repeated by varying seven times the position of the radioactive source itself (placed in perfectly central position and shifted by $\Delta x = \pm 2$ mm, $\Delta y = \pm 2$ mm, $\Delta z = \pm 2$ mm) in order to make possible to evaluate the systematic errors associated to the uncertainty on the radioactive source position during experimental runs. All simulations have been performed by using the Geant4 electromagnetic package (opt4), specifically optimized for reproducing ion tracking and relative physics interactions from a MeV-energy scale up to 100 TeV.

Subsequently, all simulated outputs obtained per each detector at each magnetic field intensity have been smeared with the respective experimental detector response functions, each of them retrieved from a linear interpolation of widths as a function of the position of the four Gaussian-like α-peaks in the corresponding ADC spectra. An example of a pure simulated multiple α-spectrum, as well as the result of the smearing with the corresponding detector response function, is shown in Fig. D.15.

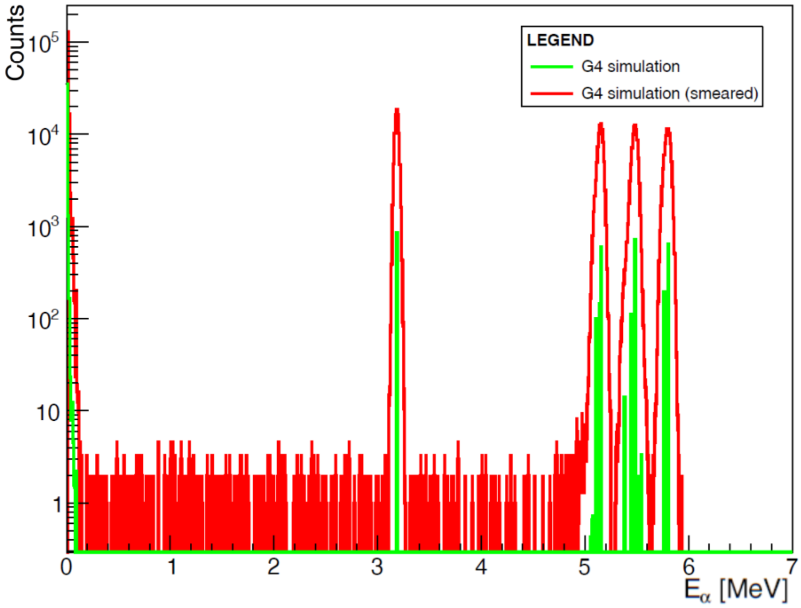

Figure D.15: Multiple α-source simulated energy spectrum acquired by detector Si1U for run 22 (measurement at B = 0 T). In green, the pure simulated Geant4 spectrum (rescaled for graphics purpose); in red, the same spectrum convoluted with the detector linear energy response function.

Simulated runs have been analyzed with the same method applied for experimental data. In order to determine the simulated detection efficiencies, in analogy to Eq. D.3 shown in Sec. D.3.2.1, all integrals of counts recorded by each detector for each α-peak have been computed and then corrected for the total number of events simulated. Integrals have been computed within the same integration boundaries used for the determination of the experimental detection efficiencies, reported in Table D.6.

Plots reporting the normalized simulated detection efficiencies for all detectors as a function of the magnetic field are shown in Fig D.16.

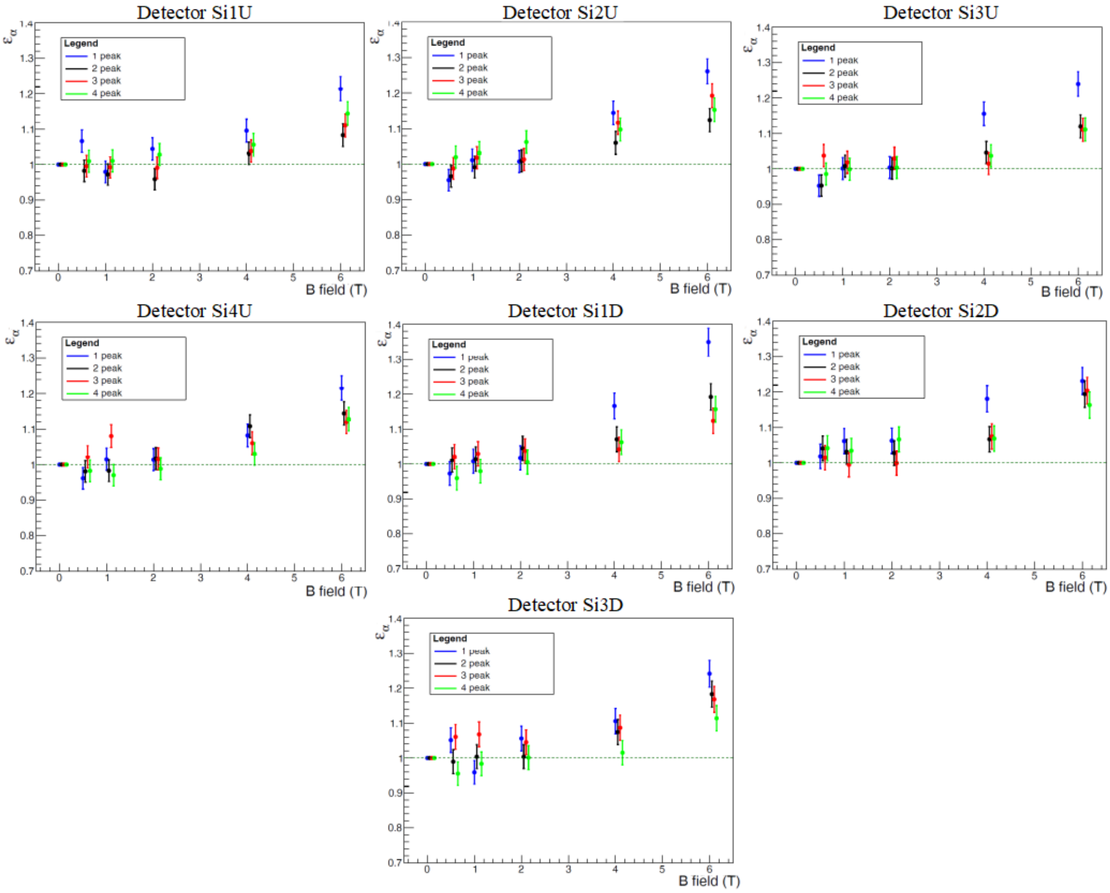
Detector Si1U

Detector Si2U

Detector Si3U

Detector Si4U

Detector Si1D

Detector Si2D

Detector Si3D

Figure D.16: Normalized simulated detection efficiencies for all silicon detectors as a function of the magnetic field intensity. In each plot, results are presented for all the α-energy peaks (^{148}Gd in blue, ^{239}Pu in black, ^{241}Am in red and ^{244}Cm in green); values are slightly separated for visualisation purpose. The dashed green line at unity shows the reference of normalization at B = 0 T.

In all cases, as expected, the simulated detection efficiencies increase with the magnetic field with a more pronounced effect for less energetic α-particles which, due to their lower kinetic energy, spiral along the magnetic field lines with a pitch less affected by differences in magnetic field intensities. Differences between the efficiencies in upper and lower detectors are attributable to statistics effect.

In the following, a comparison between the experimental and simulated α-detection efficiencies will be given and the accuracy achievable via a Geant4 description of the experimental set-up and performed measurements will be discussed.

D.3.3.2 Conversion electron sources

All runs taken with the ^{207}Bi and ^{137}Cs sources at different magnetic field intensities have been simulated. The corresponding energy spectra measured by the plastic scintillator have been retrieved, normalized with respect to the number of events simulated and superimposed, as shown in Fig. D.17.

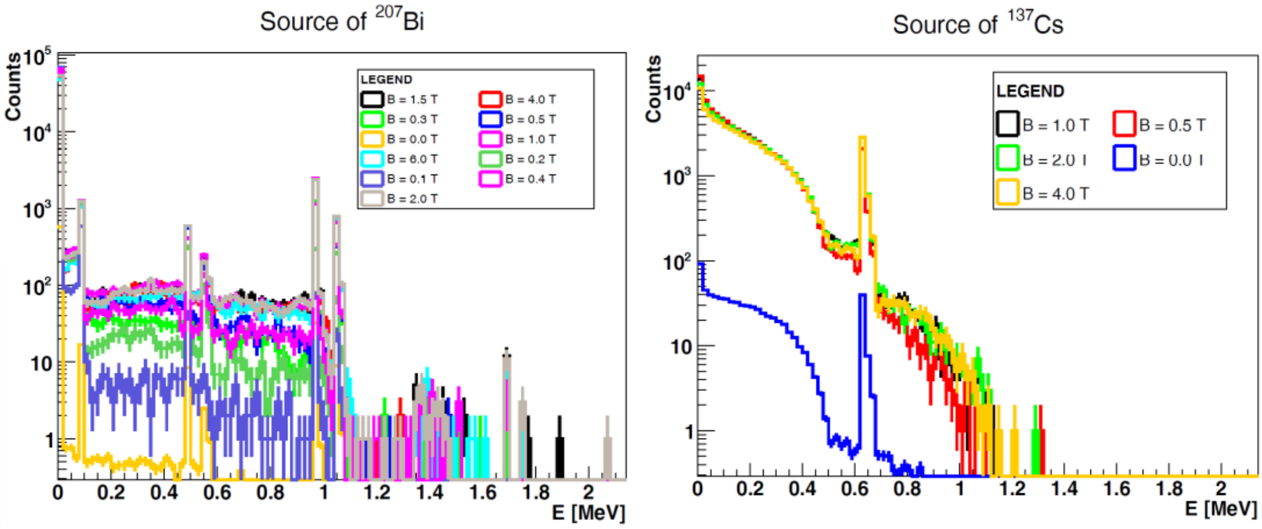

Figure D.17: Superimposed simulated ^{207}Bi (left) and ^{137}Cs (right) spectra at different magnetic field intensities, corresponding to the acquired experimental runs (for details see Table 1).

Simulations have been performed by varying different *PhysicsLists* (*Penelope*, *Goudsmit-Saunderson*, *Livermore* and *LowEMEnergyPhysics*). Simulated runs have been analyzed in the same way of the experimental QDC spectra. Details related to analysis and comparisons between the simulated and the experimental spectra will be discussed in Section D.3.4.2.

D.3.4 Comparison between experimental and simulated results

D.3.4.1 Multiple α-source

Both experimental and simulated detection efficiencies have been computed for all peaks of the multiple α-source and for all the silicon detectors active during data taking. In order to compare the results, differences between experimental and simulated values have been computed. Results obtained are reported in Fig. D.18.

The values are in almost all cases compatible with zero within the only statistics error bars. Higher discrepancies, up to a maximum of 9.34% ± 4.87% (stat.) ± 4.67% (syst.), appear relatively to the lowest energy peaks (^{148}Gd) at the highest magnetic field intensity (B = 6 T).

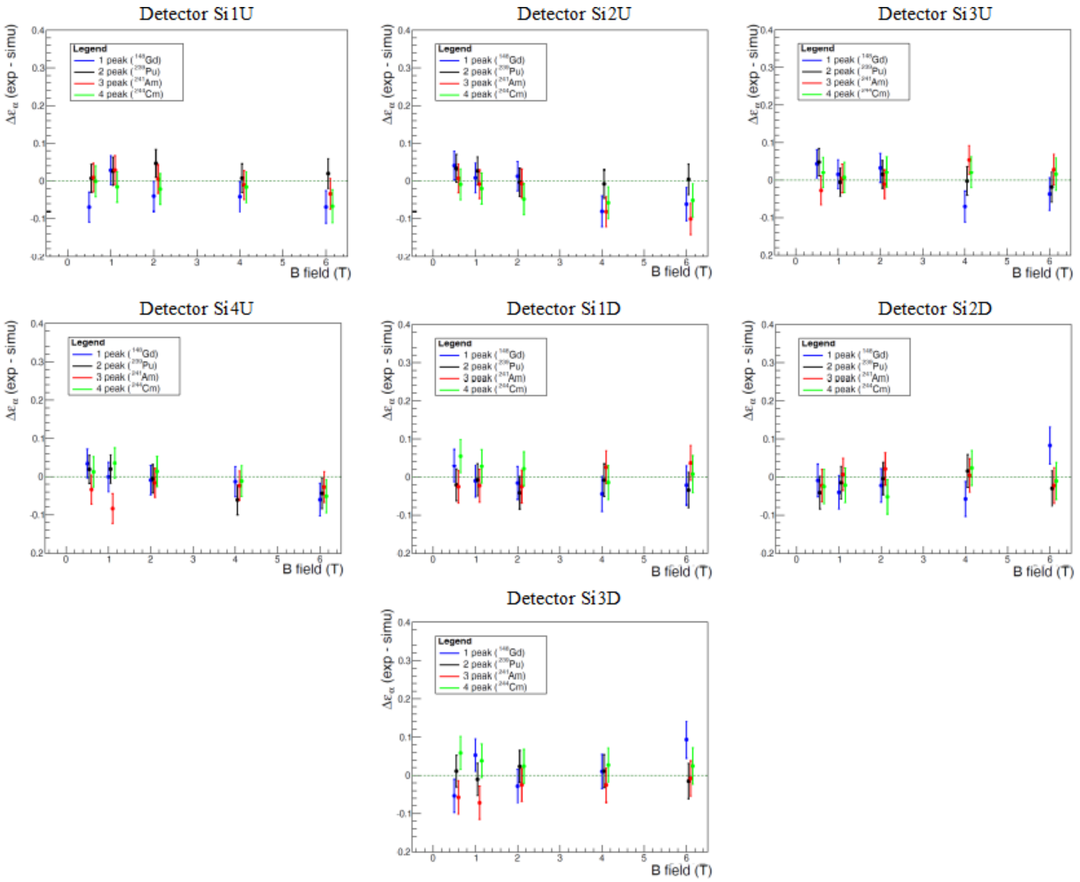

Figure D.18: Differences between normalized experimental and simulated detection efficiencies for all silicon detectors as a function of the magnetic field intensity. In each plot, results are presented for all the α-energy peaks (^{148}Gd in blue, ^{239}Pu in black, ^{241}Am in red and ^{244}Cm in green); values are slightly separated for visualisation purpose. The dashed green lines represent the reference to zero.

Slight differences emerge between upper and lower detectors, due to a lack of precision in the determination of reproduction of the exact position of the α-source during the experimental campaign; in order to evaluate the systematic associated errors for all runs, as discussed in Sec. D.3.3.1, different simulations had been performed for each run by varying several times the source position.

Globally, results evidence a precise accuracy of the Geant4 simulations in reproducing the particle transport within the WISArD magnetic field and the experimental measurements; however, since the statistics available in the experimental spectra is limited, only a first-order validation of the WISArD Geant4 simulations can be concluded. The overall quality of Geant4 reproduction of the multiple α-source campaign, as well as the possibility to use the simulations to trustworthy estimate systematic errors affecting the experimental results, will be possible only after the analysis and comparison between experimental and simulated β-spectra.

D.3.4.2 Conversion electron sources

For all experimental runs acquired with the ^{207}Bi and the ^{137}Cs sources, both the energy calibration and the energy resolution functions have been retrieved from an interpolation of the positions and widths of their respective Gaussian pedestal and converted electron peaks on the QDC spectra. Depending each on two or three parameters, these two functions have respectively the following forms:

$$E[MeV] = a + b \cdot CH + c \cdot CH^2 \tag{D.4}$$

$$\sigma[MeV] = d + e \cdot \sqrt{E} \tag{D.5}$$

where a, b, c, d and e are the coefficients obtained from the respective parabolic and linear regressions, different for each QDC spectrum considered.

In particular, the former formula has been used to convert the experimental QDC spectra into the corresponding energy spectra, while the latter has been used to smear the simulated spectra with the energy resolution of the plastic scintillator.

Both QDC energy-converted and smeared simulated spectra can then be superimposed and compared. First, it should be remarked that exact relationships are pretty impossible to be found in applied science; therefore, the values of a, b, c, d and e coefficients extracted from the different respective regressions shown in Eq. D.4 and in Eq. D.5 do not represent directly the parameter values allowing the maximal agreement between experiment and simulation, but rather a good starting point to finally retrieve them. Effectively, the only method guaranteed to converge to the global minimum of this optimisation problem is given by a complete exploration of the parameter space; this can be done by using as departure points the coefficient values obtained by the fits on the experimental runs and then by applying a gradient descend, an optimization algorithm specifically implemented to find the set of a, b, c, d and e parameters that minimizes the χ^2 value between experimental and simulated histograms by iteratively moving in the direction of steepest descent as defined by the negative of the χ^2-gradient as a function of these four coefficients. Moreover, as a complete scan of the continuous parameter space is not possible, the gradient descent algorithm can be applied to define a smaller subspace of discrete parameter value changes such that an adequately sampled grid search may be defined. In particular, each coefficient has been varied in the range [-2σ_{err}, 2σ_{err}] around the initial value, with σ_{err} representing the respective coefficient errors coming from initial data fits, and combinations with different parameter values have been computed. Finally, the set of a, b, c, d and e parameters corresponding to the minimum χ^2 value has been applied on both experimental and simulated spectra at a given magnetic field intensity to respectively describe and reproduce in the most precise way possible the experimental β-detector characteristics, as well as to allow later on quantitative conclusions on the accuracy with which Geant4 can reproduce experimental β-energy spectra.

In particular, χ^2 has been computed for each run in the energy region between 0.150 and 1.800 MeV, in order not to take into account possible errors in low-energy β-spectra Geant4 reproductions and to limit at the same time higher fluctuations in the χ^2-computation related to the low statistics present in the experimental high-energy region of the spectra.

An example of results, containing the superposition of a calibrated experimental and corresponding smeared simulated run at a given magnetic field intensities is shown in Fig. D.19. In the same figure, the plot showing the bin-per-bin differences between the experimental and the simulated run normalized to half the sum of the respective bin contents, as well as the x-axis projection of this plot, are also reported.

Additionally, in order to quantitatively evaluate the differences between simulations performed by implementing different algorithms to reproduce $\beta-$particle detection, all Geant4 simulations had been repeated by making use of different *PhysicsLists*. An example of simulated spectra computed with different *PhysicsLists*, each of them smeared with the corresponding experimental one by using the same pool of parameters and superimposed to the corresponding experimental spectrum, is reported in Fig. D.20. In order to quantitatively understand the impact of the different *PhysicsLists* in reproducing experimental spectra, once fixed the set of parameters used both for the energy calibration of the experimental runs and the smearing of the simulated spectra, the corresponding χ^2 values have been computed for all runs and all *PhysicsLists* by considering the analysis region fixed by the two cutting thresholds, set at 0.150 and 1.800 MeV respectively. Results obtained are summarized in Table D.7. For completeness, it can be noticed that the peak at roughly 1.5 MeV is less correctly reproduced by the simulations; this is due to the fact that the experimental peak also contains, in the high-energy part of the spectrum, the event pile-up contribution, which has not been replicated within the numerical simulations as not needed for the overall analysis.

As reported in Table D.7, all experimental runs have been globally better reproduced by simulations making use of the *Goudsmit-Saunderson* and the *Penelope PhysicsLists*, which both provide a fairly precise replica of the experimental spectra down to an energy of about 150 keV. This confirms the results obtained with the employment of a different set-ups and illustrated in Sec. D.2. The *PhysicsList* finally chosen for the numerical reproduction of the experimental campaign with ^{32}Ar will then be the *Goudsmit-Saunderson*. Further details on the differences between the *PhysicsLists* are illustrated in Appendix C.

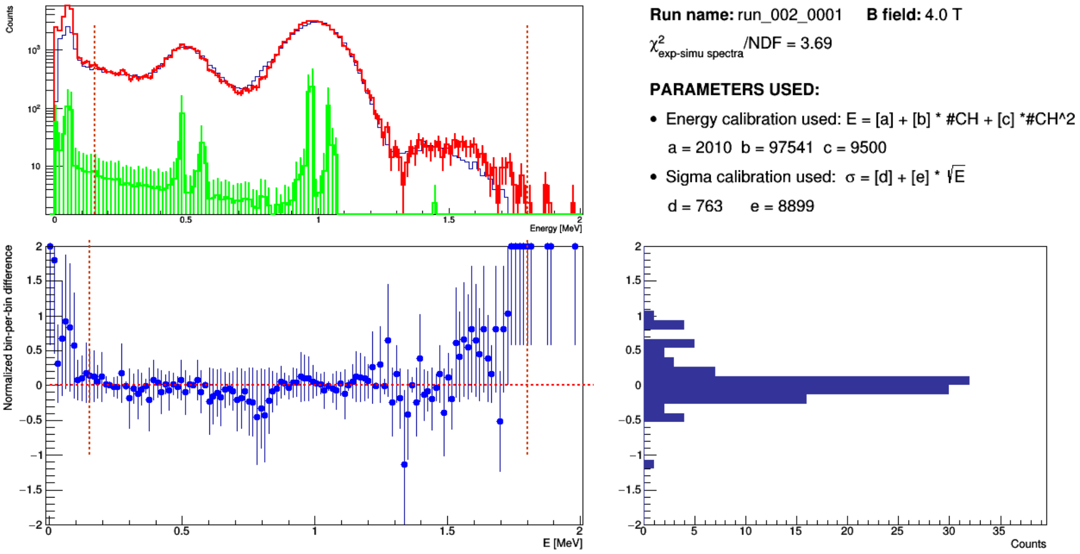

Run name: run_002_0001 **B field:** 4.0 T

$\chi^2_{\text{exp-simu spectra}}$/NDF = 3.69

PARAMETERS USED:

- Energy calibration used: E = [a] + [b] * #CH + [c] *#CH^2

  a = 2010 b = 97541 c = 9500
- Sigma calibration used: σ = [d] + [e] * √E

  d = 763 e = 8899

Figure D.19: Comparison between experimental and simulated spectra reproduced with the *Penelope PhysicsList* for run 2 (measurement at B = 4 T). Top left: superimposed calibrated experimental run (blue) and smeared Geant4 simulation (red), as well as the pure Geant4 simulation (green, rescaled for graphics purpose), with cutting thresholds (vertical dashed orange lines) delimiting the energy region for the computation of the χ^2. Top right: experimental conditions at which the run was acquired, χ^2 value and parameters (all expressed in CH) resulting from the application of the gradient descend algorithm. Bottom left: the bin-per-bin difference between calibrated experimental and smeared simulated spectra normalized to half the sum of their respective bin contents. Bottom right: the x-axis projection of the normalized bin-per-bin difference between the cutting thresholds.

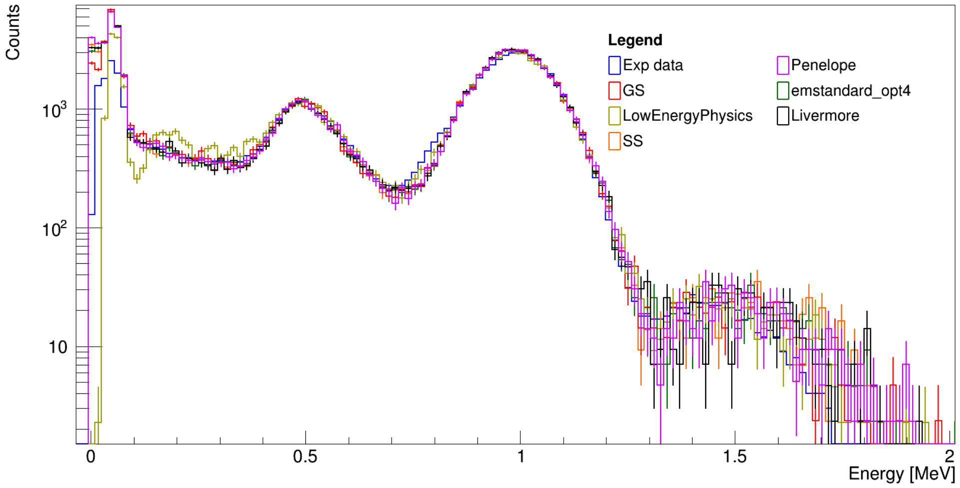

Figure D.20: Comparison between experimental and simulated spectra reproduced with different *PhysicsLists* for run 2 (measurement at B = 4 T). Superimposed calibrated experimental run (blue) and smeared Geant4 *Penelope* (violet), *Goudsmit – Saunderson* (GS, red), *emstandard_opt4* (dark green), *LowEMEnergyPhysics* (light green), *Livermore* (black) and *SingleScattering* (SS, salmon) *PhysicsLists* are shown.

Run number	**B field [T]**	**PhysicsList**	$\chi^2_{exp-simu}$**/NDF**
11	0.2	Penelope	5.22
		GS	**4.63**
		opt4	5.38
		Livermore	5.90
		LowEMEnPhysics	5.47
4	0.3	Penelope	3.94
		GS	**3.82**
		opt4	3.99
		Livermore	4.36
		LowEMEnPhysics	4.73
10	0.5	Penelope	4.04
		GS	**3.98**
		opt4	4.00
		Livermore	4.42
		LowEMEnPhysics	5.32
6	1.0	**Penelope**	**5.33**
		GS	5.21
		opt4	6.52
		Livermore	5.82
		LowEMEnPhysics	9.98
8	1.5	**Penelope**	**3.98**
		GS	4.00
		opt4	4.14
		Livermore	4.82
		LowEMEnPhysics	7.94
7	2.0	Penelope	4.44
		GS	**4.32**
		opt4	4.85
		Livermore	4.95
		LowEMEnPhysics	7.74
2	4.0	Penelope	3.82
		GS	**3.69**
		opt4	3.78
		Livermore	4.29
		LowEMEnPhysics	4.65
3	6.0	Penelope	4.14
		GS	**3.89**
		opt4	4.29
		Livermore	4.36
		LowEMEnPhysics	6.54

Table D.7: Summary of the correspondence between the run numbers, the magnetic field intensities at which the runs with the ^{207}Bi source were acquired, the *PhysicsLists* used and the correspondent χ^2 value obtained from the comparison between simulated and experimental spectra in the region delimited by the cutting thresholds. In bold, the *PhysicsList* leading to the minimal χ^2 for each run.

Bibliography

[1] E. Rutherford, “The scattering of alpha and beta particles by matter and the structure of the atom,” *Phil. Mag. Ser. 6*, vol. 21, pp. 669–688, 1911.

[2] J. Chadwick, “Possible Existence of a Neutron,” *Nature*, vol. 129, p. 312, 1932.

[3] C. D. Anderson, “The Apparent Existence of Easily Deflectable Positives,” *Science*, vol. 76, pp. 238–239, 1932.

[4] J. C. Street and E. C. Stevenson, “New Evidence for the Existence of a Particle of Mass Intermediate Between the Proton and Electron,” *Phys. Rev.*, vol. 52, pp. 1003–1004, 1937.

[5] C. M. G. Lattes, H. Muirhead, G. P. S. Occhialini, and C. F. Powell, “Processes Involving Charged Mesons,” *Nature*, vol. 159, pp. 694–697, 1947.

[6] G. D. Rochester and C. C. Butler, “Evidence for the Existence of New Unstable Elementary Particles,” *Nature*, vol. 160, pp. 855–857, 1947.

[7] S. L. Glashow, “The renormalizability of vector meson interactions,” *Nucl. Phys.*, vol. 10, pp. 107–117, 1959.

[8] A. Salam, “Weak and Electromagnetic Interactions,” *Conf. Proc. C*, vol. 680519, pp. 367–377, 1968.

[9] S. Weinberg, “A Model of Leptons,” *Phys. Rev. Lett.*, vol. 19, pp. 1264–1266, 1967.

[10] M. Gell-Mann, “The Eightfold Way: A Theory of strong interaction symmetry,” *unpublished*, 1961.

[11] R. Workman *et al.*, “Review of Particle Physics,” *Prog. Theor. Exp. Phys.*, p. 083C01, 2022.

[12] J. J. Aubert *et al.*, “Experimental Observation of a Heavy Particle J,” *Phys. Rev. Lett.*, vol. 33, pp. 1404–1406, 1974.

[13] J. E. Augustin *et al.*, “Discovery of a Narrow Resonance in e^+e^- Annihilation,” *Phys. Rev. Lett.*, vol. 33, pp. 1406–1408, 1974.

[14] S. W. Herb *et al.*, “Observation of a Dimuon Resonance at 9.5-GeV in 400-GeV Proton-Nucleus Collisions,” *Phys. Rev. Lett.*, vol. 39, pp. 252–255, 1977.

[15] F. Abe *et al.*, “Evidence for top quark production in $\bar{p}p$ collisions at $\sqrt{s} = 1.8$ TeV,” *Phys. Rev. D*, vol. 50, pp. 2966–3026, 1994.

[16] G. Aad *et al.*, “Observation of a new particle in the search for the Standard Model Higgs boson with the ATLAS detector at the LHC,” *Phys. Lett. B*, vol. 716, pp. 1–29, 2012.

[17] S. L. Glashow, J. Iliopoulos, and L. Maiani, “Weak Interactions with Lepton-Hadron Symmetry,” *Phys. Rev. D*, vol. 2, pp. 1285–1292, 1970.

[18] F. Englert and R. Brout, “Broken Symmetry and the Mass of Gauge Vector Mesons,” *Phys. Rev. Lett.*, vol. 13, pp. 321–323, 1964.

[19] P. W. Higgs, “Broken symmetries, massless particles and gauge fields,” *Phys. Lett.*, vol. 12, pp. 132–133, 1964.

[20] P. W. Higgs, “Broken Symmetries and the Masses of Gauge Bosons,” *Phys. Rev. Lett.*, vol. 13, pp. 508–509, 1964.

[21] E. Noether, “Invariante Variationsprobleme,” *Nachr. Gött.*, pp. 235–257, 1918.

[22] C. Quigg, “Notes on lepton gyromagnetic ratios.” `https://arxiv.org/abs/2105.07866`, 2021.

[23] J. I. Rivas, A. Camacho, and E. Goeklue, “Quantum spacetime fluctuations: Lamb Shift and hyperfine structure of the hydrogen atom,” *Phys. Rev. D*, vol. 84, p. 055024, 2011.

[24] C. S. Wu *et al.*, “Experimental Test of Parity Conservation in β Decay,” *Phys. Rev.*, vol. 105, pp. 1413–1414, 1957.

[25] M. Goldhaber, L. Grodzins, and A. W. Sunyar, “Helicity of neutrinos,” *Phys. Rev.*, vol. 109, pp. 1015–1017, 1958.

[26] G. Luders, “On the Equivalence of Invariance under Time Reversal and under Particle-Antiparticle Conjugation for Relativistic Field Theories,” *Kong. Dan. Vid. Sel. Mat. Fys. Med.*, vol. 28N5, no. 5, pp. 1–17, 1954.

[27] W. Pauli, "Niels Bohr and the Development of Physics," *Physics Today*, vol. 9, no. 4, p. 32, 1956.

[28] R. Jost, "A remark on the C.T.P. theorem," *Helv. Phys. Acta*, vol. 30, pp. 409–416, 1957.

[29] T. D. Lee and C.-N. Yang, "Question of Parity Conservation in Weak Interactions," *Phys. Rev.*, vol. 104, pp. 254–258, 1956.

[30] L. K. Gibbons *et al.*, "Measurement of the CP violation parameter Re(ε'/ε)," *Phys. Rev. Lett.*, vol. 70, pp. 1203–1206, 1993.

[31] A. Alavi-Harati *et al.*, "Measurements of direct CP violation, CPT symmetry, and other parameters in the neutral kaon system," *Phys. Rev. D*, vol. 67, p. 012005, 2003. [Erratum: Phys.Rev.D 70, 079904 (2004)].

[32] H. Burkhardt *et al.*, "First evidence for direct CP violation," *Phys. Lett. B*, vol. 206, pp. 169–176, 1988.

[33] NA48 Collaboration, "A precise measurement of the direct CP violation parameter Re(ε'/ε)," *EPJ C*, vol. 22, no. 2, pp. 231–254, 2001.

[34] R. Adler *et al.*, "The CPLEAR detector at CERN," *Nucl. Instrum. Meth. A*, vol. 379, pp. 76–100, 1996.

[35] A. Angelopoulos *et al.*, "First direct observation of time reversal noninvariance in the neutral kaon system," *Phys. Lett. B*, vol. 444, pp. 43–51, 1998.

[36] P. J. Clark, "CP violation in B decays at the BABAR experiment," in *Proceedings to the 24th International Workshop on Fundamental Problems of High Energy Physics and Field Theory : Protvino, Russia, June 27-29, 2001*, pp. 54–60, 2001.

[37] B. Oberhof, "Precise measurements of CP violation in B decays at Belle II," in *Proceedings to the 14th International Conference on Heavy Quarks and Leptons (HQL 2018) : Yamagata, Japan, May 27-June 1, 2018*, vol. HQL2018, p. 004, 2018.

[38] R. Aaij *et al.*, "First measurement of the *CP*-violating phase in $B_s^0 \to J/\psi(\to e^+e^-)\phi$ decays," *Eur. Phys. J. C*, vol. 81, no. 11, p. 1026, 2021.

[39] X.-D. Cheng, R.-M. Wang, and X.-B. Yuan, "Effect of K0-K¯0 mixing on CP and CPT violations in Bc±→B±KS,L0 decays," *Phys. Rev. D*, vol. 104, no. 9, p. 093005, 2021.

[40] E. Fermi, "An attempt of a theory of beta radiation. 1.," *Z. Phys.*, vol. 88, pp. 161–177, 1934.

[41] R. Stuer, "The seventh Solvay Conference: nuclear physics at the crossroads," *Boston studies in the philosophy of science*, vol. 167, 1995.

[42] N. Severijns, M. Beck, and O. Naviliat-Cuncic, "Tests of the standard electroweak model in beta decay," *Rev. Mod. Phys.*, vol. 78, pp. 991–1040, 2006.

[43] C. S. Wu and S. A. Moszkowski, *Beta Decay*. Interscience monographs and texts in physics and astronomy, v. 16, New York: New York, Interscience Publishers, 1966.

[44] R. P. Feynman and M. Gell-Mann, "Theory of Fermi interaction," *Phys. Rev.*, vol. 109, pp. 193–198, 1958.

[45] J. C. Hardy and I. S. Towner, "Superallowed $0^+ \to 0^+$ nuclear β decays: 2020 critical survey, with implications for V_{ud} and CKM unitarity," *Phys. Rev. C*, vol. 102, no. 4, p. 045501, 2020.

[46] R. J. Finkelstein and S. A. Moszkowski, "Mesonic Corrections to the Beta-Decay Coupling Constants," *Phys. Rev.*, vol. 95, no. 6, pp. 1695–1697, 1954.

[47] J. D. Jackson, S. B. Treiman, and H. W. Wyld, "Coulomb corrections in allowed beta transitions," *Nucl. Phys.*, vol. 4, pp. 206–212, 1957.

[48] N. Severjins, "Weak interaction studies by precision experiments in nuclear beta decay," in *Lecture Notes of the 2019 Euroschool On Exotic Beams*, 2019.

[49] M. González-Alonso, O. Naviliat-Cuncic, and N. Severijns, "New physics searches in nuclear and neutron β-decay," *Prog. Part. Nucl. Phys.*, vol. 104, pp. 165–223, 2019.

[50] Y. Yokoo and M. Morita, "Radiative Corrections To Nuclear Beta Decay," *Progr. Theor. Phys. Suppl.*, vol. 60, pp. 37–46, 1976.

[51] F. Gluck, "Order-alpha radiative correction calculations for unoriented allowed nuclear, neutron and pion beta decays," *Comput. Phys. Commun.*, vol. 101, pp. 223–231, 1997.

[52] B. R. Holstein, "Recoil Effects in Allowed beta Decay: The Elementary Particle Approach," *Rev. Mod. Phys.*, vol. 46, p. 789, 1974. [Erratum: Rev.Mod.Phys. 48, 673–673 (1976)].

[53] B. R. Holstein, "Electromagnetic corrections to allowed nuclear beta decay," *Phys. Rev. C*, vol. 9, pp. 1742–1747, 1974.

[54] N. Severijns and O. Naviliat-Cuncic, “Structure and symmetries of the weak interaction in nuclear beta decay,” *Phys. Scripta T*, vol. 152, p. 014018, 2013.

[55] W. J. Marciano and A. Sirlin, “Improved calculation of electroweak radiative corrections and the value of V(ud),” *Phys. Rev. Lett.*, vol. 96, p. 032002, 2006.

[56] O. Naviliat-Cuncic, “V_{ud} from Nuclear Mirror Transitions,” in *Proceedings to the 7th International Workshop on the CKM Unitarity Triangle*, 2013.

[57] D. Počanić *et al.*, “Precise measurement of the $\pi^+ \to \pi^0 e^+ \nu_e$ branching ratio,” *Phys. Rev. Lett.*, vol. 93, no. 18, 2004.

[58] A. Falkowski, M. González-Alonso, and O. Naviliat-Cuncic, “Comprehensive analysis of beta decays within and beyond the standard model,” *J. High Energy Phys.*, vol. 2021, no. 4, 2021.

[59] T. Kurtukian-Nieto *et al.*, “High-precision β-decay half-life measurements of proton-rich nuclei for testing the CVC hypothesis,” in *Proceedings to the 2011 AIP Conference*, vol. 1409, pp. 171–174, 2011.

[60] B. Blank *et al.*, “Branching ratio of the super-allowed β decay of ^{10}C,” *Eur. Phys. J. A*, vol. 56, no. 6, p. 156, 2020.

[61] V. Egorov *et al.*, “Beta-neutrino angular correlation in the decay of ^{18}Ne,” *Nucl. Phys. A*, vol. 621, pp. 745–753, 1997.

[62] V. Vorobel *et al.*, “Beta-neutrino angular correlation in the decay of ^{14}O,” *Eur. Phys. J. A*, vol. 16, pp. 139–147, 2003.

[63] E. G. Adelberger *et al.*, “Positron neutrino correlation in the $0^+ \to 0^+$ decay of ^{32}Ar,” *Phys. Rev. Lett.*, vol. 83, pp. 1299–1302, 1999. [Erratum: Phys.Rev.Lett. 83, 3101 (1999)].

[64] A. Gorelov *et al.*, “Scalar interaction limits from the β-ν correlation of trapped radioactive atoms,” *Phys. Rev. Lett.*, vol. 94, no. 14, 2005.

[65] P. A. Vetter *et al.*, “Measurement of the β-ν correlation of ^{21}Na using shakeoff electrons,” *Phys. Rev. C*, vol. 77, no. 3, 2008.

[66] J. S. Allen *et al.*, “Determination of the beta-decay interaction from electron-neutrino angular correlation measurements,” *Phys. Rev.*, vol. 116, no. 134, 1959.

[67] T. A. Carlson *et al.*, "Recoil Energy Spectrum of the Sodium Ions Following the $\beta-$decay of ^{23}Ne," *Phys. Rev.*, vol. 132, no. 2239, 1963.

[68] C. H. Johnson *et al.*, "Precision measurement of the recoil energy spectrum from the decay of ^{6}He," *Phys. Rev.*, vol. 132, no. 1149, 1963.

[69] J. B. Vise *et al.*, "The electron-neutrino angular correlation in beta decay of ^{6}He," *Nucl. Phys.*, vol. 25, no. 483, 1961.

[70] J. B. Vise *et al.*, "Electron-neutrino angular correlation in the decay of ^{6}He," *Phys. Rev.*, vol. 132, no. 2573, 1963.

[71] X. Fléchard *et al.*, "Measurement of the β-ν correlation coefficient $a_{\beta\nu}$ in the β-decay of trapped ^{6}He^{+} ions," *J. Phys. G: Nucl. Part. Phys.*, vol. 38, 2011.

[72] G. Li *et al.*, "Tensor Interaction Limit Derived From the α-β-$\bar{\nu}$ Correlation in Trapped ^{8}Li Ions," *Phys. Rev. Lett.*, vol. 110, no. 9, p. 092502, 2013.

[73] M. G. Sternberg *et al.*, "Limit on tensor currents from ^{8}Li β-decay," *Phys. Rev. Lett.*, vol. 115, p. 182501, 2015.

[74] M. T. Burkey *et al.*, "Improved limit on tensor currents in the weak interaction from ^{8}Li β-decay," *Phys. Rev. Lett.*, vol. 128, p. 202502, 2022.

[75] P. Müller *et al.*, "β-nuclear-recoil correlation from ^{6}He decay in a laser trap," *Phys. Rev. Lett.*, vol. 129, p. 182502, 2022.

[76] M. Beck, *Progress at the WITCH Experiment towards Weak Interaction Studies*. PhD dissertation, Katholieke Universiteit Leuven, 2011.

[77] V. Kozlov, *WITCH, a Penning trap for weak interaction studies*. PhD dissertation, Katholieke Universiteit Leuven, 2005.

[78] M. Beck *et al.*, "First detection and energy measurement of recoil ions following beta decay in a Penning trap with the WITCH experiment," *Eur. Phys. J. A*, vol. 47, no. 45, 2011.

[79] B. Blank *et al.*, "Wisard: Weak interaction studies with ^{32}Ar decay," *CERN-INTC-2016*, 2016.

[80] P. D. Shidling *et al.*, "TAMUTRAP facility: Penning trap facility for weak interaction studies," *Hyperfine Interact.*, vol. 240, no. 40, 2019.

[81] L. Hayen *et al.*, “High precision analytical description of the allowed β-spectrum shape,” *Reviews of Modern Physics*, vol. 90, no. 1, 2018.

[82] S. Vanlangendonck, D. Atanasov, F. Cresto, *et al. in preparation*, 2022.

[83] F. Wauters *et al.*, “Precision measurements of the ^{60}Co β-asymmetry parameter in search for tensor currents in weak interactions,” *Phys. Rev. C*, vol. 82, p. 055502, 2010.

[84] N. Severijns *et al.*, “Fundamental weak interaction studies using polarised nuclei and ion traps,” *Hyperfine Interact.*, vol. 129, pp. 223–226, 2000.

[85] F. Wauters *et al.*, “Beta asymmetry parameter in the decay of ^{114}In,” *Phys. Rev. C*, vol. 80, no. 6, 2009.

[86] B. Holstein, “Limit on Fierz interference in nuclear beta decay,” *Phys. Rev. C*, vol. 16, no. 2, pp. 753–756, 1977.

[87] D. Combs, G. Jones, W. Anderson, F. Calaprice, L. Hayen, and A. Young, “A look into mirrors: A measurement of the β-asymmetry in ^{19}Ne decay and searches for new physics.” `https://arxiv.org/abs/2009.13700`, 2020.

[88] H. Saul *et al.*, “Limit on the Fierz Interference Term b from a Measurement of the Beta Asymmetry in Neutron Decay,” *Phys. Rev. Lett.*, vol. 125, no. 11, p. 112501, 2020.

[89] W. Byron *et al.*, “An Overview of the ^{6}He CRES Experiment,” in *Proceedings to the 14th International Conference on Heavy Quarks and Leptons (HQL 2018) : Yamagata, Japan, May 27-June 1, 2018*, vol. HQL2018, p. 004, 2018.

[90] N. Severijns, M. Beck, and O. Naviliat-Cuncic, “Tests of the standard electroweak model in nuclear beta decay,” *Reviews of Modern Physics*, vol. 78, no. 3, p. 991–1040, 2006.

[91] N. Aghanim *et al.*, “Planck 2018 results. VI. Cosmological parameters,” *Astronomy&Astrophysics*, vol. 641, 2020.

[92] V. Cirigliano, M. Gonzalez-Alonso, and M. L. Graesser, “Non-standard Charged Current Interactions: beta decays versus the LHC,” *J. High Energy Phys.*, vol. 02, p. 046, 2013.

[93] J. van Klinken *et al.*, “Left-Right Symmetry in Nuclear Beta Decay under Investigation with a New Bhabha Polarimeter,” *Phys. Rev. Lett.*, vol. 50, pp. 94–97, 1983.

[94] V. A. Wichers, T. R. Hageman, J. Van Klinken, H. W. Wilschut, and D. Atkinson, “Bounds on Right-handed Currents From Nuclear Beta Decay,” *Phys. Rev. Lett.*, vol. 58, pp. 1821–1824, 1987.

[95] M. Skalsey, D. W. Holdsworth, D. A. L. Paul, and A. Rich, “Positron polarization from the decay of ^{25}Al relative to $^{26}\mathrm{Al}^{m}$,” *Phys. Rev. C*, vol. 39, pp. 986–991, 1989.

[96] A. S. Carnoy, J. Deutsch, T. A. Girard, and R. Prieels, “Limits on nonstandard weak currents from the polarization of ^{14}O and ^{10}C decay positrons,” *Phys. Rev. C*, vol. 43, pp. 2825–2834, 1991.

[97] A. N. Ivanov, R. Höllwieser, N. I. Troitskaya, M. Wellenzohn, and Y. A. Berdnikov, “Theoretical description of the neutron beta decay in the standard model at the level of 10^{-5},” *Phys. Rev. D*, vol. 104, no. 3, p. 033006, 2021.

[98] H. Abele, “The neutron. Its properties and basic interactions,” *Prog. Part. Nucl. Phys.*, vol. 60, pp. 1–81, 2008.

[99] J. Liechti *et al.*, “Production of polarized ^{12}N with the ^{12}C(p, ^{12}N)n_0 reaction,” *Nucl. Phys. A*, vol. 533, pp. 292–306, 1991.

[100] B. Erozolimsky, I. Kuznetsov, I. Stepanenko, and Y. A. Mostovoi, “Corrigendum: Corrected value of the beta-emission asymmetry in the decay of polarized neutrons measured in 1990,” 1997. [Erratum: Phys.Lett.B 412, 240–241 (1997)].

[101] E. Thomas, “Positron Polarization in the Decay of Polarized ^{12}N: a Precision Test of the Standard Model,” *Nucl. Phys. A*, vol. 694, p. 559, 2001.

[102] R. I. Steinberg, P. Liaud, B. Vignon, and V. W. Hughes, “New Experimental Limit on T Invariance in Polarized-Neutron beta Decay,” *Phys. Rev. Lett.*, vol. 33, pp. 41–44, 1974.

[103] B. Erozolimskij, A. Frank, Y. Mostovoj, S. Arzumanov, and L. Vojtsik, “Measurement of the spin-electron correlation coefficient in the decay of polarized neutrons and the determination of the Gsub(A)/Gsub(V) ratio,” *Sov. J. Nucl. Phys.*, vol. 30, no. 9, pp. 692–701, 1979.

[104] L. J. Lising and others (emiT Collab), “New limit on the D coefficient in polarized neutron decay,” *Phys. Rev. C*, vol. 62, p. 055501, 2000.

[105] T. Soldner, L. Beck, C. Plonka, K. Schreckenbach, and O. Zimmer, “New limit on T violation in free neutron decay,” *Nucl. Phys. A*, vol. 721, pp. 469–472, 2003.

[106] F. Calaprice, “The use of atomic beam and optical methods in the study of fundamental symmetries,” *Hyperfine Interact.*, vol. 22, pp. 83–93, 1985.

[107] J. H. Christenson, J. W. Cronin, V. L. Fitch, and R. Turlay, “Evidence for the 2π Decay of the K_2^0 Meson,” *Phys. Rev. Lett.*, vol. 13, pp. 138–140, 1964.

[108] P. Delahaye *et al.*, “The MORA project,” *Hyperfine Interact.*, vol. 240, no. 1, 2019.

[109] M. B. Schneider, F. P. Calaprice, A. L. Hallin, D. W. MacArthur, and D. F. Schreiber, “Limit on $\mathrm{Im}(C_S C_A{}^*)$ from a test of t invariance in ^{19}Ne beta decay,” *Phys. Rev. Lett.*, vol. 51, pp. 1239–1242, Oct 1983.

[110] R. Huber, J. Lang, S. Navert, J. Sromicki, K. Bodek, S. Kistryn, J. Zejma, O. Naviliat-Cuncic, E. Stephan, and W. Haeberli, “Search for time-reversal violation in the β decay of polarized ^{8}Li nuclei,” *Phys. Rev. Lett.*, vol. 90, p. 202301, May 2003.

[111] V. Araujo-Escalona *et al.*, “Simultaneous measurements of the β-neutrino angular correlation in ^{32}Ar pure Fermi and pure Gamow-Teller transitions using β-proton coincidences,” *Phys. Rev. C*, vol. 101, p. 055501, 2020.

[112] V. Khachatryan *et al.*, “Search for heavy neutrinos and W bosons with right-handed couplings in proton-proton collisions at $\sqrt{s_{NN}}$ = 8 TeV,” *Eur. Phys. J. C*, vol. 74, no. 11, p. 3149, 2014.

[113] A. M. Sirunyan *et al.*, “Search for a heavy right-handed W boson and a heavy neutrino in events with two same-flavor leptons and two jets at $\sqrt{s_{NN}} = 13$ TeV,” *JHEP*, vol. 05, p. 148, 2018.

[114] J. Hardy and I. Towner *J. Phys. G: Nucl. Part. Phys.*, vol. 29, 2003.

[115] M. González-Alonso and O. Naviliat-Cuncic, “Prospects for precision measurements in nuclear beta decay at the LHC era.” `https://arxiv.org/abs/1304.1759`, 2013.

[116] D. Schardt and K. Riisager, “Beta-neutrino recoil broadening in β-delayed proton emission of ^{32}Ar and ^{33}Ar,” *Z. Phys. A - Hadron Nucl.*, vol. 345, pp. 265–271, 1993.

[117] G. Audi and A. H. Wapstra, “The 1995 update to the atomic mass evaluation,” *Nucl. Phys. A*, vol. 595, pp. 409–480, 1995.

[118] K. Blaum, G. Audi, D. Beck, G. Bollen, F. Herfurth, A. Kellerbauer, H.-J. Kluge, E. Sauvan, and S. Schwarz, “Masses of ^{32}Ar and ^{33}Ar for fundamental tests,” *Phys. Rev. Lett.*, vol. 91, p. 260801, Dec 2003.

[119] B. Blank *et al.*, “Detailed study of the decay of ^{32}Ar,” *Eur. Phys. J.*, vol. 57, no. 1, p. 28, 2021.

[120] M. P. Curie, *Radioactivité*. Paris: Hermann (éditions), 1935. *Original document in French*.

[121] S. Esposito and O. Pisanti, eds., *Neutron physics for nuclear reactors: Unpublished writings by Enrico Fermi*. 2010.

[122] G. J. Beyer, E. Hagebo, A. F. Novgorodov, and H. L. Ravn, “The role of diffusion in ISOL targets for the production of radioactive ion beams,” *CERN-EP-2002-096*, Nov. 2002.

[123] B. Harss, R. C. Pardo, K. E. Rehm, *et al.*, “The role of diffusion in ISOL targets for the production of radioactive ion beams,” *Rev. Sci. Instrum.*, vol. 71, no. 2, pp. 380–387, 2000.

[124] J. Vollaire *et al.*, *Linac4 design report*, vol. 6/2020 of *CERN Yellow Reports: Monographs*. Geneva: CERN, 9 2020.

[125] K. Johnston, “The ISOLDE Facility, Recent Highlights and the HIE-ISOLDE Project,” *DAE Symp. Nucl. Phys.*, vol. 60, pp. 19–20, 2015.

[126] T. J. Giles, R. Catherall, V. Fedosseev, U. Georg, E. Kugler, J. Lettry, and M. Lindroos, “The high resolution spectrometer at ISOLDE,” *Nucl. Instrum. Methods B*, vol. 204, pp. 497–501, 2003.

[127] M. J. G. Borge and B. Jonson, “ISOLDE past, present and future,” *J. Phys. G Nucl. Part. Phys.*, vol. 44, no. 4, p. 044011, 2017.

[128] T. Nilsson *et al.*, “REX-ISOLDE - Post accelerated radioactive beams at CERN-ISOLDE,” *AIP Conf. Proc.*, vol. 576, no. 1, p. 265, 2001.

[129] J. P. Ramos *et al.*, “Intense ^{31,35}Ar beams produced with a nanostructured CaO target at ISOLDE,” *Nucl. Instrum. Methods B*, vol. 320, pp. 83–88, 2014.

[130] “SRIM - The Stopping and Range of Ions in Matter.” `http://www.srim.org/`. Accessed: 21 June 2022.

[131] “Micron Semiconductor Ltd.” `http://www.micronsemiconductor.co.uk/`. Accessed: 05 May 2022.

[132] “CAEN SpA.” `https://www.caen.it/products/a1422h/`. Accessed: 05 May 2022.

[133] “AIFIRA accelerator.” `https://www.in2p3.cnrs.fr/sites/institut_in2p3/files/page/2020-04/4-Doc-BARBERET.pdf`. Accessed: 05 May 2022.

[134] “ELJEN Technology.” `https://eljentechnology.com/products/plastic-scintillators`. Accessed: 05 May 2022.

[135] “ON Semiconductor Corporation.” `https://www.onsemi.com/`. Accessed: 01 May 2022.

[136] C. Neacsu, R. Lica, G. Pascovici, C. Mihai, and S. Rothe, “A miniaturized low-power SiPM-based β-detector for the ISOLDE Fast Tapestation,” *Nucl. Instrum. Methods A*, vol. 1006, 2022.

[137] “FASTER, a Fast Acquisition System for Nuclear Research.” `http://faster.in2p3.fr/`. Accessed: 05 May 2022.

[138] “CRADLE++ - Customisable RAdioactive Decay for Low Energy Particle Physics: A C++ event generator.” `https://github.com/leenderthayen/CRADLE`. Accessed: 27 June 2022.

[139] “ENSDF - Evaluated Nuclear Structure Data Files.” `http://www.nndc.bnl.gov/ensdf/`. Accessed: 27 June 2022.

[140] “Geant4 - Geometry ANd Tracking version 4.” `https://geant4-dev.web.cern.ch/`. Accessed: 28 June 2022.

[141] E. J. Nyström, “On the numerical integration of differential equations,” *Acta Soc. Sci. Fenn.*, vol. 50, pp. 1–55, 1925.

[142] “Geant4 - Electromagnetic physics.” `https://geant4.web.cern.ch/collaboration/working_groups/electromagnetic`. Accessed: 28 June 2022.

[143] S. Goudsmit and J. L. Saunderson, “Multiple Scattering of Electrons,” *Phys. Rev.*, vol. 57, pp. 24–29, 1940.

[144] S. Goudsmit and J. L. Saunderson, “Multiple Scattering of Electrons. II,” *Phys. Rev.*, vol. 58, pp. 36–42, 1940.

[145] I. Kawrakow and A. F. Bielajew, “On the representation of electron multiple elastic-scattering distributions for Monte Carlo calculations,” *Nucl. Instrum. Methods B*, vol. 134, no. 3, pp. 325–336, 1998.

[146] “ET - Enterpises Ltd.” https://et-enterprises.com/. Accessed: 21 November 2022.

[147] M. González-Alonso and J. Martin Camalich, “Isospin breaking in the nucleon mass and the sensitivity of β decays to new physics,” *Phys. Rev. Lett.*, vol. 112, no. 4, p. 042501, 2014.

[148] E. Kugler, “The ISOLDE facility at the CERN PS booster,” *Nucl. Instrum. Meth. B*, vol. 79, pp. 322–325, 1993.

[149] K. H. Reich, “The CERN Proton Synchrotron Booster,” *IEEE Trans. Nucl. Sci.*, vol. 16, pp. 959–961, 1969.

[150] A. Newborough, M. Buzio, and R. Chritin, “Upgrade of the CERN Proton Synchrotron Booster Bending Magnets for 2 GeV Operation,” *IEEE Trans. Appl. Supercond.*, vol. 24, no. 3, p. 0500304, 2014.

[151] P. Hoff, “Production of radioactive nuclides at ISOLDE,” *Nucl. Instrum. Meth. B*, vol. 79, no. 1, pp. 335–338, 1993.

[152] “ISOLDE yield database.” `https://isoyields2.web.cern.ch/`. Accessed: 09 May 2022.

[153] Y. Martinez Palenzuela *et al.*, “Enhancing the extraction of laser-ionized beams from an arc discharge ion source volume,” *Nucl. Instrum. Meth. B*, vol. 431, pp. 59–66, 2018.

[154] P. Schmidt, F. Ames, G. Bollen, O. Forstner, G. Huber, M. Oinonen, and J. Zimmer, “Bunching and cooling of radioactive ions with REXTRAP,” *Nucl. Phys. A*, vol. 701, pp. 550–556, 2002.

[155] “LabVIEW.” https://www.ni.com/en-us/shop/labview.html.

[156] D. Atanasov, F. Cresto, M. Pomorski, M. Versteegen, *et al.*, “Weak Interaction Studies with Radioactive ion-beams WISArD,” *in preparation*, 2022.

[157] C. Petrone, B. Bordini, M. Buzio, and S. Russenschuck, “A transducer for measuring the field quality in superconducting solenoids,” *IEEE Trans. App. Supercond.*, vol. 30, no. 4, pp. 1–5, 2020.

[158] N. Adimi *et al.*, “Detailed β-decay study of ^{33}Ar,” *Phys. Rev. C*, vol. 81, p. 024311, 2010.

[159] H. A. Bethe, “Moliere’s theory of multiple scattering,” *Phys. Rev.*, vol. 89, pp. 1256–1266, 1953.

[160] L. Urban, “A Model for Multiple scattering in Geant4.” CERN-OPEN-2006-077, 2006.

[161] D. Liljequist, “Critical path length for the similarity of elastic multiple scattering processes,” *J. Appl. Phys.*, vol. 62, no. 2, pp. 333–341, 1987.

[162] J. Apostolakis, V. Grichine, V. Ivanchenko, M. Maire, and L. Urban, “The recent upgrades in the ”standard” electromagnetic physics package,” in *XV International Conference on Computing in High Energy and Nuclear Physics (CHEP-06)*, (Mumbai, India), Feb. 2006.

[163] J. Apostolakis, A. Bagulya, S. Elles, V. N. Ivanchenko, O. Kadri, M. Maire, and L. Urban, “The performance of the geant4 standard EM package for LHC and other applications,” *J. Phys.: Conf. Ser.*, vol. 119, p. 032004, Jul 2008.

[164] V. N. Ivanchenko, O. Kadri, M. Maire, and L. Urban, “Geant4 models for simulation of multiple scattering,” vol. 219, no. 3, p. 032045, 2010.

[165] F. Salvat, “PENELOPE-2008 - A Code System for Monte Carlo Simulation of Electron and Photon Transport.” NEA report NEA/NSC/DOC, 2009.

[166] “RSICC Computer Code Collection.” Report CCC-715, LANL, Los Alamos, 2002.

[167] S. Agostinelli and al. (Geant4 Collaboration), “Geant4 — a simulation toolkit,” *Nucl. Instrum. Methods A*, vol. 506, no. 3, pp. 250–303, 2003.

[168] G. J. Lockwood, G. H. Miller, and J. A. Halbleib, “Simultaneous Integral Measurement of Electron Energy and Charge Albedos,” *IEEE Transactions on Nuclear Science*, vol. 22, no. 6, pp. 2537–2542, 1975.

[169] G. J. Lockwood, G. H. Miller, and J. A. Halbleib, “Electron Energy Deposition in Multilayer Geometries,” *IEEE Transactions on Nuclear Science*, vol. 23, no. 6, pp. 1862–1866, 1976.

[170] J. Halbleib, R. Kensek, G. Valdez, S. Seltzer, and M. Berger, “ITS: the integrated TIGER series of electron/photon transport codes - Version 3.0,” *IEEE Transactions on Nuclear Science*, vol. 39, no. 4, pp. 1025–1030, 1992.

[171] I. Kawrakow and D. W. O. Rogers, “The egsnrc system, a status report,” in *Advanced Monte Carlo for Radiation Physics, Particle Transport Simulation and Applications* (A. Kling, F. J. C. Baräo, M. Nakagawa, L. Távora, and P. Vaz, eds.), (Berlin, Heidelberg), pp. 135–140, Springer Berlin Heidelberg, 2001.

[172] D. E. Cullen, J. H. Hubbell, and L. Kissel, "EPDL97: the evaluated photo data library '97 version." doi:10.2172/295438, 1997.

[173] S. T. Perkins, D. E. Cullen, and S. M. Seltzer, "Tables and graphs of electron-interaction cross sections from 10 eV to 100 GeV derived from the LLNL Evaluated Electron Data Library (EEDL), Z = 1–100." doi:10.2172/5691165, 1991.

[174] S. T. Perkins, D. E. Cullen, M. H. Chen, J. Rathkopf, J. Scofield, and J. H. Hubbell, "Tables and graphs of atomic subshell and relaxation data derived from the LLNL Evaluated Atomic Data Library (EADL), Z = 1–100." doi:10.2172/10121422, 1991.

[175] R. Ribberfors, "Relationship of the relativistic Compton cross section to the momentum distribution of bound electron states," *Phys. Rev. B*, vol. 12, pp. 2067–2074, 1975.

[176] J. Brown, M. Dimmock, J. Gillam, and D. Paganin, "A low energy bound atomic electron Compton scattering model for Geant4," *Nucl. Instrum. Methods B*, vol. 338, pp. 77–88, 2014.

[177] C. Marquet *et al.*, "High energy resolution electron beam spectrometer in the MeV range," *J. Instrum.*, vol. 10, 2015.

[178] R. Arnold *et al.*, "Probing new physics models of neutrinoless double beta decay with SuperNEMO," *Eur. Phys. J. C*, vol. 70, p. 927, 2010.

[179] M. J. Berger, J. H. Hubbell, S. M. Seltzer, J. S. Coursey, and D. S. Zucker, "XCOM: photon cross section database (version 1.5)," *Natl. Inst. Stand. Technol. Gaithersburg, MD,* `http://physics.nist.gov/xcom`, 2010.

[180] M. J. Berger, J. S. Coursey, and D. S. Zucker, "ESTAR, PSTAR, and ASTAR: computer programs for calculating stopping-power and range tables for electrons, protons, and helium ions (version 1.2.3)," *Natl. Inst. Stand. Technol. Gaithersburg, MD,* `http://physics.nist.gov/Star`, 2005.

[181] K. Amako *et al.*, "Validation of Geant4 electromagnetic physics versus protocol data," *IEEE Symposium Conference Record Nuclear Science,* `doi:10.3390/s20216092`, 2004.

[182] M. Batic *et al.*, "Validation of Geant4 simulation of electron energy deposition," *IEEE Transactions on Nuclear Science*, vol. 60, no. 4, p. 2934–2957, 2013.

[183] G. Wentzel, *Z. Phys.*, vol. 40, p. 590, 1927.

[184] F. Salvat, J.M. Fernandez-Varea, J. Sempa, “PENELOPE – A code system for Monte Carlo simulation of electron and photon transport,” *NEA-OECD*, 2003.